Modeling and analysis of extracellular field potentials in the brain

Modellering og analyse av ekstracellulære feltpotensialer i hjernen

Philosophiae Doctor (PhD) Thesis

Henrik Lindén

Department of Mathematical Sciences and Technology
Norwegian University of Life Sciences

Ås 2010

Thesis number 2010:12
ISSN 1503-1667
ISBN 978-82-575-0967-5

Acknowledgements

This thesis would not have been possible without the collaboration, help and support from a number of people. I would first of all like to thank my supervisor Gaute Einevoll for continuing encouragement and guidance, and for always being a very cheerful and caring person. Your dedication to science is truly inspirational. I sincerely want to thank all co-authors of the papers presented in this thesis, especially Klas Pettersen and Tom Tetzlaff with whom I have worked closely in several of the projects presented here. Thanks for all the stimulating and interesting discussions! I also want to thank Sonja Grün and Markus Diesmann for an inspiring collaboration and for providing a very nice working atmosphere during my research stay at the RIKEN Brain Science Institute, Wako, Japan, in the Fall of 2009.

Ending up doing a PhD in computational neuroscience was certainly beyond my wildest dreams when I started my physics studies at Chalmers in Gothenburg just over ten years ago (in fact I did not even know that the field existed). In retrospect I realize that there are a few people who have had a large influence on me in ending up where I did: my high school mathematics teacher Jan-Erik Holgersson (who got me interested in science), my friend and fellow philosophy student Peter Ekberg (for countless discussions on the mysteries of the brain) and physics professor Bernhard Mehlig at the MSc Programme in Complex Adaptive Systems at Chalmers (whose inspiring lectures introduced me to applying physical reasoning to biological systems). But perhaps the most important influence was Sonja Grün who was leading the Neuroinformatics and Theoretical Neuroscience Group at the Free University in Berlin where I wrote my MSc thesis around five years ago. Being a student in her lab was a great experience and after there being introduced to the field of computational neuroscience I was hooked.

I have been fortunate to be surrounded by great colleagues, both in the Computational Neuroscience group at Ås and in the group of Sonje Grün and Markus Diesmann at the RIKEN Brain Science Institute. I will not name everyone (to avoid forgetting someone), but thank you all.

Working on a thesis can be stressful at times and finishing this work would not have been possible without the great support of my family and friends. Thanks to my brother David, father Bo-Anders and mother Lisbeth for constant love and encouragement. Thanks to all friends who have helped me to remember that there are other things in life than work. And finally, I want to thank Åsa Bergman and Tonje Bones Rustad, for being there.

Abstract

In order to model processes occuring in the brain it is necessary to have reliable measures of neural activity, with a clear intepretation rooted in the biophysics of the neural tissue. One of the most important probes of neural activity is the measurement of extracellular field potentials. The potential picked up by an electrode placed inside the brain is typically filtered in to two distinct frequency bands: the high-frequency part ($\gtrsim$ 500 Hz) captures the spiking output of nearby cells (termed multi-unit activity or MUA), while the low-frequency part ($\lesssim$ 200-500 Hz) called local field potential (LFP) is thought to mainly reflect synaptic input of the cells in a local volume surrounding the electrode. The ability of the LFP to sample activity in whole populations of neurons makes it an important tool for understand neural network dynamics. Despite its wide use, there is however only limited knowledge about the relation between the measured LFP signal and the underlying neural activity.

This thesis addresses different aspects of the relation beween activity at the single-cell or population level and the measured extracellular potential. First, we characterize the salient features of extracellular potentials generated by a single synaptic input. We use a forward-modeling approach where we simulate the LFP generated by neurons with realistic morphologies. We describe how dendrites, due to passive cable properties, filter the signal between input current and measured potential, and propose simplified models of LFP generation.

Second, we show how distributions of synapses on to single cells give power-law scaling in power spectra of soma currents, soma potentials and current dipole moments.

Third, we investigate the size of the cortical region that contributes to LFP recordings. By a combination of a simplified model and numerical simulations of populations of neurons, we identify the main factors determining the size of this region. Specifically, we highlight the role of correlations in the underlying synaptic activity.

Finally, we analyze data from monkey motor cortex and relate oscillations in the LFP to temporally precise synchronized spiking activity.

In summary, the findings presented in this thesis provide building blocks for further modeling and interpretation of the LFP, as well as other extracellular potential measures such as the electroencephalogram (EEG).

Sammendrag

For å modellere prosesser i hjernen er det nødvendig med pålitelige målinger av den nevrale aktiviteten, med en klar kobling til underliggende prosesser. En av de viktigste målemetodene av nevral aktivitet er måling av ekstracellulært elektrisk potensiale. Potensialet som blir plukket opp av en måleelektrode i hjernen bli typisk splittet i to forskjellige frekvensregimer: høyfrekvensregimet ($\gtrsim$ 500 Hz) plukker opp fyring av nevroner i nærheten av elektroden (kalt 'multi-unit activity', MUA), mens lavfrekvensregimet ($\lesssim$ 200-500 Hz), som kalles 'local field potential' (LFP), reflekterer synaptisk aktivitet i celler i nærheten av elektroden. Siden LFP er et mål på aktiviteten i hele populasjoner av nevroner, er den et viktig mål for å forstå nevral nettverkdynamikk. Til tross for utbredt bruk, er det likevel liten kunnskap om sammenhengen mellom målt LFP og den underliggende nevrale aktiviteten.

Denne avhandlingen har fokus på flere aspekter ved sammenhengen mellom enkeltcelleaktivitet og aktivitet på populasjonsnivå, og det målte elektriske potensialet. Først karakteriserer vi iboende egenskaper ved elektriske potensialer fra enkeltsynapsebidrag. Så simulerer vi LFP fra nevroner med realistisk romlig struktur. Vi beskriver hvordan dendritter, gjennom sin passive membran, filtrerer signalet fra input strøm til målt elektrisk potensial, og foreslår forenklede modeller for LFP generering.

Deretter viser vi hvordan synaptisk aktivitet i enkeltnevroner gir $1/f^{\alpha}$-skalering i power spectra av transmembrane somastrømmer, soma potensialer og dipolstrømmer.

For det tredje studerer vi størrelsen på det corticale området som bidrar til LFP målingene. Ved en kombinasjon av forenklede modeller og numeriske simuleringer av populasjoner av nevroner, identifiserer vi hovedfaktorene for hva som bestemmer størrelsen på dette området. Her studerer vi spesielt korrelasjoner i den underliggende synaptiske aktiviteten.

Til sist analyserer vi data fra motor cortex til aper og relaterer oscillasjoner i LFP til synkronisitet i fyringsaktivitet.

Resultatene i denne avhandlingen vil være et bidrag til ytterligere modellering og tolking av LFP, og også av andre typer målte ekstracellulære elektriske potensialer som EEG.

List of papers:

I Pettersen K.H., Lindén H., Dale A.M., and Einevoll G.T. Extracellular spikes and multi-electrode recordings. In R. Brette, & A. Destexhe (Eds.), *Handbook of neural activity measurements.* Cambridge, UK: Cambridge University Press. (*to appear*)

II Lindén H, Pettersen K.H., and Einevoll G.T. Intrinsic dendritic filtering gives low-pass power spectra of local field potentials. *Journal of Computational Neuroscience* (*to appear, available as Online First*) `http://dx.doi.org/10.1007/s10827-010-0245-4`

III Pettersen K.H., Lindén H. , Tetzlaff T., and Einevoll G.T. Linking power laws for microscopic and macroscopic neural activity. (*to be submitted*)

IV Lindén H. , Tetzlaff T., Potjans T.C., Pettersen K.H., Grün S., Diesmann M., and Einevoll G.T. How local is the local field potential? (*to be submitted*)

V Denker M., Roux S., Lindén H., Diesmann M., Riehle A., and Grün S. The local field potential reflects surplus spike synchrony. (*submitted to Cerebral Cortex, available online as preprint version:*) `http://arXiv.org/abs/1005.0361v1`

Contents

1 Introduction

The human brain is one of the most intriguing systems that we know of. Consisting of around 100 billion nerve cells with 1000 times or so more connections between them (Williams and Herrup, 1988), it makes up a highly complex system with sophisticated information-processing capabilites. Mechanisms in our brains underlie all of our emotions, cognitive abilites and conscious experiences. Thanks to our brains we are able to make inner representations of the world we are living in and to discuss these representations with each other. These abilities of our brain is also what has enabled our scientific exploration. As we humans are driven by a curiosity to understand things, it is therefore maybe not surprising that we also would like to understand the very mechanisms that make us understand; that is, the computational power of our own brain.

Dynamic processes in the brain are organized at different spatial scales; ranging from microscopic molecular mechanisms within single nerve cells to the macroscopic cooperative dynamics of large groups of neurons in different areas of the brain. Linking models of processes occuring at the single cell level to networks of neurons and ultimately to the global dynamics of the brain is one of the major challenges in modern neuroscience. But the characterization and modeling of the dynamics at different levels require reliable measures of neural activity, with a clear interpretation rooted in the biophysics of the neural tissue.

One of the most important probes of neural activity is the measurement of extracellular field potentials that arise when electrically charged ions pass through the membranes of neurons. For instance, by placing a sharp electrode in the vicinity of the somata of nerve cells it is possible to record the rapid extracellular potential fluctuation due to the spiking output of the neurons (termed action potentials) resulting from the local influx of sodium and outflux of potassium ions through the membranes of the neuron. Typically lasting only a millisecond or less, the action potential signatures are contained in the high-frequency ($\gtrsim$ 500 Hz) band of the extracellularly recorded voltage, and consequently the signal is usually high-pass filtered producing what is called multi-unit activity (MUA). Using two (stereotrode), four (tetrode) or more electrodes close together allows for triangulation to ascribe the timing of action potentials to single cells, resulting in what is called single-unit activity (SUA). With modern spike-sorting techniques it is possible to distinguish between tens of neurons within 50 μm from such an electrode setup, and up to hundreds of neurons using multi-shank electrodes (Buzsáki, 2004). With on the order of 10000 neurons in a cubic millimeter of cortex (Abeles, 1991), this however represents a substantial undersampling of the local neuronal population.

The low-frequency ($\lesssim$ 200-500 Hz) part of the extracellular voltage, termed local field potential (LFP), on the other hand, presumably represents the summed activity of a large number cells in the vicinity of the electrode and may therefore, due to a better sampling of nearby populations of neurons, be useful in understanding local network activity. The LFP is thought to mainly reflect synaptic input currents (Mitzdorf, 1985), but in contrast to the MUA signal, the relation to the underlying neural activity is far from well understood.

Scope of thesis

This thesis addresses the link between neuronal activity and extracellularly recorded potentials, in particular the LFP. Specifically, three topics are investigated:

1. **Frequency content of extracellular field potentials** (papers **I-III**)
2. **Spatial reach of LFP recordings** (paper **IV**)
3. **Relation between LFP oscillations and synchronized spiking activity** (paper **V**)

The following sections contain short introductions to each of these topics along with summaries of the results presented in the included papers I-V.

1.1 Frequency content of extracellular field potentials

The background power spectrum of extracellular potential recordings have recently received considerable interest due to ubiquitously observed $1/f^{\alpha}$ frequency scaling both in LFP signals (Milstein et al., 2009), in cortical surface potentials (ECoG)(Miller et al., 2009) as well as in the extracranial encephalogram (EEG) (e.g. Freeman et al. (2003)), with α ranging from $\sim$1 to $\sim$4. The meaning of these findings is however not clear. $1/f$-scaling is a description of scale invariance in a system and has been characterized as a hallmark of self-organized criticality found for different types of physical systems in nature, including earthquakes and avalanches (Bak et al., 1987). It has been suggested that the $1/f$-scaling in brain potentials also could be reflecting self-organized criticality in brain dynamics (Linkenkaer-Hansen et al., 2001; Buzsáki, 2006), although this is still debated (Bédard et al., 2006).

However, in order to judge if $1/f$-scaling in measured potential reflects the same scaling in neuronal activity, it is necessary to first know which filtering mechanisms are involved in the generation and volume conduction of the extracellular potential. Following this idea, Bédard et al. (2006) attempted to recreate the measured power spectrum of the LFP from the spiking activity recorded in the same region as the LFP signal, since the the input currents caused by the arrival of presynaptic spikes are thought to be the main generator of the LFP. They assumed that the recorded spike trains were statistically equivalent to the spikes arriving at the synaptic sites in the local region and that each spike gave rise to an exponentially relaxing input current. Given a certain 'drive' $D(t)$ to the neurons (consisting of the input spike trains) the total synaptic current $I(t)$ can be expressed as the convolution

$$I(t) = \int_{-\infty}^{\infty} D(t')\text{exp}[-(t-t')/\tau_s]dt' \tag{1}$$

where τ_s is the synaptic time constant. Since a convolution is equivalent to a multiplication in the Fourier domain this yields a power spectral density (PSD) of the input current given by

$$|I(\omega)|^2 = \frac{|D(\omega)|^2}{1+\omega^2\tau_s^2} \tag{2}$$

where ω denotes angular frequency. Bédard et al. found that, compared to the PSD of the recorded LFP signal, a factor $1/f$ was 'missing' and suggested that this additional factor could come from frequency-specific filtering of currents in the extracellular medium. Such a filtering effect has however been debated, as there are experimental and theoretical findings arguing both for (Gabriel et al., 1996; Bédard et al., 2004; Bédard and Destexhe, 2009; Bédard et al., 2010; Dehghani et al., 2010) and against it (Logothetis et al., 2007).

In this thesis we investigate an additional source of filtering arising from the cable properties of neuronal dendrites. Previously shown to give a filtering of the extracellular high-frequency signatures of action potentials (Pettersen and Einevoll, 2008), this mechanism is througout papers I-III shown to affect field potentials arising from synaptic currents in the frequency-range captured by the LFP. We argue that for a more accurate description of the spectral relation between input spike trains and recorded LFP ϕ, the above expression should be extended to include also this dendritic filtering:

$$\text{PSD}(\phi(\omega)) = |I(\omega)|^2 \cdot |F_{dendritic}|^2 \cdot |F_{medium}|^2 \tag{3}$$

where $F_{dendritic}$ and F_{medium} represents filters in the dendrites and in the medium, respectively.

Paper I The first paper of this thesis serves partly as a more comprehensive introduction to extracellular measurements than the present section. In particular, we outline the biophysical principles behind the generation of extracellular potentials and describe the forward-simulation scheme used throughout papers I-IV. We also discuss used assumptions of the extracellular medium.

We then present example results using the forward-modeling scheme to illustrate the salient features of the LFP generated by synaptic activity. The mechanism of dendritic filtering is illustrated with simulations of a layer 5 pyramidal cell: A single synaptic input at an apical synapse generates positive and negative deflections of the extracellular potential in vicinity of the cell. The sign of the deflection depends on the position of the recording electrode; for positions where the synaptic input current dominates the sign is negative (due to the current sink produced by the synapse) and for positions close to the soma of the cell the sign is positive (due to positive return currents through the cell's membrane). In addition, the extracellular potential shows a position-dependent filtering compared to the input current; for recordings close the synapse the deflections contains more high frequencies than recordings close to the soma. This effect can be understood from the passive cable-properties of the dendrites; for low frequencies more current propagates to the soma compartments while for higher frequencies a larger fraction of return currents leave the cell close to the synapse. This is further illustrated by injection of sinusoidal currents at ten apical synapses of the same pyramidal cell and and then plotting the amplitude (envelope) of return currents along the apical direction of the cell.

In this paper we also revisit modeling results published previously, including

- the effect of dendritic filtering on extracellular signatures of action potentials explained through the concept of a frequency-dependent dipole length (Pettersen and Einevoll, 2008),
- forward-modeling results of MUA and LFP from columnar population activity (Pettersen et al., 2008),
- and estimation of current-source density (CSD) from LFPs by using the *inverse* CSD method (*iCSD*) (Pettersen et al., 2006).

Paper II The second paper in this thesis is an extensive numerical study of the dendritic filtering effect described above. We show simulation results for a layer 5 pyramidal and a layer 4 stellate cell from cat visual cortex for input at single synapses. By injecting a white-noise current (i.e. a noise current with a flat power spectrum) we isolate the effect of the dendritic filtering from that of synaptic filtering. For the layer 5 cell the measured power spectrum of the extracellular potential is shown to be highly dependent of recording position; at most positions the power spectrum exhibits low-pass characteristics while some recording positions the dendritic filtering gives band-pass filtering. Furthermore, the frequency content of the extracellular potential is typically more flat close to the synaptic input, with a more pronounced filtering further away from the synapse. Also the layer 4 cells exhibits pronounced low-pass filtering, but in a higher frequency range ($>\sim$ 100 Hz) compared to the layer 5 cell ($>\sim$ 10 Hz). Following the idea in Pettersen and Einevoll (2008) we characterize the dendritic filtering by the corresponding frequency dependence of the current dipole moment. Since the cell due to current conservation produces no total current monopole contribution, the current dipole moment represents the first order of a multi-pole expansion of the current-source distribution generated by the synaptic input. In search for an simplified model that can account for the gross features of the extracellular potential of the layer 5 cell we investigate two approximate models: the *dipole model* where the potential around the cell is represented by the far-field dipole expression and a *two-monopole model* where the potential is generated by a current sink placed at the location of the synapse and a current source in the soma of the cell. For both models the dipole moment is adjusted to fit with the numerically obtained values for the detailed multi-compartment model. While both simplified models reproduce the results of the more detailed model both in terms of frequency content and distance-dependence of the LFP at large distances ($>\sim$ 1 mm), the performance at closer distances is not more than fair, suggesting that such simplified models may be of more use in the modeling of EEG than of LFP.

Paper III In this paper the numerical results from paper II are extended to the situation of many simultaneously active synapses on a single cell. A simplified ball-and-stick cell model is shown to qualitatively account for most of the salient features of the layer 5 pyramidal cell in terms of power spectra of soma membrane potential, dipole moment and soma current. For all these three measures the combined effect of multiple synapses is shown to give a more linear decay of the power spectra in the high-frequency limit compared to single synapses (investigated in paper II). The cable equation for the ball-and-stick model is solved in frequency space to give analytical results for the single-synapse expressions which are then integrated to give predictions of the decay slope α in the high-frequency limit. For uncorrelated white-noise input we find a systematic difference in α of 1 between the power spectra of soma currents (α=0.5), dipole moments (α=1.5) and soma membrane voltage (α=2.5) in the asymptotic high-frequency limit. For correlated input currents the asymptotic values are higher (α=1,2,3 respectively). In the frequency range typically recorded in LFP or EEG experiments, however, the power spectra typically exhibit 'quasi-linear' regimes with a slightly lower α. Even though explicit modeling of the extracellular potentials is not done in this paper, these results have, in light of the findings in paper I, direct implications for the interpretation of extracellular potentials recorded far from cells, especially the EEG.

1.2 Spatial reach of LFP recordings

A key question in the interpretation of experimentally recorded LFPs is how large the brain region that generates the signal is, or in other words how many neurons an LFP electrode can 'see'. For instance, does an oscillatory LFP signal reflect the rhythmic activity of a large brain region or just a small cell population close to the electrode? And how should one interpret that LFP signals measured at neighbouring sites have been found to be correlated several millimeters apart (Destexhe et al., 1999; Nauhaus et al., 2009)? Does this mean that the underlying neural activity is correlated between the different recording sites, or that the LFP generated in one area spreads through the tissue to the other recording sites by volume conduction?

Several recent experimental studies have investigated how local the LFP is by comparing it to other measures of neural activity such as voltage-sensitive dye (VSD) (Katzner et al., 2009), spiking activity (Kreiman et al., 2006; Xing et al., 2009) in combination with known spatial organization of cortical columns (Liu and Newsome, 2006) or ocular dominance (Berens et al., 2008). Results vary from a few hundred micrometers (Katzner et al., 2009; Xing et al., 2009) to several millimeters (Kreiman et al., 2006). One may speculate that this discrepancy could be attributed to differences in animal species, cortical areas or stimulation paradigms used. However, these studies also highlight the inherent difficulty in experimental studies to disentangle the properties of the neuronal activity from the biophysical phenomena involved in the generation of the recorded LFP signals.

Paper IV In this paper we use a biophysical forward-modeling approach to investigate which factors influence the reach of an LFP electrode placed in the center of a cylindrical neuronal population. Since the LFP is a sum of contributions from a number of cells in the vicinity of the recording electrode, the amplitude of the signal is expected to grow with the size of the population. We reason that if the amplitude reaches a finite value for a certain population radius, a natural definition of the reach of the electrode may be the population radius where the amplitude has reached e.g. 95 % of the maximum value. By using a simplified model we first identify the main determining factors of the LFP reach: *i*) the distance-dependence of single cell LFP contributions, *ii*) the increase in number of cells with increasing population radius, and *iii*) the amount of correlation between single cell LFP contributions. Only if the single-cell contributions decay as $1/r^2$ or more rapidly, and the contributions from different cells are uncorrelated, does the LFP amplitude converge to a constant value, otherwise it grows unbounded with population radius.

We then investigate these effects in populations of morphologically reconstructed neurons of three different cell types (a layer 3 pyramidal, a layer 4 stellate and a layer 5 pyramidal cell). The single-cell decay shows, for all cell types, a $1/r^2$-decay far from the electrode with a slower decay close to the electrode. For uncorrelated synaptic input, this results in a spatial reach of a few hundred micrometers, with the shortest reach and highest amplitude at the cortical level of the cell somata. If synaptic inputs are correlated, the reach is in some cases substantially larger, in fact it is shown to be limited only by either the size of the contributing population, or the spatial extent of the correlations in synaptic input. The reach for a population of more symmetric layer 4 cells is less affected by input correlations than the more asymmetric layer 5 pyramidal cells, and this is explained by how well correlations in synaptic input are transferred to correlation between LFP contributions. Finally, we discuss how these findings might reconcile the different results of previous experimental studies and the possible implications for the interpretation of correlated LFP signals at different recording positions.

1.3 Relation between LFP oscillations and synchronized spiking activity

Oscillatory components in LFP signals have been observed in a wide range of brain regions and experimental settings. These components are typically classified according to their dominating frequency range and behavioral correlates (Buzsáki and Draguhn, 2004). The role of oscillations in brain function has been a topic of intensive study (see e.g. the book by Buzsáki (2006)) but how different aspects of rhythmic activity in networks of neurons are related to LFP oscillations is not clear.

In motor cortex, LFP oscillations in the β-frequency range ($\sim$ 15-45 Hz) have been observed during movement preparation (Murthy and Fetz, 1992; Donoghue et al., 1998; Rickert et al., 2005) while lower-frequency components typically dominate during movement onset and execution (Rickert et al., 2005; Roux et al., 2006). Unlike the lower-frequency components (Mehring et al., 2003), β-oscillations show no tuning-preferences for movement direction and their role in motor computation has rather been related to attention and sensorimotor integration than to movement execution (Murthy and Fetz, 1992; Rickert et al., 2005).

At the single-cell level neurons have been shown to spike at a preferred phase of the β-oscillation (Murthy and Fetz, 1996; Denker et al., 2007) suggesting that the LFP oscillations reflect synchronized spiking activity at the frequency of the oscillation. Furthermore, during periods of movement preparation, spiking activity from pairs of neurons have been shown to synchronize with millisecond temporal precision, independent of their modulation in firing rate (Riehle et al., 1997; Kilavik et al., 2009). This has been interpreted as a sign of temporally precise activation of groups of neurons (in line with the hypothesis of so-called cell assemblies (Hebb, 1949)). A clear relation between LFP oscillations and the timing of synchronized spiking activity, although often assumed, has however not been demonstrated.

Paper V In this paper we analyze data recorded from monkey motor cortex during the preparatory period of a movement task to investigate the link between LFP oscillations and temporally precise spike synchrony. LFPs and spikes are recorded with different electrodes with a spacing of 400 μm and the relation between spiking activity and LFP oscillations is investigated. Average LFP from signals filtered close to the β-range (10-22 Hz) are computed by spike-triggered averages (STA) in a time window centered on the spike times. To avoid contamination of spike signatures in the LFP, only spikes and LFP recorded with different electrodes are considered. We separate between spiking events from only one neuron (isolated spikes, ISO) and synchronized spiking events (with a temporal precision of 3 ms) between pairs of neurons (chance coincidences, CC). If the occurrence of synchronized (coincident) events is higher than the chance-level expected by the individual neuron firing rates, these are labeled Unitary Events (UE), according to the previously developed Unitary Events method (Grün et al., 2002).

We find that STAs of synchronized spiking activity (CC and UE) have a significantly higher magnitude than those of isolated spikes (ISO). Moreover, the spike-triggered average of UE is larger than that of CC. The STAs exhibit a clear β-frequency component, and the STAs are typically centered on the onward phase of the oscillations. We then perform further analysis to identify which factors cause the difference in STA magnitude. By extracting the phase and instantaneous amplitude (envelope) of the LFP signal we investigate their relation to spiking separately. We find that synchronously emitted spikes are better phase-locked to the LFP oscillation than isolated ones. For chance coincidences (CC) this can be explained by a predictor obtained from the phase-locking of single neurons. For spike synchrony above the chance level (UE), the pronounced phase-locking can however not be explained in this way. Amplitude of LFP oscillations are only weakly related to the probability of synchronized spiking, but synchronized events occuring during high-amplitude oscillations are on average better locked to the LFP than low amplitudes.

We interpret these results as an indication that LFP oscillations carry information about the activation of temporally precise patterns of synchronized network activity (cell assemblies). However, since neurons in motor cortex may use several parallel coding schemes (Riehle et al., 1997), only a fraction of spikes are involved in this type of activation. Finally, we present and discuss a conceptual model to estimate the level of participation from the phase distribution of the LFP at spike times.

2 General discussion and future directions

The work presented in this thesis provides building blocks for the modeling and interpretation of extracellular field potentials recorded both inside (LFP) and on the surface of the brain (ECoG), and outside the scull (EEG).

In papers I-II we describe the biophysical principles behind the generation of extracellular potentials from nerve cells, and how to study them using computer simulations. We describe how dendrites, due to passive cable properties, give low-pass filtering effects between synaptic currents and measured potentials. We use the concept of current dipole moments to explain this frequency-filtering effect, and present simplified models of the generation of extracellular potentials to represent the complicated morphological structure of realistic neurons.

In paper III we show that when neurons receive input at synapses homogeneously spread over the dendritic structure, this gives power spectra with $1/f^\alpha$ power-law scaling, in soma potential as well as in dipole moment (representing the single-cell contribution to the EEG), for intermediate to high frequencies.

In paper IV we study the spatial reach of cortical LFP recordings by combining a simplified model with detailed numerical simulations, to identify which factors influence the spatial summation of the recorded LFP signal. In particular, we highlight the role of correlations in synaptic activity.

Finally, in paper V we investigate the relation between LFP oscillations and synchronized spiking activity in experimentally recorded data, thereby linking the mescoscopic LFP signal to the concept of cell assemblies.

All of the presented papers thus have a clear ambition to bridge models at different levels of description; from neuronal activity at one level to measurable quantities at another:

- from the activation of single synapses to contributions in LFP and EEG,
- from single-synapse filtering to power-law expressions in EEG contributions for many simultaneously active synapses
- from spatial decay of single-cell LFP contributions to spatial reach of the population LFP signal, and
- from synchronized spiking activity to LFP oscillations.

In most of these cases the bridge in levels of description also represents a bridge in spatial scale; from microscopic (single-synapse or single-cell level) to macrosopic (population-level LFP/EEG). A reduction in complexity of the microscopic models is therefore necessary, which is the motivation to introduce simplified models: e.g. the dipole current moment as a simplification of more complicated current-source density distributions, and the ball-and-stick model to represent the salient features of more complicated dendritic structures.

2.1 Towards large-scale modeling of LFP / EEG

Such simplified models will be useful when embarking on future projects of linking large-scale network models to measured LFP or EEG signals. Some attempts in this direction have already been made (see e.g. Mazzoni et al.

(2008, 2010)), using simpler models of LFP generation than the ones presented here. It should be a natural ambition of network modelers to provide predictions of measurable quantities such as LFP, EEG and VSD signals, and for this, biophysically realistic models of the signal generation are needed. The work presented in this thesis provides starting points for such pursuits.

There are, however, still many issues open for investigation. For instance,

- How do the details of dendritic structure influence the magnitude of EEG contributions from different neuronal populations?
- How do contributions from several simultaneously active populations determine the laminar variation in LFP signals? (Lindén et al., 2009)
- Does the dendritic filtering described in this thesis influence the spatial reach of different frequency components of the LFP?
- Do the predictions of the models presented here change when using (non-linear) conductance-based models of synapses and other active membrane conductances?

When compared to experimental recordings, these models should also be combined with accurate models of filtering in the extracellular medium for the LFP (e.g. Bédard et al. (2004)) and with effects resulting from non-isotropies when signals pass through different types of tissue for the EEG (Nunez, 2006).

The forward-modeling approach used here could also be extended to make accurate models of the VSD signal, in line with recently published work by Chemla and Chavane (2010).

The advances in modeling of extracellular field potentials are dependent on appropriate simulation technology. We are currently developing a Python-based toolbox under the working name 'LFPy' that runs in combination with the NEURON software (Carnevale and Hines, 2006), with the aim of providing this toolbox to a wider group of users.

References

Abeles, M. (1991). *Corticonics: Neural Circuits of the Cerebral Cortex*. Cambridge University Press.

Bak, P., Tang, C., and Wiesenfeld, K. (1987). Self-organized criticality: An explanation of the 1/f noise. *Phys. Rev. Lett.*, 59(4):381–384.

Bédard, C. and Destexhe, A. (2009). Macroscopic models of local field potentials and the apparent 1/f noise in brain activity. *Biophys J*, 96(7):2589–603.

Bédard, C., Kröger, H., and Destexhe, A. (2004). Modeling extracellular field potentials and the frequency-filtering properties of extracellular space. *Biophys J*, 86(3):1829–42.

Bédard, C., Kröger, H., and Destexhe, A. (2006). Does the 1/f frequency scaling of brain signals reflect self-organized critical states? *Phys. Rev. Lett.*, 97(11):4.

Bédard, C., Rodrigues, S., Roy, N., Contreras, D., and Destexhe, A. (2010). Evidence for frequency-dependent extracellular impedance from the transfer function between extracellular and intracellular potentials : Intracellular-lfp transfer function. *J Comput Neurosci*.

Berens, P., Keliris, G. A., Ecker, A. S., Logothetis, N. K., and Tolias, A. S. (2008). Comparing the feature selectivity of the gamma-band of the local field potential and the underlying spiking activity in primate visual cortex. *Front. Syst. Neurosci.*, 2:2.

Buzsáki, G. (2004). Large-scale recording of neuronal ensembles. *Nat Neurosci*, 7(5):446–51.

Buzsáki, G. (2006). *Rhythms of the brain*. Oxford University Press.

Buzsáki, G. and Draguhn, A. (2004). Neuronal oscillations in cortical networks. *Science*, 304(5679):1926–9.

Carnevale, N. T. and Hines, M. L. (2006). *The NEURON Book*. Cambridge University Press.

Chemla, S. and Chavane, F. (2010). A biophysical cortical column model to study the multi-component origin of the VSDI signal. *NeuroImage*, 53(2):420–38.

Dehghani, N., Bédard, C., Cash, S. S., Halgren, E., and Destexhe, A. (2010). Comparative power spectral analysis of simultaneous electroencephalographic and magnetoencephalographic recordings in humans suggests nonresistive extracellular media : EEG and MEG power spectra. *J Comput Neurosci*.

Denker, M., Roux, S., Timme, M., Riehle, A., and Grun, S. (2007). Phase synchronization between LFP and spiking activity in motor cortex during movement preparation. *neurocomp*, 70(10-12):2096–2101.

Destexhe, A., Contreras, D., and Steriade, M. (1999). Spatiotemporal analysis of local field potentials and unit discharges in cat cerebral cortex during natural wake and sleep states. *J Neurosci*, 19(11):4595–608.

Donoghue, J. P., Sanes, J. N., Hatsopoulos, N. G., and Gaál, G. (1998). Neural discharge and local field potential oscillations in primate motor cortex during voluntary movements. *j neurophysiol*, 79(1):159–73.

Freeman, W. J., Holmes, M. D., Burke, B. C., and Vanhatalo, S. (2003). Spatial spectra of scalp EEG and EMG from awake humans. *Clin Neurophysiol*, 114(6):1053–68.

Gabriel, S., Lau, R. W., and Gabriel, C. (1996). The dielectric properties of biological tissues: II. measurements in the frequency range 10 hz to 20 ghz. *Phys Med Biol*, 41(11):2251–69.

Grün, S., Diesmann, M., and Aertsen, A. (2002). Unitary events in multiple single-neuron spiking activity: I. detection and significance. *Neural Comput*, 14(1):43–80.

Hebb, D. O. (1949). *The organization of behavior: a neuropsychological theory*. New York: Wiley.

Katzner, S., Nauhaus, I., Benucci, A., Bonin, V., Ringach, D., and Carandini, M. (2009). Local origin of field potentials in visual cortex. *Neuron*, 61(1):35–41.

Kilavik, B. E., Roux, S., Ponce-Alvarez, A., Confais, J., Grün, S., and Riehle, A. (2009). Long-term modifications in motor cortical dynamics induced by intensive practice. *J Neurosci*, 29(40):12653–63.

Kreiman, G., Hung, C. P., Kraskov, A., Quiroga, R. Q., Poggio, T., and DiCarlo, J. J. (2006). Object selectivity of local field potentials and spikes in the macaque inferior temporal cortex. *Neuron*, 49(3):433–45.

Lindén, H., Potjans, T. C., Einevoll, G. T., Grün, S., and Diesmann, M. (2009). Modeling the local field potential by a large-scale layered cortical network model. In *Front. Neur. Conference Abstract: Neuroinformatics 2009.*

Linkenkaer-Hansen, K., Nikouline, V. V., Palva, J. M., and Ilmoniemi, R. J. (2001). Long-range temporal correlations and scaling behavior in human brain oscillations. *J Neurosci*, 21(4):1370–7.

Liu, J. and Newsome, W. T. (2006). Local field potential in cortical area mt: stimulus tuning and behavioral correlations. *J Neurosci*, 26(30):7779–90.

Logothetis, N. K., Kayser, C., and Oeltermann, A. (2007). In vivo measurement of cortical impedance spectrum in monkeys: implications for signal propagation. *Neuron*, 55(5):809–23.

Mazzoni, A., Panzeri, S., Logothetis, N. K., and Brunel, N. (2008). Encoding of naturalistic stimuli by local field potential spectra in networks of excitatory and inhibitory neurons. *PLoS Comput Biol*, 4(12):e1000239.

Mazzoni, A., Whittingstall, K., Brunel, N., Logothetis, N. K., and Panzeri, S. (2010). Understanding the relationships between spike rate and delta/gamma frequency bands of lfps and eegs using a local cortical network model. *NeuroImage*, 52(3):956–72.

Mehring, C., Rickert, J., Vaadia, E., de Oliveira, S. C., Aertsen, A., and Rotter, S. (2003). Inference of hand movements from local field potentials in monkey motor cortex. *Nat Neurosci*, 6(12):1253–4.

Miller, K. J., Sorensen, L. B., Ojemann, J. G., and den Nijs, M. (2009). Power-law scaling in the brain surface electric potential. *PLoS Comput Biol*, 5(12):e1000609.

Milstein, J., Mormann, F., Fried, I., and Koch, C. (2009). Neuronal shot noise and brownian 1/f2 behavior in the local field potential. *PLoS ONE*, 4(2):e4338.

Mitzdorf, U. (1985). Current source-density method and application in cat cerebral cortex: investigation of evoked potentials and EEG phenomena. *Physiol Rev*, 65(1):37–100.

Murthy, V. N. and Fetz, E. E. (1992). Coherent 25- to 35-hz oscillations in the sensorimotor cortex of awake behaving monkeys. *Proc Natl Acad Sci USA*, 89(12):5670–4.

Murthy, V. N. and Fetz, E. E. (1996). Synchronization of neurons during local field potential oscillations in sensorimotor cortex of awake monkeys. *J Neurophysiol*, 76(6):3968–82.

Nauhaus, I., Busse, L., Carandini, M., and Ringach, D. L. (2009). Stimulus contrast modulates functional connectivity in visual cortex. *Nat Neurosci*, 12(1):70–6.

Nunez, P. L. (2006). *Electric Fields of the Brain: The Neurophysics of EEG.* Oxford University Press.

Pettersen, K. and Einevoll, G. (2008). Amplitude variability and extracellular low-pass filtering of neuronal spikes. *Biophys J*, 94(3):784–802.

Pettersen, K. H., Devor, A., Ulbert, I., Dale, A. M., and Einevoll, G. T. (2006). Current-source density estimation based on inversion of electrostatic forward solution: effects of finite extent of neuronal activity and conductivity discontinuities. *Journal of Neuroscience Methods*, 154(1-2):116–33.

Pettersen, K. H., Hagen, E., and Einevoll, G. T. (2008). Estimation of population firing rates and current source densities from laminar electrode recordings. *J Comput Neurosci*, 24(3):291–313.

Rickert, J., de Oliveira, S. C., Vaadia, E., Aertsen, A., Rotter, S., and Mehring, C. (2005). Encoding of movement direction in different frequency ranges of motor cortical local field potentials. *J Neurosci*, 25(39):8815–24.

Riehle, A., Grün, S., Diesmann, M., and Aertsen, A. (1997). Spike synchronization and rate modulation differentially involved in motor cortical function. *Science*, 278(5345):1950–3.

Roux, S., Mackay, W. A., and Riehle, A. (2006). The pre-movement component of motor cortical local field potentials reflects the level of expectancy. *Behav Brain Res*, 169(2):335–51.

Williams, R. W. and Herrup, K. (1988). The control of neuron number. *Annu Rev Neurosci*, 11:423–53.

Xing, D., Yeh, C.-I., and Shapley, R. M. (2009). Spatial spread of the local field potential and its laminar variation in visual cortex. *J Neurosci*, 29(37):11540–9.

3 Papers

3.1 Paper I

Extracellular spikes and multi-electrode recordings

Klas H. Pettersen [1], Henrik Lindén [1], Anders M. Dale [2],
and Gaute T. Einevoll [1]

[1] Dept. of Mathematical Sciences and Technology,
Norwegian University of Life Sciences,
Ås, Norway

[2] Departments of Neurosciences and Radiology,
University of California,
San Diego, La Jolla, California

Contents

1 Introduction

Extracellular recordings have been, and still are, the main workhorse when measuring neural activity in vivo. In single-unit recordings sharp electrodes are positioned close to a neuronal soma, and the firing rate of this particular neuron is measured by counting *spikes*, that is, the standardized extracellular signatures of action potentials [30]. For such recordings the interpretation of the measurements is straightforward, but complications arise when more than one neuron contribute to the recorded extracellular potential. For example, if two firing neurons of the same type have about the same distance from their somas to the tip of the recording electrode, it may be very difficult to sort the spikes according to from which neuron they originate.

The use of two (*stereotrode* [49]), four (*tetrode* [23, 32, 76, 89]) or more [9] close-neighbored recording sites allows for improved spike sorting, since the different distances from the electrode tips or contacts allow for triangulation. With present recording techniques and clustering methods one can sort out spike trains from tens of neurons from single tetrodes and hundreds of neurons with multishank electrodes [9].

Information about spiking is typically extracted from the high frequency band ($\gtrsim$ 500 Hz) of extracellular potentials. Since these high-frequency signals generally stem from an unknown number of spiking neurons in the immediate vicinity of the electrode contact, it is called *multi-unit activity (MUA)*. The low-frequency part ($\lesssim$ 500 Hz) of extracellular potentials is called the *local field potential (LFP)*. In in vivo recordings the LFP is typically due to dendritic processing of synaptic inputs, not firing of action potentials [14, 43, 53, 67]. The interpretation of LFP is difficult as it is a less local measure of neural activity than MUA; the LFP measured at any point will typically have sizable contributions from neurons located several hundred micrometers away [5, 34, 36, 41–43, 45, 67, 90]. The analysis of LFP data has thus generally been restricted to the estimation of *current source density (CSD)*, the volume density of net transmembrane currents through the neuronal membranes [53, 60, 65], based on linear (laminar) multi-electrode recordings [13, 14, 57, 75, 86]. While CSD analysis cannot separate out contributions from different spatially intermingled neuronal populations (unlike the newly developed *laminar population analysis (LPA)* [14]), the CSD is still easier to interpret than the less localized LFP signal. New silicon-based multicontact probes in various other geometrical arrangements, such as 'multi-shank' [9] or 'needlepad' [63], are rapidly being developed, and the *inverse current-source density (iCSD)* method has been introduced to estimate CSDs in such situations [37, 38, 65].

The estimation of CSD from measured LFP is a so called 'inverse problem' which cannot be solved without imposing additional constraints on the form of the CSD [37, 38, 60, 65]. However, the corresponding 'forward problem', i.e., calculation of the LFP from a known CSD distribution, is well-posed [14, 37, 60, 65]. Likewise, the extracellular potential generated by neurons, both the LFP and the MUA, can be calculated if one knows the transmembrane currents through, and spatial positions of, all parts of the neuronal membranes, and also the extracellular conductivity in the surrounding medium [14, 22, 29, 43, 66, 67].

In the 1960s Rall used such a neuronal forward-modeling scheme to calculate extracellular potentials related to action-potential firing and synaptic interaction using simplified equivalent-cylinder geometries [73, 74]. Thirty years later Holt and Koch combined this scheme with compartmental modeling based on morphologically reconstructed pyramidal neurons, to calculate the extracellular signature of an action potential [29]. This modeling scheme has later been used to calculate other extracellular spike signatures of single neurons [21, 22, 51, 66], MUA from populations of firing neurons [67], and LFP from synaptically activated neurons and neuronal populations [14, 43, 67]. A convenient feature of the forward-modeling scheme is that due to the linearity of Maxwell's equations, the contributions to the extracellular potential from the various neuronal sources add up linearly, and the calculation of extracellular potentials from joint activity in populations with thousands of morphologically reconstructed neurons may even be done on desktop computers [67].

In the next section we describe the biophysical origin of the extracellular potentials and the mathematical formalism connecting it to the underlying neural activity. In Section 3 we illustrate the biophysical forward-modeling scheme by investigating the LFP generated by a single pyramidal neuron activated by apical synapses. This example also illustrates some general salient features of LFP, in particular an unavoidable low-pass filtering effect due to the dendritic distribution of transmembrane return currents [43] (also in the absence of inherent frequency-dampening in the extracellular medium [2, 46]). In Section 4 we describe results from a forward-modelling study of the influence of the dendritic morphology on the size and shape of the extracellular spike [66], and in Section 5 we correspondingly investigate the LFP and MUA generated by a synaptically activated model population of about 1000 morphologically reconstructed pyramidal neurons, mimicking the sensory-evoked response in a population of layer-5 neurons in rat whisker (barrel) cortex [67]. In Section 6 we discuss the problem of CSD estimation, and in particular outline the principles behind the iCSD method [37, 38, 65]. Some concluding remarks are given in the final section.

2 Biophysical origin of extracellular potentials

From an electrical point of view cortical tissue consists of a tightly packed collection of neurons and other cells embedded in a low-resistance extracellular medium filling less than a fifth of the total volume [64]. The low resistance of the extracellular medium implies that neighboring cells typically are electrically decoupled and that the difference between the extracellular potential recorded at different positions will be small, typically less than a millivolt. In contrast, the potential difference across the highly resistant cell membranes, that is, the membrane potential, is typically between 50 and 100 millivolts.

2.1 Biophysical forward-modeling formula

The extracellular potentials are generated by transmembrane currents, and in the commonly used *volume conductor theory* the system can be envisioned as a three-dimensional smooth extracellular continuum with the transmembrane currents represented as *volume current sources* [64]. In this theoretical framework the fundamental relationship describing the extracellular potential $\phi(t)$ at position $\mathbf{r}$ due to a transmembrane current $I_0(t)$ at position $\mathbf{r}_0$ is given by [25, 64]

$$\phi(\mathbf{r},t) = \frac{1}{4\pi\sigma}\frac{I_0(t)}{|\mathbf{r}-\mathbf{r}_0|} \quad . \tag{1}$$

Here the extracellular potential ϕ is set to be zero infinitely far away from the transmembrane current, and σ is the *extracellular conductivity*, assumed to be *real*, *scalar* (the same in all directions) and *homogeneous* (the same at all positions).

The validity of Eq. (1) relies on several assumptions:

A. *Quasistatic approximation of Maxwell's equations:* This amounts to neglecting the terms with the time derivatives of the electric field $\mathbf{E}$ and the magnetic field $\mathbf{B}$ from the original Maxwell's equation, i.e.,

$$\nabla \times \mathbf{E} = -\frac{\partial \mathbf{B}}{\partial t} \approx 0 \ , \tag{2}$$

$$\nabla \times \mathbf{B} = \mu_0 \mathbf{j} + \mu_0 \epsilon_0 \frac{\partial \mathbf{E}}{\partial t} \approx \mu_0 \mathbf{j} \ , \tag{3}$$

so that the electric (Eq. 2) and magnetic (Eq. 3) field equations effectively decouple [25]. With $\nabla \times \mathbf{E} = 0$ it follows that the electric field $\mathbf{E}$ in the extracellular medium is related to an extracellular potential ϕ via

$$\mathbf{E} = -\nabla\phi \quad . \tag{4}$$

For the frequencies inherent in neural activity, i.e., less than a few thousand hertz, the quasistatic approximation seems to be well justified (see, e.g., argument on p. 426 of [25]).

B. *Linear extracellular medium:* Linear relationship between the current density $\mathbf{j}$ and the electrical field $\mathbf{E}$,

$$\mathbf{j} = \sigma\mathbf{E} \quad . \tag{5}$$

This constitutive relation is quite general, and σ in Eq. (5) may in principle be (i) a *tensor*, accounting for different conductivities in different directions [60], (ii) *complex*, accounting also for capacitive effects [64], and/or (iii) *position-dependent*, that is, vary with spatial position. (Note that Eq. (5) is valid only in the frequency domain. In the time domain $\mathbf{j}$ is generally given as a temporal convolution of σ and $\mathbf{E}$ [4]. However, in the case of a frequency independent σ, cf. point E below, Eq. (5) will also be valid in the time domain.)

C. *Ohmic (resistive) medium*: Imaginary part of the conductivity σ is assumed to be zero, that is, the capacitive effects of the neural tissue is assumed to be negligible compared to resistive effects. This appears to be well fulfilled for the relevant frequencies in extracellular recordings [46, 64].

D. *Isotropic (scalar) extracellular conductivity:* Conductivity σ is assumed to be the same in all directions, i.e., $\sigma_x = \sigma_y = \sigma_z = \sigma$. Recent cortical measurements indeed found the conductivities to be comparable across different directions in cortical grey matter; in white matter, however, the conductivity was found to be anisotropic [46]. Early measurements on frog and toad cerebella also revealed anisotropy in the conductivity [60].

E. *Frequency-independent extracellular conductivity:* Conductivity σ is assumed to be the same for all relevant frequencies, i.e., $\sigma(\omega)$ is constant. The validity of this assumption is still debated: while some studies have measured negligible frequency dependence [46, 60], other investigations have suggested otherwise [1–3, 20]; cf. chapter by Bedard and Destexhe in present volume.

F. *Homogeneous extracellular conductivity:* Extracellular medium is assumed to have the same conductivity everywhere. This appears to be roughly fulfilled within cortical gray matter [46] and frog and toad cerebella [60], but maybe not in the hippocampus [47]. Further, white matter has a lower conductivity than cortical grey matter which in turn has a lower conductivity than the cell-free cerebral spinal fluid (CSF) [64].

While Eq. (1) requires all assumptions A-F to be fulfilled, the expression can be generalized to apply also for other situations. For example:

- If assumption E is violated and σ varies with frequency, Eq. (1) can still be used separately for each Fourier component $\hat{I}_0(\omega)$ of the transmembrane current $I_0(t)$ with $\sigma(\omega)$ inserted in the denominator of the equation. Since the extracellular potential ϕ is linear in the transmembrane current I_0, a simple Fourier sum over the contributions from all Fourier components will provide the total extracelluar potential [66]; see also chapter by Bedard and Destexhe in present volume.

- For the case where the conductivity is anisotropic, i.e., assumption D is violated, the equations still apply if the denominator $4\pi\sigma|\mathbf{r}-\mathbf{r}_0|$ is replaced by $4\pi\sqrt{\sigma_y\sigma_z(x-x_0)^2+\sigma_z\sigma_x(y-y_0)^2+\sigma_x\sigma_y(z-z_0)^2}$ [60].

- In situations with piecewise constant conductivities, for example with discontinuities in σ at the interfaces between grey and white matter or between the grey matter and the cortical surface, assumption F is violated. However, a generalized version of Eq. (1) can be derived based on the 'method of images' [14, 22, 61, 65].

Eq. (1) applies to the situation with a single transmembrane current I_0, but since contributions from several transmembrane current sources add linearly, the equation straightforwardly generalizes to a situation with many transmembrane current sources. With N current point sources the formula in Eq. (1) generalizes to

$$\phi(\mathbf{r},t)=\frac{1}{4\pi\sigma}\sum_{n=1}^{N}\frac{I_n(t)}{|\mathbf{r}-\mathbf{r}_n|} \quad . \tag{6}$$

In Fig. 1 we illustrate this formula for the situation where all transmembrane currents comes from a single compartmentalized 'ball-and-stick' neuron; it is clear that

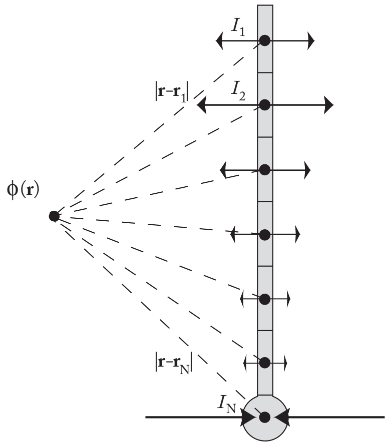

Figure 1: Illustration of mathematical formula Eq. (6) providing the extracellular potential from transmembrane currents in a single neuron. The size and direction of the arrows illustrate the amplitudes and directions of the transmembrane currents.

the measured extracellular potential will not only depend on the position of the electrode, but also the distribution of transmembrane currents.

Fig. 1 further illustrates an important 'conservation' law when calculating extracellular potentials due to neural activity: Kirchhoff's current law implies that the net transmembrane current (including the capacitive current) coming out of a neuron at all times must equal zero. Thus with the neuron depicted in Fig. 1 divided into N compartments, one must at all times have $\sum_{n=1}^{N} I_n(t) = 0$. Therefore a one-compartment model cannot generate any extracellular potential since the net transmembrane current necessarily will be zero. The simplest model producing an extracellular potential is a two-compartment model where transmembrane current entering the neuron at one compartment leaves at the other compartment. The simplest possible multipole configuration is thus the current *dipole*.

2.2 Numerical forward-modeling scheme

The numerical evaluation of extracellular potentials naturally splits into two stages [29, 43, 66, 67]:

1. Calculation of transmembrane currents for all neuronal membrane segments using multicompartment neuron models [79], typically using neural simulation tools such as NEURON [10] or Genesis [7].

2. Calculation of the extracellular potential on the basis of the modeled transmembrane currents and their spatial position using a forward-modeling formula similar to Eq. (6).

When a neuron is split into N compartments, the formula in Eq. (6) should be used with $\mathbf{r}_n$ corresponding to a characteristic 'mean' position for compartment n, e.g., the center of a spherical soma compartment or the mid-point of a cylindrical dendritic compartment. This scheme corresponds to the so called *point-source* approximation [29, 66] since all transmembrane currents into the extracellular medium from a particular compartment are assumed to go through a single point. Another scheme, the *line-source* approximation, assumes the transmembrane currents from each cylindrical compartment to be evenly distributed along a line corresponding to the cylinder axis [29, 66]. A line-source formula, analogous to the point-source formula in Eq. (6), can be found in Ref. [66] (Eq. 2). Unless otherwise noted all forward-modeling calculations with morphologically reconstructed neurons presented in this chapter use the line-source approximation. Further, a frequency-independent, scalar and homogeneous extracellular conductivity with a numerical value of $\sigma = 0.3$ S/m [25] is assumed.

2.3 Current-source density (CSD)

The forward-modeling formula in Eq. (6) can be mathematically reformulated as

$$\phi(\mathbf{r}, t) = \frac{1}{4\pi\sigma} \iiint\limits_V \frac{C(\mathbf{r}', t)}{|\mathbf{r} - \mathbf{r}'|} \, d^3r' \quad . \tag{7}$$

when we introduce the quantity $C(\mathbf{r}, t) \equiv \sum_{n=1}^{N} I_n(t)\, \delta^3(\mathbf{r} - \mathbf{r}_n)$. Here $\delta^3(\mathbf{r})$ is the three-dimensional Dirac δ-function, and the volume integral goes over all transmembrane currents. The quantity $C(\mathbf{r}, t)$ is called the *current source density (CSD)*, has dimension A/m^3, and is in general interpreted as the volume density of current entering or leaving the extracellular medium at position $\mathbf{r}$ [53, 60, 64]. A negative $C(\mathbf{r}, t)$ corresponds to current leaving the extracellular medium and is thus conventionally called a *sink*. Likewise, current entering the extracellular medium is called a *source*. The CSD is easier to relate to the underlying neural activity than the extracellular potential itself, and current-source density analysis has thus become a standard tool for analysis of the low-frequency part (LFP) of such potentials recorded with linear (laminar) multielectrodes [60, 65].

While Eq. (7) gives the numerical recipe for calculating the extracellular potential given the CSD, a formula providing the opposite relationship can also be derived. Following Refs. [60, 61, 64] we have for the situation with an ohmic extracellular medium that current conservation requires

$$\nabla \cdot \mathbf{j}_{tot} = \nabla \cdot (\sigma \mathbf{E} + \mathbf{j}_s) = 0 \quad , \tag{8}$$

where $\mathbf{j}_s$ is the so called *impressed* transmembrane currents entering the extracellular medium [61, 64]. With the additional use of Eq. (4) one obtains

$$\nabla \cdot \Big(\sigma(\mathbf{r}) \nabla \phi(\mathbf{r}, t) \Big) = -C(\mathbf{r}, t) \quad , \tag{9}$$

where $C(\mathbf{r}, t) \equiv -\nabla \cdot \mathbf{j}_s(\mathbf{r}, t)$. This equation is not only valid for the case with position-dependent σ, but also when it depends on direction, i.e., is a tensor [60]. In the special case where σ is isotropic and homogeneous, the equation simplifies to

$$\sigma \nabla^2 \phi(\mathbf{r}, t) = -C(\mathbf{r}, t) \quad . \tag{10}$$

This equation, called Poisson's equation, is well known from standard electrostatics where it describes how potentials are generated by electrical charges (with the conductivity σ replaced by the dielectric constant ε) [31]. As emphasized in Ref. [64], however, these two versions of Poisson's equation represent different physical processes.

3 Local-field potential (LFP) from single neuron

3.1 Characteristic features of LFP

To illustrate the forward-modeling scheme and highlight some salient features of LFP we here calculate the extracellular potential around a reconstructed layer-5 model pyramidal neuron from cat visual cortex [48] receiving a single excitatory synaptic input in the apical dendrite. For simplicity the neuron is considered to have purely passive neuronal membranes and to be excited by a synaptic input current $I_s(t)$ modeled as an α-function, that is,

$$I_s(t) = I_0\, t/\tau_s\, e^{1-t/\tau_s}\, \theta(t) \ \ , \tag{11}$$

where $\theta(t)$ is the Heaviside unit step function. A time constant $\tau_s = 1$ ms is chosen, and I_0 is set to give a peak EPSP amplitude in the soma of about 0.5 mV. The model is linear, that is, all calculated extracellular and intracellular potentials are proportional to I_0, making the model somewhat easier to analyze than when nonlinear currents are involved. However, most qualitative features is expected to be unchanged if we, e.g., considered excitation by a set of conductance-based synapses instead.

In Fig. 2A we show the calculated extracellular potential traces at a set of positions outside the neuron. An important feature which is immediately apparent is that the shape and amplitude of the extracellular potentials depend on position. Near the apical synaptic input the extracellular signature is always negative, reflecting that the excitatory current-synapse providing a current sink dominates the sum in the forward-model formula, cf. Eq. (6). At positions close to the soma the extracellular potential is always positive, reflecting that return currents in the soma area dominate the sum. At other positions, for example above the synapse, a biphasic extracellular potential is observed. Interestingly, there is not a monotonous decay of the amplitude with distance from the synaptic input: large extracellular responses are observed close to the soma, almost a millimeter away.

Another important feature is the observed increased half-width of the extracellular potentials recorded close to the soma compared to those in the vicinity of the synaptic input. This is illustrated by the two insets showing magnified extracellular potential traces in Fig. 2A. In the upper inset close to the synapse the width is 4.2 ms, while the width at the lower inset close to soma is 7.1 ms, both widths measured at 50% of the trace's peak amplitudes. Thus the extracellular potential close to the synaptic input contains higher frequencies than the extracellular potential far away from the synaptic current generator.

This feature can be understood on the basis of passive cable properties of the neuron. The transmembrane currents dominating the extracellular potentials close to the soma have been low-pass filtered and have a wider temporal profile compared to the transmembrane currents close to the synaptic input. This is illustrated in Fig. 2C where the transmembrane current profile is seen to have a much larger half-width at the soma (∼6.5 ms) compared to at the dendritic segment containing the synapse (∼2.5 ms).

An analogous low-pass filtering is seen from the temporal shapes of the apical and somatic membrane potentials, respectively, in Fig. 2E. Here the apical EPSP

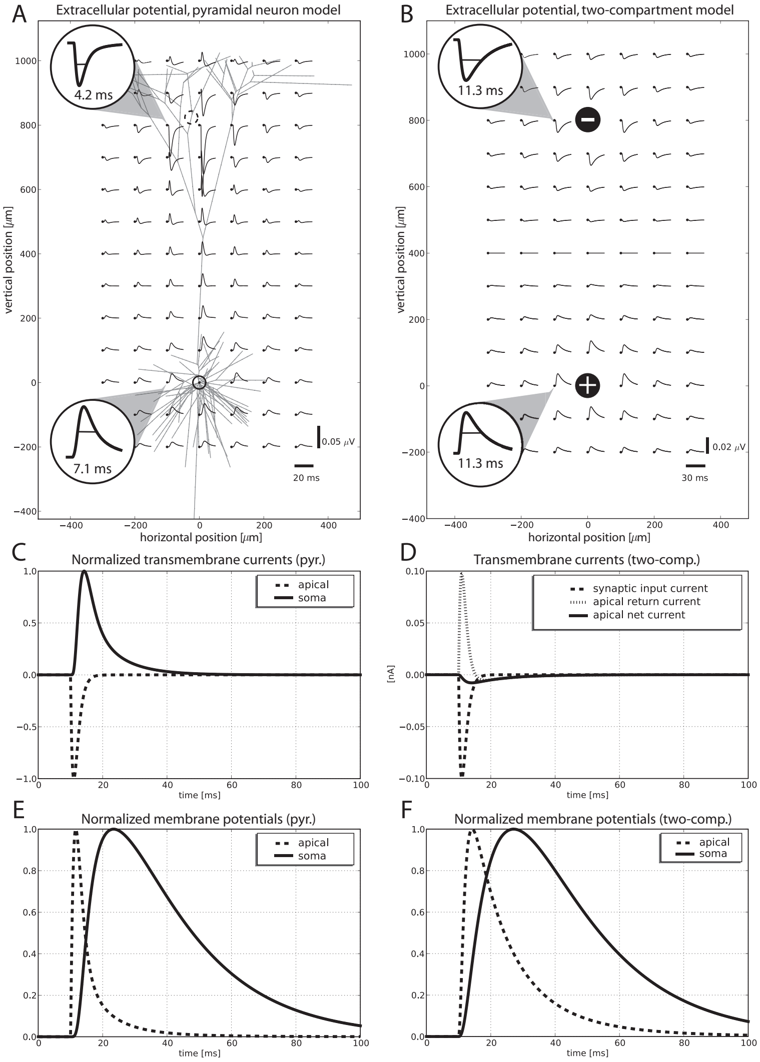

Figure 2: Calculated extracellular potentials following an excitatory synaptic input into purely passive neuron models. The synapse is current-based and modeled as an α-function $I_s(t - t_{on})$ (Eq. 11) with $\tau_s = 1$ ms, $I_0 = 0.1$ nA and the onset time t_{on} set to 10 ms. (A) Results for reconstructed L5 pyramidal neuron from Ref. [48] with active channels removed. Passive parameters: membrane resistivity $R_m = 30000\ \Omega\text{cm}^2$, axial resistivity $R_i = 150\ \Omega$cm, membrane capacitance $C_m = 0.75\ \mu\text{F/cm}^2$. Potentials are shown in a 20 ms window starting 2 ms prior to synaptic onset. Dashed circle denotes position of synapse. (B) Results for analogous two-compartment neuron model. The apical (top) and soma (bottom) compartments have resistive (r_a,r_s) and capacitive (c_a,c_s) membrane elements, are connected to each other via the resistance r_{as}. The same synaptic current as in A is inserted into the apical compartment. Model parameters: r_a=318 MΩ, r_s=95 MΩ, r_{as}=358 MΩ, c_a=71 pF, c_s=236 pF. The point-source approximation is used, cf. Eq. (6). (C) Normalized transmembrane currents at the synaptic input segment and at the soma for the pyramidal neuron in *A*. Half-widths are 2.5 ms and 6.5 ms, respectively. (D) Synaptic input current, return current, and net transmembrane current for the apical compartment in two-compartment model. Half-widths are 2.5 ms, 2.3 ms and 5.2 ms, respectively. (E) Normalized membrane potential for synaptic input segment and soma segment for the pyramidal neuron model. Half-widths are 4.1 ms and 33 ms, respectively. (F) Normalized membrane potential of apical and soma compartments of two-compartment model. Half-widths are 13 ms and 38 ms, respectively. Extracellular potentials in insets in *A* and *B* are scaled arbitrarily.

peaks already a couple of milliseconds after synaptic onset and has a half-width of about 4 ms. In contrast the somatic EPSP peaks about 15 ms after synaptic onset and has a half-width of more than 30 ms. The low-pass filtering effect is thus stronger for the membrane potential than for the transmembrane current, and thus also compared to the extracellular potentials.

In Fig. 2B we further show calculated extracellular potential traces for an analogous two-compartment model, the simplest neuron model that produces an extracellular potential. The spatial extension corresponds to the distance between the single synapse and the soma for the reconstructed neuron in Fig. 2A. This model has only five parameters, the resistances (r_a,r_s) and capacitances (c_a,c_s) of the apical and soma compartments, respectively, and the intercompartment resistance (r_{as}).

The pattern of extracellular responses in the two-compartment model is seen to resemble the pattern for the reconstructed pyramidal neuron in that large negative responses are observed close to the apical compartment while large positive responses are observed close to the soma compartment. However, in the two-compartment model the net transmembrane current in the soma compartment is forced by Kirchhoff's current law to be identical in size, but with opposite sign, compared to the apical compartment. What goes in at one compartment, must leave at the other. Since only these two compartments contribute to the sum in the forward-modeling formula for the extracellular potential (that is, $N = 2$ in Eq. 6), the temporal form of the extracellular potential will be the same everywhere; only the sign and size of an overall amplitude will vary. This is illustrated by the two insets showing magnified extracellular traces in Fig. 2B which both have half-widths of 11.3 ms. There is thus no *position-dependent* filtering of frequency components in the two-compartment model. At least three neuron compartments are needed to capture such an effect.

There is, however, low-pass filtering also inherent in the two-compartment model as illustrated by the larger half-width of the extracellular potential (11.3 ms) observed in Fig. 2B compared to the half-width of the synaptic input current (2.5 ms) in Fig. 2D. This reflects that in a two-compartmental model like this, where both compartments have a resistive and a capacitive component, the axial current going between the compartments is not equal to the imposed synaptic current in the apical compartment. Instead it is the difference between the synaptic current and the return current of the apical compartment. This axial current corresponds in magnitude to the net transmembrane currents at the two compartments, and as illustrated in Fig. 2D these net transmembrane currents are both smaller in amplitude and temporally wider than the synaptic current. In Fig. 2F we in fact observe an even larger low-pass filtering effect for the membrane potential compared to results for the reconstructed model neuron in Fig. 2E.

In Lindén et al. [43] we discuss in detail how the LFP patterns depend on neuronal morphologies, spatial positions of the driving synapse, as well as electrode recording positions.

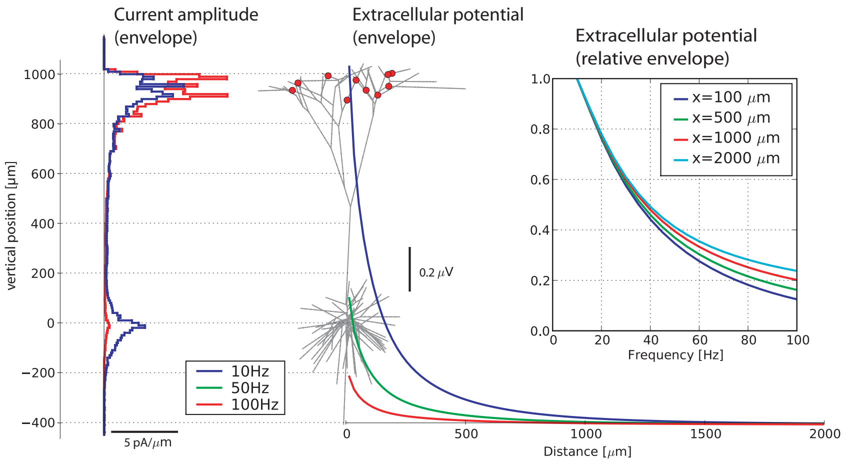

Figure 3: Illustration of frequency-filtering of LFP for the passive layer-5 pyramidal model neuron in Fig. 2A receiving simultaneous sinusoidal input currents $I_s(t) = I_0 \cos(2\pi f t)$ at 10 apical synapses (red dots in middle panel). The middle panel shows the envelope (amplitude) of the sinusoidally varying extracellular potential plotted at different lateral positions at the level of the soma (x-direction). The left panel shows the envelope of the linear current-source density of the *return current* along the depth direction (z-direction) for f=10 Hz and f=100 Hz. The right panel shows the relative magnitude of envelopes of the extracellular potential as a function of frequency for different lateral distances from the soma. Here curves are normalized to unity for the lowest frequency considered, f=10 Hz.

3.2 Low-pass filtering of LFP

The frequency content of LFP and EEG signals has attracted significant interest in particular since power laws, i.e., power spectra scaling as $1/f^{\beta}$, have commonly been observed [2, 4, 8, 18, 27, 44, 50, 52, 55, 70]. Suggested explanations of these observed power laws have invoked a variety of neural network mechanisms [19, 39, 50, 52], as well as frequency filtering inherent in the extracellular medium [2, 4, 19]. The results above, elaborated in [43], point to an additional source of frequency filtering of the LFP and EEG: extended dendritic morphologies will due to their passive cable properties unavoidably give a separate frequency-filtering effect for the extracellular potentials. In fact there are two dendrite-based filtering mechanisms: (i) a higher fraction of the apical synaptic input current will propagate to the soma for low frequencies than high frequencies, and (ii) extracellular potentials recorded far away from the synaptic input current will have more low frequencies than those recorded close to the input current due to the low-pass filtering of the return current by the dendritic tree. The simple two-compartment model only displayed the first type of filtering, while the reconstructed pyramidal neuron model displayed both types.

A comprehensive investigation of these filtering effects is beyond the scope of this chapter; for this we refer to Lindén et al. [43]. However, some example results illustrating the important principles are shown in Fig. 3. The same pyramidal neuron as in Fig. 2A is considered, now with sinusoidal currents $I_s(t) = I_0 \cos(2\pi f t)$ inserted at ten apical synapses. The extracellular potential is simulated along an axis oriented perpendicular to the primary apical dendrite at the level of the soma.

The amplitude of the extracellular potential is plotted in the main (middle) panel. The most obvious feature is the amplitude differences in the extracellular potential for the different frequencies: the amplitude is much larger for the lowest frequency ($f = 10$ Hz) than for the highest frequency ($f = 100$ Hz), even with the same input current amplitude I_0.

The somatic transmembrane current is usually the most important source for the extracellular potential for proximal recordings at the level of soma. As the frequency increases, the current profile of the return currents tend to become more localized around the synaptic inputs, i.e., a larger fraction of the current returns through the dendrites near the synapses. This is clearly seen in the current profile to the left in Fig. 3. The 100 Hz sinusoid has a much larger current apically, and a much smaller current basally, than the 10 Hz sinusoid.

In the right part of Fig. 3 we illustrate how the low-pass filtering effect of the extracellular potential depends on the distance from soma. Here all curves are normalized to unity for the lowest frequency considered, f=10 Hz. When the frequency is increased, more of the current return apically, further away from any recording position at the depth level of the soma. This implies that the extracellular potential becomes smaller, since the difference in distances between the contributions to the potential from the synaptic input current and the return current will be smaller. Since the distance between the synaptic current generator and the return currents is relatively larger for recordings near the soma than for recordings further away in the lateral direction, the frequency decay of the extracellular potential will be steeper near the soma (small x) than for the distal recordings (large x).

The decay in extracellular amplitude as a function of frequency is not only seen in recordings at the level of the soma, but is also prominent for recordings at the level of the synaptic input (results not shown). The reason is the same: the potential is the sum of the transmembrane currents weighted inversely with distance to the sources, and when the typical distance between the synaptic current generator and the return currents gets smaller, the extracellular potential will also become smaller.

The low-pass filtering effect described here is a general feature always present for spatially extended neuronal-membrane structures [43], and in the next section we will show its impact on the extracellularly recorded signature from an action potential.

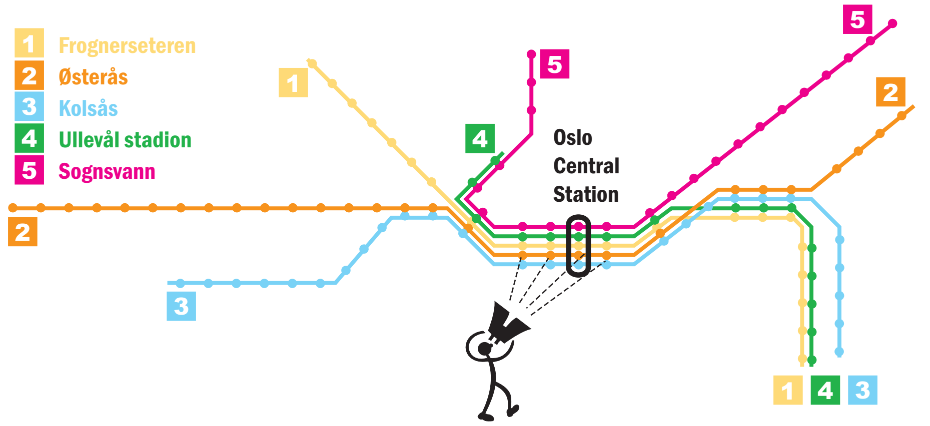

Extracellular vs. intracellular potentials. Intracellular and extracellular potentials are often confused: modelers sometimes compare their model predictions of *intracellular* potentials (which are easier to model) with recorded *extracellular* potentials (which are easier to measure). As seen in Figs. 2 and 4 the connection between intracellular and extracellular is not trivial, however. A light-hearted metaphor is illustrated by the above map of the Oslo subway system. With its branchy structure of different lines ('dendrites') stretching out from the hub at Oslo Central Station ('soma'), the subway system resembles a neuron. If we pursue this analogy, the subway stations (marked with dots) may correspond to 'neuronal compartments' and the net number of passengers entering or leaving the subway system at each station to the net 'transmembrane current' at this compartment. If more passengers enter than leave the subway system at a point in time, it means that the number of people in the subway system, i.e., the 'intracellular membrane potential', increases. (If we introduce a 'capacitive current' corresponding to the *change* in the number of people inside each station, we can even get a 'current conservation law'.) The intracellular soma membrane potential, crucial for predicting the generation of neuronal action potentials (which luckily have no clear analogy in normal subway traffic), would then correspond to the number of passengers within the subway station at Oslo Central Station. The extracellular potential on the other hand would be more similar to what could be measured by an eccentric observer counting passengers flowing in and out of a few neighboring subway stations (with binoculars on the top of a large building maybe). While the analogy is not perfect, it should illustrate that intracellular and extracellular potentials are correlated, but really two different things. Adapted from Ref. [68].

4 Extracellular signatures of action potentials

4.1 Example forward-modeling result

In a typical single- or multielectrode recording spikes from tens of neurons may be intermingled [9]. When developing automated algorithms for detecting and sorting these spikes according to their true neural source [15, 16, 26, 35, 40, 69, 71, 72, 77, 80, 82, 85, 88], several issues arise: For example, which types of neurons are most likely to be seen in the recordings, which neuronal parameters are important for the

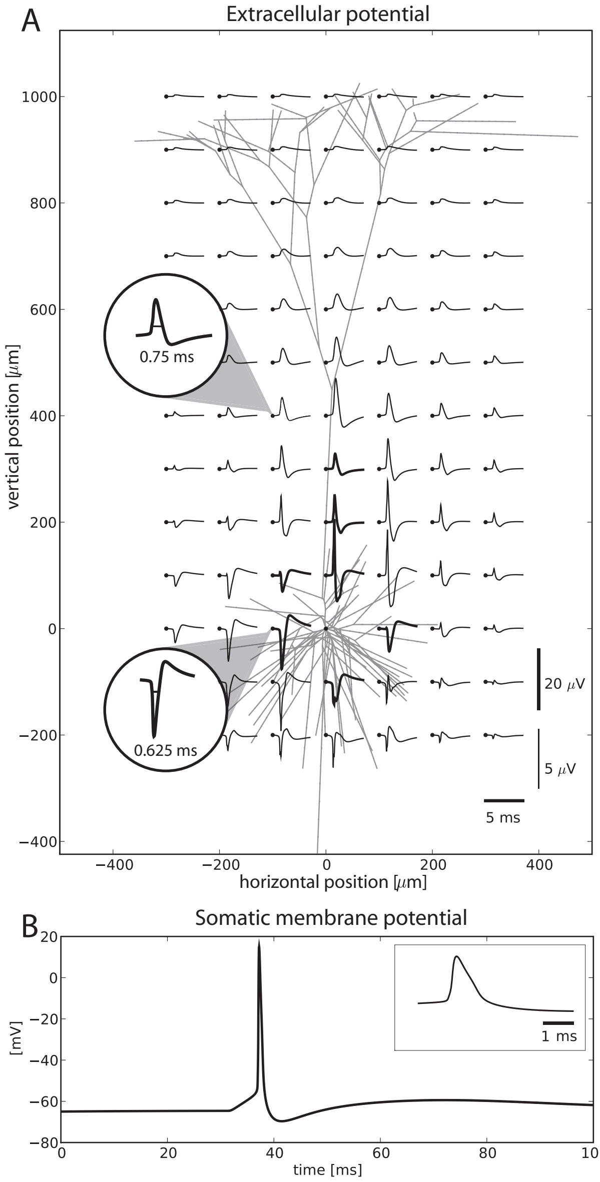

Figure 4: (A) Calculated extracellular signature of an action potential in layer-5 pyramidal model neuron taken from Ref. [48]. Neuron is stimulated with apical excitation and basal inhibition similar to 'stimulus input pattern 1' (SIP1) in Ref. [67]. Traces show extracellular potential in 5 ms window around time of spiking. Thick lines corresponds to 20 μV scaling, thin lines to 5 μV scaling. Extracellular potentials in the two insets are scaled arbitrarily. (B) Somatic membrane potential during simulation. Inset shows soma potential for same 5 ms time window as for the extracellular potentials in A.

spike amplitude and shape, and which parameters determine the decay of the spike amplitude with increasing distance from the neuron? These are important questions also for the interpretation of multi-unit activity (MUA), the high-frequency content of the extracellular potential [14, 66, 67, 78, 86], and for the question of why the firing of neurons in the brain appear to be so sparse [81].

An example forward-modeling result for the extracellular potential related to an action potential is shown in Fig. 4A. Again the layer-5 pyramidal model neuron of Ref. [48] is used, this time including active conductances. A combined pattern of apical excitation and basal inhibition is used to excite the action potential, similar to what is labeled 'stimulus input pattern 1' (SIP1) in Ref. [67]. The largest extracellular responses are seen closest to the soma (thick lines in Fig. 4A). As the shortest distance considered is as large as 100 μm, the spike amplitudes depicted in the figure are nevertheless all smaller than 20 μV (see Fig. 3 in [67] for a close-up picture of spike shapes closer to the soma). The lowest inset in the figure, showing a magnified extracellular potential, illustrates the typical shape of recorded extracellular spikes: a sharp, deep dip (sodium phase) followed by a shallower, but longer-lasting, positive bump (potassium phase).

As for the spatial LFP patterns in Fig. 2, the extracellular spike is also seen to have an inverted sign apically compared to basally. Further, a position-dependent low-pass filtering effect is also observed: the magnified extracellular potential in the top inset in Fig. 4A is seen to be wider than at the lower inset closer to the soma. With the extracellular spike-width defined as the width of the sodium phase at 25% of its maximum, a widening from 0.625 to 0.75 ms is observed. This implies that the higher frequencies attenuate faster than the lower frequencies when moving away from the soma. A spike-width increase with increasing distance from the soma has been seen experimentally, and explanations for this in terms of extracellular-medium effects has been suggested [1, 3]. However, it is still debated whether such effects are present in cortical tissue: while some investigators have measured low-pass filtering effects in the extracellular medium [20], other investigators found no such effect [46, 60].

Below we outline how the neuron *morphology*, combined with its *cable properties*, can provide an alternative, or supplementary, explanation for the distance-dependent low-pass filtering effect of extracellular spikes [66]. Section 2 explained why a neuron model has to contain at least two compartments to produce an extracellular potential at all, and in Section 3 it was shown that a two-compartment model could not produce any *distance-dependent* low-pass filtering effect. In Ref. [66] we investigated the effect of the neuronal morphology and the passive dendritic parameters on the extracellular spike signature in detail, in particular the distance dependence of the spike amplitude and low-pass filtering. A variety of neuronal morphologies was considered, both morphologically reconstructed pyramidal (Fig. 5A) and stellate cells (Fig. 5C) and simplified models built up of dendritic sticks ('ball-and-stick', 'ball-and-star', 'ball-and-bush', cf. Fig. 1 in Ref. [66]). While the shape of the intracellular action potential vary from neuron to neuron, we wanted to focus on how the dendritic structure affects the relationship between the intracellular and extracellular potentials [28, 88]. We thus imposed a standardized intracellular action potential (cf. Fig. 5B) in the somas of the neurons in the numerical evaluation of

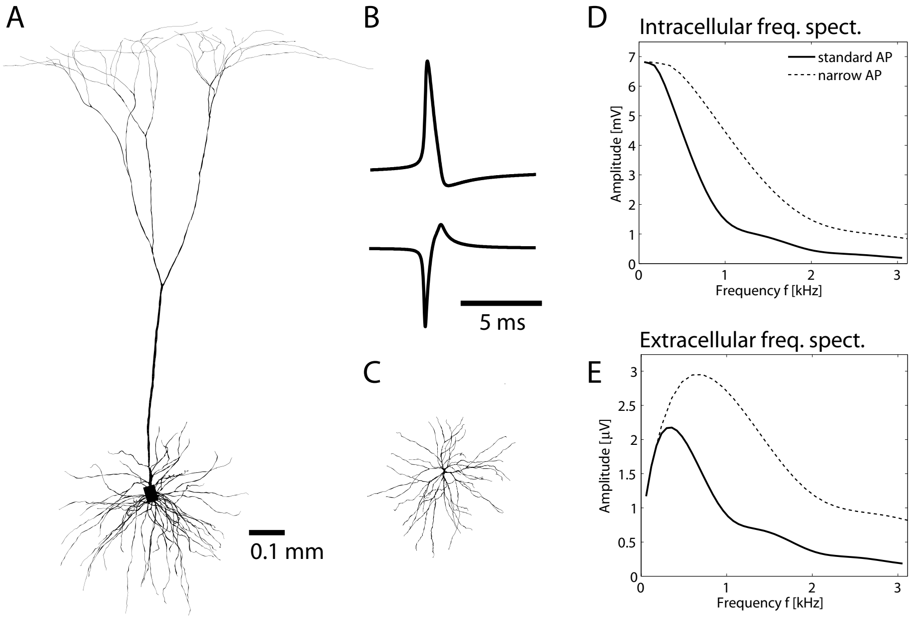

Figure 5: (A) Pyramidal layer-5 neuron used in investigation of extracellular spikes [66]. (B) Upper: 'Standard' action potential (AP) used in model study, half-amplitude spike width is 0.55 ms. Lower: Typical shape of corresponding extracellular spike near soma for 'standard' AP. Extracellular spike width is 0.44 ms (see text for definition). (C) Stellate layer-4 neuron used in investigation [66]. (D) Frequency spectrum of intracellular voltage for 'standard' AP in B, and a corresponding 'narrow' AP with identical form but exactly half the spike width. (E) Frequency spectrum of extracellular voltage traces of 'standard' spike in B (solid), and corresponding extracellular voltage trace for 'narrow' spike (dashed). Reconstructed neuron morphologies taken from Ref. [48]. See Ref. [66] for further information.

the extracellular spike signatures. In accordance with the qualitative observation in Fig. 4A all neuron models were found to exhibit a distance-dependent low-pass filtering effect, that is, larger spike widths further away from soma, cf. Figs. 6 and 7 in Ref. [66]. However, the amplitudes of the spikes were found to be quite different, both their size and their dependence on distance from soma. For example, with identical intracellular action potentials, the spike-amplitude 60 μm away from soma was found to be about 40 mV for the pyramidal neuron, but only about 10 mV for the stellate neuron.

To obtain a better understanding of the phenomenon we also developed a conceptually simpler and more intuitive theory accounting for the observed variation in spike shape and amplitude [66]. This theory also produced analytical predictions of the dependence of the spike amplitude on the dendritic parameters, predictions that later were confirmed by numerical calculations. The essential idea behind the theory is that during an action potential, the soma can be viewed as a voltage source driving current into the soma-attached dendrites, and that the size and shape of the extracellular signature will qualitatively depend on (i) the magnitudes of the axial currents entering the dendrites from the soma, (ii) what distances from the soma the imposed axial currents on average returns through the dendritic membranes and (iii) the number and geometrical arrangement of dendrites. In fact it was found that many of the salient features of the extracellular spike could be understood by considering the simple ball-and-stick neuron model where the soma is modeled as a single compartment and the dendrite as a simple cable stick [33, 66]. With the soma considered as a voltage source, the various soma-attached dendrites are effectively decoupled from each other. Consequently the total extracellular potential generated by a more complex neuron can be approximated as a superposition of contributions from a collection of soma-attached dendritic sticks pointing in different directions [66].

4.2 Dendritic sticks and AC length constant

A concept we found essential to get both an intuitive and quantitative handle on the crucial spatial distribution of the return current along the dendritic stick, is the so called *alternating current (AC) length constant* [66]

Imagine a ball-and-stick neuron model (cf. Fig. 6) where the dendritic stick is infinitely long. This *infinite* ball-and-stick neuron is assumed to receive a constant (DC) somatic transmembrane current. Since the membrane currents at all times have to sum to zero, the same amount of current has to return to the extracellular medium through the dendritic stick. The density function of the dendritic return current has the functional form of an exponential decay with the *length constant* (or *space* constant) λ describing the steepness of the decay [12, 66]. More precisely, the length constant is the dendritic position where the steady-state transmembrane return current has decreased to $1/e$ of its value at the soma end, or equivalently, λ is the position where the dendritic return current has its center of gravity. The center of gravity is then defined as the mean of the normalized transmembrane current density weighted by dendritic position.

The length constant is not only useful for describing the neuron's intrinsic qual-

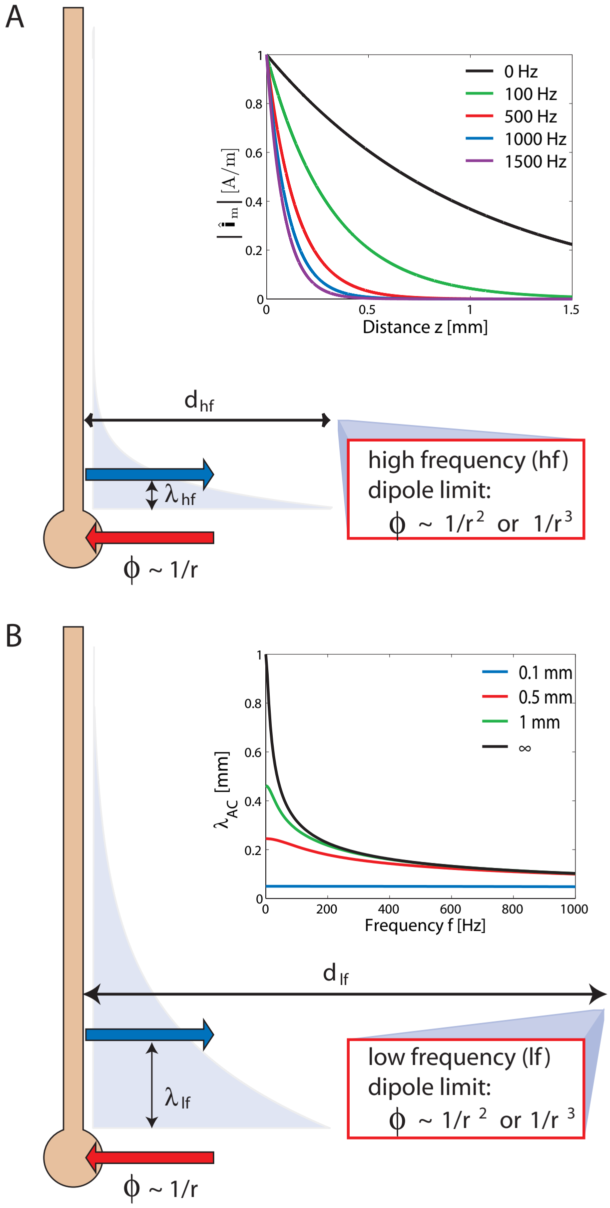

Figure 6: Illustration of ball-and-stick neuron and its frequency-dependent dipole sizes and corresponding far-field limits. (A) For high frequencies (hf), the center of gravity (blue arrow) of the dendritic return current is close to soma. Therefore, the AC length constant λ_{hf} is small and transition to the far-field limit occurs around a distance d_{hf}, relatively close to the neuron. Inset: Transmembrane return-current profile along an infinite dendritic stick for different frequencies [66]. Parameter: stick diameter 2 mm, membrane and axial resistivities $R_{\mathrm{m}} = 30000\ \Omega\mathrm{cm}^2$, $R_{\mathrm{i}} = 150\ \Omega\mathrm{cm}^2$, membrane capacitance $C_{\mathrm{m}} = 1\ \mu\mathrm{F/cm}^2$. $\lambda_{\mathrm{AC}}^{\infty}$ is 317 mm, 145 mm, 103 mm, and 84 mm for 100 Hz, 500 Hz, 1000 Hz, and 1500 Hz, respectively. (B) For low frequencies (lf) the AC length constant λ_{lf} is relatively large and the far-field limit is reached for a larger distance d_{lf} than for the higher frequency in A. Inset: AC length constant $\lambda_{\mathrm{AC}}(\omega)$ as a function of frequency for ball-and-stick models of different length; parameter values for diameter, resistivity and capacitance are the same as in A.

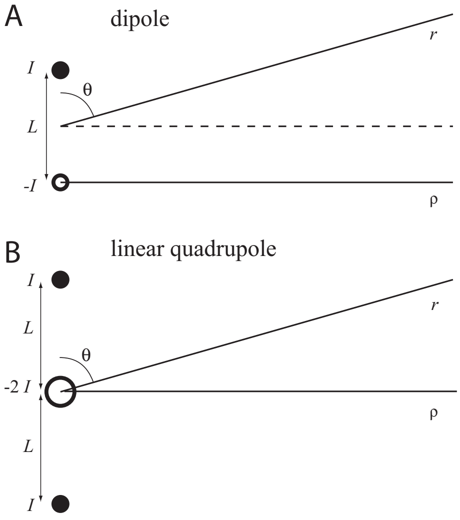

Figure 7: Illustration of (A) current dipole and (B) linear current quadrupole.

ities (for example electrotonic compactness), it is also useful for understanding the extracellular potentials generated by the neuron. For example, when computing the extracellular potential far away from the neuron (far-field limit), the ball-and-stick neuron model can be approximated by a dipole model [66]. The parameters of the dipole model will then be the dipole current, which equals the somatic current, and the dipole size, which essentially is given by the dendritic length constant, cf. Fig. 7A. For infinite dendritic sticks under the DC condition this length constant is given by $\lambda = \sqrt{dR_\mathrm{m}/4R_\mathrm{i}}$, where d is the stick diameter, R_m is membrane resistivity [$\Omega\mathrm{cm}^2$] and R_i is the axial resistivity [Ωcm] [12].

As the length constant is important for understanding several aspects of a neuron (electrotonic compactness, extracellular far-field potential), it is useful to define a general length constant which is not restricted to infinite sticks and DC conditions. In analogy to the definition of the standard DC space constant λ, Ref. [66] define the AC length constant, $\lambda_\mathrm{AC}(\omega)$, to be the mean of the absolute value of the current density amplitude weighted with distance, when the dendritic stick is driven by a sinusoidal voltage in the soma-end of the stick. This length constant will be frequency dependent through the angular frequency $\omega = 2\pi f$. For a finite stick this corresponds to (in complex notation)

$$\lambda_\mathrm{AC}(\omega) = \frac{\int_0^l z|\hat{\mathbf{i}}_\mathrm{m}(z)|\mathrm{d}z}{\int_0^l |\hat{\mathbf{i}}_\mathrm{m}(z)|\mathrm{d}z} \ , \tag{12}$$

where the stick is assumed to be extended along the positive z-axis from $z = 0$ (soma end) to $z = l$. $\hat{\mathbf{i}}_\mathrm{m}(z)$ denotes the complex transmembrane current density at position z along the stick (where the real part corresponds to the physical transmembrane current). In the inset in Fig. 6A we show normalized values for $|\hat{\mathbf{i}}_\mathrm{m}(z)|$ as a function of distance from the soma for an infinite ball-and-stick neuron for different frequencies. The higher the frequency, the closer to the soma the return current is seen to be. This is reflected in the frequency-dependence of the AC length constant $\lambda_\mathrm{AC}(\omega)$ as seen in the inset of Fig. 6B: the highest frequencies have the shortest AC length constants. This latter panel also shows that shorter dendritic sticks have shorter $\lambda_{\mathrm{AC}}(\omega)$, as expected since the closed ends will force the return currents out closer to the soma. This effect will be most pronounced for the lower frequencies.

For an infinite stick an analytical formula can be found for the AC length constant. In this special case Eq. 12 reduces to [33, 66]

$$\lambda_{\mathrm{AC}}^{\infty}(\omega) = \lambda\sqrt{2/[1+\sqrt{1+(\omega\tau)^2}]}\ , \tag{13}$$

where τ denotes the membrane time constant, $\tau = R_{\mathrm{m}}C_{\mathrm{m}}$.

4.3 Low-pass filtering for the ball-and-stick neuron

In Ref. [66] numerical investigations of the extracellular signature of action potentials in ball-and-stick neurons also revealed a characteristic spike-width increase when moving away from soma, similar to what is seen for the pyramidal neuron in Fig. 4A. Here we will outline how a reduced model, a dipole model with a soma compartment attached to a conflated dendritic stick, can explain the phenomenon. In Section 3 we showed that a two-compartment neuron model, i.e., a dipole model with a *fixed* dipole length, cannot express such position-dependent low-pass filtering. The crucial element introduced here is that the dipole model must have a *frequency-dependent dipole length* based on λ_{AC}.

Far way (i.e., far-field limit) from a current dipole with current strength I and length L the extracellular potential is given by [31, 66]

$$\phi_{\mathrm{far,d}}(r,\theta) = \frac{1}{4\pi\sigma}\frac{I\,L}{r^2}\cos\theta\ \ , \tag{14}$$

when polar coordinates are used, cf. Fig. 5A. This model shows a $1/r^2$ decay when moving in any direction where θ is fixed. However, when moving perpendicular to the dipole (e.g., along the ρ-axis in Fig. 5A) the extracellular potential decays as a quadrupole, i.e., as $1/r^3$ [66] .

The distance dependence is more complicated for proximal extracellular potentials than for far-field potentials. Close to the soma compartment, the soma current will dominate the potentials, and in this region the distance dependence will be given by the monopole expression

$$\phi_{\mathrm{m}}(r,\theta) = \frac{1}{4\pi\sigma}\frac{I}{r}\ \ , \tag{15}$$

that is, the amplitude decays as $1/r$. This dipole neuron model therefore predicts a transition in the power of the distance dependence of the extracellular potential from -1 close to the soma to -2 (or -3) in the far-field limit.

If the soma membrane potential oscillates at an angular frequency ω, current will flow from the extracellular medium through the soma and up into the dendritic stick with the same frequency with an amplitude we denote $I(\omega)$. A simple model for the generated extracellular potential around the ball-and-stick neuron can now be made: Near the soma the amplitude of oscillating extracellular potential can be descibed by Eq. (15) with I replaced by $I(\omega)$, and in the far-field limit the extracellular potential amplitude can be described by Eq. (14) with I replaced by $I(\omega)$ and L with $\lambda_{\mathrm{AC}}(\omega)$ from Eq. (12) [66]. From the dendrite's point of view the soma action potential can be seen as a voltage source enforcing the characteristic intracellular voltage waveform. Since the dendritic stick itself has linear response properties, this waveform can be Fourier decomposed, and each frequency can be treated separately. The extracellular signature of the action potential can thus be found by a simple linear superposition [66].

The extracellular signature at a particular position will depend crucially on whether the frequency components are in the 'close-to-soma-regime' (Eq. 15), in the 'far-field limit' (Eq. 14), or somewhere in between. The following question thus arises: what decides the distance for which the far-field limit is reached? Clearly, the transition to the far-field limit must depend on the dipole length, that is, $\lambda_{\mathrm{AC}}(\omega)$. Thus the transition to the far-field limit for each component will depend on frequency. Further, since the highest frequencies will have the smallest $\lambda_{\mathrm{AC}}(\omega)$, these components will reach the far-field limit (where the distance-decay is sharper and the signal rapidly diminishes) closer to soma. Fig. 6 illustrates this low-pass filtering effect for the dipole-model approximation of the ball-and-stick neuron.

4.4 Parameter dependence of spike amplitude

In addition to explaining the position-dependent low-pass filtering of the extracellular spike, the dipole model approximation of the ball-and-stick neuron can also explain essential features of the size and distance dependence of the spike-amplitude [66]: For the infinite ball-and-stick neuron it is possible to derive an analytical expression for the frequency-dependent *transfer function* $\mathbf{T}$ describing how a soma membrane potential 'transfers' to an extracellular potential. With a complex notation (boldface) the soma membrane potential for a given angular frequency ω can be represented as $\mathbf{V}_0(t;\omega) = \hat{\mathbf{V}}_0(\omega)e^{j\omega t}$, where $\hat{\mathbf{V}}_0$ contains both the amplitude and phase of the sinusoidal potential and $j = \sqrt{-1}$. The physical soma membrane potential will then be the real part of this complex quantity, $V_0(t;\omega) = \mathrm{Re}\{\mathbf{V}_0(t;\omega)\}$. The complex Fourier amplitude of the extracellular potential $\hat{\mathbf{\Phi}}(\mathbf{r},\omega)$ for a ball-and-stick model can thus be related to the complex soma potential $\hat{\mathbf{V}}_0(\omega)$ through the transfer function $\mathbf{T}(\mathbf{r},\omega)$, i.e., $\hat{\mathbf{\Phi}}(\mathbf{r},\omega) = \mathbf{T}(\mathbf{r},\omega)\hat{\mathbf{V}}_0(\omega)$ [66]. Since the DC-subtracted intracellular somatic action potential $V_0(t)$ can be expressed by a Fourier series, $V_0(t) = \sum_{k=1}^{\infty} \mathrm{Re}\{\hat{\mathbf{V}}_0(\omega_k)e^{j\omega_k t}\}$, the measured extracellular response to any such DC-subtracted somatic action potential can be expressed as

$$\phi(\rho, z, t) = \sum_{k=1}^{\infty} \mathrm{Re}\{\mathbf{T}(\mathbf{r},\omega_k)\hat{\mathbf{V}}_0(\omega_k)e^{j\omega_k t}\} \ . \tag{16}$$

The transfer function for the ball-and-stick neuron has a rather complex analytical form [66]. To investigate the parameter dependence of the spike amplitude we instead use the much simpler dipole model with a frequency-dependent dipole length given by the length constant of the infinite ball-and-stick model in Eq. (13).

Near the soma the monopole contribution from the soma membrane current will dominate, and the extracellular potential will decay as $|\hat{\mathbf{\Phi}}(\omega)| \sim |\hat{\mathbf{I}}(\omega)|/4\pi\sigma r$, where the somatic membrane current $\mathbf{I}$ is related to the somatic membrane potential through the dendrite's admittance, $\hat{\mathbf{I}} = \hat{\mathbf{Y}}\hat{\mathbf{V}}_0$, see [66]. The transfer function $\mathbf{T}$ will therefore be given by $\hat{\mathbf{Y}}/4\pi\sigma r$ in the near-field approximation, and for high frequencies ($\omega\tau \gg 1$), the transfer function can be shown to be [66]

$$|\mathbf{T}_{\mathrm{near}}| \sim \frac{d^{3/2}}{\sigma r}\left(\frac{f C_{\mathrm{m}}}{R_{\mathrm{i}}}\right)^{1/2} . \tag{17}$$

In the far-field approximation the potential is given by the dipole or quadrupole expressions (when moving laterally, see above), $\hat{\mathbf{\Phi}}(\omega) \sim \hat{\mathbf{I}}(\omega)L/4\pi\sigma r^2$ or $\hat{\mathbf{\Phi}}(\omega) \sim \hat{\mathbf{I}}(\omega)L^2/4\pi\sigma r^3$, respectively [66]. We then assume $L \approx \lambda_{\mathrm{AC}}^{\infty}(\omega)$ (Eq. 13), and for $\omega\tau \gg 1$ we have $\lambda_{\mathrm{AC}}^{\infty}(\omega) \sim \lambda/\sqrt{\omega\tau} \sim \sqrt{d/fR_{\mathrm{i}}C_{\mathrm{m}}}$. With a reasonable time constant such as $\tau = 20$ ms, this high-frequency approximation holds for frequencies $f \gg 8$ Hz, i.e., all the dominant frequencies of the action potential. The far-field transfer functions can with these assumptions be shown to be [66]

$$|\mathbf{T}_{\mathrm{far,d}}| \sim \frac{d^2}{\sigma r^2 R_{\mathrm{i}}} \ , \ \ |\mathbf{T}|_{\mathrm{far,q}} \sim \frac{d^{5/2}}{\sigma r^3 f^{1/2} R_{\mathrm{i}}^{3/2} C_{\mathrm{m}}^{1/2}} \ , \tag{18}$$

where 'far,d' means far-field dipole expression and 'far,q' means far-field quadrupole expression (applicable when moving perpendicular to the ball-and-stick neuron [66]). In Pettersen and Einevoll [66] a host of numerical simulations were done to investigate to what extent these analytical predictions are accurate, not only for individual frequency components but also for the full action potential. The numerical calculations indeed confirmed their validity, cf. Fig. 9 in Ref. [66].

The transfer-function expressions in Eqs. (17) and (18) give some interesting qualitative insights:

1. Close to the soma the higher frequencies are amplified compared to the low frequencies, $|T| \sim \sqrt{f}$. Thus close to the soma the extracellular action potential will typically appear sharper than the intracellular action potential.
2. Far away this high-frequency amplification is either vanished ('far,d', $|T| \sim f^0$) or reversed ('far,q', $|T| \sim 1/\sqrt{f}$).
3. $|T|$ is independent of the membrane resistivity R_m.
4. $|T|$ decreases with increasing intracellular resistivity R_i.
5. $|T|$ may, depending on distance from soma, increase or decrease with increasing capacitance C_m.
6. $|T|$ increases with increasing dendritic diameter d, that is, $T \sim d^k$ where $k = 1.5 - 2.5$.

While Eqs. (17) and (18) were derived for a simple ball-and-stick, similar expressions can easily be derived for more complicated neuron models, see Ref. [66] for details. For example, for the linear quadrupole model depicted in Fig. 7B the quadrupolar far-field expression in Eq. (18) applies in all angular directions [66].

The last entry in the above list (point 6) suggests an important connection between the extracellular spike amplitude and the dendritic diameters. Since the contributions from different soma-attached dendrites add up, the point suggests a rule of thumb: *A neuron's extracellular spike amplitude is approximately proportional to the sum of the dendritic cross-sectional areas of all dendritic branches connected to the soma* [66]. Thus, neurons with many, thick dendrites connected to soma will produce large-amplitude spikes, and will therefore have the largest radius of visibility.

In Ref. [66] we confirmed this rule of thumb for the two morphologically reconstructed cells shown in Fig. 5A and C.. The pyramidal neuron had more soma-attached dendrites than the stellate cell (11 vs. 6) and they were thicker as well (average diameter of 3.0 μm vs. 2.1 μm). In the numerical simulations the ratio between the peak-to-peak extracellular spike amplitudes of the pyramidal and stellate neurons were found to be 3.3, 3.7, and 4.0 at 20 μm, 60 μm, and 100 μm distances, respectively (see Table 1 in [66] for details). The above rule of thumb ($|T| \sim d^2$) predicts this ratio to be 4.5, in reasonable agreement with the numerical results. The agreement is even better if one considers that the d^2-rule is expected to be best far away from the soma. Strictly speaking, a $d^{3/2}$-rule is predicted close to the soma (Eq. 17). The latter rule predicts the ratio to be 3.3, exactly what is calculated for the smallest distance (20 μm).

4.5 Active dendritic conductances

So far, we have only considered action potentials from neurons with electrically passive dendrites. This assumption makes the problem of translating intracellular potentials in the soma to extracellular potentials recorded outside the neuron *linear* and, importantly, independent of the detailed form of the intracellular action potential, i.e., independent of the detailed properties of the active soma conductances responsible for generating the action potential. Thus the analytical insights reviewed in the previous subsection apply in principle to all different intracellular action-potential waveforms.

However, real neurons have active conductances also in the dendrites [83]. In general, this makes the problem nonlinear, and the trick of considering each frequency component of the action potential separately is no longer applicable. Instead one has to use comprehensive compartmental models including all active conductances explicitly. Gold and coworkers [21, 22] have done thorough investigations of the extracellular signatures of spikes from pyramidal neurons in hippocampus CA1 and fitted compartmental models to reproduce simultaneously recorded intracellular and extracellular waveforms. An important result from their studies was that extracellular waveforms provide tighter constraints on the model parameters than the intracellularly recorded somatic action potentials. This suggested that extracellular action potentials could be a a good source of data for constraining compartmental models [21].

Their results are also in qualitative agreement with many of the observations seen above for the purely passive dendrites: (i) the spike width was seen to increase with distance from the soma (cf. Fig. 5A in Ref. [22]), (ii) the amplitude was seen to decay with soma distance with a power between 1 and 2 for distances less than 50 μm (cf. Fig. 14 in Ref. [22]), and (iii) the amplitude was seen to change significantly to

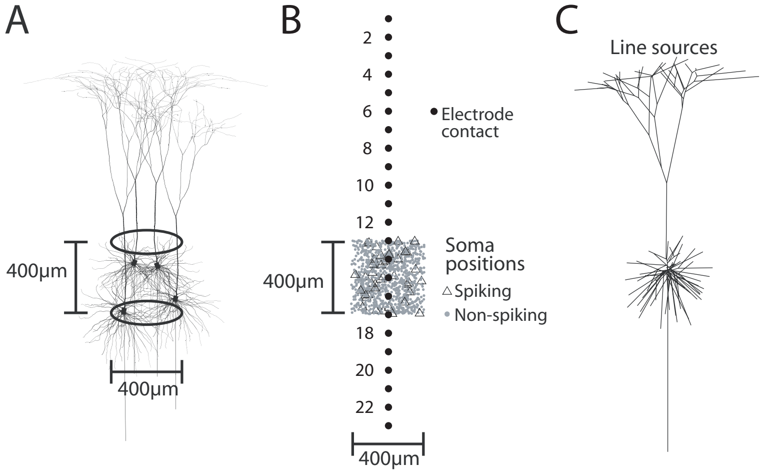

Figure 8: (A) Schematic illustration of the population of reconstructed layer-5 pyramidal neurons considered in forward-modeling study [67]. (B) Somas of pyramidal neurons placed randomly inside a cylindrical annulus with height 0.4 mm, outer diameter 0.4 mm and inner diameter 0.1 mm. One thousand neurons were non-spiking (dots), while 40 neurons (triangles) produced a single spike following synaptic stimulation . Extracellular potential was simulated at assumed electrode contact positions along the center axis of the population (filled circles). (C) Illustration of line-source method: the transmembrane current from each neural segment is modelled as a linear current source of uniform current density. Note that each neural branch (section) depicted in the panel may consist of several segments.

varying intracellular resistivity R_i and capacitance C_m, but not so much to varying membrane resistivity [21].

5 Extracellular potentials from columnar population activity

In Sections 3 and 4 we considered extracellular potentials generated by activity in single neurons. Extracellularly recorded signals like LFP and MUA do not stem from single neurons, however, rather from *populations* of neurons. The forward-modeling scheme applied above for single neurons applies equally well to populations of neurons, and here we outline results from our modeling study of the generated LFP and MUA by a synaptically activated, spatially confined population of layer-5 neurons [67], mimicking a population of large pyramidal cells in a sensory neocortical column [56].

In this pilot MUA and LFP forward-modeling study we sought to answer questions like: Is the MUA really a more local measure of neural activity than LFP? How sharply does the MUA and LFP decay outside the active population? To what extent is the MUA a measure of the *population firing rate*? Do existing CSD analysis methods estimate the true CSD accurately?

5.1 Columnar population model

The simulated population in Pettersen et al. [67] consisted of 1040 layer-5 pyramidal neurons of the type shown in Fig. 5A. Their somas were placed stochastically in a cylinder with both diameter and height of 0.4 mm, see Fig. 8. The population was constructed based on a single neuron model template, but with two different synaptic input patterns. To get MUA responses in reasonable agreement with experimental data [14, 78], only 40 of the neurons received a net synaptic input sufficiently strong to generate a single action potential within a time window of about 20 ms. The net synaptic input to the remaining 1000 neurons was tuned such that no action potential was generated. To introduce temporal jitter in the synaptic activation of the neurons in the population, the neuronal templates were stochastically shifted in the time domain assuming a Gaussian distribution with a standard deviation of 5 ms. The extracellular potential was computed at 23 positions, every 0.1 mm along the center axis of the population, see Fig. 8B. For the present modeling example we found that a balanced combination of apical excitation and basal inhibition was needed to get realistic LFP amplitudes compared to experimental LFP data, since apical excitation alone did not give large enough LFP amplitudes for a population of about 1000 cells. Both single-trial and trial-averaged population responses were calculated. A set of 40 trials was considered in the trial-averaging procedure, and each trial differed in their stochastic distribution of both the position and time-shifting for the individual neurons.

5.2 Population response

With more than 1000 synaptically activated pyramidal neurons, the LFP response was found to be very robust, different trials gave virtually identical results. For the MUA, the detailed temporal structure of single-trial signals was found to vary considerably on a millisecond scale, reflecting the stochastic firing of specific neurons located close to the electrode contacts (cf. Fig. 4 in [67]). The stochastic placement of the soma positions in the model thus makes single-trial MUA a much more noisy measure of neural activity than LFP. However, the trial-averaged MUA over 40 trials was seen to be quite reproducible and, importantly, independent of the form of synaptic input pattern providing the excitation.

Trial-averaged responses for the LFP and MUA data obtained in our forward modeling scheme are shown in Fig. 9A and B. Note that while synaptically evoked LFP can be seen at most electrode contacts, MUA can essentially only be seen at the contacts inside the vertical distribution of somas in the population, i.e., between contacts 13 and 17.

5.3 Spatial spread of LFP and MUA signals

If one measures extracellular potentials in cortex with two adjacent electrodes, say, 0.5 millimeter apart and find that their LFP signals are correlated, two possible interpretations come to mind. Either (i) the two electrodes may measure neural activity from two separate neural populations which happen to have correlated synaptic input activity, or (ii) the LFP generated by a single population may spread to the

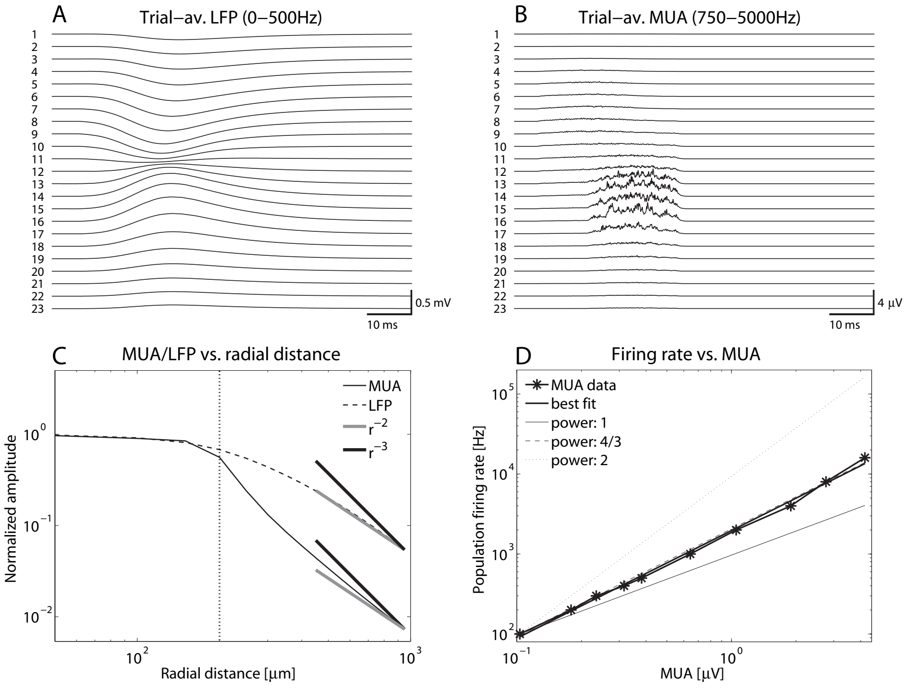

Figure 9: Trial-averaged (A) local field potential and (B) multi-unit activity recorded at center axis of cylindrical population of 1040 layer-5 pyramidal neurons receiving apical excitation and basal inhibition. The depicted LFP is obtained by (i) low-pass filtering of the calculated extracellular potential ($<$500 Hz) and (ii) trial-averaging (n=40). The MUA is obtained by (i) band-pass filtering between 750-5000 Hz, (ii) rectification, and (iii) trial-averaging (n=40). 40 of 1040 neurons fire an action potential stochastically within time window of 20 ms. For details of numerical simulation, see Ref. [67]. (C) Decay of amplitude of 'area under graph' MUA and LFP calculated at electrode 15 (middle of population) as a function of lateral distance from the population center, cf. Fig. 15 in [67]. The vertical dotted line illustrates the lateral edge of the soma distribution corresponding to a radial distance of 200 μm. (D) Relationship between 'true' firing rate and estimates based on MUA signal, cf. Fig. 13 in [67]. The depicted MUA is the average MUA for the 5 electrode contacts running through the center of the population (electrode contacts 13-17, see Fig. 8). The population size was varied and all neurons within the population were spiking. The power law giving the best fit to the data has a coefficient of 1.346.

two electrodes by *volume conduction* [64]. Likewise, if the MUA signals of the two electrodes are observed to be correlated, this can also be due to correlated firing in two spatially separated populations or volume conduction of the MUA signal from a single population.

From the discussion in Section 4 one would expect the LFP generated by a population to have a larger spatial spread, i.e. larger volume conduction, than the corresponding MUA: the LFP contains lower frequencies than the MUA and will thus have longer characteristic AC length constants and consequently decrease less steeply with distance. These expectations were confirmed by numerical simulations [67]: Fig. 9C illustrates the distance-decay of the MUA and LFP signals from our model population in a direction perpendicular to its center axis. The MUA is seen to decay sharply outside the population ($r > 200$ μm), whereas the LFP is seen to spread much further . For example, at a position 0.3 mm outside the population cylinder, i.e., 0.5 mm from the population center, the magnitude of the LFP signal is seen to be reduced with about a factor five compared to the value at the population center, whereas the MUA is reduced by a factor 30. Thus compared to the LFP, observed correlations of the MUA signal between adjacently placed electrodes are more likely to be due to correlated firing in two different populations. However, these are just example results, and more systematic studies are needed to elucidate, e.g., the neural origin of LFPs recorded in cortex [41–43].

5.4 MUA as a measure of population firing rate

The MUA, obtained by high-pass filtering ($\gtrsim$ 500 Hz) with subsequent rectification of the extracellular signal, has been assumed to measure the population firing rate for a group of neurons around the electrode contacts [6, 14, 78, 86]. In Ref. [67] we used the present population forward-modeling study to test this assertion: since we can set the population firing rate ourselves in this model world, we have a gold standard against which the calculated MUA signal can be compared.

Two different regimes can be expected [67]: The first regime corresponds to very low firing rates. Here the various extracellular signatures from firing in the nearby neurons contributing to the MUA will not overlap significantly in time. Thus even with biphasic extracellular signatures (cf. Fig. 4A), there will be little cancelation between positive and negative phases of the extracellular potential. A linear relationship between the MUA and the population firing rate is thus expected.

The other regime corresponds to very high population firing rates. In this high-firing limit the MUA was found to grow roughly as the square root of the population firing rate [67]. Here there will be strong temporal overlap in the sum over extracellular signatures from all contributing neurons, and the summation is better viewed as a sum over randomly drawn positive and negative contributions to the extracellular potential. If the positive and negative contributions are similar in size, the rectified summed signal is expected to grow as the square root of the number of contributions, i.e., as the square root of the population firing rate.

It is, however, a priori unclear what ranges of population firing rates correspond to the different regimes; this will depend on neuronal morphologies and densities (as well as the physical characteristics of the electrode). In Pettersen et al. [67] it was found that for realistic population firing-rates and trial-averages over 40 trials, there is a large regime where the relationship between the MUA and population firing rate is well approximated by raising the population firing rate to a power of 3/4, i.e., intermediate between the linear and the square-root regimes. This implied that a good estimate of the population firing rate can be obtained by raising the MUA to the power 4/3, see double-logarithmic plot in Fig. 9D. Indeed, this rule clearly improved the population firing rate estimates for the examples considered in Ref. [67] compared to results from using the standard linear rule. However, it is unclear to what extent this rule extends to other situations.

6 Estimation of current-source density (CSD) from LFP

The previous Sections 3, 4, and 5 all considered forward-modeling of extracellular potentials, that is, the calculation of extracellular potentials from known activity in neurons. The present section deals with the opposite problem, namely how the underlying neural activity can be estimated based on measurements of the extracellular potential or more specifically the LFP. An estimation of transmembrane current through a particular segment of a particular neuron is in practice out of the question; in principle, one can only extract one unknown current source per electrode contact and an infinite number of different current-source constellations can produce the extracellular potential recorded on a finite number of electrode contacts.

A common strategy has been to use multicontact LFP recordings to estimate the current-source density (CSD), that is, the volume density of net current entering or leaving the extracellular medium, see Section 2.3. A microscopic view inside the cortical tissue reveals an inhomogeneous, densely packed collection of neural segments acting as current sources. The CSD is a more mesoscopic concept and can be interpreted as the average transmembrane current for a piece of neural tissue in a volume element a few tens of micrometers across. In practice the maximum possible spatial resolution in the estimation of CSD will be limited by the intercontact distance, typically 100 μm or more.

6.1 Standard CSD method

The traditional CSD estimation is based on LFP recordings with laminar (linear) multielectrode arrays with a constant inter-contact distance h inserted perpendicularly to the cortical surface [13, 14, 53, 75, 78, 86]. Motivated by the prominent laminar structure of cortical tissue where the changes in the lateral directions are much smaller than in the vertical direction, it has been common to assume an infinite activity diameter in the lateral (xy) plane, i.e., perpendicular to the laminar electrode oriented in the z-direction. Variation of the extracellular potential in the x- and y-directions can then be neglected, so that Eq. (10) simplifies to its one-dimensional version:

$$\sigma \frac{d^2\phi(z,t)}{dz^2} = -C(z,t) \ . \qquad (19)$$

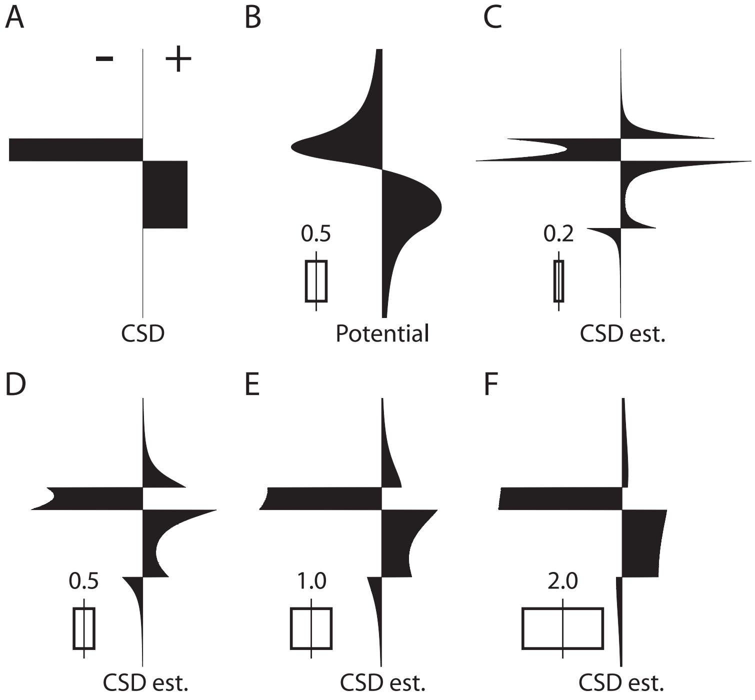

Figure 10: Illustration of errors inherent in standard CSD estimation method for one-dimensional recordings for simplified CSD profile, similar to Ref. [60]. (A) Example CSD depth profile, (B) corresponding LFP at center axis when the CSD distribution has a diameter-to-height ratio of 0.5. (C–F) Estimated CSDs for increasing diameter-to-height ratios, as indicated by the number and inset in the lower left of each panel. All estimates are based on the double spatial-derivative formula of the standard CSD method, i.e., Eq. (20). Arbitrary units, negative values to the left and positive to the right.

A natural estimator for the CSD at electrode position z_j has thus been [60]

$$C(z_j) = -\sigma \frac{\phi(z_j + h) - 2\phi(z_j) + \phi(z_j - h)}{h^2} \tag{20}$$

or variations thereof, including additional spatial smoothing filters [17, 86]. With N electrode contacts the above estimator can predict the CSD only at the $N-2$ interior contact positions. However, a trick allowing for the estimation of the CSDs also at the top and bottom electrodes has been suggested [87].

If we define the domain of electrode contact j located at position z_j as the domain from $z_j - h/2$ to $z_j + h/2$, it is natural to assume that the estimate $C(z_j)$ should correspond to the average CSD within this domain. In Ref. [65] it was instead shown from electrostatic theory that the process of discretizing the one-dimensional Poisson equation into Eq. 20 corresponds to assuming all CSD within each electrode's domain to be located in an infinitely thin (and infinitely wide) sheet at the height of the electrode-contact. However, a possibly larger source of estimation error stems from the assumption of an infinite activity diameter perpendicular to the laminar electrode. This was noted already by Nicholson and Freeman in 1975 [60] who showed that small 'columnar' activity diameters ($\sim$ 1 mm or less) may give large errors in the estimated CSD. The numerical example from Ref. [60] is reproduced here in Fig. 10, and for the small source diameters the estimated CSD is clearly seen to be erroneous, predicting, for example, spurious sinks and sources. Indeed Nicholson and Freeman [60] recommended and later pursued a full three dimensional CSD analysis based on the full Poisson equation (Eq. 10) which required technically demanding measurements of extracellular potentials in all three spatial directions [62]. With the advent of the present silicon-based multielectrodes such a CSD estimation scheme can now become more practically feasible [9].

6.2 Inverse CSD methods

In Pettersen et al. [65] a new method for estimation of CSD was introduced, the *inverse CSD (iCSD)* method. The core idea behind this method is to exploit the well-known forward-modeling scheme for calculation of the LFP from given a CSD distribution: With an assumed form of the CSD distribution parameterized by N unknown parameters, the forward solution can be calculated and inverted to give estimates of these N parameters based on N recorded potentials. This iCSD approach has several inherent advantages:

- The method does not rely on a particular geometrical arrangement of the N electrode contacts recording the LFP signals. It is thus not only applicable to linear multielectrodes [65], but can also be straightforwardly be generalized to other multielectrode geometries [37, 38].

- A priori constraints, such as knowledge about the lateral size of columnar activity, can be built directly into the iCSD estimator [14, 38, 65, 67].

- Unlike the standard CSD method, the iCSD method can also predict CSD at the positions of the boundary electrode contacts [37, 38, 65].

- Discontinuities and direction dependence of the extracellular conductivity can be incorporated [14, 65].

To present the iCSD idea more explicitly we now consider a situation where one has recordings from N electrode contacts. Further, the CSD has been parameterized by N parameters describing the weights of the different contributions to the CSD [65]. Regardless of the choice of parametrization, the CSD is now uniquely determined by the N weight parameters $\{C_1, C_2, \ldots, C_N\}$. The LFP due to this CSD distribution can then be calculated at the N electrode contact positions using electrostatic theory (e.g., using Eq. (7) if σ is scalar and homogeneous). Due to the linearity of electrostatic theory the LFP grows linearly with the CSD weight parameters, and their relationship can thus be formulated in matrix form as [65]

$$\mathbf{\Phi} = \mathbf{F}\mathbf{C} \ . \tag{21}$$

Here $\mathbf{\Phi} = [\phi_1 \ \phi_2 \ \ldots \ \phi_N]^T$ is a vector containing the extracellular potential, and $\mathbf{C} = [C_1 \ C_2 \ \ldots \ C_N]^T$ is a corresponding vector containing the CSD parameters. $\mathbf{F}$ is an $N \times N$ matrix containing the mapping from CSDs to extracellular potentials found from electrostatic theory. If $\mathbf{F}$ is constructed properly, it will be invertible, and an estimate of the N unknown CSD parameters $\hat{\mathbf{C}}$ can then be estimated from the N recorded potentials by a simple matrix multiplication with the inverse matrix $\mathbf{F^{-1}}$:

$$\hat{\mathbf{C}} = \mathbf{F}^{-1}\mathbf{\Phi} \tag{22}$$

To illustrate the calculation of the matrix $\mathbf{F}$ we can consider the most common situation where a laminar electrode array with equidistant electrode contacts is inserted perpendicularly into, say, sensory cortex [13, 14, 53, 75, 78, 86]. For simplicity we further assume the stimulus-evoked CSD to be located in infinitely thin, circular disks centered on the N electrode contacts. Each disk is further assumed to have the same CSD throughout the disk and to be positioned in the horizontal plane perpendicular to an inserted laminar electrode array [65]. For this 'δ-source' method a simple formula is obtained for the matrix elements, and the method also has some additional interest since it turns out to correspond to the standard CSD method in the limit of infinitely large discs [65]. From electrostatic theory we have that the extracellular potential at a position z at the center axis due to an infinitely thin current-source disk placed in z' is given by $\phi = (\sqrt{(z-z')^2 + R^2} - |z - z'|)C^{\mathrm{p}}/2\sigma$, where C^{p} now is the *planar* CSD, R is the radius of the disks, and σ is the extracellular conductivity [61, 65]. This implies that the matrix elements f_{jk} of the matrix $\mathbf{F}$ is given by

$$f_{jk} = \left(\sqrt{(z_j - z_k)^2 + R^2} - |z_j - z_k| \right) h/2\sigma \ , \tag{23}$$

where $C_j = C_j^{\mathrm{p}}/h$ and $z_j - z_k = h(j-k)$. This *δ-source* iCSD method is now completely specified by Eqs. (22) and (23), and as shown, e.g., in Fig. 7 of Ref. [65], even this simple δ-source CSD method completely outperforms the standard CSD method when the population activity is spatially confined.

In Ref. [65] two other variations of the iCSD method were also investigated: the *step* iCSD method, where the CSD is assumed to be step-wise constant in the z-direction, and the *spline* iCSD method based on cubic-splines interpolation. A

GUI-based MATLAB toolbox for estimating the CSD from laminar multielectrode recordings has been developed based on these three iCSD methods and can be downloaded from *http://software.incf.org/*.

These two latter methods were generalized and further developed by Leski et al. [37] who developed iCSD method for estimation of CSD based on three-dimensional recordings. In this situation the advantage of the iCSD method is even larger compared to the standard CSD method in that the fraction of electrode contacts at the boundary is much higher. For example, their electrode grid consisted of $4 \times 5 \times 7$ contacts, for which 110 of the 140 electrode contacts are the boundary and thus outside the scope of the standard CSD method. From their studies Leski et al. concluded that a spline iCSD method was a good choice for this three-dimensional situation [37].

The iCSD method has now also been implemented for the case with two-dimensional recordings [38], e.g., recordings done with multishank laminar electrodes [9]. As for the 1D method, a GUI-based MATLAB toolbox has been developed to facilitate easy use of the method [38].

6.3 Validation of iCSD with population forward modeling

The results from forward-modeling of synaptically evoked activity in a population of morphologically reconstructed pyramidal neurons in Section 5 are well suited to test the iCSD approach, and to compare the accuracy of this method with the standard CSD method. Here we consider the situation where the LFP is recorded by a laminar electrode array oriented perpendicular to the cortical layers and penetrating the population through its center [67], but these forward-modeling population results have also been used for testing of the iCSD approach for recordings with multishank laminar electrodes [38].

As discussed above the CSD should be considered as the average net transmembrane current within a particular volume element. In Fig. 11A we show the actual CSD at the center of the columnar model population shown in Fig. 8, i.e., the average transmembrane current of a centered cylindrical volume element of height 0.1 mm and radius 0.2 mm, plotted as a function of time. The spatial spread of this CSD is illustrated in Fig. 11B. Here, the CSD at a particular time ($t = 25$ ms, cf. Fig. 9A) was computed for cylindrical annuli with rectangular cross-sectional areas of 0.05 mm×0.1 mm. It is seen that the CSD varies only moderately as a function of radial distance when inside the column. One further sees that even though the somas are restricted to radial distances less than 0.2 mm, the dendrites gives non-negligible CSD outside this boundary.

The next four panels in Fig. 11 illustrate the accuracy of the CSD estimation methods in this model situation. The estimated CSD along the (virtual) laminar electrode from the standard CSD method is shown in Fig. 11C. This CSD is estimated by using Eq. (20) on model LFPs at the (virtual) electrode contacts at the center axis of the column, cf. Fig. 8B, except at the top and bottom contacts were the method of Ref. [87] is used. Comparison with Fig. 11A shows that the standard CSD method predicts spurious sinks and sources below and above the actual CSD. Further, the size (amplitude) of the actual sources and sinks are underestimated by

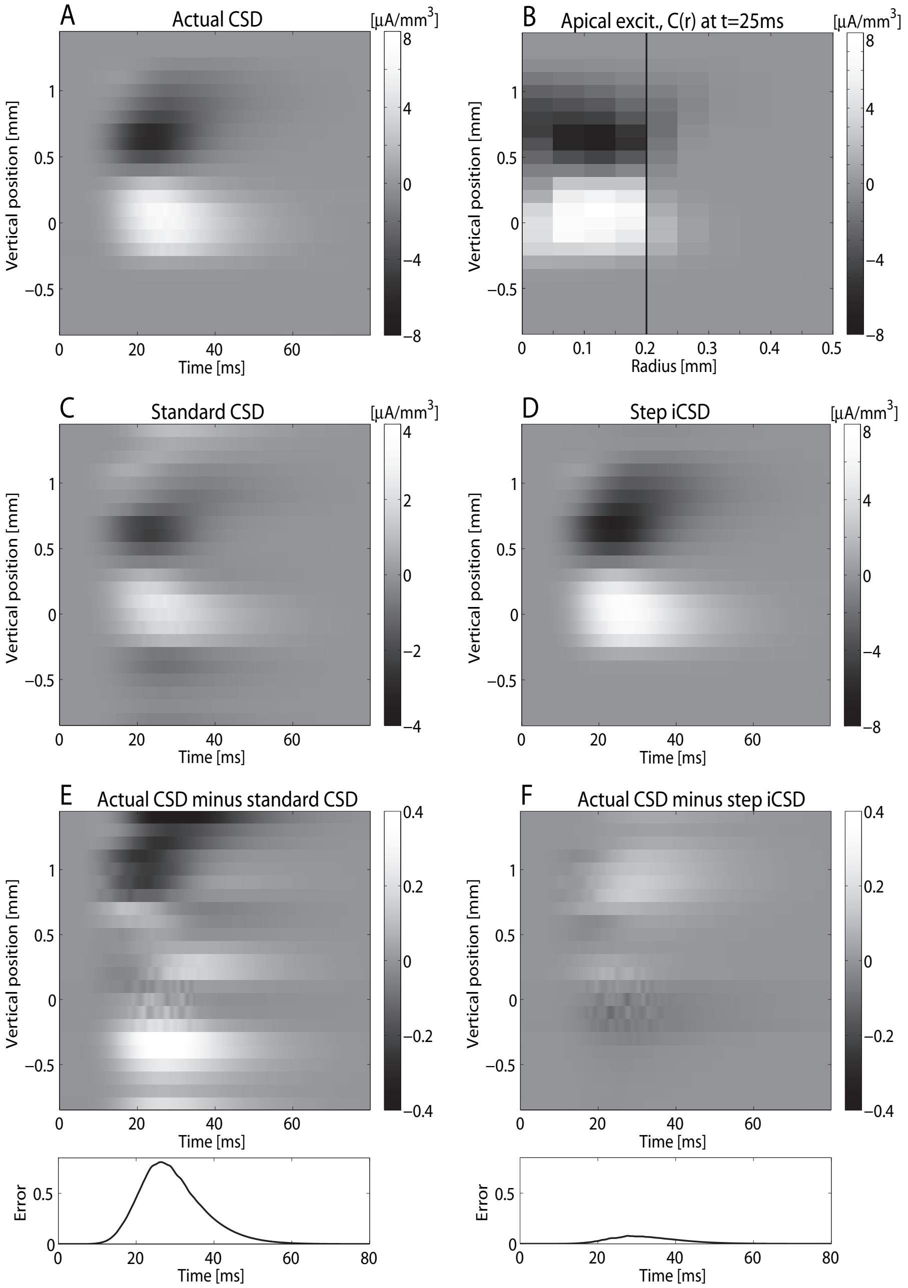

Figure 11: Illustration of CSD of model population and CSD estimation errors for different CSD methods. (A) Actual CSD within the column, i.e., average of CSD in centered cylindrical volume of height 0.1 mm and diameter 0.4 mm. (B) Radial CSD distribution at particular point in time ($t = 25$ ms) as a function of depth and radial distance from population center. Computed by averaging over volume elements consisting of annuli with rectangular cross-sectional area of 0.05 mm×0.1 mm. (C) CSD estimate from using the standard CSD-method on the modelled LFPs along center axis of the population. Top and bottom estimates are found by the using the method of Ref. [87]. (D) CSD estimate from the step iCSD method. (E-F) Difference between the actual CSD and estimates from the standard (E) and step iCSD methods (F), respectively. Both the actual CSD and the estimated CSDs were normalized to have a maximum amplitude of unity prior to error estimation and plotting [67].

about a factor of two.

Fig. 11D shows the CSD estimated from the step iCSD method [67]. This method assumes piecewise constant CSD distribution in the vertical direction. A columnar diameter of 0.4 mm is assumed in the iCSD method, the diameter of the cylindrical box to which the soma positions are restricted. This is clearly less than the spatial extension of the actual CSD seen in Fig. 11B, but anyhow a natural parameter choice. Despite the somewhat unnatural assumptions regarding the form of the CSD, the step iCSD estimates are seen to be very similar to the actual CSD seen in Fig. 11A. The much improved CSD estimates from the step iCSD method compared to the standard CSD method is further illustrated in the panels E and F showing the relative mean-square differences between the actual and estimated CSD for the two CSD estimation methods (see Ref. [67] for detailed specification of the error estimate); the error of the standard CSD method estimates is much larger than for the iCSD step method. For further discussion see Pettersen et al. [67].

7 Concluding remarks

The main topic of this chapter has been the forward-modeling of extracellular potentials, i.e., the calculation the extracellular potentials from activity in neurons or populations of neurons. So far there has been relatively few modeling studies pursuing such calculations; in fact, the first full-fledged study of this type using morphologically reconstructed neurons was done less than fifteen years ago [29]. With the advent of new public databases of reconstructed neurons such as *http://www.neuromorpho.org/* and ever more powerful computers, we expect that the relatively straightforward forward-modeling scheme for calculating extracellular potentials will be more frequently used in the years to come.

An important set of applications of this forward-modeling scheme will be the validation of methods for analysis of LFP and MUA data, as exemplified by the testing of the iCSD method in Fig. 11 or the testing of the MUA as a measure of population firing rate, cf. Fig. 9D and Ref. [67]. The forward-modeling scheme will likewise be useful for testing and development of new methods for analysis of multielectrode data such as the so called *laminar population analysis (LPA)* [14] or spike-sorting algorithms [9, 40].

To improve the accuracy and reliability of the forward-modeling scheme it is important to establish good, experimentally validated models for the impedance properties of the extracellular media in all relevant types of neural tissue. Ideally one could envision experimental setups and protocols allowing for in situ measurement of the extracellular conductivity in conjunction with each multielectrode recording. Further, a more detailed understanding and accurate model representation of the electrical properties of the various types of multielectrodes are needed [24, 54, 58, 59].

Acknowledgement
Trygve Solstad is acknowledged for a thorough reading of an early version of the chapter. This work was supported by the Research Council of Norway (eVita, NOTUR, NevroNor).

References

[1] Bédard, C., Kröger, H., and Destexhe, A. (2004). Modeling extracellular field potentials and the frequency-filtering properties of extracellular space. *Biophys J* **86**, 1829–1842.

[2] Bédard, C., Kröger, H., and Destexhe, A. (2006a). Does the 1/f frequency scaling of brain signals reflect self-organized critical states? *Phys Rev Lett* **97**, 118102.

[3] Bédard, C., Kröger, H., and Destexhe, A. (2006b). Model of low-pass filtering of local field potentials in brain tissue. *Phys Rev E Stat Nonlin Soft Matter Phys* **73**, 051911.

[4] Bédard, C. and Destexhe, A. (2009). Macroscopic models of local field potentials and the apparent 1/f noise in brain activity. *Biophys J* **96**, 2589–2603.

[5] Berens, P., Keliris, G.A., Ecker, A.S., Logothetis, N., and Tolias, A.S. (2008) Comparing the feature selectivity of the gamma-band of the local field potential and the underlying spiking activity in primate visual cortex. *Frontiers in Systems Neuroscience*, 10.3389/neuro.06/002.2008

[6] Blomquist, P., Devor, A., Indahl, U. G., Ulbert, I., Einevoll, G. T., and Dale, A. M. (2008) Estimation of thalamocortical and intracortical network models from joint thalamic single-electrode and cortical laminar-electrode recordings in the rat barrel system, *submitted*.

[7] Bower, J. M. and Beeman, D. (1998). *The Book of GENESIS: Exploring Realistic Neural Models with the GEneral NEural SImulation System, Second edition* (Springer-Verlag, New York).

[8] Buzsaki, G. (2006). *Rhythms of the brain* (Oxford University Press, New York, NY).

[9] Buzsáki, G. (2004). Large-scale recording of neuronal ensembles. *Nat Neurosci* **7**, 446–451.

[10] Carnevale, N. T. and Hines, M. L. (2006). *The NEURON Book* (Cambridge University Press).

[11] Csicsvari, J., Hirase, H., Czurkó, A., Mamiya, A., and Buzsáki, G. (1999). Oscillatory coupling of hippocampal pyramidal cells and interneurons in the behaving Rat. *J Neurosci* **19**, 274–287.

[12] Dayan, P. and Abbott, L. F. (2001). *Theoretical Neuroscience* (MIT Press).

[13] Di, S., Baumgartner, C., and Barth, D. S. (1990). Laminar analysis of extracellular field potentials in rat vibrissa/barrel cortex. *J Neurophysiol* **63**, 832–840.

[14] Einevoll, G. T., Pettersen, K. H., Devor, A., Ulbert, I., Halgren, E., and Dale, A. M. (2007). Laminar population analysis: estimating firing rates and evoked synaptic activity from multielectrode recordings in rat barrel cortex. *J Neurophysiol* **97**, 2174–2190.

[15] Fee, M. S., Mitra, P. M., Kleinfeld, D. (1996). Automatic sorting of multiple unit neuronal signals in the presence of anisotropic and non-Gaussian variability *J Neurosci Methods* **69**, 175–188.

[16] Franke, F., Natora, M., Boucsein, C., Munk, M. H. J., and Obermayer K. (2010). An online spike detection and spike classification algorithm capable of instantaneous resolution of overlapping spikes. *J Comp Neurosci*

[17] Freeman, J. A. and Nicholson, C. (1975). Experimental optimization of current source-density technique for anuran cerebellum. *J Neurophysiol* **38**, 369–382.

[18] Freeman, W. J., Holmes, M. D., Burke, B.C., ãnd Vanthalo, S. (2003) Spatial spectra of scalp EEG and EMB from awake humans. *Clinical Neurophysiology* **114**, 1053–1068.

[19] Freeman, W. J. and Zhai, J. (2009) Simulated power spectral density (PSD) of background electrocorticogram (ECoG). *Cogn Neurodyn* **3**, 97–103.

[20] Gabriel, S., Lau, R. W., and Gabriel, C. (1996). The dielectric properties of biological tissues: III. Parametric models for the dielectric spectrum of tissues. *Phys Med Biol* **41**, 2271–2293.

[21] Gold, C., Henze, D. A., and Koch, C. (2007). Using extracellular action potential recordings to constrain compartmental models. *J Comput Neurosci* **23**, 39–58.

[22] Gold, C., Henze, D. A., Koch, C., and Buzsáki, G. (2006). On the origin of the extracellular action potential waveform: A modeling study. *J Neurophysiol* **95**, 3113–3128.

[23] Gray, C. M., Maldonado, P. E., Wilson, M., and McNaughton, B. (1995). Tetrodes markedly improve the reliability and yield of multiple single-unit isolation from multi-unit recordings in cat striate cortex. *J Neurosci Methods* **63**, 43–54.

[24] Grimnes, S. and Martinsen, Ø. G. (2008). *Bioimpedance and Bioelectricity basics*, 2nd ed. (Academic Press).

[25] Hämäläinen, M., Hari, R., Ilmoniemi, R., Knuutila, J., and Lounasmaa, O. (1993). Magnetoencephalography theory, instrumentation, and applications to noninvasive studies of the working human brain. *Rev Mod Phys* **65**, 413–497.

[26] Harris, K. D., Henze, D. A., Csicsvari, J., Hirase, H., and Buzsaki, G. (2000) Accuracy of tetrode spike separation as determined by simultaneous intracellular and extracellular measurements. *J Neurophysiol* **84**, 401–414.

[27] He, B. J., Zempel, J. M., Snyder, A. Z., Raichle, M. E. (2010) The temporal structures and functional significance of scale-free brain activity. *Neuron* **66**, 353–369.

[28] Henze, D. A., Borhegyi, Z., Csicsvari, J., Mamiya, A., Harris, K. D., and Buzsaki, G. (2000) Intracellular features predicted by extracellular recordings in the hippocampus in vivo. *J Neurophysiol* **84**, 390–400.

[29] Holt, G. R. and Koch, C. (1999). Electrical interactions via the extracellular potential near cell bodies. *J Comput Neurosci* **6**, 169–184.

[30] Hubel, D. H. (1957). Tungsten Microelectrode for Recording from Single Units. *Science* **125**, 549–550.

[31] Jackson, J. (1998). *Classical electrodynamics* (Wiley, Hoboken, NJ).

[32] Jog, M. S., Connolly, C. I., Kubota, Y., Iyengar, D. R., Garrido, L., Harlan, R., and Graybiel, A. M. (2002). Tetrode technology: advances in implantable hardware, neuroimaging, and data analysis techniques. *J Neurosci Methods* **117**, 141–152.

[33] Johnston, D. and Wu, S. M.-S. (1994). *Foundation of Cellular Neurophysiology* (MIT Press).

[34] Katzner, S., Nauhaus, I., Benucci, A., Bonin, V., Ringach, D. L., and Carandini, M. (2009). Local origin of field potentials in visual cortex. *Neuron* **61**, 35–41.

[35] Kim, S. and McNames, J. (2007). Automatic spike detection based on adaptive template matching for extracellular neural recordings. *J Neurosci Meth* **165**, 165–174.

[36] Kreiman, G., Hung, C.P, Kraskov, A., Quiroga, R.Q., Poggio, T., and DiCarlo, J.J. (2006) Object selectivity of local field potentials and spikes in the macaque inferior temporal cortex. *Neuron* **49**, 433–445.

[37] Leski, S., Wojcik, D. K., Tereszczuk, J., Swiejkowski, D. A., Kublik, E., and Wrobel, A. (2007). Inverse current-source density method in 3D: reconstruction fidelity, boundary effects, and influence of distant sources. *Neuroinformatics* **5**, 207–222.

[38] Leski, S., Pettersen, K. H., Tunstall, B., Einevoll, G. T., Gigg, J., and Wojcik, D. K.. Inverse Current Source Density method in two dimensions: Inferring neural activation from multielectrode recordings. *Submitted*

[39] Levina, A., Herrmann, J. M., and Geisel, T. (2007) Dynamical synapses causing self-organized criticality in neural networks. *Nature Physics* **3**, 857–860.

[40] Lewicki, M. S. (1998). A review of methods for spike sorting: the detection and classification on neural action potentials. *Network: Comp. Neural Syst.* **9**, R53–R78.

[41] Lindén, H., Pettersen, K. H., Tetzlaff, T., Potjans, T., Denker, M., Diesmann, M., Grün, S., Einevoll, G. T. (2009). Estimating the spatial range of local field potentials in a cortical population model. *BMC Neurosci* **10(Suppl. 1)**, 224.

[42] Lindén, H., Potjans, T., Einevoll, G. T., Denker, M., Grün, S., and Diesmann, M. (2009). Modeling the large-scale layered cortical network model. *Frontiers in Neuroinformatics.* Conference Abstract: 2nd INCF Congress of Neuroinformatics. doi: 10.3389/conf.neuro.11.2009.08.046

[43] Lindén, H., Pettersen K. H., and Einevoll, G. T. (2010) Intrinsic dendritic filtering gives low-pass power spectra of local field potentials. *J Comput Neurosci*

[44] Linkenkaer-Hansen, K., Nikouline, V. V., Palva, J. M., and Ilmoniemi, R. J. (2001). Long-Range Temporal Correlations and Scaling Behavior in Human Brain Oscillations *J Neurosci* **21**, 1370–1377

[45] Liu, J. and Newsome, W. T. (2006) Local field potential in cortical area MT. Stimulus tuning and behavioral correlations, *J Neurosci* **26**, 7779–7790.

[46] Logothetis, N. K., Kayser, C., and Oeltermann, A. (2007). In vivo measurement of cortical impedance spectrum in monkeys: implications for signal propagation. *Neuron* **55**, 809–823.

[47] López-Aguado, L., Ibarz, J. M., and Herreras, O. (2001) Acitivity-dependent changes of tissue resisitivity in the CA1 region in vivo are layer-specific: Modulation of evoked potentials. *Neuron* **108**, 249–262.

[48] Mainen, Z. F. and Sejnowski, T. J. (1996). Influence of dendritic structure on firing pattern in model neocortical neurons. *Nature* **382**, 363–366.

[49] McNaughton, B. L., O'Keefe, J., and Barnes, C. A. (1983). The stereotrode: a new technique for simultaneous isolation of several single units in the central nervous system from multiple unit records. *J Neurosci Methods* **8**, 391–397.

[50] Miller, K. J., Sorensen, L. B., Ojemann, J. G., and den Nijs, M. (2009). Power-law scaling in the brain surface electric potential. *PLoS Comp Biol* **5**, e1000609.

[51] Milstein, J. N. and Koch, C. (2008). Dynamic moment analysis of the extracellular electric field of a biologically realistic spiking neuron. *Neural Comput* **20**, 2070–2084.

[52] Milstein, J., Mormann, F., Fried, I., and Koch., C (2009). Neuronal shot noise and Brownian 1/f^2 behavior in the local field potential. *PLoS ONE 4*, e4338.

[53] Mitzdorf, U. (1985). Current source-density method and application in cat cerebral cortex: investigation of evoked potentials and EEG phenomena. *Physiol Rev* **65**, 37–100.

[54] Moffitt, M. A. and McIntyre C. C. (2005). Model-based analysis of cortical recording with silicon microelectrodes. *Clin Neurophysiol* **116**, 2240–2250.

[55] Monto, S., Palva, S., Voipio J., and Palva, J. M. (2008) Very slow EEG fluctuations predict the dynamics of stimulus detection and oscillation amplitudes in humans. *J Neurosci* **28**, 8268–8272.

[56] Mountcastle, V. B. (1997). The columnar organization of the neocortex. *Brain* **120**, 701–722.

[57] Nadasdy, Z., Csicsvari, J., Penttonen, M., Hetke, J., Wise, K., and Buzsaki, G. (1998). Extracellular recording and analysis of neuronal activity: From single cells to ensembles, in *Neuronal Ensembles*, ed. H. Eichenbaum and J. L. Davis (Wiley: New York).

[58] Nelson, M. J., Pouget, P., Nilsen, E. A., Patten, C. D., and Schall, J. D. (2008) Review of signal distortion through metal microelectrode recording circuits and filters. *J Neurosic Methods* 169, 141–157.

[59] Nelson, M. J. and Pouget, P. (2010) Do electrode properties create a problem in interpreting local field potential recordings? *J Neurophysiol* 103, 2325–2317.

[60] Nicholson, C. and Freeman, J. A. (1975). Theory of current source-density analysis and determination of conductivity tensor for anuran cerebellum. *J Neurophysiol* **38**, 356–368.

[61] Nicholson, C. and Llinas, R. (1971). Field potentials in the alligator cerebellum and theory of their relationship to Purkinje cell dendritic spikes. *J Neurophysiol* **34**, 509–531.

[62] Nicholson, C. and Llinás, R. (1975). Real time current source-density analysis using multi-electrode array in cat cerebellum. *Brain Res* **100**, 418–424.

[63] Normann, R. A., Maynard, E. M., Rousche, P. J., and Warren, D. J. (1999). A neural interface for a cortical vision prosthesis. *Vision Res* **39**, 2577–2587.

[64] Nunez, P. L. (2006). *Electric Fields of the Brain: The Neurophysics of EEG* (Oxford University Press).

[65] Pettersen, K. H., Devor, A., Ulbert, I., Dale, A. M., and Einevoll, G. T. (2006). Current-source density estimation based on inversion of electrostatic forward solution: Effects of finite extent of neuronal activity and conductivity discontinuities. *J Neurosci Methods* **154**, 116–133.

[66] Pettersen, K. H. and Einevoll, G. T. (2008). Amplitude variability and extracellular low-pass filtering of neuronal spikes. *Biophys J* **94**, 784–802.

[67] Pettersen, K. H., Hagen, E., and Einevoll, G. T. (2008). Estimation of population firing rates and current source densities from laminar electrode recordings. *J Comput Neurosci* **24**, 291–313.

[68] Pettersen, K.H. and Einevoll, G.T. (2009). Neurophysics: what the telegrapher's equation has taught us about the brain, in *An anthology of developments in clinical engineering and bioimpedance: Festschrift for Sverre Grimnes*, Ø. Martinsen and Ø. Jensen (eds.) (Unipub, Oslo).

[69] Pouzat C. and Chaffiol, A. (2009). Automatic spike train analysis and report generation. An imnplementation with R, R2HTML and STAR. *J Neurosci Meth* **181**, 119–144.

[70] Pritchard, W.S. (1992). The brain in fractal time: 1/f-like power spectrum scaling of the human electroencephalogram. *International J Neurosci* **66**, 119–129.

[71] Quian Quiroga, R., Nadasdy, R., and Ben-Shaul, Y. (2004). Unsupervised spike detection and sorting with wavelets and superparamagnetic clustering. *Neural Comp* **16**, 1661–1687.

[72] Quian Quiroga, R. (2007). Spike sorting. *Scholarpedia* **2**, 3583.

[73] Rall, W. (1962). Electrophysiology of a dendritic neuron model. *Biophys J* **2**, 145–167.

[74] Rall, W. and Shepherd, G. M. (1968). Theoretical reconstruction of field potentials and dendrodendritic synaptic interactions in olfactory bulb. *J Neurophysiol* **31**, 884–915.

[75] Rappelsberger, P., Pockberger, H., and Petsche, H. (1981). Current source density analysis: methods and application to simultaneously recorded field potentials of the rabbit's visual cortex. *Pflügers Arch* **389**, 159–170.

[76] Recce, M. and O'Keefe, J. (1989). The tetrode: a new technique for multi-unit extracellular recording. In *Soc. Neurosci. Abstr. 15:1250.*

[77] Rutishauser, U., Schuman, E. M., Mamelak, A. N., Online detection and sorting of extracellularly recorded action potentials in human medial temporal lobe recordings in vivo. *J Neurosci Methods* **154**, 204–224.

[78] Schroeder, C. E., Lindsley, R. W., Specht, C., Marcovici, A., Smiley, J. F., and Javitt, D. C. (2001). Somatosensory input to auditory association cortex in the macaque monkey. *J Neurophysiol* **85**, 1322–1327.

[79] Segev, I. and Burke, R. (1998). Compartmental model of complex neurons, in *Methods in Neuronal Modeling: From Ions To Network*, ed. C. Koch and I. Segev (MIT Press, Cambridge, MA).

[80] Shoham, S. and Nagarajan, S. S. (2004) . The theory of CNS recording, in *Neuroprosthetics: Theory and Applications*, ed. K. W. Horch and G. S. Dhillon, pp. 448–471 (World Scientific, New Jersey)

[81] Shoham, S., O'Connor, D. H., and Segev, R. (2006). How silent is the brain: is there a "dark matter" problem in neuroscience? *J Comp Physiol A* **192**, 777–784.

[82] Smith, L.S. and Mtetwa, N. (2007). A tool for synthesizing spike trains with realistic interference. *J Neurosci Methods* **159**, 170–180.

[83] Stuart, G., Spruston, N., and Häusser, M. (eds.) (2007). *Dendrites, 2nd ed.* (Oxford University Press, Oxford).

[84] Sukov, W. and Barth, D. S. (1998). Three-dimensional analysis of spontaneous and thalamically evoked gamma oscillations in auditory cortex. *J Neurophysiol* **79**, 2875–2884.

[85] Takekawa, T., Isomura, Y., and Fukai, T. (2010) Accurate spike sorting for multiunit recordings. *European J Neurosci* **31**, 263–272.

[86] Ulbert, I., Halgren, E., Heit, G., and Karmos, G. (2001). Multiple microelectrode-recording system for human intracortical applications. *J Neurosci Methods* **106**, 69–79.

[87] Vaknin, G., DiScenna, P. G., and Teyler, T. J. (1988). A method for calculating current source density (CSD) analysis without resorting to recording sites outside the sampling volume. *J Neurosci Methods* **24**, 131–135.

[88] Wehr, M., Pezaris, J. S., and Sahani, M. (1999) Simultaneous paired intracellular and tetrode recordings for evaluation the performance of spike sorting algorithms. *Neurocomp* **26-27**, 1061–1068.

[89] Wilson, M. A. and McNaughton, B. L. (1993). Dynamics of the hippocampal ensemble code for space. *Science* **261**, 1055–1058.

[90] Xing, D., Yeh, C.-I., and Shapley, R. M. (2009) Spatial spread of the local field potential and its laminar variation in visual cortex. *J Neurosci* **29**, 11540–11549.

3.2 Paper II

J Comput Neurosci
DOI 10.1007/s10827-010-0245-4

Intrinsic dendritic filtering gives low-pass power spectra of local field potentials

Henrik Lindén · Klas H. Pettersen · Gaute T. Einevoll

Received: 31 August 2009 / Revised: 30 March 2010 / Accepted: 6 May 2010

Abstract The local field potential (LFP) is among the most important experimental measures when probing neural population activity, but a proper understanding of the link between the underlying neural activity and the LFP signal is still missing. Here we investigate this link by mathematical modeling of contributions to the LFP from a single layer-5 pyramidal neuron and a single layer-4 stellate neuron receiving synaptic input. An intrinsic dendritic low-pass filtering effect of the LFP signal, previously demonstrated for extracellular signatures of action potentials, is seen to strongly affect the LFP power spectra, even for frequencies as low as 10 Hz for the example pyramidal neuron. Further, the LFP signal is found to depend sensitively on both the recording position and the position of the synaptic input: the LFP power spectra recorded close to the active synapse are typically found to be less low-pass filtered than spectra recorded further away. Some recording positions display striking band-pass characteristics of the LFP. The frequency dependence of the properties of the *current dipole moment* set up by the synaptic input current is found to qualitatively account for several salient features of the observed LFP. Two approximate schemes for calculating the LFP, the *dipole* approximation and the *two-monopole* approximation, are tested and found to be potentially useful for translating results from large-scale neural network models into predictions for results from electroencephalographic (EEG) or electrocorticographic (ECoG) recordings.

Keywords Local field potential · Single neuron · Forward modeling · Frequency dependence · EEG

1 Introduction

Extracellular recordings have been, and still are, among the most used methods for probing neural activity. This popularity mainly stems from the spike-counting abilities of sharp electrodes: when placed sufficiently close to a particular neuronal soma, such electrodes will measure a sequence of standardized extracellular potential signatures, each signalling the presence of an action potential in that particular neuron. Information about spiking is commonly extracted from the high frequency band ($\gtrsim$ 500 Hz) of the recorded extracellular potentials. The interpretation of the *local field potential (LFP)*, i.e., the low-frequency part ($\lesssim$ 500 Hz) of extracellular potentials, is generally not so straightforward. The LFP appears to be dominated by dendritic processing of synaptic inputs, not firing of action potentials (Nunez and Srinavasan 2006; Einevoll et al. 2007; Pettersen et al. 2008), and the LFP measured at any

Action Editor: Abraham Zvi Snyder

H. Lindén · K. H. Pettersen · G. T. Einevoll
Department of Mathematical Sciences and Technology,
Norwegian University of Life Sciences,
PO Box 5003, 1432, Ås, Norway

H. Lindén
e-mail: Henrik.Linden@umb.no

K. H. Pettersen
e-mail: Klas.Pettersen@umb.no

G. T. Einevoll (✉)
Center for Integrative Genetics,
Norwegian University of Life Sciences,
Ås, Norway
e-mail: Gaute.Einevoll@umb.no

point will have sizable contributions from neurons located many hundred micrometers away (Kreiman et al. 2006; Liu and Newsome 2006; Berens et al. 2008; Lindén et al. 2008, 2009a; Katzner et al. 2009; Xing et al. 2009).

The advent of new silicon-based multicontact electrical probes in various geometrical arrangements, such as 'multi-shank' (Buzsáki 2004) or 'needlepad' (Normann et al. 1999), offers new exciting opportunities for massively parallel recordings of LFP. Thus LFP certainly has the potential of becoming one of the most important experimental measures when probing neural *population* activity (Mitzdorf 1985; Arieli 1992; Di et al. 1990; Einevoll et al. 2007; Kreiman et al. 2006; Nauhaus et al. 2009). This will require, however, a substantial improvement in our understanding of the link between the underlying activity in neurons and the recorded LFP signal. The present model study aims to add to this understanding by investigating the contribution to the LFP signal from individual neurons receiving synaptic stimulation. Due to the linearity of electromagnetism, a recorded LFP signal will be built up by a linear sum of such contributions from individual neurons located in the vicinity of the electrode contact. The insight gained by studying the LFP signals generated by individual neurons will thus be of great help when embarking on the larger project of linking measured LFPs to activity in populations of neurons or comprehensive neural networks (Lindén et al. 2009a, b).

In the present study we particularly address the question on the origin of observed frequency spectra in LFP and EEG (electroencephalography) recordings (Pritchard 1992; Freeman et al. 2003; Bedard et al. 2006b; Buzsaki 2006; Bedard and Destexhe 2009; Milstein et al. 2009; Miller et al. 2009). In Pettersen and Einevoll (2008) we described an unavoidable low-pass frequency-filtering effect of the extracellular action-potential signature due to the electrical cable properties of the neuronal dendrites. In the present paper we find for our example layer-5 pyramidal neuron that the same intrinsic dendritic filtering effect also strongly affects frequencies down to about 10 Hz, i.e., well into the typical LFP and EEG frequency bands. Moreover, we find the detailed frequency-filtering effects to vary strongly with recording position: for apical synaptic stimulation the low-pass filtering effects are most prominent for recording positions near the soma, and vice versa. We also consider a spatially more compact layer-4 stellate neuron. The same low-pass filtering effect is observed, although with a higher cut-off frequency than for the spatially more extended layer-5 pyramidal neuron.

The use of dipole and other multipole moments in the modeling of bioelectric signals has a long history (Plonsey 1969; Plonsey and Barr 2007). The *current dipole* concept has been particularly important in the interpretation of EEG signals, but there one has typically considered 'mesoscopic' current dipoles representing the collective effect from large number of activated neurons (Nunez and Srinavasan 2006). In a recent study, however, we found the current dipole momentfrom a *single* neuron to be a very useful concept for gaining thorough understanding of the characteristics of extracellular signatures of action potentials (Pettersen and Einevoll 2008). Likewise, we here find the concept to be very useful for obtaining better understanding of the results from our numerically comprehensive calculations of LFPs generated by synaptic activation of individual neurons with complex dendritic morphologies. Further, used in combination with the standard far-field dipole approximation from electrostatics (Jackson 1998; Plonsey and Barr 2007), this quantity is even found to provide quantitatively accurate predictions of the LFP a millimeter or more away from the neuron. This dipole approximation, as well as a *two-monopole* approximation also explored here (Freeman 1980), may even find its use in ambitious large-scale neural network modeling schemes aspiring to predict results from EEG recordings or ECoG recordings, i.e., recordings done at the cortical surface.

Preliminary results from this project were presented earlier in poster format (Lindén et al. 2008).

2 Methods

2.1 Forward modeling of extracellular potentials

Extracellular potentials are generated by transmembrane currents, and in the presently used *volume conductor theory* the system is envisioned as a 3-dimensional smooth extracellular continuum with the transmembrane currents represented as *volume current sources* (Nunez and Srinavasan 2006). In volume conductor theory the fundamental formula for the contribution to the extracellular potential $\phi(\mathbf{r}, t)$ from the activity in an N-compartment neuron model is given by (Nicholson and Freeman 1975; Holt and Koch 1999; Pettersen and Einevoll 2008; Pettersen et al. 2008)

$$\phi(\mathbf{r}, t) = \frac{1}{4\pi\sigma} \sum_{n=1}^{N} \frac{I_n(t)}{|\mathbf{r} - \mathbf{r}_n|} \, . \tag{1}$$

Here $I_n(t)$ denotes the transmembrane current in compartment n positioned at $\mathbf{r}_n$, and σ is the extracellular conductivity. This formula relies on a set of assumptions and approximations: The first is the use of the *quasistatic approximation* of Maxwell's equations. This amounts to neglecting the terms with time derivatives of the electric field **E** and magnetic field **B** from the original Maxwell's equations so that the electromagnetic field effectively decouples into separate 'quasistatic' electric and magnetic fields (Hämäläinen et al. 1993). Then the electric field **E** in the extracellular medium is related to the extracellular potential ϕ via $\mathbf{E} = -\nabla\phi$. For frequencies inherent in neural activity, i.e., less than a few thousand hertz, the quasistatic approximation seems to be well fulfilled (Hämäläinen et al. 1993).

Further, the formula assumes an infinite volume conductor where the electrical properties of the extracellular medium are assumed to be (1) *linear* and *frequency independent* (Logothetis et al. 2007), i.e., $\mathbf{j} = \sigma\mathbf{E}$ where $\mathbf{j}$ is the current density, (2) *ohmic*, i.e., no imaginary part of σ (Nunez and Srinavasan 2006; Logothetis et al. 2007), (3) *position-independent*, i.e., σ is the same everywhere, and (4) *isotropic*, i.e., same σ in all directions (Logothetis et al. 2007). For a more comprehensive discussion of these assumptions regarding the extracellular medium see Pettersen et al. (2010).

In a numerical scheme based on compartmental neuron models, the formula in Eq. (1) can be used directly with the position $\mathbf{r}_n$ set to correspond to a characteristic 'mean' position of compartment n, e.g., the center of a spherical soma compartment or the mid-point of a cylindrical dendritic compartment. This scheme corresponds to the so called *point-source* approximation since all transmembrane currents leaving or entering the extracellular medium from a particular compartment are assumed to go through a single point (Holt and Koch 1999; Pettersen and Einevoll 2008). Another scheme, the *line-source* approximation, assumes the transmembrane currents from each cylindrical compartment to be evenly distributed along a line corresponding to the cylinder axis (Holt and Koch 1999; Pettersen and Einevoll 2008; Pettersen et al. 2008). A line-source formula, analogous to the point-source formula in Eq. (1), can be found in Eq. (2) of Pettersen and Einevoll (2008) . All forward-modeling calculations presented in this paper use the line-source approximation with the extracellular conductivity set to $\sigma = 0.3$ S/m (Hämäläinen et al. 1993).

2.2 Compartmental neuron modeling

All simulations were carried out using the NEURON simulation environment (Carnevale and Hines 2006) which was controlled via a Python interface (Hines et al. 2009). We used two different reconstructed cell morphologies, a layer-5 pyramidal cell and a layer-4 stellate cell from cat visual cortex (Mainen and Sejnowski 1996), both downloaded from *ModelDB* at http://senselab.med.yale.edu/. To assure sufficient numerical precision the length of each compartment of the model neurons was chosen to be maximum one tenth of the electrotonic length at 100 Hz. This gave a total of 1,072 compartments for the layer-5 cell and 343 compartments for the layer-4 cell for our default choice of passive membrane parameters (see below). Simulations in NEURON were performed at a time resolution of 0.0625 ms. The default passive membrane parameters of the cell models were: specific membrane resistance R_m=30 kΩ cm^2, specific axial resistance R_a=150 Ω cm, and specific membrane capacitance C_m=1.0 μF/cm^2 (Mainen and Sejnowski 1996). In the testing of the dependence of LFP power spectra on model parameters we also considered specific membrane resistances R_m and specific axial resistances R_a corresponding to 1/10 and 10 times the default values.

In one application the synaptic input current $I_s(t)$ was modeled as an α-function, that is,

$$I_s(t) = I_0 \frac{t}{\tau_s} e^{1-t/\tau_s}\, \theta(t) \quad , \tag{2}$$

where $\theta(t)$ is the Heaviside unit step function. Note that an excitatory synaptic input corresponds to a negative value of the current amplitude I_0. Simulations with this stimulus was run for 100 ms prior to onset of the α-current to avoid any possible inaccuracies from up-start effects.

The input currents used for calculating LFP power spectra were created as a sum of sinusoidal currents,

$$I_s(t) = I_0 \sum_{f=1}^{1000} \sin(2\pi f t + \gamma_f) \tag{3}$$

where γ_f represents a random phase for each frequency contribution. This current contains all frequencies between 1 Hz and 1,000 Hz in steps of 1 Hz, has a flat frequency spectrum, and is for the purpose of this study equivalent to a 'white-noise' input current. The simulations were run for 1,200 ms. The calculated LFP signals from the last 1,000 ms were used in the evaluation of the power spectra which were obtained by squaring the Fourier amplitudes of the calculated LFP for each frequency.

Since the cable equation describing the present passive neuron is linear, the assumption of current synapses and passive neuronal membrane model makes the overall model linear. This means that all calculated extracellular and intracellular potentials will be proportional to the current amplitude I_0. Further, in the case of a sinusoidal input current, all extracellular and intracellular potentials will also be sinusoidally oscillating with the same frequency, although in general with a different phase. The linearity of the model makes it easier to analyze. However, we expect that most of the observed qualitative features would remain if we, e.g., instead had considered excitation by conductance-based synapses.

2.3 Current dipole moments

Current dipole moments in the x-, y-, and z-directions were calculated as follows:

$$p_x(t) = \sum_{n=1}^{N} x_n \, I_n(t) \ , \quad p_y(t) = \sum_{n=1}^{N} y_n \, I_n(t) \ ,$$

$$p_z(t) = \sum_{n=1}^{N} z_n \, I_n(t) \ . \tag{4}$$

where x_n, y_n, and z_n are the x, y and z positions of compartment n. When the synaptic input current is sinusoidal, i.e., $I_s(t) = I_0 \sin(2\pi f t)$, these dipole moments will due to the linearity of the system be of the form

$$p_x(t) = p_{0x}(f) \sin(2\pi f t + \gamma_{fx}) \ ,$$

$$p_y(t) = p_{0y}(f) \sin(2\pi f t + \gamma_{fy}) \ ,$$

$$p_z(t) = p_{0z}(f) \sin(2\pi f t + \gamma_{fz}) \ . \tag{5}$$

In the special case when the phases are identical, i.e., $\gamma_{fx} = \gamma_{fy} = \gamma_{fz} \equiv \gamma_f$, the system simplifies to a sinusoidally oscillating dipole along a *fixed axis*,

$$\mathbf{p}_{\mathrm{fa}}(t) = \mathbf{p}_0(f) \sin(2\pi f t + \gamma_f) \tag{6}$$

where $\mathbf{p}_0(f)$ is a frequency-dependent vector given by

$$\mathbf{p}_0(f) \equiv p_{0x}(f)\mathbf{e}_x + p_{0y}(f)\mathbf{e}_y + p_{0z}(f)\mathbf{e}_z \ . \tag{7}$$

(Note that the system also reduces to a fixed-axis oscillating dipole when one of γ_{fx}, γ_{fy}, or γ_{fz} is off by a factor π compared to the two others; then the factor π can be eliminated by changing the sign of the 'amplitude' in front of the particular sinus function.)

In the application of the dipole approximation for LFP generation in Sections 3.5 and 3.6 we assume the phases of the three cartesian dipole-moment components to be the same (modulo a factor π) so that a linear dipole is obtained. In order to specify the direction of this linear dipole, one also has to decide the directions of the three components relative to each other. Here we set these directions, for all frequencies considered, to correspond to the current-dipole component directions found in the low frequency limit (1 Hz). With such slowly oscillating input currents the phase shifts between the dipole components are negligible, and the assignment of directions follows directly from evaluating the sign of, say, the x and y components of the current dipole at the first peak for the z component.

3 Results

3.1 Example local field potentials

In Fig. 1 we show examples of patterns of extracellular potential traces around reconstructed neurons. These extracellular potentials are generated by single synaptic inputs for various synaptic positions and neuronal dendritic morphologies. The synaptic input currents are in all examples chosen as α-functions (cf. Eq. (2)) with a time constant of 2 ms and a peak amplitude of 1 nA. In the following we will denote such synaptically generated extracellular potentials as *local field potentials (LFPs)*.

In Fig. 1(a) we show results for a reconstructed layer-5 pyramidal neuron, taken from Mainen and Sejnowski (1996), receiving a single excitatory synaptic input at an apical branch. The form of the injected synaptic current is illustrated by the inset panel. An important feature which is immediately apparent is that the shape and amplitude of the LFPs depend strongly on the recording position. Near the apical synaptic input the LFP signature is generally negative, reflecting that the excitatory current synapse providing a current sink dominates the sum in the forward-model formula, cf. Eq. (1). At positions close to the soma the LFP is always positive, reflecting that return currents in the soma area dominate the sum.

This characteristic dipolar structure is further illustrated by the contour plots shown in the figures as grey solid and dashed lines. These logarithmic contour plots show how the maximum value for LFP signal amplitude, i.e., maximum positive or negative deviation of LFP from baseline following the synaptic input, varies with position. For spatial positions above and to the left of the synaptic input in Fig. 1(a), this largest deviation corresponds to a negative LFP peak, and the dashed contour lines in this region thus corresponds to 'equi-LFP' lines with negative numerical values of the LFP. For spatial positions around the soma, positive LFP peaks dominate, and the solid contour lines correspondingly represent 'equi-LFP' lines with positive values of the LFP. Regardless of the sign of the maximum LFP amplitude, we generally observe a rapid decay of the LFP signal amplitude with distance: when moving away from the neuron, each new contour line represents a reduction of the LFP amplitude by a factor two compared to the previous contour line.

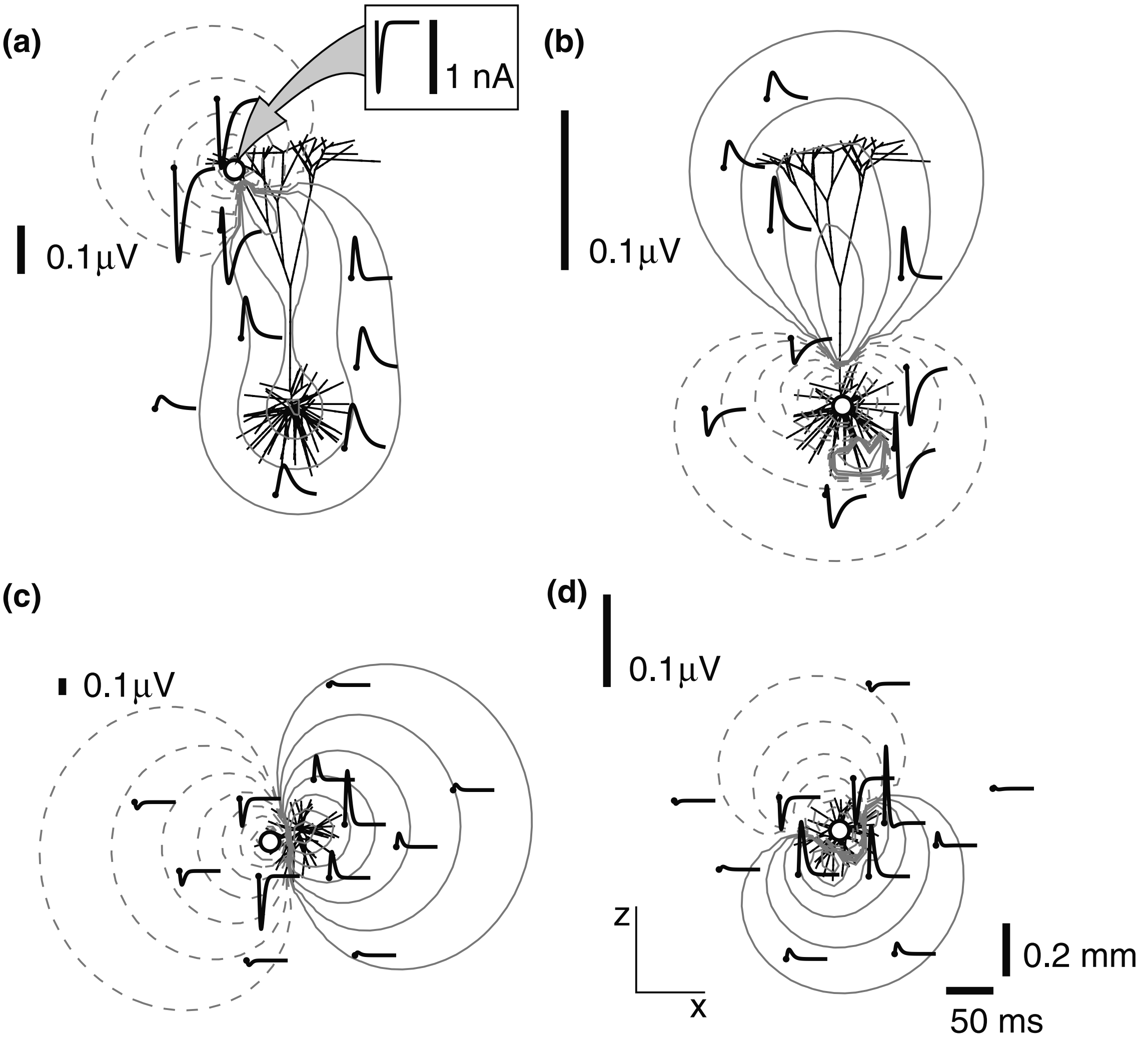

Fig. 1 Examples of calculated local field potentials (LFPs) following an excitatory synaptic input into purely passive neuron models. The synapse is current-based and modeled as an α-function (Eq. (2)) with an amplitude of 1 nA, i.e., $I_0 = -1$ nA, and a time constant $\tau_s = 2$ ms; see panel inset in (**a**) for illustration of synaptic current. Neuron models are passive with the following specific electric parameters: membrane resistivity $R_m = 30$ kΩ cm^2, axial resistivity $R_i = 150$ Ω cm, membrane capacitance $C_m = 1$ μF/cm^2. Extracellular potentials (*thick solid lines*) at selected spatial positions (marked with dots on trace starting points) are shown in 50 ms windows. Grey contour lines illustrate maximal extracellular potential (LFP) amplitudes, i.e., maximum positive or negative deviation of LFP from baseline following the synaptic input. Contour plots are logarithmic and based on $\log_2$, i.e., the LFP amplitude decays by a factor 2 between each contour line. Solid contour lines are 'equi-LFP' lines corresponding to positive values for the LFP amplitude, dashed contour lines to negative values of the LFP amplitude. (**a**) Results for reconstructed L5 pyramidal neuron (*solid branch structure*) from Mainen and Sejnowski (1996) with single excitatory synapse (*solid dot*) on apical branch. The neuron has been rotated so that both the synapse and soma are in the 2D plane of the plot. (**b**) Corresponding results as in (**a**) for a single excitatory synapse in soma. (**c**) Results for reconstructed L4 stellate neuron from Mainen and Sejnowski (1996) with single excitatory synapse on distal branch. (**d**) Corresponding results for a single excitatory synapse in soma

An excitatory synaptic input onto the *basal* dendrites of the pyramidal neuron will typically give the opposite pattern: negative LFPs around the basal synaptic input and positive LFPs around the apical dendrites (results not shown). However, due to the asymmetric dendritic branching with a dominant apical dendrite, even an excitatory input onto the soma gives a prominent dipolar spatial pattern for the extracellular potentials. This is demonstrated in Fig. 1(b). Here we show results from injecting the same current used in Fig. 1(a) into the soma instead of into the apical synapse, and a spatial LFP pattern similar to what might be expected for an excitatory basal input is indeed observed. In Fig. 1(b), however, we see that the amplitudes of the LFP signal are generally much smaller than for the situation with apical excitation depicted in Fig. 1(a). A qualitative explanation is that presumably more of the injected synaptic current returns to the extracellular medium closer to the injection point in the case with somatic input, than for input onto the apical dendrite. There will thus be more cancelation of the contributions from the various terms in the sum in Eq. (1).

A close inspection of the equipotential contour lines in Fig. 1(b) reveals a deviation from the simple dipolar pattern. In a region inside the basal dendritic tree just below the soma, the LFP signals with the largest magnitudes are seen to be positive, not negative as expected from the dipolar structure. In this region the early positive peak prominently seen in the potential trace to the right of and below the soma, has a larger magnitude than the peak of the following negative LFP signal. If we instead had plotted equipotential contour lines for the dominant, i.e., late, LFP peak, a clean dipolar pattern would have been seen.

The layer-5 pyramidal neuron in Fig. 1(a) and (b) has a characteristic 'open-field' dendritic structure where the synaptic input currents and the bulk of the return currents may be substantially separated in space (Johnston and Wu 1995). This will imply a sizable current dipole and, in turn, a sizable contribution to the experimentally recorded LFPs. For example, in panel (a) the distance between the position of the apical synaptic input and the soma, where a large part of the return current exits, is about a millimeter.

In Fig. 1(c) and (d) we show corresponding results for a layer-4 stellate neuron where the dendritic structure has a spherically symmetric appearance, implying a more 'closed-field' structure (Lorente de Nó 1947; Rall 1962; Johnston and Wu 1995). As shown in panel (c), a distal synaptic input onto a dendritic branch will nevertheless produce a dipolar LFP pattern around the stellate neuron where the dipole axis will be oriented along a line between the synaptic input and the soma. Only when the set of distal inputs are distributed symmetrically around the soma can significant cancelation effects on the resulting LFP be expected. However, the cancelation can never be expected to be complete due to unavoidable asymmetry in the dendritic structure. The dendritic asymmetry as seen from the soma for the present stellate neuron is illustrated in Fig. 1(d) where the LFP pattern following a synaptic input into the soma is shown. Also for this situation a dipolar pattern of LFPs is observed, albeit generally with reduced amplitudes compared to the distal-excitation situation in (c). A comprehensive investigation of the dependence of sizes and shapes of the LFP patterns on the neuronal morphologies and synaptic input positions is beyond the scope of the present paper, but the results in Fig. 1 caution us that one must be careful before a priori neglecting contributions to experimentally recorded LFP from populations of neurons with stellate dendritic structures.

Close inspection of Fig. 1(a) reveals another qualitative feature: the LFP signals close to the synaptic inputs positions have 'narrower' temporal traces compared to signals further away. In other words, the LFPs recorded close to the synaptic inputs have more power at higher temporal frequencies than LFPs recorded further away. This position-dependent temporal filtering of the LFP is also revealed by the shift in the times of the peaks of negative LFPs compared to the peak times for the positive LFPs in Fig. 1(a): we find, for example, that the peak of the purely negative LFP trace depicted immediately above the synaptic current-injection point, occurs 5 ms before the maximum of the purely positive LFP trace depicted immediately below the soma. This effect may at least partially underlie observed asynchronous positive and negative peaks of LFPs found in depth-resolved intracortical recordings in humans; in Fig. 2 in Godey et al. (2001) the negative LFP peak at around 45 ms in electrode H'1 is, for example, seen to occur about 5 ms prior to the positive LFP peak seen in electrode H'3.

This intrinsic dendritic filtering effect is a generic and unavoidable feature of spatially extended neuronal structures (Pettersen and Einevoll 2008), but the detailed characteristics of it will be determined by dendritic morphology, electrical cable properties of the dendrites, positions of the current-injecting synapses, as well as the recording position.

3.2 LFP power spectra depend on recording positions

In Fig. 2 we show calculated LFP power spectra, i.e., the square of Fourier amplitudes, for extracellular potentials in the frequency range between 1 and 1,000 Hz. Note the double-logarithmic axes. The same passive layer-5 pyramidal neuron as in the upper panels of Fig. 1 is considered, and we show LFP power spectra found from white-noise current injection (Eq. (3)) into the position of the synapse on the apical branch in Fig. 1(a). For easy comparison we have also drawn lines corresponding to $1/f$ and $1/f^2$ power laws of the LFP in an auxiliary panel.

An immediate observation is that the shape of the spectra is very different at the different recording positions and consequently that no general power-law behavior of the LFP spectra is found. The highest frequencies are to a large extent retained at positions close to the synaptic input, where the frequency at which

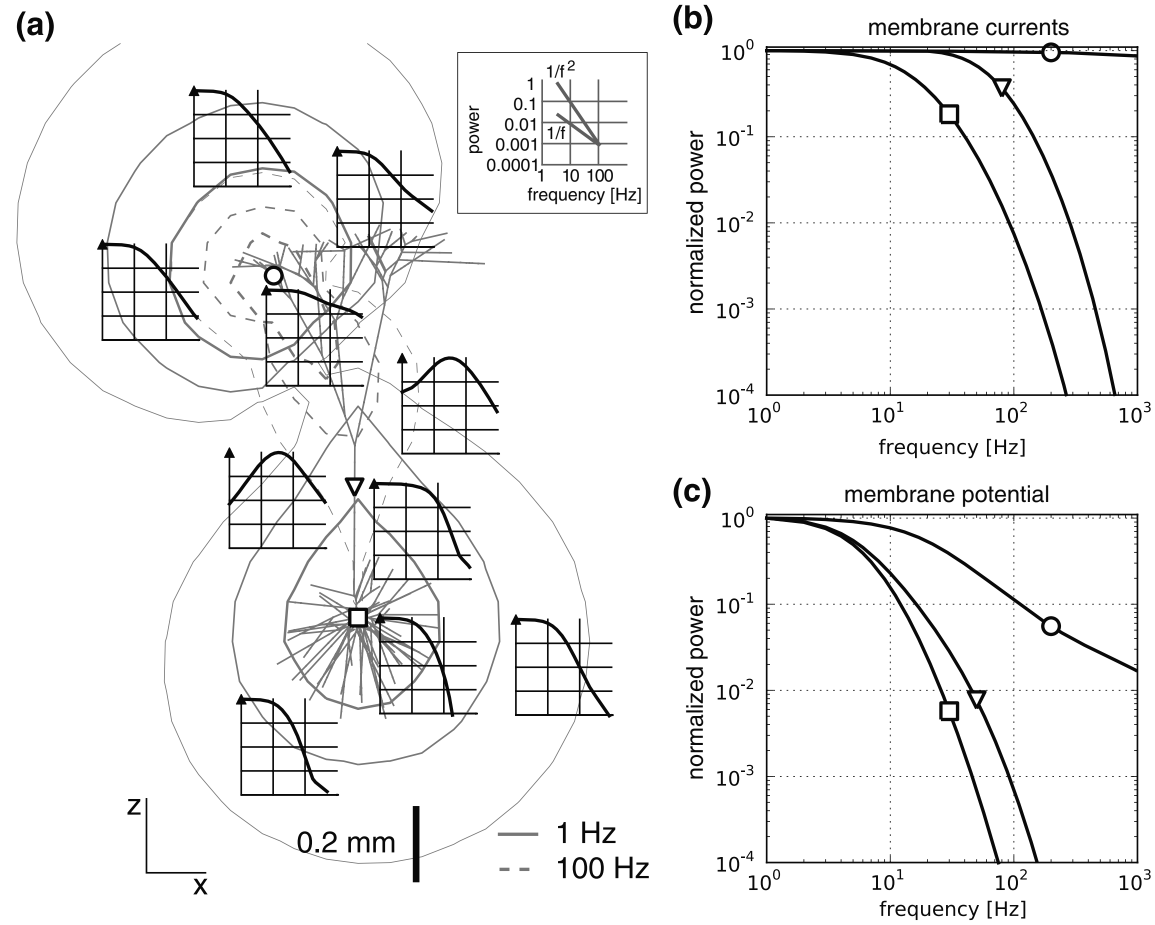

Fig. 2 (**a**) Calculated power spectra of local field potentials (LFPs) following injection of white-noise current into a purely passive layer-5 pyramidal neuron (*grey solid branch structure*) from Mainen and Sejnowski (1996). The current injection point on the apical branch is marked with a circle. Same passive parameters as in Fig. 1. Doubly logarithmic power spectra in the frequency range 1–1,000 Hz of extracellular potentials (*thick solid lines*) are shown at selected spatial positions (*marked by filled arrows*). The power spectra are normalized to the maximum value in the range 1–1,000 Hz. See separate legend box in the upper right part of panel (**a**) for description of the logarithmic frequency and power axes. Logarithmic contour plot with *grey solid lines* illustrate the decay of the 1-Hz power, i.e., square of Fourier amplitude, of the extracellular potential with distance from neuron. The power decays by a factor 4 between each contour line. *Grey dashed contour lines* correspondingly illustrate the decay of the 100-Hz power. (**b**) Normalized doubly-logarithmic power spectra of transmembrane currents at three different positions (synaptic current-injection point, circle; intermediate position, triangle; soma, square) marked with corresponding symbols in (**a**). (**c**) Same as (**b**), but for membrane potential

the power is reduced to one hundredth, is seen to be substantially above 100 Hz. In fact, the position immediately below the synaptic input shows a very modest low-pass filtering effect, and the power at 1,000 Hz is still as large as one tenth of the 1 Hz amplitude. The low-pass filtering effect is seen to be much stronger at the recording position closest to the soma where the ‘one-hundredth cut-off frequency’ is seen to be slightly less than 100 Hz. At some positions outside the main stalk of the apical dendrite one even observes a striking band-pass effect: the largest LFP power is found for frequencies between 10 and 100 Hz.

The above observations can be qualitatively understood by inspection of the corresponding power spectra of the membrane currents in Fig. 2(b). The membrane current at the synaptic injection point has by construction a flat (white-noise) spectrum (marked with a circle), and LFPs recorded in the vicinity of this current-injection point will thus retain substantial contributions from high frequencies. Due to the passive electrical properties of the dendritic cable structure, the somatic membrane current will be low-pass filtered as seen in the power spectrum for the soma (marked with a square). LFPs recorded in the vicinity of the soma will be dominated by this soma membrane current and will thus exhibit similar power spectra. This is indeed confirmed by visual comparison with the power spectra of the LFPs recorded closest to the soma which shows essentially the same power spectrum.

The membrane current at the intermediate position on the dominant apical dendrite (marked with a triangle) has a smaller low-pass filtering effect compared to the soma membrane current, and the low-pass filtering effect of the LFPs recorded in the vicinity of this point is correspondingly smaller as well. Here a somewhat poorer agreement between the LFP spectrum and the corresponding membrane-current spectrum is observed. This reflects that the membrane area, and thus membrane current, around this intermediate position is small compared to both the basal and apical dendritic regions. Thus the recorded LFP signal will get significant contributions from the apical and basal parts of the dendritic tree, and the LFP power spectrum will be determined by a mixture of membrane-current contributions.

For comparison we also show in Fig. 2(c) the power spectra for the membrane *potential* at the same three positions on the pyramidal neuron. A much stronger low-pass filtering effect is observed for the membrane potentials compared to the membrane currents. Since the LFPs are determined by a weighted sum over membrane currents and not membrane potentials, the membrane potential is expected to be a poor predictor of the LFP. This is indeed confirmed by comparison of the power spectra of the membrane potential and the LFPs.

3.3 LFP power spectra depend on synaptic position, neuronal morphology and neuron parameters

In Fig. 3(a) we show the corresponding LFP power spectra for the situation where the synapse is at the soma of the layer-5 neuron instead of at an apical branch, cf. Fig. 1(b). Here the situation is reversed compared to Fig. 2(a): a strong low-pass filtering effect is now seen at the recording positions outside the apical dendrite, while the high frequencies are to a large extent retained at the recording position immediately outside the soma. This confirms the rule that LFP power spectra will exhibit less low-pass filtering close to the synaptic input position than further away (in analogy with the observation in Pettersen and Einevoll (2008) that the extracellular spike signature will become more low-pass filtered when moving away from soma).

In Fig. 3(b) we show LFP power spectra for the layer-4 stellate neuron receiving synaptic input at a distal part of a dendrite, in analogy to Fig. 1(c). Also here we see prominent low-pass filtering effects, although with a higher cut-off frequency and less variation of power spectra with recording positions compared to the layer-5 neuron. This illustrates that the dendritic morphology of the neuron strongly affects their contribution to the LFP signal, and in particular that the length of the dendrites is an important parameter determining the frequency dependence of the intrinsic dendritic filtering (Pettersen and Einevoll 2008).

While Figs. 2 and 3 together illustrate the strong dependence of the intrinsic dendritic filtering effect of the LFP on recording position, synaptic input position and dendritic morphology, Fig. 4 illustrates how this filtering effect is affected by the passive electrical parameters in the neuron model. To highlight the qualitative effects we look at the extreme and likely unrealistic situations where the specific membrane resistance R_m and specific axial resistance R_a are increased or reduced by an order of magnitude compared to the default parameter values.

In Fig. 4(a) and (b) we show how the power spectra shown in Fig. 2(a) for the layer-5 neuron with apical synaptic input are changed when R_m is reduced (Fig. 4(a)) or increased (Fig. 4(b)) by a factor ten, respectively, compared to the default value R_m=30 kΩ cm^2 used in Fig. 2(a). In Fig. 4(a) where the membrane resistance R_m is reduced by a factor ten, we see that the low-pass cut-off frequencies are shifted to higher values compared to the results for the default parameters in Fig. 2(a). This can be qualitatively understood since the reduction of the membrane resistance implies a corresponding reduction of the membrane time constant $\tau_m = R_m C_m$ by a factor ten. This in turns implies that the characteristic frequencies of the system, such as low-pass cut-off frequencies, will be increased. We also observe that the characteristic band-pass spectra for positions outside the apical dendritic stalk in Fig. 2(a) is absent in Fig. 4(a). This illustrates that this resonance-like phenomenon depends on a detailed interplay between the neuronal morphology and its electrical cable properties. The inverse relationship between the membrane resistance R_m, and thus membrane time constant τ_m, and the characteristic frequencies of the system is further illustrated by observations of the depicted spatial pattern of equipotential contour lines in Fig. 4(a). For this reduced membrane-resistance case the 100-Hz contour line is much more spatially extended and thus similar to the 1-Hz contour lines, than for the default situation in Fig. 2(a).

The opposite effect is observed in Fig. 4(b) where the specific membrane resistance is increased by a factor ten, and the typical cut-off frequencies as expected are shifted towards smaller values compared to the default

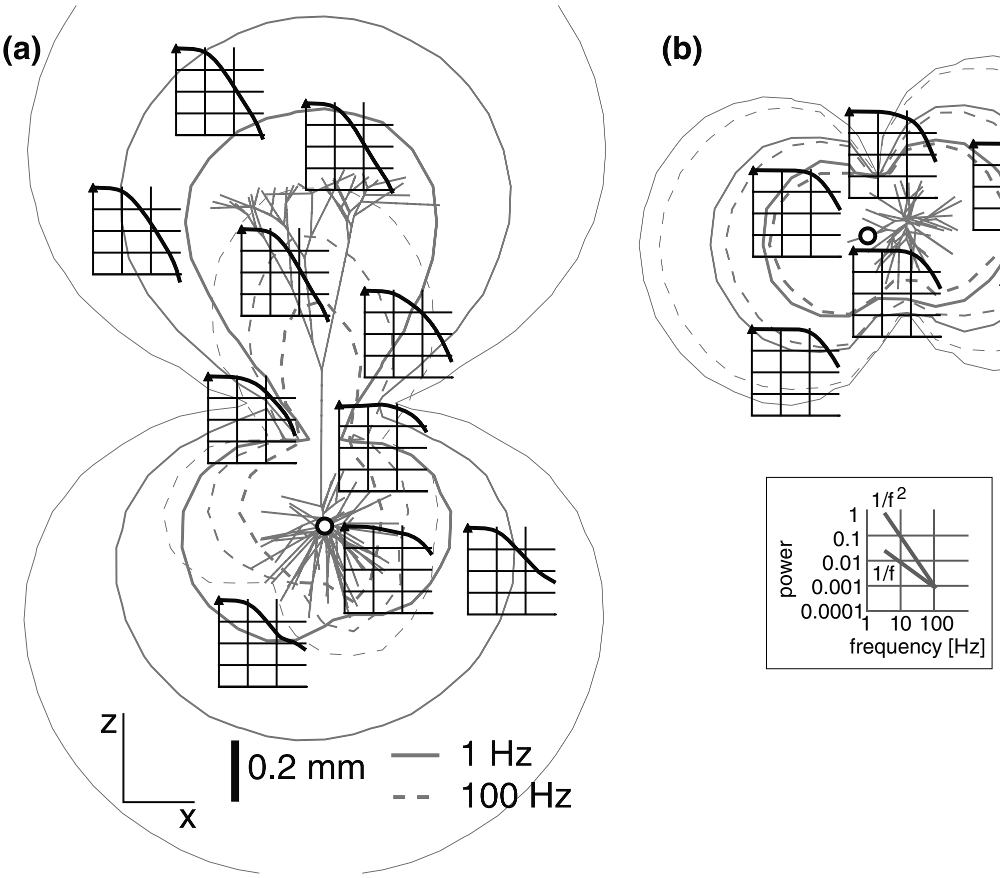

Fig. 3 Calculated power spectra of local field potentials (LFPs) following injection of white-noise current into (**a**) the *soma* of the layer-5 pyramidal neuron considered in Fig. 2 and (**b**) and a dendritic synapse of the layer-4 stellate cell (cf. Fig. 1(c)). The current injection points are marked with circles. See caption of Fig. 2 for detailed explanation of the plots

situation. But the change compared to the results in Fig. 2(a) based on the default value of R_m, is less compared to decreasing the value of R_m by a factor of ten, cf. Fig. 4(a). This illustrates the fact that a change of the membrane resistance not only changes the membrane time constant, but also the frequency-dependent length constant of the current dipole (cf. Eqs. 10–11 in Pettersen and Einevoll 2008). The overall change of the LFP spectra will thus depend on the detailed interplay between these variables and morphological quantities of the neuron and thus not follow a simple scaling rule suggested by considering changes in the membrane time constant alone.

The other key passive parameter is the specific axial resistance R_a, and in Fig. 4(c) and (d) we correspondingly show how the power spectra are altered when this parameter is reduced (Fig. 4(c)) or increased (Fig. 4(d)) by a factor ten, respectively, compared to the default value R_a=150 Ω cm used in Fig. 2(a). In Fig. 4(c) where R_a is reduced by a factor ten, we see that the 100-Hz equipotential contour lines resemble the 1-Hz contour lines much more than for the results for the default value of R_a in Fig. 2(a). This can be qualitatively understood on the basis of the length constant of the current dipole for an infinite cable which is proportional to $1/\sqrt{R_a}$ (Koch 1998; Pettersen and Einevoll 2008). A reduced axial resistance implies a longer length constant, which in turn implies that the neuronal dendrites become electrically more compact. In analogy with the small low-pass filtering effect observed for frequencies below 100 Hz for the short-stick stellate neuron in Fig. 3(b), we see in Fig. 4(c) that the low-pass filtering cut-off in general is shifted to higher frequencies compared to the results for the default parameters in Fig. 2(a). This general shift of salient spectral features towards higher frequencies is also seen in the 'band-pass' spectra outside the stalk of the apical dendrite. Here the band-pass peak is shifted upwards by almost an order of magnitude compared to the result for the default value of R_a shown in Fig. 2(a). The opposite effect is observed in Fig. 4(d) where the specific axial resistance R_a is increased by a factor ten: since the length constant is reduced, the neurons will be electrically less compact and the typical low-pass cut-off frequencies reduced.

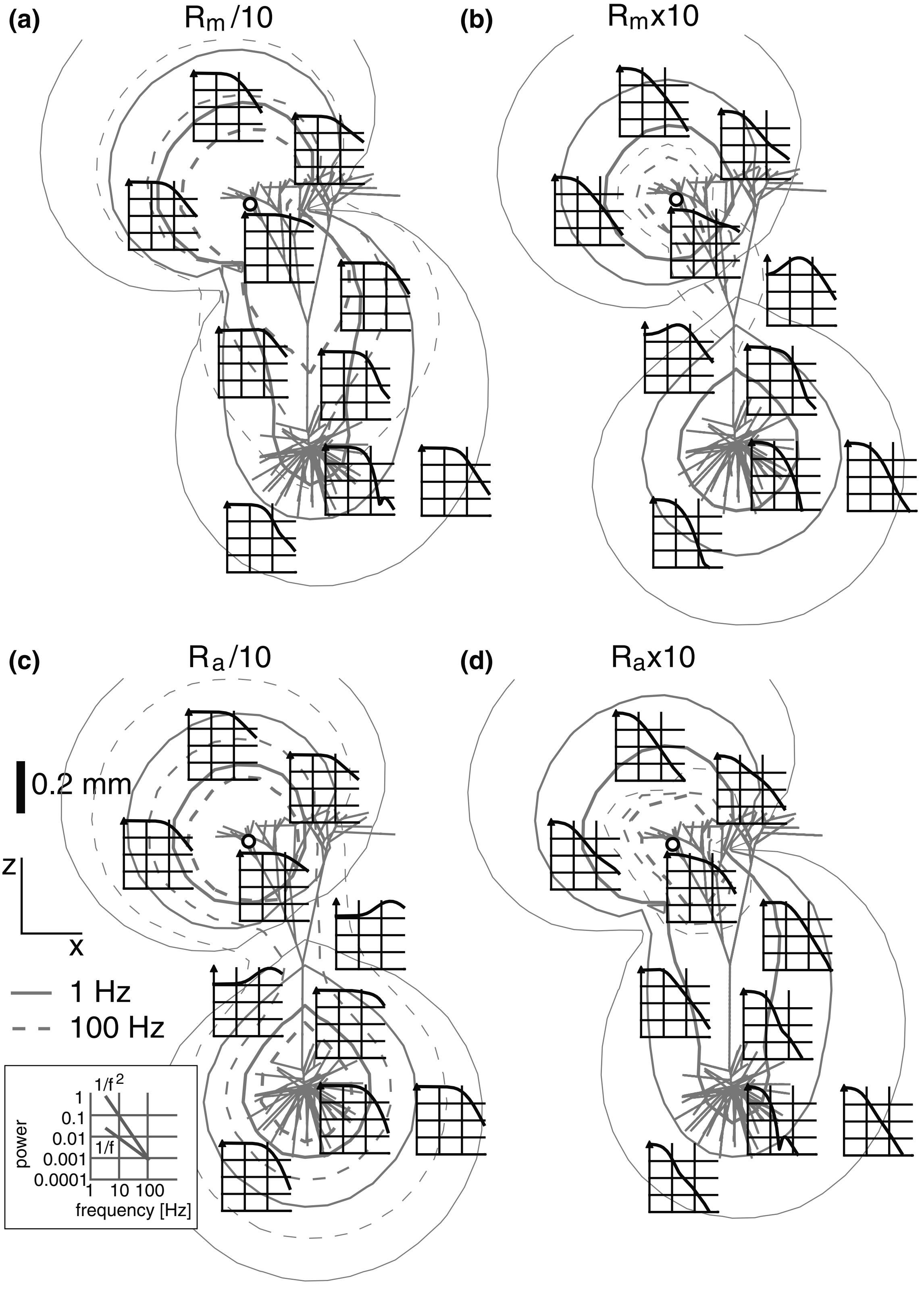

Fig. 4 Calculated power spectra of local field potentials (LFPs) for the same situation as in Fig. 2(a), but different passive neuron parameters. (**a**) As in Fig. 2, but with specific membrane resistance reduced by a factor ten to R_m=3 kΩ cm^2. (**b**) As in Fig. 2, but with specific membrane resistance increased by a factor ten to R_m=300 kΩ cm^2. (**c**) As in Fig. 2, but with specific axial resistance reduced by a factor ten to R_a=15 Ω cm. (**d**) As in Fig. 2, but with specific axial resistance increased by a factor ten to R_a=1,500 Ω cm. See caption of Fig. 2 for detailed explanation of the plots

3.4 Frequency dependence of membrane-current distribution

The previous subsections demonstrated the ubiquity of an intrinsic dendritic low-pass filtering effect of the LFP. They also demonstrated that the power spectra vary strongly with recording position, and that the details of the spectra are determined by an interplay between neuronal morphology, synaptic input position and passive cable parameters. Figure 2 also illustrated the salient role of the transmembrane return currents in determining the characteristics of LFPs. In Fig. 5 we

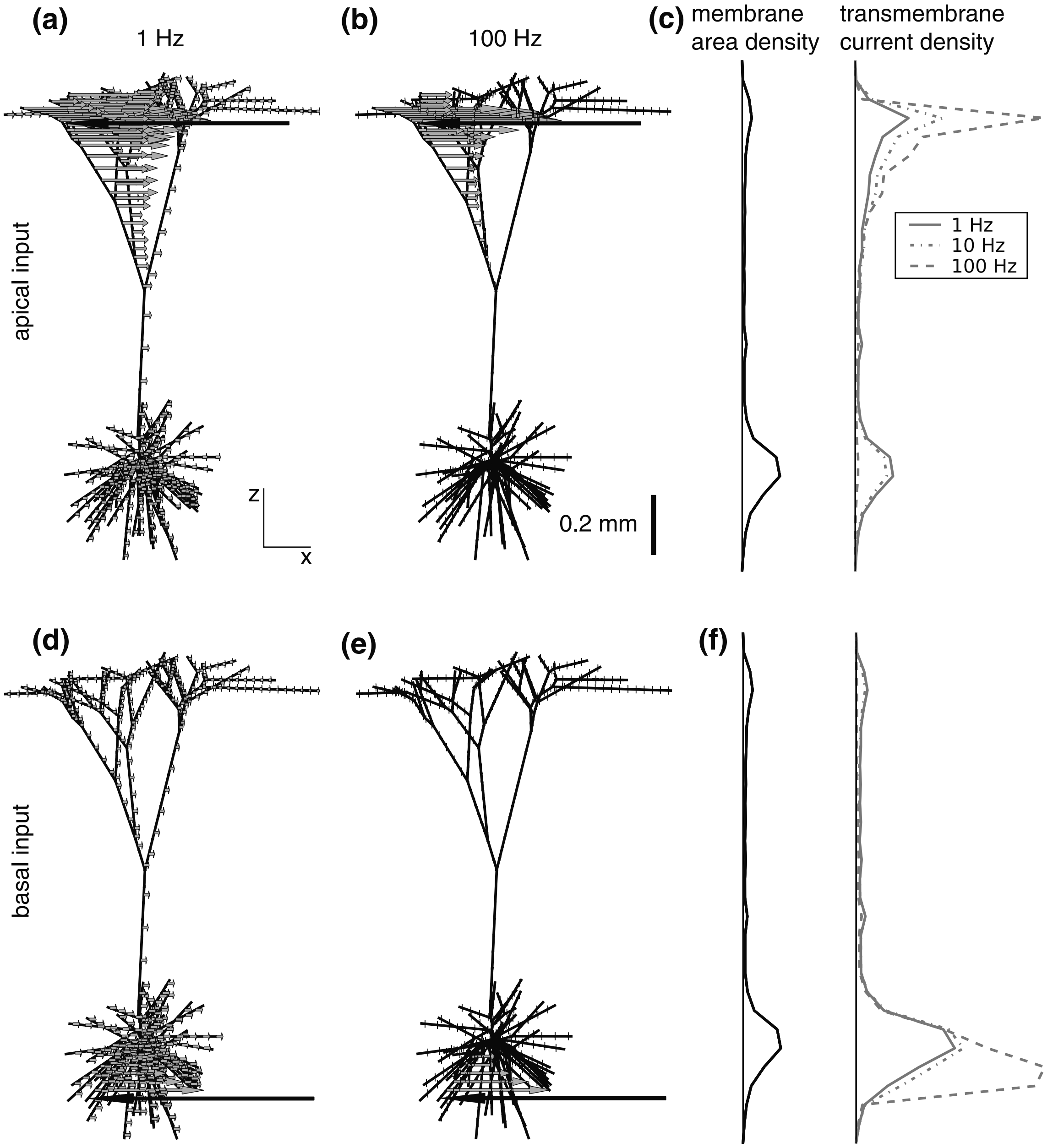

Fig. 5 Illustration of frequency dependence of distribution of transmembrane currents following sinusoidal current injection into apical (*upper row*) or basal (*lower row*) synapse (*thick arrow in neuron figures*). The length of the rightward oriented arrows in the neuron figures in panels (**a**), (**b**), (**d**), and (**e**) represents the amplitude of transmembrane return currents following injection of currents at apical (**a**, **b**) and basal (**d**, **e**) positions, see thick leftward oriented arrow. The depth distributions of the transmembrane return currents for 1 Hz (*solid*), 10 Hz (*dash-dotted*), and 100 Hz (*dashed*) are shown in panels (**c**) and (**f**) for apical and basal excitation, respectively. Note that the lengths of the arrows representing the return currents are normalized to have the same maximum return current in panels (**a**), (**b**), (**d**) and (**e**). In reality the amplitude of maximum transmembrane return currents is much larger for 100 Hz than for 1 Hz, see panels (**c**) and (**f**). The depth distribution of the total membrane area is also shown in panels (**c**) and (**f**)

illustrate further the core physical effect underlying this observed intrinsic dendritic low-pass filtering. In panel (a) the spatial distribution of transmembrane return currents (rightward arrows) following injection of a sinusoidal input current (1 Hz) in the apical dendrite (single thick leftward-oriented arrow) is shown. The length of the return-current arrows illustrates the amplitude of the corresponding sinusoidal return currents. As seen in panel (a) a substantial part of the apically injected current returns through the soma and basal dendrites. The corresponding return-current pattern for a 100 Hz sinusoidal current is shown in panel (b). Here, essentially none of the injected current returns through the basal region, all of it returns through the apical dendrites.

The effect is more clearly quantified by the curves in the panel (c) in Fig. 5, showing the depth distribution of total return current along the vertical extension of the pyramidal neuron. For the 1-Hz situation almost half of the return current leaves through the basal region where the depth distribution essentially follows the depth distribution of the total membrane area, see panel Fig. 5(c). For the 100-Hz case, on the other hand, almost all return current leaves through the apical dendrites. For 10 Hz an intermediate situation is observed.

In terms of generation of LFP both the 1-Hz and the 100-Hz situations depicted in Fig. 5(a)–(b) correspond to ‘open-field’ situations; see, e.g., Johnston and Wu (1995): the weighted mean position of the return currents is for both frequencies spatially displaced from the current injection point. However, the spatial distance between the current injection point and the mean position at which it returns to the extracellular medium, i.e., the *current dipole length* (Pettersen and Einevoll 2008), is very different in the two cases. For 1 Hz this dipole length is about half the distance between the current injection point and the soma, while for 100 Hz it is reduced to less than one tenth of this distance. The current dipole *strength*, which essentially corresponds to the absolute value of the current dipole *moment* described in Eqs. (4)–(6), is determined by the injected current multiplied by these current dipole lengths. Consequently, the dipole strength will be much larger for the 1-Hz situation than for the 100-Hz situation. At positions some distance away from the neuron, the LFP can be expected to be approximately proportional to this current dipole strength (Pettersen and Einevoll 2008). On these grounds the large reduction of the LFP in the 100-Hz situation compared to the 1-Hz situation seen in the power spectra of Fig. 2, is thus not unexpected.

The above example with apical synaptic inputs onto a large pyramidal neuron is the textbook example of an ‘open-field’ situation which may generate large extracellular potentials (Johnston and Wu 1995). However, as seen in the panels (d–f) in Fig. 5, also a synaptic input onto a basal dendrite provide a current dipole. As seen in panels (d) and (f) a sizable fraction of the return current crosses the membrane in the apical dendrites for a 1 Hz sinusoidal current injected into the soma. For a 100 Hz injection current, however, essentially all of the return current leaves at the basal part of the neuron, cf. panels (e) and (f) in Fig. 5.

3.5 Current multipole approximations for LFP generation

In Pettersen and Einevoll (2008) it was found that the extracellular potential signature of action potentials could be well understood qualitatively, and to some extent also quantitatively, on the basis of frequency-dependent current dipoles accounting for the gross features of the spatial pattern of transmembrane currents. For action potential signatures the dominant frequencies are typically a few hundred hertz. For such high frequencies the relevant current dipole lengths are expected to be governed by the electrical cable properties of the dendrites protruding from the soma (Pettersen and Einevoll 2008). For the lower frequencies dominating the LFP, the current dipole length will to a larger extent be governed by the spatial extension of the entire dendritic structure. In Fig. 5, for example, we see for the apical-excitation case that roughly half of the injected synaptic current returns through the basal region, while the other half returns around the synapse. This implies that the current dipole length will be about half the vertical distance between soma and synapse.

Multipole expansions, where the electrical potentials are built up as sums over contributions from the various multipole terms (monopole, dipole, quadrupole, ...), have a long tradition in electrostatics (Plonsey 1969; Jackson 1998). Lately, this approach has also been used to investigate the origin of the extracellular potential signatures of action potentials (Pettersen and Einevoll 2008; Milstein and Koch 2008). In the present section we will pursue a similar approach and investigate to what extent simplified multipole expressions can account for the results based on our comprehensive multicompartment forward-modeling scheme. In panel (a) of Fig. 6 we show the LFP-power contour plot resulting from our multicompartment modeling scheme for the situation where a 1 Hz sinusoidal current is injected into a particular apical synapse (marked with an open dot). This comprehensive multicompartment line-source scheme will provide the ‘gold-standard’

Fig. 6 Illustration of various multipole (*dipole*, *two-monopole*) approximations for LFP modeling. (**a**) Contour plot illustrating the variation of the 1-Hz power, i.e., square of Fourier amplitude, of the LFP with distance from neuron following sinusoidal current injection into an apical synapse (*circle*). Full multicompartment forward-modeling scheme is used, i.e., Eq. (1). The arrows illustrate the 'vertical' and 'horizontal' directions considered in detail in panels (**d**)–(**g**). (**b**) Same as A for *dipole approximation*, i.e., Eq. (8). (**c**) Same as (**a**) for *two-monopole approximation*, i.e., Eq. (10). (**d**) LFP power along the 'vertical' direction (see panel (**a**)) for multicompartment, dipole, and two-monopole modeling schemes, respectively. Distance is measured relative to apical synapse (*circle*). Results for 1 Hz and 100 Hz sinusoidal current injections are shown, normalized to the multicompartment value for 1 Hz. (**e**) Same as (**d**) for the 'horizontal' direction as measured out from soma. Results are normalized to the multicompartment value for 1 Hz. (**f**) Frequency dependence of the LFP power for three particular distances from the neuron (0.1 mm, 1 mm, 10 mm) in the 'vertical' direction. The spectra are normalized so that the LFP power for the multicompartment model for 1 Hz at the distance 10 μm is unity. (**g**) Same as (**f**) for the 'horizontal' direction. Note that also here the spectra are normalized so that the multicompartment LFP power for 1 Hz at the distance 10 μm in the 'vertical' direction is unity

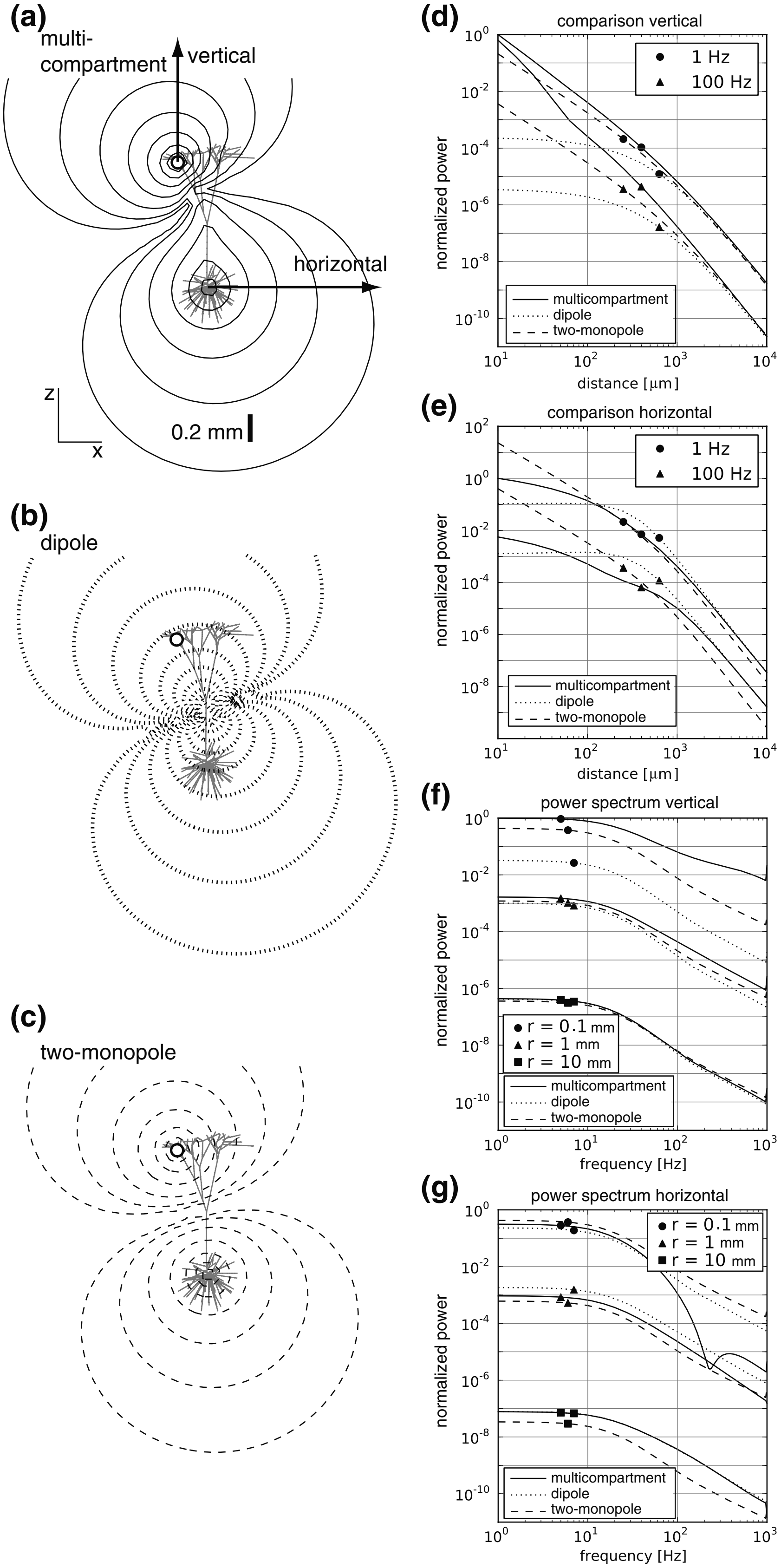

results against which our multipole approximations will be compared.

Due to current conservation there will be no current *monopole* contribution to the LFP, and the first non-zero contribution will in general come from current *dipoles*. In the far-field limit, i.e., when the distance r to the current dipole is much larger than the current dipole length, the dipole LFP expression is given by (Pettersen and Einevoll 2008):

$$\phi_{\mathrm{d}}(\mathbf{r}, t) = \frac{1}{4\pi\sigma} \frac{|\mathbf{p}(t)| \cos\theta}{r^2} \quad . \tag{8}$$

Here $\mathbf{p}(t)$ is a *current dipole moment* which in general is given by

$$\mathbf{p}(t) = p_x(t)\,\mathbf{e}_x + p_y(t)\,\mathbf{e}_y + p_z(t)\,\mathbf{e}_z \tag{9}$$

where $p_x(t)$, $p_y(t)$, and $p_z(t)$ are defined in Eq. (4). Further, θ is the polar angle relative to the dipole axis and r the radial distance to the dipole position (see, e.g., Fig 2(a) in Pettersen and Einevoll (2008) for an illustration). With a sinusoidal input current it follows from the linearity of the model that the individual components, i.e., $p_x(t)$, $p_y(t)$, $p_z(t)$, also will vary sinusoidally in time, cf. Eq. (5). In general the phases of the different components $(\gamma_{fx}, \gamma_{fy}, \gamma_{fz})$ in Eq. (5) will be different, and the system will then not reduce to a dipole oriented along a particular fixed spatial direction. In the present application, however, we do the approximation of assuming identical phases, i.e., $\gamma_{fx} = \gamma_{fy} = \gamma_{fz} = \gamma_f$. We then obtain a sinusoidally oscillating dipole along a *fixed axis* with an oscillatory current dipole moment given by $\mathbf{p}_{\mathrm{fa}}(t) = \mathbf{p}_0(f) \sin(2\pi f t + \gamma)$, cf. Eq. (6).

In panel (b) of Fig. 6 we show the LFP-power contour plots assuming this *dipole approximation*. This plot is found by applying $\mathbf{p}_{\mathrm{fa}}$ from Eq. (6) in the dipole expression in Eq. (8) to get the LFP signal. For this plot the current dipole has been placed in the 'middle' of the neuron, i.e., straight above the soma at a height corresponding to halfway between the lowest and uppermost points of the dendritic structure. A visual comparison of the dipole-approximation results with the corresponding multicompartment results in panel (a) reveals a very good agreement at distances far away from the neuron. Close to the neuron the agreement is as expected poor.

An obvious question to ask is how far away from the neuron one has to be in order for the dipole-approximation to work. As illustrated by panels (d) and (e) in Fig. 6, this depends on direction. Here we focus on two directions: (1) vertically up from the position of the apical input current (labeled 'vertical', cf. panel (a)), and (2) horizontally out from the soma (labeled 'horizontal', cf. panel (a)). The resulting LFP power for the 'vertical' direction is shown in panel (d). For the 1-Hz situation depicted in panels (a) and (b) we see that the dipole approximation (dotted line) gives predictions in excellent agreement with the multicompartment model (solid line) for distances larger than about 1 mm. In panel (d) we also show the corresponding comparison when the input current is oscillating at 100 Hz. Also here we observe agreement at distances larger than about a millimeter or two. The same comparison for the 'horizontal' direction is shown in panel (e), and the same excellent agreement is observed in the far-field limit. However, the transition to the far-field regime appears to occur for slightly larger distances than in the 'vertical' direction.

The results in panels (d) and (e) of Fig. 6 clearly demonstrate the expected inadequacy of the far-field dipole approximation (Eq. 8) for positions close to the neuron. The contour plot for the multicompartment model in panel (a) shows that the 1-Hz LFP power peaks both around the synaptic-input position and the soma, in accordance with the observation of the plots of the transmembrane currents in Fig. 5. This suggests an alternative *two-monopole* approximation $\phi_{\mathrm{tm}}(\mathbf{r}, t)$ for the LFP,

$$\phi_{\mathrm{tm}}(\mathbf{r}, t) = \frac{I_{\mathrm{tm}}(t)}{4\pi\sigma} \left(\frac{1}{|\mathbf{r} - \mathbf{r}_{\mathrm{syn}}|} - \frac{1}{|\mathbf{r} - \mathbf{r}_{\mathrm{soma}}|} \right) \quad , \tag{10}$$

where the current is assumed to enter or exit the neuron only at two positions: the synapse and the soma. From current conservation it follows that the current $I_{\mathrm{tm}}(t)$ entering the neuron at the apical synapse ($\mathbf{r}_{\mathrm{syn}}$) must leave at the soma ($\mathbf{r}_{\mathrm{soma}}$). In this two-monopole approximation the current $I_{\mathrm{tm}}(t)$ does *not* correspond to the true synaptic input current. Rather, $I_{\mathrm{tm}}(t)$ is set to give the correct magnitude of the current dipole moment, i.e.,

$$I_{\mathrm{tm}}(t) \equiv |\mathbf{p}_{\mathrm{fa}}(t)| / \lambda_{\mathrm{tm}} \quad . \tag{11}$$

Here $\lambda_{\mathrm{tm}} \equiv |\mathbf{r}_{\mathrm{syn}} - \mathbf{r}_{\mathrm{soma}}|$, i.e., the distance between the synapse and soma. Since the *direction* of the current dipole moment $\mathbf{p}_{\mathrm{fa}}(t)$ in general will not exactly coincide with the direction from synapse to soma, the two-monopole approximation will not converge to the dipole approximation in the far-field limit. However, with this choice of $I_{\mathrm{tm}}(t)$ one may still hope to obtain reasonably correct predictions for the LFP also for large distances.

In panel (c) of Fig. 6 we show the LFP-power contour plot for the 1-Hz situation assuming this *two-monopole approximation*, i.e., Eq. (10) with (the sinusoidally varying) $I_{\mathrm{tm}}(t)$ given by Eq. (11). A visual comparison of the contour plots for the two-monopole approximation with the corresponding multicompartment plots in panel (a) reveals qualitatively similar spatial patterns. And indeed, in panel (d) the two-monopole approximation is seen to follow the multicompartment results closely when one moves along the 'vertical' direction depicted in panel (a). The agreement is particularly good for current modulations of 1 Hz, but also for 100 Hz the two-monopole approximation is seen to give reasonable results for distances larger than a few hundred micrometers.

As seen in panel (e) of Fig. 6 the performance of the two-monopole model in the 'horizontal' direction is much poorer. For one, this model significantly deviates from the multicompartment results also for the largest distances. This error stems from the deviation between the direction of the true current dipole moment and the line between the apical synapse and the soma. This deviation can also be seen directly by close inspection of the contour plots in panels (a–c): the lines (in these 2D plots) corresponding to zero LFP power have slightly different directions for the dipole and two-monopole approximations. This 'direction error' of course also affects the LFP predictions in the 'vertical' direction, but much less so.

Secondly, the two-monopole approximation predicts much too large LFP power close to the soma, i.e., for distances smaller than about 100 micrometers in the 'horizontal' direction. Such short distances corresponds to positions well inside the bush of basal dendrites, and as seen in panels (a) and (b) in Fig. 5, the transmembrane currents in the basal region appear to be spread out all over the basal dendrites, rather than focused in the soma. The point-like monopolar expression in Eq. (10) representing the contribution from the transmembrane currents in the soma region thus clearly provides a poor approximation, as demonstrated quantitatively by the curves in Fig. 6(e).

Further, while the soma region provides the dominant contribution to the return current for the 1-Hz situation as illustrated, e.g., by the LFP power contour plots Fig. 2(a) and by the plot of the transmembrane currents in Fig. 5(a), this is not generally the case for higher frequencies. The corresponding results for the 100-Hz situation in Figs. 2(a) and 5(a) reveal that the return currents are strongly shifted in the direction of the apical synapse so that the 'center-of-gravity' of the return current is far above the soma. This explains the even larger overestimation of the LFP power by the two-monopole models seen in Fig. 6(e) for 100 Hz compared to 1 Hz, for horizontal distances from the soma less than a few hundred micrometers.

Finally, in panels (f) and (g) of Fig. 6 we investigate the power spectra due to the intrinsic low-pass filtering effect at three different distances (0.1 mm, 1 mm, 10 mm) along both 'vertical' and 'horizontal' directions. At all positions we observe sizable low-pass filtering effects for frequencies above about 10 Hz. The exact functional form of the dampening of high frequencies vary, but for the largest distances (1 mm, 10 mm) a decay of the LFP power approximately following $1/f^2$ relationships are commonly seen for frequencies above 50 Hz. For the largest distance (10 mm) the dipole approximation is seen to predict the filtering characteristics excellently. For the two-monopole approximation the success is more mixed: it works well in the 'vertical' direction, but poorly in the 'horizontal' direction. For the intermediate distance (1 mm) the success of both approximations is more limited, and for the shortest distance considered (0.1 mm) they essentially fail. For example, in the 'horizontal' direction a sharp dip in the amplitude spectrum is observed for frequencies around 200 Hz in the full multicompartment model. This effect is likely due to details of the basal dendritic structure providing subtle cancelation effects at these frequencies. Such a phenomenon can clearly not be accounted for by our two approximate models where the detailed dendritic structure has been neglected. Further, in the 'vertical' direction the full multicompartment model predicts a power-law behaviour close to $1/f$ over a wide frequency range for this shortest distance (0.1 mm). This contrasts the predicted power laws for the two approximate schemes which have much steeper frequency decays.

3.6 Current dipole approximation for LFP

In the previous section we focused on the special case where the synaptic current was provided by a single apical synapse. For this special case we found that the *dipole* approximation in Eq. (8), combined with the approximate current dipole moment $\mathbf{p}_{\mathrm{fa}}(t)$ given by Eq. (6), predicted the LFP power accurately at sufficiently large distances from the neuron, cf. Fig. 6. With the proper incorporation of *frequency-dependent* current dipole moments, the dipole approximation also appeared to explain main features of the observed high-frequency dampening in this far-field limit.

In the present section we investigate to what extent this LFP dipole approximation also applies for synapses positioned on other parts of the dendritic tree. In panel (a) of Fig. 7 we first illustrate the magnitude and direction of the current dipole moments for synapses at a few selected places on the dendritic tree. Sinusoidal input current at three different frequencies, 1 Hz, 10 Hz, and 100 Hz, are considered. The figures illustrate several qualitative points: (1) the current dipole moments are typically roughly directed along a straight line

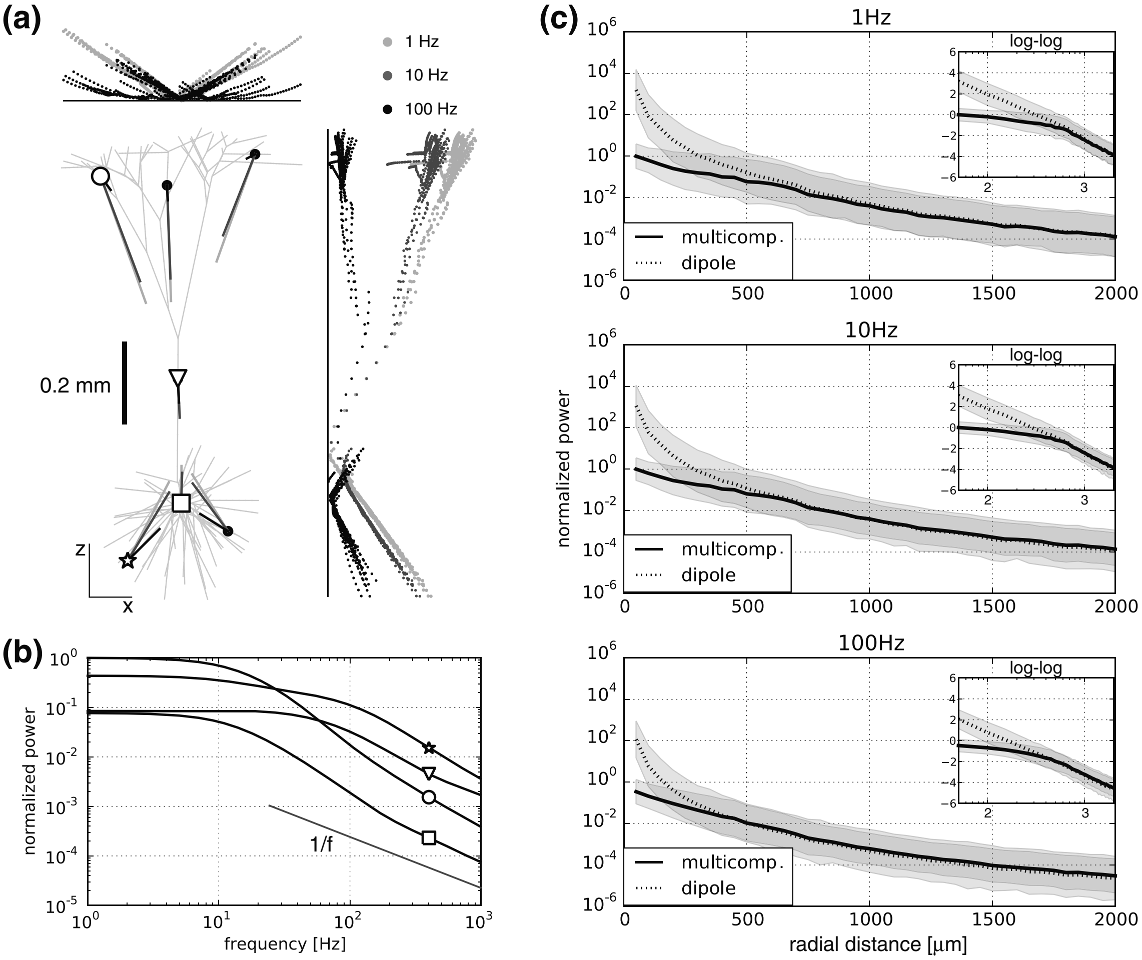

Fig. 7 Current dipole moments and the LFP dipole approximation for various synaptic positions. (**a**) Illustration of direction and amplitudes of current dipole moments $\mathbf{p}_0$ (cf. Eq. (7)) for a set of synaptic positions (black dots) superimposed on the dendritic structure. The figure shows the projection of these dipole moments into the 2D plane of the figure for the 1-Hz, 10-Hz, and 100-Hz situations. Lengths of line segments are proportional to current dipole-moment amplitudes. Dot plots on the right illustrates the magnitude of the vertical component p_{0z}, cf. Eq. (5), versus the vertical position of the synapse for the full number of synapses (1,072; one for each compartment in the multicompartment model). Dot plots above correspondingly illustrate the magnitude of the horizontal component p_{0x} for the same group of synapses (for the 1-Hz and 100-Hz situations, only). Color code: 1 Hz sinusoidal synaptic current: light grey, 10 Hz: darker grey, 100 Hz: black. (**b**) Illustration of frequency dependence of power of current dipole moments, i.e., square of Fourier amplitudes $\mathbf{p}_0(f)$ defined by Eq. (6), for four different synaptic positions marked in (**a**) distal apical dendrite (*circle*), main apical dendrite (*triangle*), soma (*square*), basal dendrite (*star*). The same synaptic current is injected for all four situations, and the results have been normalized to the power of the current dipole moment for the distal apical-dendrite case for 1 Hz. (**c**) Illustration of accuracy of LFP dipole approximation for full group of 1,072 synaptic input positions considered in (**a**). Mean values of logarithms of LFP values from full multicompartment model ϕ (Eq. (1)) are illustrated by solid lines. Surrounding grey bands above and below these lines correspond to the LFP values within the standard deviation (of the logarithm of LFP) around the mean. Results are shown as a function of radial distance from the 'mid-point' of the neuron (i.e., straight above the soma at a height corresponding to halfway between the lowest and uppermost points of the dendritic structure). For each radial distance r the LFP is evaluated separately for the 1,072 synaptic positions considered. Further, for each of these synaptic positions the LFP is calculated at a randomly selected spatial point with the constraint that the vertical position, i.e., z-value, does not go above or below the vertical extension of the neuron. The mean value at each radial distance corresponds to the mean of the logarithm of these 1,072 calculated LFP values. Likewise, the standard deviation at each radial distance corresponds to the standard deviation of the logarithm of these 1,072 calculated LFP values. The dashed lines, with the surrounding grey bands, correspondingly illustrate the mean and standard deviation of the dipole-approximation values ϕ_{d} (Eq. (8)) found by using the same averaging procedure. The current dipole is placed in the 'mid-point' of the neuron as it is described above. The inset figures show the same results with double-logarithmic axes ($\log_{10}$). All results are normalized to the value of the LFP power found at the smallest distance considered (50 μm) for the 1-Hz situation in the full multicompartmental scheme

connecting the synaptic input position and the soma, and (2) the magnitude of the current dipole moments is reduced from 1 Hz to 10 Hz, and even more so from 10 Hz and 100 Hz. Thus also the current dipole moment exhibits a prominent intrinsic low-pass filtering effect.

Above and to the right of the neuron shown in Fig. 7(a) a large collection of magnitudes of the horizontal (p_{0x}, cf. Eq. (5)) and vertical (p_{0z}) components of the current dipole moment are depicted. Each point corresponds to a synapse placed in one of the 1,072 compartments representing the neuron in the multicompartment calculation scheme. The horizontal and vertical current dipole components are plotted as functions of the horizontal and vertical positions of the synapses, respectively. For the vertical component (p_{0z}) a main salient feature is immediately apparent: for 1 Hz the magnitude of the current dipole moment is roughly proportional to the distance from the soma region. This applies for synapses both above and below the soma. A closer inspection of the figure reveals that for the 1-Hz input the 'center-of-mass'-position, i.e., the synaptic position for which a current input gives no current dipole moment, is more than 0.1 mm above the soma on the thick apical dendrite. Thus also a synaptic current injected into the soma will give a sizable current dipole moment, and consequently also a sizable LFP, cf. Fig. 1(b).

The lack of generation of a current dipole moment does in any case not mean that no LFP will be generated since higher order multipole moments will not be zero. For example, injection of current at the synaptic position about 0.1 mm above the soma resulting in a negligible current dipole moment, gives a sizable current quadrupole moment. We confirmed this by direct numerical evaluations of an LFP power contour plot for this situation which indeed revealed a 'clover-like' spatial pattern characteristic for quadrupoles (results not shown).

The rough proportionality of the vertical component of the current dipole moment with distance from soma seen for the 1-Hz situation in Fig. 7(a), suggests that the current dipole qualitatively can be pictured as a fixed amount of *net* current entering in the synapse region, i.e., the synaptic input current minus the return current in the vicinity of the synapse, with the same net current leaving from the soma region. Then the vertical component of the dipole moment will be roughly proportional to the vertical distance between synapse and soma, in correspondence with what is observed in Fig. 7(a).

Qualitatively similar results are observed for the current dipole moment in the 10-Hz situation. The magnitude of the dipole moments are generally somewhat smaller than for 1 Hz, reflecting that the net current propagating from the synapse to the soma, thus setting up the current dipole, is reduced due to the electrical cable properties of the dendritic structure. For 100 Hz a quite different picture is seen. Here a very small vertical component of the current dipole moment is seen for apical synapses, reflecting that most of the injected current return to the extracellular medium in the apical region, cf. Fig. 5(b). The distribution of the magnitudes of the horizontal components p_{0x}, shown above the depicted neuron in Fig. 7(a), is less characteristic. But also here the 100 Hz dipole components are generally seen to be much smaller than the 1 Hz dipole components.

In Fig. 7(b) we illustrate the frequency dependence of the dipole moments further. Here we show the power of the dipole moments, i.e., $|\mathbf{p}_0(f)|^2$ where $\mathbf{p}_0(f)$ is defined by Eq. (6), for frequencies between 1 and 1,000 Hz, generated by injecting currents at four different synaptic positions. Prominent low-pass filtering effects are observed for all situations, but the detailed form of the power spectra vary. The strongest low-pass filtering is seen for inputs at the apical synapse (marked with a circle in panel (a)) and in the soma (square in panel (a)). The low-pass filtering effect is weaker and shifted to higher frequencies for inputs on the main apical dendrite (triangle in panel (a)) and on the basal dendrite (star in panel (a)). This further illustrates that the low-pass filtering effect seen in power spectra of extracellular potentials not only depends on the position of the recording electrode, but also on the distribution of the synaptic inputs generating the potentials.

Calculated current dipole moments, such as the ones depicted in Fig. 7(a), can now be used to calculate the LFP at various spatial positions using the dipolar expression in Eq. (8). In panel (c) we compare results for the LFP power calculated by this dipolar expression against the results from the full multicompartment model for our three different frequencies (1 Hz, 10 Hz, 100 Hz). The panels compare, as a function of radial distance, the mean and the spread of the logarithms of the LFP power calculated using the dipole-approximation with the corresponding values found from using the full multicompartment scheme. These statistical measures are found by averaging over results from injecting current at the 1,072 different synaptic positions considered, see caption of Fig. 7 for details.

For the largest distances (∼1–2 mm) considered in the plots in Fig. 7(c), one is approaching the far-field regime, and the dipole approximation can be expected to be fairly precise. This is indeed observed in the plots. The averages of the observed dipolar LFP power are seen to approach the multicompartment LFP power for the largest distances for all three frequencies considered (1 Hz, 10 Hz, 100 Hz). As illustrated by the inset figures showing the same results in double-logarithmic plots, the multicompartment results for the LFP power indeed decay as $1/r^4$, characteristic for a current dipole, for radial distances above ~1 mm. Interestingly, the far-field limit appears to be reached faster, i.e., for smaller radial distances, in the 100-Hz situation than in the 1-Hz situation. This can be understood on the basis of the shorter effective current-dipole length for the 100-Hz situation seen in Fig. 7(a): since the transition to the far-field regime depends on the ratio between the current-dipole length and the radial distance, a shorter current dipole length implies an earlier transition to the the far-field regime when moving away from the neuron.

For the smallest radial distances considered (<0.5 mm), we observe as expected that the dipole approximation generally does a poor job of predicting the LFP power. As seen for all three frequencies considered in Fig. 7(c), the dipole approximation following a $1/r^4$ dependence, tends to overestimate the LFP in this regime. Note that in panels (d–e) in Fig. 6 it was found that the dipole approximation instead underestimated the true LFP for the shortest distances. The difference is simply due to the different origin and directions of the axes considered, i.e., distance along the 'vertical' and 'horizontal' directions starting in the apical synapse and the soma, respectively, in panels (d–e) in Fig. 6 versus the radial distance measured from the dipole position at the middle of the neuron in Fig. 7(c).

4 Discussion

4.1 Intrinsic dendritic low-pass filtering effect

The origin of the observed frequency spectra of EEG and extracellularly recorded potentials in the brain (LFP) has attracted considerable interest (Pritchard 1992; Beggs and Plenz 2003; Bedard et al. 2004, 2006a, b; Buzsaki 2006; Pettersen and Einevoll 2008; Bedard and Destexhe 2009; Miller et al. 2009; Milstein et al. 2009). We previously showed that there is an unavoidable low-pass frequency-filtering effect of the extracellular action-potential signature due to the electrical cable properties of the neuronal dendrites (Pettersen and Einevoll 2008). In action potentials the dominant frequencies are typically a few hundred hertz, but a main finding in the present paper is that the same intrinsic dendritic filtering effect also pertain to the lower frequencies dominating in typical LFP and EEG spectra, and is particularly prominent for large layer-5 pyramidal neurons. Our model results have demonstrated an omnipresent low-pass filtering effect on the LFP spectra following synaptic activation. For our example pyramidal neuron we generally observed sizable filtering effects for frequencies above ~10 Hz. The magnitude and form of this filtering effect will naturally depend on, e.g., the morphology of the dendritic structure and spatial distribution of activated synapses of the neuron in question. However, all neurons will to some degree exhibit such filtering of their contributions to the overall LFP, and any theory aspiring to explain the physical origin of measured LFP or EEG spectra must therefore also consider this intrinsic dendritic filtering effect.

In an important study Bedard et al. (2006b) attempted to model observed LFP power spectra on the basis of simultaneously recorded spiking activity spectra. They concluded that a factor $1/f$ was 'missing' to account for the observed LFP power spectra for frequencies less than ~70 Hz, and they suggested that this missing factor could be due to frequency attenuation in the extracellular medium itself. The present study suggests as an alternative, or maybe supplementary, explanation that the intrinsic dendritic-filtering effect may contribute to a missing factor $1/f$ in their model for LFP power spectra. For the present large pyramidal neuron the LFP signal is expected to be dominated by contributions from neurons less than about 0.5 mm away (Lindén et al. 2009a). For the 'vertical direction' in Fig. 6(f) we found that the LFP power spectra for the shortest distance considered (0.1 mm) indeed are in qualitative accordance with a $1/f$ decay, at least between 10 Hz and 100 Hz. In the 'horizontal' direction in Fig. 6(g), however, a steeper decay with frequency was observed for this short distance (0.1 mm), but this observation may have been confounded by an observed resonance phenomenon around 200 Hz for this particular modeling example. In any case, the conclusion from our study is not the prediction of a a particular power-law behaviour for the LFP, rather that the intrinsic dendritic filtering effect must be included when attempting to model such spectra. Experimental LFPs stem from a sum of numerous contributions from a population of neurons in the vicinity of the recording electrode (Liu and Newsome 2006; Berens et al. 2008; Katzner et al. 2009; Xing et al. 2009). A more comprehensive numerical investigation of the LFPs generated by such populations of neurons is thus needed to draw firmer conclusions on this (Lindén et al. 2008, 2009a).

A striking observation in our study is that the recorded LFP signal from a single synaptic event varies dramatically with the recording position. The extracellular signature of a particular synaptic event will vary not only in magnitude and temporal shape, but also in overall sign (cf. Fig. 1). Likewise, the form of the LFP power spectra will depend strongly on the recording position: a large variation in the typical low-pass cut-off frequencies is seen, and band-pass properties are even observed at some spatial locations. The experimental LFP observed will correspond to a weighted sum over contributions from many different types of neurons, located at different distances from the recording electrode, receiving numerous synaptic inputs targeting different parts of dendritic trees. As the dominant contributions to the sum providing the LFP cannot be expected to be independent of cortical area and depth, one cannot *a priori* expect common power laws for all observed LFP or EEG power spectra.

Our study revealed a systematic dependence of the intrinsic dendritic-filtering effect on the distance from the recording position to the synaptic input. In general, the high-frequency attenuation of the LFP will be less at positions close to the active synapse where the LFP gets large contributions from the synaptic input current itself. Farther away the LFP will get stronger contributions from the transmembrane *return* currents which in general will be low-pass filtered versions of the synaptic input current (due to the electrical cable properties of the dendrites). In the present paper this was most explicitly illustrated by the set of LFP power spectra in Figs. 2–4, but the effect is generic and also applies to, for example, extracellular action potential signatures (Pettersen and Einevoll 2008; Pettersen et al. 2010). This points to a way to infer the spatial distribution of active synapses acting on a neural population from recordings with linear (laminar) multielectrodes inserted perpendicularly on the cortical layers (Einevoll et al. 2007): the current source-density (CSD) profile informs about the vertical extension of an activated population of, say, layer-5 pyramidal neurons, but may not *per se* be able to distinguish the situations with *inhibitory* synapses acting in the basal dendritic region from *excitatory* synapses acting in the apical region. In both cases one will observe a sink-source dipole with the current sink in the apical region. However, the present results suggest that in the former case there will be more high-frequency components in the CSD at vertical positions inside the basal bush than at vertical positions at the level of the apical dendrites. In the latter case the situation will be reversed.

4.2 Dipole and two-monopole approximations to the LFP

The use of current dipoles in the modeling of bioelectric signals, and in particular EEG signals, is not new (Plonsey 1969; Freeman 1980; Nunez and Srinavasan 2006; Grech et al. 2008). In the application to EEG signals one has typically aimed to account for the observed signals in terms of contributions from a set of 'mesoscopic' current dipole sources, and the distances between the current dipoles and the EEG recording position have typically been assumed to be so large that the far-field dipole approximation apply (Nunez and Srinavasan 2006; Grech et al. 2008). Here we have focused on the fundamental microscopic dipoles underlying these mesoscopic dipole sources, namely the current dipoles set up by individual neurons (Murakami and Okada 2006; Pettersen and Einevoll 2008).

As in the analysis of the extracellular signature of action potentials (Pettersen and Einevoll 2008) we find the *current dipole moment* to be a crucial concept for gaining both qualitative and quantitative understanding of the relationship between the underlying activity in the neuron and the generated extracellular potentials. For the action-potential signature investigated in Pettersen and Einevoll (2008) this dipole moment was typically found to be determined by the electrical properties of the dendritic branches protruding out from the soma. Consequently the *current dipole length*, a measure of the distance between the soma and the average spatial position at which the return currents pass the dendritic membrane, was found to depend mainly on dendritic parameters such as diameter, capacitance, and axial and membrane resistances. In contrast, for the lowest frequencies considered in the present LFP spectra (<10 Hz), we found here that the main dendritic feature determining the current dipole length, and the current dipole moment, appeared to be the spatial distance between the active synapse and the soma (cf. Fig. 7(a)). At such low frequencies rough estimates of the direction and relative magnitude of the current dipole moments for various synaptic inputs can thus be obtained by anatomical considerations alone. However, in general the frequency-dependent current dipole moment (cf. Fig. 7(b)) will be determined by a combination of morphological and electrical membrane properties.

Used in combination with the well-known far-field dipole expression in Eq. (8), the current dipole moment was shown to predict the 'true' LFP (found in our comprehensive multicompartment scheme) accurately at large distances, i.e., a few millimeters away from the neuron. We also found that this dipole approximation could account for salient features of the intrinsic low-pass filtering effect, i.e., that the low-pass frequency filtering of the LFP could be traced back to low-pass frequency filtering of the current-dipole moment.

As expected we found this far-field approximation to break down close to the neuron, partially because it does not explicitly represent the two dominant contributions from the synapse and soma regions, respectively. We thus also investigated a *two-monopole* approximation, i.e., a 2-compartment model where all transmembrane current is assumed to enter the neuron at one point (the synapse) and leave at the other (the soma). Further, the transmembrane current was set to give the right *magnitude* of the current dipole moment. For our example in Fig. 6 we found the two-monopole approximation to give very good predictions in the vicinity of the active synapse, much better than the dipole approximation. However, for our example with excitation of an apical synapse, we found the two-monopole approximation to predict far too big LFPs for positions inside the bush of basal dendrites. There are likely two main reasons for this discrepancy: (1) For situations where the return current indeed is focused in the soma region (such as for low-frequency apical synaptic inputs onto the layer-5 example neuron), the true transmembrane current in the soma region is, due to the extensive basal dendritic structure, much more diffuse than what is implicitly assumed in the two-monopole model. (2) For high-frequency synaptic input the cable properties of the neuron will in general reduce the amount of return current leaving from the soma region, and the 'center-of-gravity' of the return current will be positioned closer to the position of the synaptic input, cf. Fig. 5. This will naturally violate the assumption inherent in the two-monopole approximation where the return monopole is set to be at the soma.

An alternative version of the two-monopole model would be to move the return-current monopole from the soma to the position of the center-of-gravity for the return current. This center-of-gravity position will depend on frequency, and such a two-monopole approximation would likely yield more accurate results than the present two-monopole model. However, the calculation of the center-of-gravity position will involve numerical solution of the full compartmental model to obtain all transmembrane currents, making the implementation of the approximation almost as cumbersome as using the comprehensive line-source scheme. A main advantage of the present two-monopole model is that the position of the two monopoles is determined solely by the neuronal morphology and thus easy to specify (even though specification of the magnitude of the monopole currents requires knowledge about the dipole-moment magnitude, which in turn must be calculated based on knowledge of all transmembrane currents).

4.3 Network modeling of LFP, ECoG and EEG

A natural ambition of neural network modeling should be to predict not only spike trains, but also extracellular potentials. One approach for achieving this would be to simulate networks of multicompartmental neurons so that the generation of action potentials and the transmembrane currents needed to evaluate extracellular potentials, could be calculated simultaneously. However, spiking neural networks are more commonly modeled by means of 1-compartment neurons which by design do not generate an extracellular potential: a neuron model must have at least two compartments to generate an extracellular potential (Pettersen et al. 2010). In such cases ad hoc formulas relating synaptic currents to LFP have been used to provide LFP predictions from network simulations, see, e.g., Mazzoni et al. (2008).

The forward-modeling scheme offers a method for testing of such putative add-on formulas for predicting extracellular potentials. Our present work unfortunately does not suggest any such simplifying formula for prediction of LFPs recorded well inside the active cortical tissue. For the present pyramidal neuron we expect the LFP signal to get most of its contributions from neurons within a radius of less than 0.5 mm (Lindén et al. 2009a), an estimated spatial range of the LFP in qualitative accordance with recent experimental estimates (Katzner et al. 2009; Xing et al. 2009). As seen in Fig. 6 both the dipole approximation (Eq. 8) and the two-monopole approximation (Eq. 10) generally give inaccurate results of the LFP for such small distances. Simplifying formulas based on these approximations thus appears ruled out. This observation thus clearly questions the approach of interpreting intracortical LFP recordings in terms of contributions from dipolar sources (Church et al. 1985; Yvert et al. 2001).

The development of simplified schemes for predicting contributions to extracellular potentials recorded at the cortical surface (ECoG) is maybe more feasible. As seen in Fig. 6(d) the two-monopole approximation does fairly well, in particular for the 1-Hz situation, in the vertical direction for positions more than 0.1 mm or so above the apical synapse. This suggests that this two-monopole approximation may be useful for predicting ECoG signals. In fact a similar two-monopole approximation was suggested by Freeman (1980) to interpret ECoG signals recorded by electrode arrays placed on the brain surface. However, here we only explored the two-monopole approximation for the situation with an apical synapse where the LFP recorded immediately above is dominated by a rather focal sink. Even in this situation, the agreement with the correct multicompartmental results was not more than fair. With other synaptic inputs which generate more diffuse patterns for transmembrane currents in the apical dendritic tree, a lesser performance of the two-monopole approximation must be expected. A more comprehensive investigation also considering morphologies of other neuron types expected to give large contributions to the ECoG signal (e.g., supragranular pyramidal neurons), is needed to evaluate this approximation scheme further.

The prospect for developing simplified schemes for predicting contributions to extracellular potentials recorded at the scalp (EEG) seems much better. Here the distances from the neural origin of the electrical signal are sufficiently large for the dipole approximation described in Eq. (8) to give accurate results. This formula describes the contribution to the recorded electrical potentials at a particular electrode contact from a particular neuron receiving synaptic input currents through a particular synapse, information that in principle may be calculated and predicted in large-scale neural network modeling (Jirsa and Haken 1997; Jirsa et al. 2002; Coombes 2005). However, the magnitude and direction of the current dipole moment for the various synaptic inputs, must either be assumed or calculated using multicompartmental modeling, in order for the formula to be workable. The *two-monopole* approximation in Eq. (10) is an alternative. Here the only spatial information needed is the positions of the soma and the active synapse, but the magnitude of the transmembrane current I_{tm} must still be assumed or calculated using multicompartmental modeling.

A caveat of the present work in the context of predicting EEG signals is that the extracellular conductivity σ has been assumed to be constant. This assumption is clearly violated when the electrical contacts are positioned outside the cortical tissue as in EEG recordings, but our present approach can be generalized to take into account such inhomogeneous electrical media using the same techniques as in the well-established forward modeling of EEG signals from mesoscopic current dipoles (Nunez and Srinavasan 2006).

4.4 Assumptions in forward modeling scheme

Our present LFP forward modeling scheme based on Eq. (1) assumes the extracellular conductivity σ to be the same everywhere ('homogeneous'), the same in all directions ('isotropic'), and also purely ohmic, i.e., no imaginary part from capacitive effects (Nunez and Srinavasan 2006; Logothetis et al. 2007). Finally, σ is assumed to be the same for all relevant frequencies. The validity of this latter assumption is still debated: while some studies have measured negligible frequency dependence (Nicholson and Freeman 1975; Logothetis et al. 2007), other investigations have suggested otherwise (Gabriel et al. 1996; Bedard et al. 2004, 2006a, b; Bedard and Destexhe 2009). However, if warranted, the present modeling formalism can be generalized to include also a frequency-dependent electrical conductivity $\sigma(f)$. More discussion on the assumptions regarding σ, and also ways of generalizing Eq. (1) when they do not apply, can be found in Pettersen et al. (2010).

Acknowledgements This work was supported by the Research Council of Norway (eScience, NOTUR). We thank one of the reviewers for bringing relevant literature on human depth-resolved LFP recordings to our attention.

References

Arieli, A. (1992). Novel strategies to unravel mechanisms of cortical function: From macro- to micro-electrophysiological recordings. In A. Aertsen, & V. Braitenberg (Eds.), *Information processing in the cortex*. New York: Springer.

Bedard, C., Kröger H., & Destexhe A. (2004). Modeling extracellular field potentials and the frequency-filtering properties of extracellular space. *Biophysical Journal*, *86*, 1829–1842.

Bedard, C., Kröger, H., & Destexhe, A. (2006a). Model of low-pass filtering of local field potentials. *Physical Review E*, *73*, 051911.

Bedard, C., Kröger, H., & Destexhe, A. (2006b). Does the 1/f frequency scaling of brain signals reflect self-organized critical states? *Physical Review Letters*, *97*, 118102.

Bedard, C., & Destexhe, A. (2009) Macroscopic models of local field potentials and the apparent 1/f noise in brain activity. *Biophysical Journal*, *96*, 2589–2603.

Beggs, J. M., & Plenz, D. (2003). Neuronal avalanches in neocortical circuits. *Journal of Neuroscience*, *23*, 11167–11177.

Berens, P., Keliris, G. A., Ecker, A. S., Logothetis, N., & Tolias, A. S. (2008). Comparing the feature selectivity of the gamma-band of the local field potential and the underlying spiking activity in primate visual cortex. *Frontiers in Systems Neuroscience, 2*(2). doi:10.3389/neuro.06/002.2008.

Buzsáki, G. (2004). Large-scale recording of neuronal ensembles. *Nature Neuroscience*, *7*, 446–451.

Buzsáki, G. (2006). *Rhythms of the brain*. New York: Oxford University Press.

Carnevale, N. T., & Hines, M. L. (2006). *The NEURON book*. Cambridge, UK: Cambridge University Press.

Church, P., Leduc, A., & Beique, R. A. (1985). Sensitivity analysis of depth EEG electrodes to dipolar electric sources. *IEEE Transactions on Biomedical Engineering*, *32*, 554–560.

Coombes, S. (2005). Waves, bumps, and patterns in neural field theories. *Biological Cybernetics*, *93*, 91–108.

Di, S., Baumgartner, C., & Barth, D. S., (1990). Laminar analysis of extracellular field potentials in rat vibrissa/barrel cortex. *Journal of Neurophysiology*, *63*, 832–840.

Einevoll, G. T., Pettersen, K. H., Devor, A., Ulbert, I., Halgren, E., & Dale, A. M. (2007). Laminar population analysis: Estimating firing rates and evoked synaptic activity from multielectrode recordings in rat barrel cortex. *Journal of Neurophysiology*, *97*, 2174–2190.

Freeman, W. J. (1980). Use of spatial deconvolution to compensate distortion of EEG by volume conduction. *IEEE Transactions on Biomedical Engineering*, *27*, 421–429.

Freeman, W. J., Holmes, M. D., Burke, B. C., & Vanthalo, S. (2003). Spatial spectra of scalp EEG and EMB from awake humans. *Clinical Neurophysiology*, *114*, 1053–1068.

Gabriel, S., Lau, R. W., & Gabriel, C. (1996). The dielectric properties of biological tissues: III. Parametric models for the dielectric spectrum of tissues. *Physics in Medicine & Biology*, *41*, 2271–2293.

Godey, B., Schwartz, D., de Graaf, J. B., Chauvel, P., & Liegeois-Chauvel, C. (2001). Neuromagnetic source localization of auditory evoked fields and intracerebral evoked potentials: A comparison of data in the same patients. *Clinical neurophysiology*, *112*, 1850–1859.

Grech, R., Cassar, T., Muscat, J., Camilleri, K. P., Fabri, S. G., Zervakis, M., et al. (2008). Review on solving the inverse problem in EEG source analysis. *Journal of Neuroengineering and Rehabilitation 5*, 25.

Hämäläinen, M., Hari, R., Ilmoniemi, R. J., Knuutila, J., & Lounasmaa, O. V. (1993). Magnetoencephalography theory, instrumentation, and applications to noninvasive studies of the working human brain. *Reviews of Modern Physics*, *65*, 413–449.

Hines, M. L, Davison, A. P. & Muller E. (2009). NEURON and Python. *Frontiers in Neuroinformatics*, *3*, 1.

Holt, G. R. & Koch, C. (1999). Electrical interactions via the extracellular potential near cell bodies. *Journal of Computational Neuroscience*, *6*, 169–184.

Jackson, J. (1998). *Classical Electrodynamics*. NJ: Wiley, Hoboken.

Jirsa, V. K., & Haken, H. (1997). A derivation of a macroscopic field theory of the brain from the quasi-microscopic neural dynamics. *Physica D*, *99*, 503–526.

Jirsa, V. K., Jantzen, K. J., Fuchs, A., & Kelso, J. A. S. (2002). Spatiotemporal forward solution of the EEG and MEG using network modeling. *IEEE Transactions on Medical Imaging*, *21*, 493–504.

Johnston, D., & Wu, S. M.-S. (1995) *Foundations of cellular neurophysiology*, (Chapter 14). Cambridge, MA: MIT Press.

Katzner, S., Nauhaus, I., Benucci, A., Bonin, V., Ringach, D. L., & Carandini, M. (2009). Local origin of field potentials in visual cortex. *Neuron*, *61*, 35–41.

Koch, C. (1998). *Biophysics of computation*. New York, NY: Oxford.

Kreiman, G., Hung, C. P, Kraskov, A., Quiroga, R. Q., Poggio, T., & DiCarlo, J. J. (2006). Object selectivity of local field potentials and spikes in the macaque inferior temporal cortex. *Neuron*, *49*, 433–445.

Lindén, H., Pettersen, K. H., & Einevoll, G. T. (2008). Frequency scaling in local field potentials: A neuron population forward modelling study Frontiers in Neuroinformatics. *Conference Abstract: Neuroinformatics*, 2008. doi:10.3389/conf.neuro.11.2008.01.026.

Lindén, H., Pettersen, K. H., Tetzlaff, T., Potjans, T., Denker, M., Diesmann, M., et al. (2009a). Estimating the spatial range of local field potentials in a cortical population model. *BMC Neuroscience*, *10*(1), 224.

Lindén, H., Potjans, T. C., Einevoll, G. T., Grün, S., & Diesmann, M. (2009b). Modeling the local field potential by a large-scale layered cortical network model. *Frontiers in Neuroinformatics*, Conference Abstract: 2nd INCF Congress of Neuroinformatics. doi:10.3389/conf.neuro.11.2009.08.046.

Liu, J., & Newsome, W. T. (2006). Local field potential in cortical area MT. Stimulus tuning and behavioral correlations. *Journal of Neuroscience*, *26*, 7779–7790.

Logothetis, N. K., Kayser, C., & Oeltermann, A. (2007). *In vivo* measurement of cortical impedance spectrum in monkeys: Implications for signal propagation. *Neuron*, *55*, 809–823.

Lorente de Nó, R. (1947). Action potential of the motoneurons of the hypoglossus nucleus. *Journal of Cellular and Comparative Physiology*, *29*, 207–287.

Mainen, Z. F., & Sejnowski, T. J. (1996). Influence of dendritic structure on firing pattern in model neocortical neurons. *Nature*, *382*, 363–366.

Mazzoni, A., Panzeri, S., Logothetis, N. K., & Brunel, N. (2008). Encoding of naturalistic stimuli by local field potential spectra in networks of excitatory and inhibitory neurons. *PLoS Computers in Biology*, *4*, e1000239.

Miller, K. J., Sorensen, L. B., Ojemann, J. G., & den Nijs, M. (2009). Power-law scaling in the brain surface electric potential. *PLoS Computers in Biology*, *5*, e1000609.

Milstein, J. N., & Koch, C. (2008). Dynamic moment analysis of the extracellular electric field of a biologically realistic spiking neuron. *Neural Computation*, *20*, 2070–2084.

Milstein, J., Mormann, F., Fried, I., & Koch., C (2009). Neuronal shot noise and Brownian 1/f^2 behavior in the local field potential. *PLoS ONE*, *4*, e4338.

Mitzdorf, U. (1985). Current source-density method and application in cat cerebral cortex: Investigation of evoked potentials and EEG phenomena. *Physiological Reviews*, *65*, 37–99.

Murakami, S., & Okada, Y. (2006). Contributions of principal neocortical neurons to magnetoencephalography and electroencephalography signals. *Journal of Physiology*, *575*, 925–936.

Nauhaus, I., Busse, L., Carandini, M., & Ringach, D. L. (2009). Stimulus contrast modulates functional connectivity in visual cortex. *Nature Neuroscience*, *12*, 70–76.

Nicholson, C., & Freeman, J. A. (1975). Theory of current source-density analysis and determination of conductivity tensor for anuran cerebellum. *Journal of Neurophysiology*, *38*, 356–368.

Normann, R. A., Maynard, E. M., Rousche, P. J., & Warren, D. J. (1999). A neural interface for a cortical vision prosthesis. *Vision Research*, *39*, 2577–2587.

Nunez, P. L., & Srinavasan, R. (2006). *Electric fields of the brain: The neurophysics of EEG*. Oxford: Oxford University Press.

Pettersen, K. H., & Einevoll, G. T. (2008). Amplitude variability and extracellular low-pass filtering of neuronal spikes. *Biophysical Journal*, *94*, 784–802.

Pettersen, K. H., Hagen, E., & Einevoll, G. T. (2008). Estimation of population firing rates and current source densities from laminar electrode recordings. *Journal of Computational Neuroscience*, *24*, 291–313.

Pettersen, K. H., Lindén, H., Dale, A. M., & Einevoll, G. T. (2010). Extracellular spikes and current-source density. In R. Brette, & A. Destexhe (Eds.), *Handbook of neural activity measurements*. Cambridge, UK: Cambridge University Press.

Plonsey, R. (1969). *Bioelectric phenomena*. New York: McGraw-Hill.

Plonsey, R., & Barr, R. C. (2007). *Bioelectricity: A quantitative approach*. New York: Springer.

Pritchard, W. S. (1992). The brain in fractal time: 1/f-like power spectrum scaling of the human electroencephalogram. *International Journal of Neuroscience*, *66*, 119–129.

Rall, W. (1962). Electrophysiology of a dendritic neuron model. *Biophysical Journal*, *2*, 145–167.

Xing, D., Yeh, C.-I., & Shapley, R. M. (2009). Spatial spread of the local field potential and its laminar variation in visual cortex. *Journal of Neuroscience*, *29*, 11540–11549.

Yvert, B., Fischer, C., Bertrand, O., & Pernier, J. (2001). Localization of human supratemporal auditory areas from intracerebral auditory evoked potentials using distributed source models. *NeuroImage*, *28*, 140–153.

3.3 Paper III

LINKING POWER LAWS FOR MICROSCOPIC AND MACROSCOPIC NEURAL ACTIVITY

KLAS H. PETTERSEN, HENRIK LINDÉN, TOM TETZLAFF AND GAUTE T. EINEVOLL

Dept. of Mathematical Sciences and Technology,
Norwegian University of Life Sciences, Ås, Norway

Abstract. The cable equation is solved in frequency space for a ball and stick neuron with noisy input currents spread homogeneously throughout the dendritic stick. The power spectral densities (PSDs) of the soma potential and the soma current are related to the *single-neuron contribution to the electroencephalogram* (EEG), and all PSDs are shown to express $1/f^{\alpha}$ power laws for high frequencies.

For *uncorrelated* white-noise input the asymptotic high frequency limit gives α-values of 0.5, 1.5 and 2.5 for the soma current, EEG and the soma potential, respectiviely. For *correlated* white-noise input the respective values are 1, 2 and 3. However, for the frequency range typically recorded in experiments, i.e., up to one or two hundred hertz, log-log plots of the corresponding PSDs often express quasi-linear regimes with power about 0.5 less than the asymptotic value.

The theory presented may not only give valuable insight to why neural recordings often obey power laws, but might also be of importance to general $1/f$-theory, as this is an example of how a basic physics equation can transfer white noise input to colored $1/f^{\alpha}$-noise where different physical entities express different powers α.

Keywords: 1/f, power law, power spectrum, power spectral density, soma potential, electroencephalogram, EEG

1. Introduction

Ever since Hans Berger recorded the first human electroencephalogram (EEG) in 1924 [2] its features have been under extensive study, especially since many of them are directly related to disease and to states of consciousness. In the last decades, the underlying background spectra (the power spectral density, PSD) of the EEG has also attracted great attention. The PSD is typically well fit by a $1/f^{\alpha}$ power law, with α typically in the range from 1 to 2 [4, 8]. There are several theories with such a scale invariance as its fingerprint, among the most popular are fractal geometry [15] and the theory of self-organized critical states [1]. The origin of the $1/f$-noise in EEG is, however, still not known. Linking features seen in global recordings, such as the EEG, to features in the underlying local activity, such as single neuron activity, is still a major challenge within the field of neuroscience.

Power laws are recorded at both the macroscopic level, e.g., for the EEG, and at the level of single neurons. The PSD of the sub-threshold soma potential of individual neurons are shown to exhibit a $1/f^{\alpha}$ power law, however with a much larger power α than for the EEG. For the sub-threshold soma potential α is typically ranging from 2 to 3 [7, 20, 11, 21, 5]. As for the EEG, this power law seems to be very robust; it has been observed across species, brain regions and different experimental set-ups, such as cultured hippocampal layer V neurons [7], pyramidal layer IV–V neurons from rat neocortex *in vitro* [11, 21] and neocortical neurons from cat visual cortex *in vivo* [20, 5].

Here, we present an *analytic solution* of the ball and stick neuron model with white noise input currents spread homogeneously throughout the dendritic stick. We show that this model produces a $1/f^{\alpha}$ power law in the soma potential typically with $1.5 < \alpha < 2.5$ for uncorrelated white noise input ($\alpha = 2.5$ in the asymptotic high-frequency limit) and

$2 < \alpha < 3$ for correlated white noise input ($\alpha = 3$ in the asymptotic high-frequency limit), in agreement with the range recorded experimentally [7, 20, 11, 21, 5]. A simulation of a morphologically reconstructed pyramidal neuron with a constant density of white noise input currents throughout the dendrites is also in agreement with this result.

We also show analytically that in a purely resistive extracellular medium the corresponding single neuron contribution to the EEG will express a $1/f^{\alpha}$ power law with $1 < \alpha < 2$ for correlated input ($\alpha = 2$ in the asymptotic high-frequency limit), and typically $\alpha \sim 1.5$ for uncorrelated white noise input ($\alpha = 1.5$ is the asymptotic high-frequency limit), also this in agreement with the range seen in experimental recordings [4, 8].

The analytical expressions derived for the ball and stick neuron link the apparent power laws seen in the PSDs of the soma current, the soma potential and the single neuron contribution to the EEG to underlying single neuron parameters, and show how the exact power α is influenced by parameters like the dendritic length and diameter, soma diameter and membrane impedance. Thus, the analytical expressions derived do not only explain the $1/f$ background noise of the EEG as a possible intrinsic single-neuron effect, they also link microscopic measures like single neuron recordings of the soma potential to macroscopic measures like the EEG. Although the main focus of the paper is the analytical ball and stick neuron model, a morphologically reconstructed layer V neuron from cat visual cortex [14] is also shown to express approximate power laws in the respective PSDs for higher frequencies.

The theory presented may not only be an interesting analysis of the cable equation, but may also be interesting with respect to $1/f$-theory in general, as this is an example of how a basic physics equation can transfer white noise input to colored noise with a PSD approximated by $1/f^{\alpha}$ for high frequencies, where α have different values depending on the physical entity under consideration and the coherence in the noisy input currents.

2. Theory and Methods

In the present paper both the ball and stick model and the reconstructed neuron model are purely passive, ensuring that linear theory can be used. The input currents are white noise currents and the density of input currents are constant throughout the dendrites. The white noise currents are allowed to have a given coherence $c = c(\omega)$, i.e., any pair of white noise input currents may have a frequency-depended correlation, described by c.

When allowing for coherence, the expressions for the PSDs are split into two terms with different parameter dependency: one describing the contribution due to correlated input currents and one describing the contribution due to uncorrelated input currents, with a weighting of the two terms given by the coherence c.

The analytical considerations rest on the cable equation in frequency space, first solved for a single synaptic input at an arbitrary position. The single-synapse solution is used as a basis for the case of input currents spread evenly throughout the dendritic cable. When the PSDs are computed for many inputs, we end up with Riemann sums where the individual terms correspond to single input contributions. The input currents are allowed to have a given correlation, and in the limit where the neuron is assumed to be continuously bombarded throughout the dendrite, the Riemann sums goes to analytically solvable integrals, one describing uncorrelated input currents and one describing correlated input currents.

For the numerical simulations, the NEURON Simulation Environment [6] with the supplied Python interface [9] was used.

2.1. **Cable equation.**

For a cylinder the cable equation is given by

$$\lambda^2 \frac{\partial^2 V(x,t)}{\partial x^2} = \tau_{\mathrm{m}} \frac{\partial V(x,t)}{\partial t} + V(x,t) \ , \tag{1}$$

with the length constant $\lambda = \sqrt{1/g_\mathrm{m} r_\mathrm{i}} = \sqrt{dR_\mathrm{m}/4R_\mathrm{i}}$ and the time constant $\tau_\mathrm{m} = c_\mathrm{m}/g_\mathrm{m} = R_\mathrm{m}C_\mathrm{m}$. R_m, C_m and R_i are the specific membrane resistance, the specific membrane capacitance and the inner resistivity, respectively, and have dimensions $[R_\mathrm{m}] = \Omega\mathrm{m}^2$, $[C_\mathrm{m}] = \mathrm{F/m}^2$ and $[R_\mathrm{i}] = \Omega\mathrm{m}$. Lower-case letters are used to describe the electrical properties per unit length of the cable: $g_\mathrm{m} = 1/r_\mathrm{m} = \pi d/R_\mathrm{m}$, $c_\mathrm{m} = \pi d C_\mathrm{m}$ and $r_\mathrm{i} = 4R_\mathrm{i}/\pi d^2$, with units $[g_\mathrm{m}] = 1/\Omega\mathrm{m}$, $[c_\mathrm{m}] = \mathrm{F/m}$ and $[r_\mathrm{i}] = \Omega/\mathrm{m}$. In frequency space, and with dimensionless variables $X = x/\lambda$ and $T = t/\tau_\mathrm{m}$, the general solution can be expressed [19, 18]

$$\hat{\mathbf{V}} = \mathbf{C}_1 \cosh(\mathbf{q}L - \mathbf{q}X) + \mathbf{C}_2 \sinh(\mathbf{q}L - \mathbf{q}X) \ , \tag{2}$$

where boldface denotes complex numbers and $\mathbf{q}^2 = 1 + j\omega\tau_\mathrm{m}$, see Appendix A. $\hat{\mathbf{V}} = \hat{\mathbf{V}}(x, \omega)$ is the complex membrane potential containing the amplitude and phase of the signal, and the derivation is based on circuit theory with complex entities, where the complex potentials are related to the measurable potential through the Fourier components of the potential,

$$V(x,t) = \sum_{k=0}^{\infty} \mathrm{Re}\{\hat{\mathbf{V}}(x,\omega) e^{j\omega_k t}\} \ . \tag{3}$$

2.2. **Single input current at arbitrary dendritic position.** The solution of the cable equation for a ball and stick neuron with a single input current at an arbitrary position is derived by solving the cable equation separately for the neural compartment proximal to the input current and for the neural compartment distal to the input current, and combining them through a common voltage boundary condition $\hat{\mathbf{V}}_\mathrm{in}$ at the connection point. For the proximal stick, Ohm's law in combination with the lumped soma admittance will give the boundary condition at the opposite side, and for the distal stick a sealed end boundary is applied at the opposite side. In this configuration the boundary condition $\hat{\mathbf{V}}_\mathrm{in}$ acts as the driving force of the system. The potential $\hat{\mathbf{V}}_\mathrm{in}$ can, however, be transformed to its corresponding current $\hat{\mathbf{I}}_\mathrm{in}$ by multiplying the potential $\hat{\mathbf{V}}_\mathrm{in}$ with the total neuron input admittance $\hat{\mathbf{Y}}_\mathrm{in}$.

Following this approach the complex soma current, $\hat{\mathbf{I}}_\mathrm{s}$, is derived in Appendix A (see Fig. 2*A* for an illustration of the ball and stick model),

$$\hat{\mathbf{I}}_\mathrm{s}(\omega, X) = \frac{(\mathbf{Y}_\mathrm{s}/\mathbf{Y}_\infty)\cosh(\mathbf{q}L - \mathbf{q}X)}{(\mathbf{Y}_\mathrm{s}/\mathbf{Y}_\infty)\cosh(\mathbf{q}L) + \sinh(\mathbf{q}L)} \hat{\mathbf{I}}_\mathrm{in} \ , \tag{4}$$

and by applying Ohm's law $\hat{\mathbf{V}}_\mathrm{s} = \hat{\mathbf{I}}_\mathrm{s}/\mathbf{Y}_\mathrm{s}$, to the soma compartment the soma potential becomes

$$\hat{\mathbf{V}}_\mathrm{s}(\omega, X) = \frac{(1/\mathbf{Y}_\infty)\cosh(\mathbf{q}L - \mathbf{q}X)}{(\mathbf{Y}_\mathrm{s}/\mathbf{Y}_\infty)\cosh(\mathbf{q}L) + \sinh(\mathbf{q}L)} \hat{\mathbf{I}}_\mathrm{in} \ , \tag{5}$$

where $\mathbf{Y}_\mathrm{s}$ is the somatic membrane admittance $\mathbf{Y}_\mathrm{s} = 4\pi d_\mathrm{s}^2 \mathbf{q}^2/R_\mathrm{m}$, d_s is the soma diameter, r_i is the inner (axial) resistance per unit length of the stick and $\mathbf{Y}_\infty = \frac{\mathbf{q}}{\lambda r_\mathrm{i}}$ is the input admittance of an infinite stick. The frequency dependence is through the variables $\mathbf{Y}_\mathrm{s} = \mathbf{Y}_\mathrm{s}(\mathbf{q}(\omega))$, $\mathbf{Y}_\infty = \mathbf{Y}_\infty(\mathbf{q}(\omega))$ and $\mathbf{q} = \mathbf{q}(\omega)$, with $\mathbf{q}(\omega) = \sqrt{1 + j\omega\tau}$.

The single neuron contribution to the EEG is based on the dipole moment of the neuron, which is the source both for the EEG and the MEG [17], as the far field limit is reached in both measures. Although the properties of the conductivities within the brain, dura matter, scull, scalp and the surrounding air may influence the EEG, these can be accounted for by applying, e.g., a three- or four sphere model of the head [17]. If purely resistive surrounding mediums are assumed within the EEG frequency range, the PSD of the single-neuron dipole moment will express the same frequency dependence as the PSD for the single-neuron contribution to the EEG [17]. The dipole moment is in general a sum of currents weighted by the distance to a common reference. For continuous current source densities, as is the case for a neuronal cable, the sum is replaced by an integral, and the dipole-moment contribution from the stick of length l is given by

$$\hat{\mathbf{p}}(\omega) = \int_0^l \hat{\mathbf{i}}_{\mathrm{m}}(x,\omega) x \, \mathrm{d}x \ , \tag{6}$$

where $\hat{\mathbf{p}}$ and $\hat{\mathbf{i}}_{\mathrm{m}}$ are the complex dipole moment and membrane return current, respectively, and the dipole moment is directed along the x-axis. In Appendix A the dipole moment for a ball and stick neuron with dimensionless length $L = l/\lambda$ and a single synaptic input at an arbitrary position $X = x/\lambda$ is shown to be

$$\hat{\mathbf{p}}(\omega, X) = -\frac{\hat{\mathbf{I}}_{\mathrm{in}}}{\mathbf{Y}_\infty r_{\mathrm{i}}} \frac{-\cosh(\mathbf{q}L - \mathbf{q}X) + (\mathbf{Y}_{\mathrm{s}}/\mathbf{Y}_\infty)\sinh(\mathbf{q}X) + \cosh(\mathbf{q}X)}{(\mathbf{Y}_{\mathrm{s}}/\mathbf{Y}_\infty)\cosh(\mathbf{q}L) + \sinh(\mathbf{q}L)} \ . \tag{7}$$

2.3. **Evenly distributed input currents.** The passive ball and stick neuron model is linear, and Eqs. 5–7 can therefore be summed up for input currents at different positions. When the input currents are evenly distributed throughout the stick, both the somatic membrane current, $\hat{\mathbf{I}}_{\mathrm{in}}$, the dipole moment, $\hat{\mathbf{p}}$, and the soma potential, $\hat{\mathbf{V}}_{\mathrm{in}}$, can be expressed as Riemann sums with the different input currents as driving forces. Thus, the entities can be expressed by the following transfer functions,

$$\hat{\mathbf{I}}_{\mathrm{s}}^k = \hat{\mathbf{I}}_{\mathrm{in}}^k \mathbf{T}_I^k \ , \ \hat{\mathbf{p}}^k = \hat{\mathbf{I}}_{\mathrm{in}}^k \mathbf{T}_p^k \ , \ \hat{\mathbf{V}}_{\mathrm{s}} = \hat{\mathbf{I}}_{\mathrm{in}}^k \mathbf{T}_V^k \ , \tag{8}$$

where k is an index corresponding to an input current at position X_k, and the transfer functions are denoted $\mathbf{T}$ with a lower index describing the entity, I for soma current, p for dipole moment and V for soma potential, respectively.

The Riemann sums are the basis for the derivation of the total PSDs, which, through the *coherence*, $c(\omega)$, of the signals, can be divided into separate terms for uncorrelated and correlated input currents. For a general transfer functions $\mathbf{T}^k$ the PSD can be expressed,

$$PSD(\omega) = \sum_{k=1}^N \sum_{l=1}^N \hat{\mathbf{I}}_{\mathrm{in}}^k(\omega)\mathbf{T}^k(\omega)(\hat{\mathbf{I}}_{\mathrm{in}}^l(\omega)\mathbf{T}^l(\omega))^* = v\left[(1-c)\sum_{k=1}^N \mathbf{T}^k(\mathbf{T}^k)^* + c\sum_{k=1}^N\sum_{l=1}^N \mathbf{T}^k(\mathbf{T}^l)^*\right] \ , \tag{9}$$

where $v = v(\omega)$ is the PSD of the input currents and $c = c(\omega)$ is their coherence. In the continuum limit we multiply the sums by $\rho \mathrm{d}x$, where $\rho = N/l$ is the density of input currents and $\mathrm{d}x$ is the infinitesimal length $\mathrm{d}x = l/N$, and let the sums go to integrals,

$$PSD(\omega) = v(\omega)\left[\rho(1-c(\omega))\int_0^l |\mathbf{T}(x,\omega)|^2 \mathrm{d}x + \rho^2 c(\omega)\left|\int_0^l \mathbf{T}(x,\omega)\mathrm{d}x\right|^2\right] \ . \tag{10}$$

Here $v(\omega) = v$ and $c(\omega) = c$ will be assumed to be constants. The first term of Eq. 10 describes the uncorrelated input, while the second term describes the correlated input, as can be seen by putting the coherence c either to zero (for uncorrelated input) or to 1 (for correlated input). When the integrals are solved, the PSDs are typically expressed as fractions, and for later convenience we denote the dimensionless numerators as N, the dimensionless denominators as D, and we put the dimensions into an amplitude A, and we express the solutions of Eq. 10 in the following form

$$PSD_n(W) = A_n N_n(W)/D_n(W) \ . \tag{11}$$

Here, we have introduced the dimensionless frequency $W = \omega\tau_{\mathrm{m}}$, and $n = 1$ denotes the PSD for uncorrelated soma current, $n = 2$ is the PSD for correlated soma current, $n = 3$ is the PSD for uncorrelated dipole moment, $n = 4$ is the PSD for correlated dipole moment, $n = 5$ is the PSD for uncorrelated soma potential and $n = 6$ is the PSD for correlated soma potential, see Table 1. Hence, the PSD for the *soma current* for a given coherence c will be $PSD(W) = (1-c)A_1N_1/D_1 + cA_2N_2/D_2$, and with similar PSD expressions for the dipole moment and the soma potential, but with terms of $n = 3$ and $n = 4$ for the dipole moment and $n = 5$ and $n = 6$ for the soma potential. The amplitudes A_n are defined in Table 1 , while the numerators N_n are constructed to give an asymptotic high-frequency value of 1, and are given by

(12)

$$N_n = \begin{cases} (\mathrm{Re}\{\mathbf{q}\}\sin(2\mathrm{Im}\{\mathbf{q}\}L) + \mathrm{Im}\{\mathbf{q}\}\sinh(2\mathrm{Re}\{\mathbf{q}\}L))\lvert\mathbf{q}\rvert/\sqrt{2}\lvert\sinh(\mathbf{q}L)\rvert^2 W & \text{for } n = \{1,5\} \\ 1, & \text{for } n = \{2,6\} \\ N_3, & \text{for } n = 3 \\ \lvert\coth(\mathbf{q}L) - 1/\sinh(\mathbf{q}L)\rvert^2, & \text{for } n = 4 \end{cases}$$

with

$$\begin{aligned} N_3 =& [-\mathrm{Re}\{\mathbf{q}\}(B^2(\mathrm{Re}\{\mathbf{q}\}^2 + \mathrm{Im}\{\mathbf{q}\}^2) - 2)\sin(2\mathrm{Im}\{\mathbf{q}\}L) \\ & + \mathrm{Im}\{\mathbf{q}\}(B^2(\mathrm{Re}\{\mathbf{q}\}^2 + \mathrm{Im}\{\mathbf{q}\}^2) + 2)\sinh(2\mathrm{Re}\{\mathbf{q}\}L) \\ & + 2\mathrm{Re}\{\mathbf{q}\}\mathrm{Im}\{\mathbf{q}\}B\cos(2\mathrm{Im}\{\mathbf{q}\}L) \\ & + 2\mathrm{Re}\{\mathbf{q}\}\mathrm{Im}\{\mathbf{q}\}B(\cosh(2\mathrm{Re}\{\mathbf{q}\}L) - 2) \\ & - 4\sin(\mathrm{Im}\{\mathbf{q}\}L)[B(\mathrm{Re}\{\mathbf{q}\} - \mathrm{Im}\{\mathbf{q}\}) \\ & \times (\mathrm{Re}\{\mathbf{q}\} + \mathrm{Im}\{\mathbf{q}\})\sinh(\mathrm{Re}\{\mathbf{q}\}L) + \mathrm{Re}\{\mathbf{q}\}\cosh(\mathrm{Re}\{\mathbf{q}\}L)] \\ & - 4\mathrm{Im}\{\mathbf{q}\}\sinh(\mathrm{Re}\{\mathbf{q}\}L)\cos(\mathrm{Im}\{\mathbf{q}\}L)] \\ & /[2\mathrm{Re}\{\mathbf{q}\}\mathrm{Im}\{\mathbf{q}\}\sqrt{\mathrm{Re}\{\mathbf{q}\}^2 + \mathrm{Im}\{\mathbf{q}\}^2}(\cos(2\mathrm{Re}\{\mathbf{q}\}L) - \cosh(2\mathrm{Re}\{\mathbf{q}\}L))]\ . \end{aligned} \tag{13}$$

The denominators D_n are given by

$$D_n = \lvert\mathbf{q}\rvert^{n-2}\ \lvert\mathbf{q}\coth(\mathbf{q}L) + 1/B\rvert^2\ , \tag{14}$$

see Appendix B. Here, $B = d_s^2/d\lambda$ is a dimensionless constant. One should note that both N_n and D_n are dimensionless, as all the parameters $\mathbf{q}(W)$, L, B and W are dimensionless. When the PSDs are expressed according to Eqs. 11–14, the terms involved are particularly simple in the high-frequencies limit: the asymptotic high-frequency value of N_n is one, and the asymptotic high-frequency value of D_n is $1/W^{n/2}$ (see Results).

TABLE 1. Parameters and powers in the amplitudes of the PSDs.

Case	n	A_n	$A'_n = A_n/(2\pi\tau_\mathrm{m})^{n/2}$
Uncorr. curr.	1	$\rho\lambda/\sqrt{2}$	$\rho d/4\pi^{1/2}R_\mathrm{i}^{1/2}C_\mathrm{m}^{1/2}$
Corr. curr.	2	$\rho^2\lambda^2$	$\rho^2/8\pi R_\mathrm{i}C_\mathrm{m}$
Uncorr. dipolemom.	3	$\rho\lambda^3/\sqrt{2}$	$\rho d^{3/2}/32\pi^{3/2}R_\mathrm{i}^{3/2}R_\mathrm{i}C_\mathrm{m}^{3/2}$
Corr. dipolemom.	4	$\rho^2\lambda^4$	$\rho^2 d^2/64\pi^2 R_\mathrm{i}^2 C_\mathrm{m}^2$
Uncorr. pot.	5	$\rho\lambda(r_\mathrm{i}\lambda/B)^2/\sqrt{2}$	$\rho d^{1/2}/16\pi^{7/2}R_\mathrm{m}d_s^2 R_\mathrm{i}^{1/2}C_\mathrm{m}^{5/2}$
Corr. pot.	6	$\rho^2\lambda^2(r_\mathrm{i}\lambda/B)^2$	$\rho^2 d/32\pi^4 R_\mathrm{m}d_s^2 R_\mathrm{i}C_\mathrm{m}^3$

The amplitudes A_n related to the different power spectral densities, PSD_n, defined in Eq. 11. The right column shows the weighted amplitude A'_n related to the asymptotic value of PSD_n through $\lim_{f\to\infty} PSD_n = A'_n/f^{n/2}$.

2.4. **Numerical simulations.** For comparison with the analytical results a ball and stick neuron model and a layer V pyramidal neuron from cat visual cortex [14] were simulated using the NEURON Simulation Environment [6] with the supplied Python interface [9]. Both models had a purely passive membrane, with a specific membrane resistance $R_\mathrm{m} = 3\ \Omega\mathrm{m}^2$, specific axial resisitivity $R_\mathrm{i} = 1.5\ \Omega\mathrm{m}$ and specific membrane capacitance $C_\mathrm{m} = 0.01\ \mathrm{F/m}^2$. Simulations were performed with a time resolution of 0.0625 ms and resulting data used for analysis had a time resolution of 0.25 ms. Simulations were in all applications run for a time period of 1200 ms were the first 200 ms were removed before analysis to avoid transient upstart effects in the simulations.

2.4.1. *Morphologies.* A digital cell reconstruction of the layer 5 pyramidal cell was downloaded from ModelDB (http://senselab.med.yale.edu/) and the axon compartments were removed. To ensure numerical precision compartmentalization was done so that no dendritic compartment was larger than 1/30 of the electrotonic length at 100 Hz (using the function lambda_f(100) in NEURON), which resulted in 3214 compartments. The soma was modeled as a single compartment.

The ball and stick neuron was modeled with a total of 201 segments, one segment was the iso-potential soma segment with length 20 μm and diameter 20 μm, and 200 segments belonged to the attached dendritic stick of length 1 mm and diameter 2 μm.

2.4.2. *Input currents.* Simulations were performed with the same white-noise current injection into each compartment separately. The white-noise input current was constructed as a sum of sinusoidal currents

$$I(t) = I_0 \sum_{f=1}^{1000} \sin(2\pi f t + \varphi_f) \tag{15}$$

where φ represents a random phase for each frequency contribution. Due to linearity of the cable equation the contributions of individual synapses could be combined to compute the PSD of the soma potential, the soma current and the dipole moment resulting from current injection into all N compartments. In correspondence with Eq. 9, the weighting of the input currents from different segments i with membrane areas A_i was done differently for uncorrelated and correlated input currents. The uncorrelated PSDs, PSD_u, were computed according to

$$PSD_u(\omega) = \sum_{i=1}^{N} \left(\rho_i A_i |x_i(\omega)|^2 \right) \ , \tag{16}$$

while the correlated PSDs, PSD_c were computed according to

$$PSD_c(\omega) = \left| \sum_{i=1}^{N} \left(\rho_i A_i x_i(\omega) \right) \right|^2 \ . \tag{17}$$

Here, $x_i(\omega)$ denotes the Fourier components of the signal $x(t)$ (either soma potential, soma current or dipole moment due to input in one segment), the product $\rho_i A_i$ gives the total number of input currents into one segment i, and for a homogeneous density of input currents with respect to membrane area the density ρ_i is assumed to be constant throughout the neuron.

2.4.3. *Calculation of dipole moment.* The total dipole moment $\vec{p}$ was in the numerical computations assumed to equal the dipole moment in one direction only: the direction along the stick for the ball and stick model, and the direction along the apical dendrite for the pyramidal neuron model, both denoted as the x-component, p_x. For the ball and stick neuron this is exact, but for the pyramidal neuron this is an approximation. However, both the asymmetry of the pyramidal neuron and the fact that the component perpendicular to the surface of the scalp dominates the EEG [17, 16] ensures that this is a good approximation. The dipole moment is then given by

$$p_x = \sum_{i=1}^{N} x_i I_i(t) \ , \tag{18}$$

where x_i is the position and I_i is the transmembrane current of compartment i.

3. Results

Expression for the soma current, the dipole moment and the soma potential for a single input current at an arbitrary position is derived for the ball and stick neuron, Eqs. 5–7, as well as analytical expressions for the PSDs of the same entities when the input currents are evenly distributed throughout the dendritic stick, Eqs 11–14. Eq. 11 describes PSDs for uncorrelated input currents ($n = \{1, 3, 5\}$) and correlated input currents ($n = \{2, 4, 6\}$) separately, which can be combined to form an expression with any given coherence in the input currents.

Fig. 1 shows typical PSDs of the soma current, dipole moment and the soma potential both for a layer 5 pyramidal neuron (right) and for the ball and stick neuron model (left) when correlated or uncorrelated white noise input currents are spread with a constant density throughout the dendrites. A striking observation from these plots is the linear or quasi-linear appearance of the PSD slopes seen for high frequencies in the log-log plots. This indicates that there might be an underlying $1/f^\alpha$ power law, and the values for different α's are printed in the figure based on a negative discrete log-log derivative, $-\Delta(\log PSD)/\Delta(\log f)$, within a small frequency interval close to 1000 Hz. In general one can see that the α's are highest for the soma potential, a bit lower for the dipole moment and lowest for the soma current. For the soma potential and the soma current it is also seen from the α values that the frequency dependence of the PSD is about half a power less for uncorrelated input than for correlated input both for the ball and stick neuron and the pyramidal neuron. For the dipole moment the relation is less clear: for the ball and stick neuron the uncorrelated- and correlated dipole moment are almost indistinguishable, while for the pyramidal neuron the difference in powers α is more than one.

However, even though the reconstructed pyramidal neuron is very different from the ball and stick neuron in that it has both a highly branched structure and a varying diameter along its neural sections with a pronounced tapering, both models produce linear or quasi-linear slopes for high frequencies in the log-log plot. Although the slopes are a bit different between the two neuron models for the dipole moment, they are very similar for the soma current and the soma potential. With this as a motivation we here present a further study of the analytical expressions derived for the ball and stick neuron.

3.1. Series expansion of the PSDs.

Due to the frequency- and position-dependent membrane filtering of the input currents illustrated in Fig. 2*B*, the PSDs shown in Fig. 1 possibly express power laws with different α's for high frequencies. To further study this the numerators N_n and denominators D_n will be asymptoticly expanded for $W \to \infty$. For the numerators the four first terms in an asymptotic series expansion of Eq. 12 then gives (see Appendix C)

$$N_n = \begin{cases} 1, & \text{for } n = \{2,4,6\} \\ 1 + 1/2W + 3/8W^2 + 1/16W^3 + \dots, & \text{for } n = 1 \\ 1 + 1/\sqrt{2W} + (4-B^2)/2^{3/2}W + (3B^2/8-1)/\sqrt{2}W^2 + \dots, & \text{for } n = 3 \\ 1 + 1/2W + 3/8W^2 + 1/16W^3 \dots, & \text{for } n = 5\ . \end{cases} \tag{19}$$

The corresponding series expansion of the denominator of Eq. 14 gives

$$D_n = W^{n/2} + \frac{\sqrt{2}}{B}W^{(n-1)/2} + \frac{1}{B^2}W^{(n-2)/2} + \frac{1}{\sqrt{2}B}W^{(n-3)/2} + \dots\ . \tag{20}$$

All six numerators have 1 as their asymptotic high-frequency value, whereas different powers are dominating the six denominators. Note, however, that the dominating power of the denominator is related to n through $\lim\limits_{W\to\infty} D_n \to W^{n/2}$, and the asymptotic value

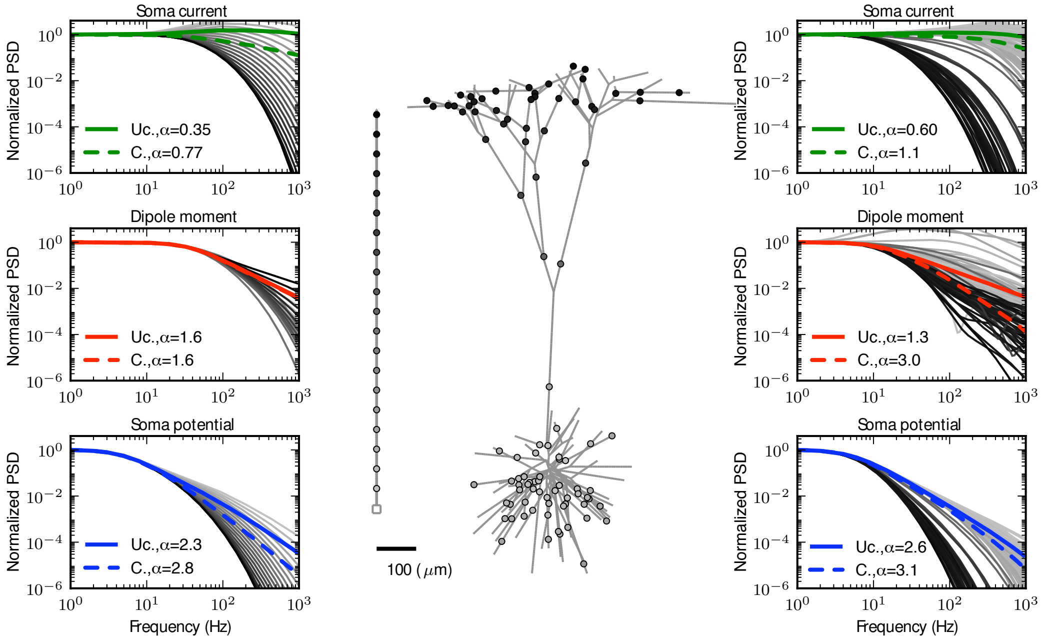

FIGURE 1. Normalized PSDs of the soma current (row 1), the dipole moment (row 2) and the soma potential (row 3) of the ball and stick neuron (left) and the pyramidal neuron (right). The neuron models have a constant density (with respect to membrane area) of white noise input currents onto the dendrites. The whole, colored lines show the uncorrelated case, while the broken colored lines show the correlated case. A cascade of PSDs from 20 single current inputs for the ball and stick neuron and 107 single current inputs for the pyramidal neuron is shown in grey, with the most distal synapses in dark grey and the proximal in light grey, with corresponding greyscale for the filled circles at the respective neuron morphology. The α values printed in the legends describe the powers of the power laws for the slope going through the two points at 950 Hz and 1000 Hz. The ball and stick neuron is simulated with 200 dendritic segments, while the pyramidal neuron is simulated with 3214 dendritic segments. Note that for the ball and stick dipole moment the uncorrelated case almost perfectly overlie the correlated case.

for the PSDs will be

$$\lim_{W\to\infty} PSD_n \to A_n/W^{n/2} \ . \tag{21}$$

Thus, for high frequencies the six PSDs considered express asymptotic power laws with powers $\alpha = \{1/2, 1, 3/2, \ldots, 3\}$.

A re-inspection of the slopes for ball and stick model PSDs in Fig. 1 and a comparison to the asymptotic values of Eq. 21 tells us that although the curves might look linear in the log-log plot for high frequencies, the expressed powers α are still quite a bit off from their asymptotic values, possibly with an exception for the uncorrelated dipole moment. Fig. 3 shows the the first four terms of the numerator (left) and denominator (right) for default parameters ($R_\mathrm{m} = 3\ \Omega\mathrm{m}^2$, $R_\mathrm{i} = 1.5\ \Omega\mathrm{m}$, $C_\mathrm{m} = 0.01\ \mathrm{F/m}^2$, $l = 1$ mm, $d = 2\ \mu$m and $d_\mathrm{s} = 20\ \mu$m). It is clear from the left column that in all cases except for the uncorrelated dipole moment ($n = 3$) the numerator is dominated by the highest order term, 1, for frequencies $f \gtrsim 10$ Hz. Actually, for the correlated cases the numerator exactly equals 1 (see Eq. 12). For the uncorrelated dipole moment the highest order term is not the largest term before $f \gtrsim 300$ Hz.

For all the denominators it is clear that the highest order term only becomes the largest term for frequencies $f \gtrsim 300$ Hz. However, even though the highest order term is the largest term for frequencies larger than about 300 Hz, it is clear from the left panels of

Fig. 1 that even at 1000 Hz the PSDs typically have α values smaller than their asymptotic value.

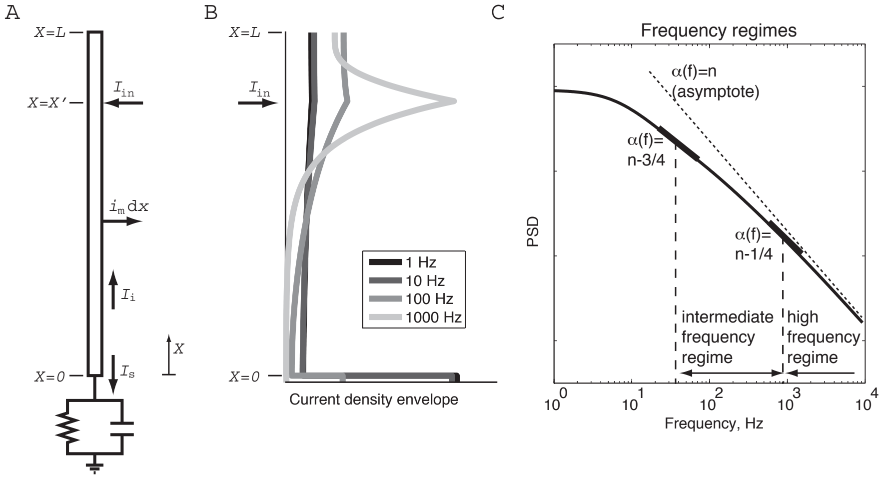

FIGURE 2. (A) Schematic illustration of the ball and stick neuron model with input at a given position $X = X'$. The lumped soma is assumed to be iso-potential and located at $X = 0$. (B) The densities of the return-current envelopes for a ball and stick neuron with input at $X = 0.8$ for different frequencies. The somatic return currents are illustrated as current densities from a soma section with length 20 μm placed below the stick. For 1 Hz, 10 Hz, 100 Hz and 1000 Hz the amplitudes of the somatic return currents are about 1/7.3, 1/7.5, 1/22 and 1/3100 of the input current, respectively. Default parameters are used for the ball and stick neuron model: a stick diameter $d = 2$ μm, somatic diameter of $d_s = 20$ μm, stick length of $l = 2$ mm, specific membrane resistance of $R_m = 3$ Ωm^2, inner resistivity of $R_i = 1.5$ Ωm and a specific membrane capacitance of $C_m = 0.01$ F/m^2. (C) Schematic illustration of the log-log plot of a PSD, illustrating the intermediate frequency regime (*if*-regime) and the high frequency regime (*hf*-regime), which is defined relatively to the asymptotic value of the slope α.

3.2. **Apparent power laws in the PSDs.** To further study the log-log decay rate of the PSDs given by the power α, a negative log-log derivative of the PSDs, $-\mathrm{d}(\log PSD_n)/\mathrm{d}(\log W)$ is computed and plotted in Fig. 4. This derivative is independent on the amplitude A_n and the slopes, α, of the PSDs are therefore completely described by the three parameters B, L and the dimensionless frequency W. Thus, for a given dimensionless length L, the power α can be mapped out in a color plot with W and B along the axis. Fig. 4 shows such a mapping, and a special attention has been given to the region where the power is about 1/2 below the asymptotic values: the black lines in each panel defines a interval around this power, as the left/lower black line is for $\alpha = n/2 - 3/4$ and the right/upper black line is for $\alpha = n/2 - 1/4$. The three columns of the figure correspond to different dimensionless lengths L, where the left column corresponds to an electrotonically compact dendrite of $L = 0.25$, the middle column is a cable of length equal to the length constant, $L = 1$, while the right column is an electrotonically non-compact dendrite of length $L = 4$. Electrotonic lengths greater than $L = 4$ gave plots that were indistinguishable by eye (not shown). The horizontal white line defines the B corresponding to our default parameters, and the three vertical lines in each panel correspond to 10 Hz, 100 Hz and 1000 Hz for our default time constant of $\tau_m = 30$ ms.

It is interesting to see how the width of the region restricted by the black curves varies between the different entities and for different values of B. For simplicity we will refer to this frequency interval as the intermediate frequency interval (*if*-interval) or intermediate frequency regime (*if*-regime), see Fig. 2*C*. The PSD within this frequency interval may often appear to be linear, especially if the interval is wide. Correspondingly, we will refer to the interval to the right of this interval as the high frequency interval (*hf*-interval). Here the PSD is approaching its asymptotic value.

For the soma potential PSDs, the *if*-interval is in general quite wide, especially for B around the default value chosen here. The exception is for correlated input currents onto very compact neurons, where the *if*-interval typically is more narrow. However, when the neuron becomes electrotonically less compact, as for $L = 1$ and $L = 4$, the *if*-intervals of the soma potential PSDs become similar between the correlated and uncorrelated case, and the overall color plots become almost indistinguishable by eye. Note, however, that the scales of the color plots are different, so that the non-compact neuron models express a log-log slope which is half a power steeper for the correlated case compared to the uncorrelated case. This means that for the less compact neurons the PSDs should be easily distinguishable due to the different steepness of the log-log slopes, while this might be harder for more compact neurons, as the PSD has quite a wide range where the slope α is about 2 both for the case of correlated- and uncorrelated input currents.

Similarly, we see that it might also be hard to distinguish the PSDs for the dipole moments on the basis of their log-log slopes, at least for values of B in the range of the default value used here. This is due to the very narrow *if*-interval for the case of uncorrelated input currents and the wide *if*-interval for the case of correlated input currents, which makes the PSD for uncorrelated input currents approach its asymptotic value of 1.5 for quite low frequencies, and for the same frequencies the PSD for correlated input currents is typically within its *if*-interval. This effect is also seen for the ball and stick neuron in Fig. 1, where the normalized PSDs are indistinguishable for the two cases. However, this seems to be a very model-specific effect, as the pyramidal neuron of Fig. 1 expresses very different PSDs for the two cases.

For the PSDs of the soma currents, correlated versus uncorrelated input currents might in some cases be easily distinguishable, as the uncorrelated PSDs typically have a region with a positive slope in the log-log plot (negative α) when the neuron is not too compact and B is not too large. However, if the frequency is large enough, also the PSD for uncorrelated input currents express a more regularly decaying slope in the log-log plot, as it approaches its asymptotic α value which is 1/2.

It is striking that for default parameters all PSDs shown in the figure, except for the dipole moment with uncorrelated input currents, first enter the *hf*-interval at about 1000 Hz. This means, that for the frequency range typically considered in experiments, the PSDs are likely in the *if*-regime or below.

3.3. **Variation with biophysical parameters.** The dimensionless parameters used in Fig. 4 nicely plot out the parameter space for the slope α. In Figs. 5–6, however, we plot the PSDs when measurable biophysical parameters are varied. The PSDs are plotted for the ball and stick neuron when all parameters except one are held at default values, while the last parameter is given different values. The parameters varied are the ones believed to change substantially from neuron to neuron; the soma diameter d_s, the stick diameter d, the stick length l and the specific membrane resistance R_m. The specific membrane resistance might not only change between neurons, but also between states, i.e. between low- and high-conductive state.

In Fig. 5 the soma diameter is varied in the two columns to the left and the stick diameter is varied in the two columns to the right. Although the biophysical parameters varied in Figs. 5–6 may appear in several of the dimensionless variables, the soma diameter only appears in the parameter B, where it appears with power two, $B = d_\mathrm{s}^2/d\lambda$. Fig. 4 showed that the parameter B is important for defining the width of the *if*-interval, and is therefore important for the decay rate of the quasi-linear log-log slopes expressed in the PSDs. This is clearly seen in the left columns of Figs. 5, as the different soma diameters

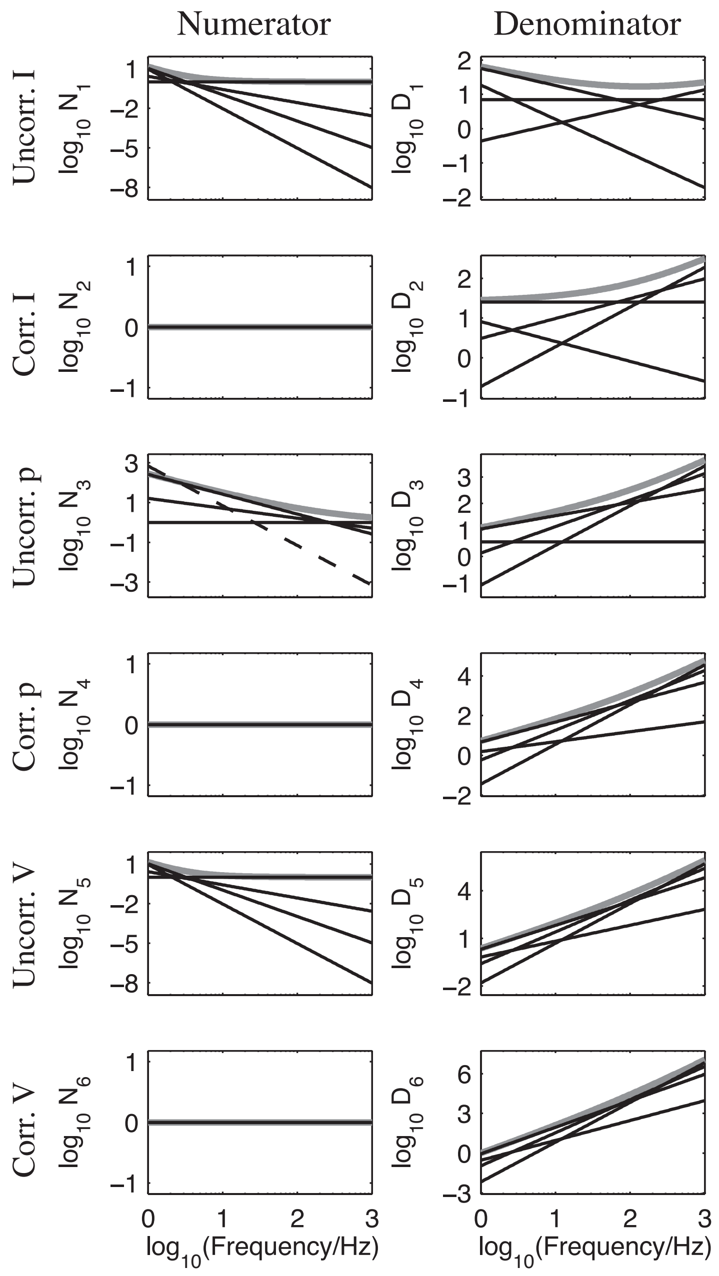

Figure 3. The first four terms of the asymptotic high-frequency series expansion of the numerator N_n (left) and the denominator D_n (right) for the ball and stick neuron with default parameters, see Eqs. 19 and 20. The rows correspond to uncorrelated soma current (row 1), correlated soma current (row 2), uncorrelated dipole moment (row 3), correlated dipole moment (row 4), uncorrelated soma potential (row 5) and correlated soma potential (row 6). The grey lines are the sums of the three first terms in the expansions, while the broken line in the N_3 panel indicates that this term is plotted with inverted sign, i.e., for default parameters the term is negative, see N_3 in Eq. 19. The default parameters used for the ball and stick neuron model: stick diameter $d = 2$ μm, soma diameter $d_\mathrm{s} = 20$ μm, stick length $l = 2$ mm, specific membrane resistance $R_\mathrm{m} = 3$ Ωm^2, inner resistivity $R_\mathrm{i} = 1.5$ Ωm and specific membrane capacitance $C_\mathrm{m} = 0.01$ F/m^2.

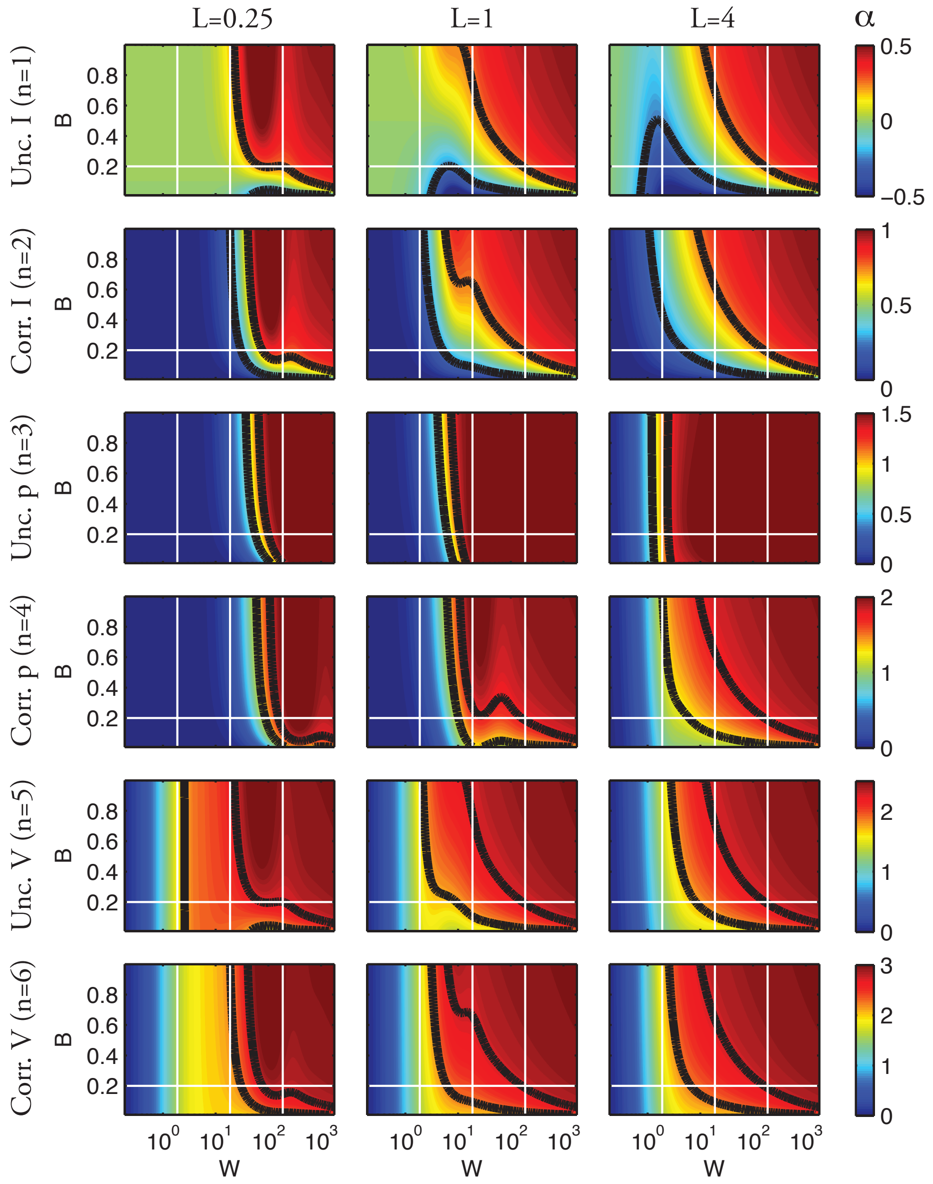

FIGURE 4. The slopes α for all power spectral densities PSD_n, $n = \{1, 2, \ldots, 6\}$, corresponding to the PSDs of uncorrelated and correlated somatic transmembrane current (row 1 and 2), uncorrelated and correlated dipole moment (row 3 and 4) and the uncorrelated and correlated soma potential (row 5 and 6) for the ball and stick neuron model with dimensionless parameters. The dimensionless parameter B is plotted along the vertical axes, while the dimensionless frequency W is plotted logarithmically along the horizontal axes. The left column is for dimensionless length $L = 0.25$, the middle for $L = 1$ and the right for $L = 4$. The horizontal white lines correspond to the default value of the parameter B, $B = 0.2$, while the vertical white lines correspond to frequencies of 10 Hz, 100 Hz and 1000 Hz for the default membrane time constant $\tau_m = 30$ ms. The black lines within each panel indicate the two powers $\alpha = n - 3/4$ and $\alpha = n - 1/4$. The plots within each row express the same color scale for α, given by the color-bar to the right.

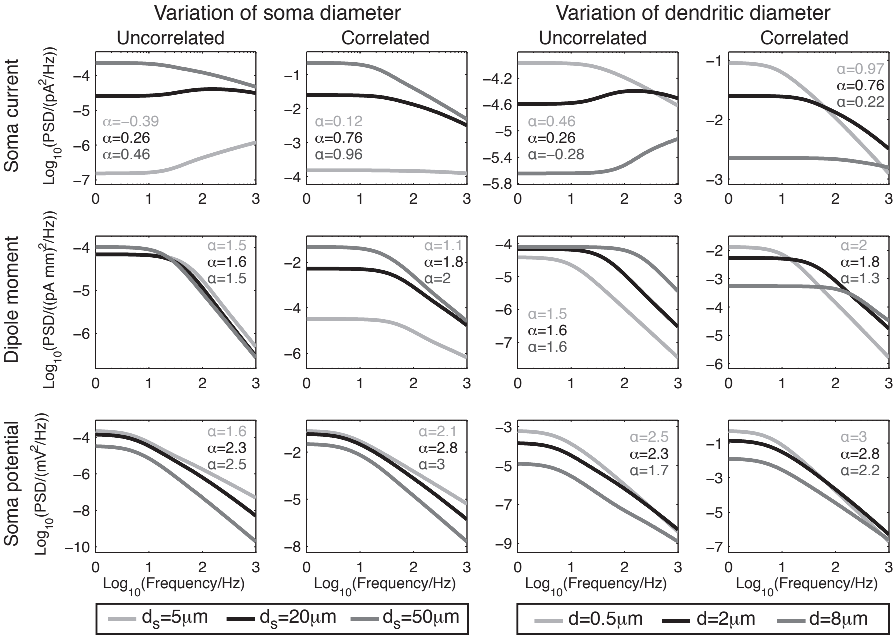

FIGURE 5. PSDs of the soma current (row 1), dipole moment (row 2) and soma potential (row 3) for the ball and stick neuron for different values of the *soma diameter* (the two left columns) and *stick diameter* (the two right columns), with their values indicated in the legends below the panels. All other parameters of the ball and stick neuron have their default values; a stick diameter $d = 2$ μm, somatic diameter of $d_{\mathrm{s}} = 20$ μm, stick length of $l = 2$ mm, specific membrane resistance of $R_{\mathrm{m}} = 3$ $\Omega\mathrm{m}^2$, inner resistivity of $R_{\mathrm{i}} = 1.5$ Ωm and a specific membrane capacitance of $C_{\mathrm{m}} = 0.01$ F/m^2. The values of α printed inside the panels describe the powers of the power laws for the slope going through the two points at 966 Hz and 1000 Hz. The upper α corresponds to the low value of the parameter varied (lightest grey), the middle α corresponds to the default parameter (black curve), while the lower α corresponds to the high value of the parameter varied (dark grey). The first and third columns show the PSDs for uncorrelated input currents, while the second and fourth columns show the PSDs for correlated input currents.

give very different values of α. The α values printed in Figs. 5–6 are the values for the slope when they are approaching 1000 Hz. In Fig. 4 the panels showed that for about 1000 Hz all slopes approached the hf-interval for the default parameters, with an exception for the PSD for the dipole moment with uncorrelated input currents, which approached the hf-interval for a much lower frequency. This is also seen for the values of α here for the default soma diameter of 20 μm. For a soma diameter of 5 μm, the value of α is much smaller, typically almost one whole power less than its asymptotic value, while for the larger soma dimeter, the slope is very close to its asymptotic value. An exception for this is the PSD for the dipole moment with uncorrelated input currents, which is very similar for all three values of the soma diameter, with a value of α just above 1.5 .

When the stick diameter is varied, the relations are inverted compared to the variation of the soma diameter: a smaller diameter gives a larger value for α around $f = 1000$ Hz. This is due to the parameter B, which relates inversely to d with the power 3/2, as d is in the denominator of the parameter B, both explicit and also implicit through λ. However, the stick diameter is also implicit in L, and thus influences the cut-off frequency as well, i.e., the frequency for which the slope has a transition from a flat region ('$\alpha \sim 0$') to a region in which the PSD is decaying in the log-log plot. All amplitudes A_n shown in Table 1 are also dependent on the stick diameter, thus the PSD amplitudes are different for different stick

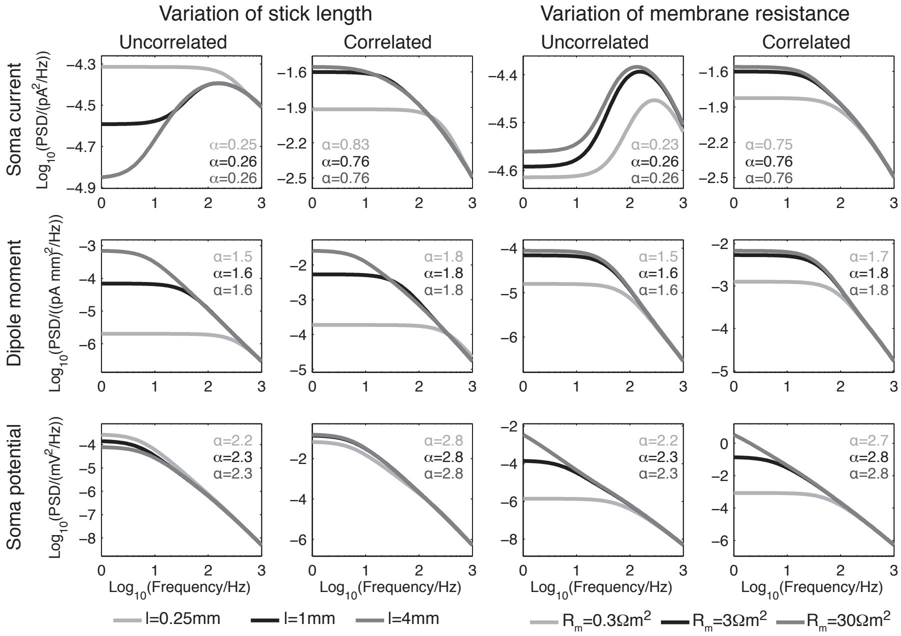

FIGURE 6. PSDs of the soma current (row 1), dipole moment (row 2) and soma potential (row 3) for the ball and stick neuron for different values of the *stick length* (the two left columns) and *specific membrane resistance* (the two right columns), with their values indicated in the legends below the panels. All other parameters of the ball and stick neuron have their default values; a stick diameter $d = 2$ μm, somatic diameter of $d_\mathrm{s} = 20$ μm, stick length of $l = 2$ mm, specific membrane resistance of $R_\mathrm{m} = 3$ $\Omega\mathrm{m}^2$, inner resistivity of $R_\mathrm{i} = 1.5$ Ωm and a specific membrane capacitance of $C_\mathrm{m} = 0.01$ F/m^2. The values of α printed inside the panels describe the powers of the power laws for the slope going through the two points at 966 Hz and 1000 Hz. The upper α corresponds to the low value of the parameter varied (lightest grey), the middle α corresponds to the default parameter (black curve), while the lower α corresponds to the high value of the parameter varied (dark grey). The first and third columns show the PSDs for uncorrelated input currents, while the second and fourth columns show the PSDs for correlated input currents.

diameters as the PSDs are approaching their respective asymptotic expressions. Contrary to this, only the amplitudes for the soma potential were depending on the soma diameter.

Fig. 6 shows the impact of stick length l in the left columns, and the specific membrane resistance, R_m, in the right columns. In all cases the slopes of the PSDs approach the same α value for 1000 Hz. For variation of l this might be rather obvious, as the only dimensionless parameter influenced is the dimensionless length L, which is not decisive for the slope of α except for low frequencies around the cut-off frequency. This is also seen in the left columns, as variation of l influences the cut-off frequency and therefore also the amplitude of the PSD for lower frequencies. A shorter stick clearly gives a higher cut-off frequency for the PSDs of the dipole moments and for the PSD for the soma current with correlated input currents. For the latter, the cut-off frequencies are also reflected in the corresponding PSD for the soma potential, but as the soma current cut-off frequencies are quite high these are reflected for high frequencies also in the PSD for the soma potential, and rather decide the width of the different frequency regimes, i.e., the width of the *if*-regime. This observation is also in accordance with Fig. 4, where the PSD for the soma potential with correlated input currents have a much narrower *if*-regime for $L = 0.25$ than for $L = 1$. For the PSD for the soma potential for uncorrelated input currents we have a rather opposite situation, where larger L gives a narrower *if*-interval. This is due to the effect seen in the corresponding PSD for the soma current, where long sticks have a positive slope for the mid-frequencies in the log-log plot, reflected in a corresponding less negative slope for the PSD of the soma potential, and hence a wider *if*-interval, as seen in Fig. 4.

When the specific membrane resistance is varied in the right columns of Fig. 6 the PSDs for the soma current with correlated input currents as well as the PSDs for the dipole moments are similar to when the stick length was varied; a higher membrane resistance gives a lower cut-off frequency. It is, however, important to note that a large R_m influences L inversely compared to how a long stick would influence (through λ), although a higher R_m also results in a lower cut-off frequency. This is because R_m only influences the dimensionless L inversely with the square root $L \propto 1/\sqrt{R_\mathrm{m}}$, while it influences the dimensionless frequency stronger, through $W = \omega\tau = 2\pi f R_\mathrm{m} C_\mathrm{m}$, and a high specific membrane resistance will therefore give a large W for a smaller frequency f. So, although a higher R_m results in a more compact neuron through the dimensionless electrotonic length L, this does not lead to a higher cut-off for the dipole moments and the soma current with correlated input currents, but actually the opposite. This effect is even more visible for the PSDs for the soma potential, where the cut-off frequency for the high R_m is for such low frequencies that it lies outside the plot. Although the effect of R_m and l might look similar for the dipole moment and the soma current with correlated input currents, there is a striking difference for the soma potential PSDs. This is because l only influences the cut-off frequency through the hyperbolic functions which are functions of $\mathbf{q}L$, while R_m influences the parameter $\mathbf{q}$, which is not only appearing inside the hyperbolic functions, but which is also appearing separately, and which has the highest power for the soma potentials.

In summary Figs. 5–6 show that soma and stick diameter influence the slope α as well as the overall amplitude of the PSDs, while l and R_m do not influence the value of α, but may influence the cut-off frequency and hence the PSD amplitude for low frequencies. An exception is the PSDs for the dipole moment with uncorrelated input currents, where variations of the different parameters has very little impact on the value of α, but all parameters except for the soma diameter influence the cut-off frequency and where the stick diameter also influences the overall amplitude.

4. Discussion

The cable equation was solved in frequency space for the ball and stick neuron with a single input current at an arbitrary position along the stick. The PSD was computed for the soma current, soma potential and the dipole moment when white noise input currents were distributed evenly throughout the dendritic stick. The dipole moment is directly proportional to the single neuron contribution to the EEG if no frequency filtering through the extracellular medium, dura matter, scull and scalp is assumed [17].

All PSDs express an asymptotic high-frequency power law $1/f^\alpha$. For *uncorrelated* white noise input currents α is 0.5, 1.5 and 2.5 for the soma current, EEG and the soma potential, respectiviely. For *correlated* white-noise input the respective values are 1, 2 and 3.

4.1. PSD dependence on functional form of noise sources.

Throughout this paper, the input currents are assumed to have a white noise distribution. This is contrary to other recent studies, e.g., in [21] the noise sources were assumed to be conductance-based, two-exponential synapses with a rise time of 0.4 ms and a decay time of 2 ms, while in [5] the noise sources were assumed to be current-based exponentially decaying synapses with a decay time of 10 ms. In both studies [5, 21] the synapses were spread evenly throughout the dendrites and were triggered according to an underlying Poissonian distribution. However, due to the linearity assumed here, the formalism is general with respect to the functional form of the input current: in Eq. 10 it is shown that the PSD for the input current, $v = v(f)$, is simply a pre-factor in the expression. Thus, for Poissonian triggered current-based synapses with the functional form of a decaying exponential, the expressions derived here for the PSDs can simply be multiplied with the PSD of the exponentially decaying function. The PSD for an exponentially decaying function is given by $v(f) \propto 1/(1+(f/f_c)^2)$, which, for frequencies much higher than the cut-off frequency $f_c = 1/(2\pi\tau_s)$, decays as $1/f^2$. This would give an additional power of two in the slopes α, and the PSDs would not be in agreement with PSDs derived from experimental recordings [7, 20, 11, 21, 5], which typically express powers α in agreement with the powers computed for white noise input evenly distributed throughout the dendrite of a ball and stick neuron model.

However, if the synaptic time constant is small enough, and the recordings only treat rather low frequencies, the synaptic PSD may not influence the overall recorded soma potentials much. For example, a time constant of $\tau_s = 2$ ms will give a cut-off frequency of about 80 Hz, while a time constant of $\tau_s = 10$ ms gives a cut off frequency of about 16 Hz. Although both these time constants would result in a PSD for the synaptic current which has a substantial impact on the overall PSD within the frequency interval discussed here, $\tau_s = 2$ ms would have a much smaller impact when the frequency interval under study is up to 100 Hz, as in [21], and if the synaptic time constant is even smaller, its PSD might be approximately white for recordings within such a low frequency interval.

However, for typical synaptic time constants and soma potential recordings that are reliable up to a few hundred herz, it seems inevitable that the synaptic PSD will influence the soma potential PSD. If so, the PSD of the synapse has to be compensated for with a mechanism which has the opposite effect on the PSD. In [5] it is shown that a non-ideal membrane capacitance can have such a compensatory effect, while in [3] it is shown that correlations in the network due to delay distributions directly can influence the power α through the resulting non-Poissonian pre-synaptic spike train statistics.

The simplest explanations may, however, be that the large number of small currents going through the membrane ensures that shot-noise (white noise due to statistical fluctuations in small currents) is dominating the membrane currents, at least for higher frequencies, and that the different PSDs are reflections of this shot noise.

4.2. **Power laws for EEG.** The PSDs for the EEG are quite different when comparing results from the ball and stick and the pyramidal neuron, see Fig. 1. The power laws seen experimentally typically express a power α between 1 and 2 [8], which is in agreement with the ball and stick neuron both with correlated and uncorrelated input currents and for uncorrelated input currents onto the pyramidal neuron, see Fig. 1. The large discrepancy between the ball and stick neuron and the pyramidal neuron PSDs for the EEG may be due to the pyramidal neuron's non-homogenous distribution of total neuronal membrane area along the the apical direction, as the branching increases the surface area of the apical part of the neuron dramatically [13]. The pyramidal neuron also has an increased membrane area basally due to the basal dendrites. In addition, also the pronounced tapering along the apical dendrite may have an impact on the PSDs.

Although Fig. 1 shows that the cut-off frequency is lower for the pyramidal neuron than for the ball and stick neuron, the cut-off frequency is still too high compared to EEG recordings, where the power law typically seems to extend down to about 1 Hz [8]. It is still unknown which types of neurons or neural structures dominate the PSD of the EEG, but from Fig. 4 one sees that long sticks (large L) and large membrane time constants τ_m will lower the cut-off frequencies for the EEG.

In addition, a non-homogeneous membrane resistance, e.g., a different membrane resistance in soma than in the dendrites, will impact the cut-off frequency dramatically (results not shown). There is also a possibility that the extracellular potentials are filtered through the extracellular medium, dura matter, scull and scalp, however, according to impedance measurements this is not very likely for the relatively low frequencies typically recorded in the EEG [17].

4.3. **Power laws for soma potential.** For experimental recordings, the soma potential typically expresses a power law in the PSD with α close to 2.5 [7, 20, 11, 21, 5]. The underlying sources for the soma potential PSD is found to be related to noisy input currents homogeneously spread throughout the dendrites [11, 21], and in [11] it was shown that for the higher frequencies of the recordings, i.e., from 5 Hz to 100 Hz, the amplitude of the $1/f$ noise was reduced when synaptic blockers (DNQX and gabazine) were used. In the same paper it was shown that the sodium channel blocker TTX did not influence the high frequency part of the spectrum, however, blocking of the sodium channels had great impact on the lower frequencies in the range 0.2 Hz to 2 Hz.

In the formalism presented here, a power α close to 2.5 corresponds to the asymptotic value of the ball and stick neuron with uncorrelated input currents spread evenly throughout the dendrites. However, a power 2.5 can also appear within the intermediate frequency regime of a ball and stick neuron where the correlated input currents dominate. A key parameter that might decide whether correlated or uncorrelated input currents dominate the soma potential PSD is the density ρ of input currents, which appear with power 2 in front of the term consisting of correlated activity, but with power 1 in front of the term consisting of the uncorrelated activity, see Eq. 10. This implies that a high density of input currents will lead to a strengthening of the contribution from correlated activity relative to uncorrelated activity. Here, ρ is assumed to be $1/\mu$m, which is roughly in agreement with the anatomical synaptic density along a dendrite, which is estimated to be about 7800 synapses along 4 mm of dendrites in an average nerve cell in mouse cortex [12]. With the value of ρ used here, the lower frequencies of the soma potential PSDs are about three orders of magnitudes larger for the PSDs resulting from correlated input currents than for the PSDs resulting from the uncorrelated input currents, see lower rows of Figs. 5 and 6.

The input current PSD used here was chosen to match the PSD amplitudes seen in the experimental data of [7, 11, 21]. Thus, a PSD of $v = (1 \text{ fA})^2/\text{Hz}$ was used, which resulted in PSDs that are about one order of magnitude larger than experimental results [7, 11, 21] for the PSDs based on correlated input currents and about two orders of magnitudes smaller than experimental results [7, 11, 21] for the PSDs based on uncorrelated input currents. Although the given choice of ρ only requires a very small coherence in the input for the correlated input to dominate over the uncorrelated input PSD, see Eq. 10, it is hard to imagine how the input currents could be correlated throughout the neuron if one assumes that the origin of the white noise currents is *shot noise* or *stochasticity within the gating properties* of ion channel currents or synaptic currents. Therefore, it is still likely that experimental results should be compared to the results computed for uncorrelated input currents. If that is the case, the typical soma potential PSD with $\alpha = 2.5$ found in experiments [7, 20, 11, 21, 5], would imply that the high-frequency asymptotic value is reached. This is not the case for the default ball and stick parameters used here, even at 1000 Hz. Note, however, that the simulation of the pyramidal neuron in Fig. 1 with uncorrelated white noise input has a slope α of exactly 2.5. This may be due to an effectively larger soma diameter for the pyramidal neuron compared to the ball and stick neuron model, possibly in combination with effectively smaller dendritic diameters in the pyramidal neuron than the default diameter used for the ball and stick neuron. The morphology of the pyramidal neurons may therefore lead to a transition towards the asymptotic value for a much smaller frequency. It might also be that such realistic morphologies in general have high-frequency asymptotic values α that are higher than for the ball and stick neuron.

In addition, all results here are based on a purely passive membrane, which is a prerequisite to be able to solve the cable equation analytically. By introducing active channels in the model, the analytical derivations would be impossible. Further, for the pyramidal neuron simulations the active mechanisms would introduce non-linearities, and the PSDs based on white-noise inputs could not simply be generalized to any input current just by multiplying the white-noise based PSD with the PSD of the input current. However, other studies have incorporated active ion channels and conductance based synapses [7, 11, 21], and active channels have been shown to change the PSDs. For example, in [21] sodium channels in soma are shown to influence the cut-off frequency and the PSD for low frequencies (below 2 Hz), but not the higher frequencies.

Here, we have focused on the analytical solution of the ball and stick neuron, and a full study of how realistic neuron morphologies and active ion channels may impact the soma potential PSD is beyond the scope of this paper. However, a simulation study in combination with experimentally recorded soma potentials and morphological reconstructions of the same neuron, preferably executed for several neurons of different morphological classes, would indeed be a very interesting set-up for a future study.

APPENDIX A. BALL-AND-STICK NEURON WITH INPUT AT ARBITRARY POSITION

The ball-and-stick neuron with current input at arbitrary position is derived by combining (i) a solution to the ball and stick neuron with an input current input at the *end* of the stick and (ii) a solution of a sealed end stick with an input current at its end.

For both cases, the expression for the axial current is used as a boundary condition. The axial current is proportional to the derivative of the membrane potential,

$$I_{\mathrm{i}}(x,t) = -\frac{1}{r_{\mathrm{i}}}\frac{\partial V(x,t)}{\partial x} \ . \tag{22}$$

In complex notation and with dimensionless units this becomes

$$\hat{\mathbf{I}}_{\mathrm{i}}(X,\omega) = -\frac{1}{r_{\mathrm{i}}\lambda}\frac{\partial \hat{\mathbf{V}}(X,\omega)}{\partial X} \ . \tag{23}$$

Similarly, the transmembrane current density is given by

$$i_{\mathrm{m}} = -\frac{\partial I_{\mathrm{i}}(x,t)}{\partial x} = \frac{1}{r_{\mathrm{i}}}\frac{\partial^2 V(x,t)}{\partial x^2} \ , \tag{24}$$

with its complex counterpart,

$$\hat{\mathbf{i}}_{\mathrm{m}}(X,\omega) = -\frac{1}{\lambda}\frac{\partial \hat{\mathbf{I}}(X,\omega)}{\partial X} = \frac{1}{r_{\mathrm{i}}\lambda^2}\frac{\partial^2 \hat{\mathbf{V}}(X,\omega)}{\partial X^2} \ . \tag{25}$$

In dimensionless variables, $X = x/\lambda$ and $T = t/\tau$, the cable equation, Eq. 1, can be expressed

$$\frac{\partial^2 V(X,T)}{\partial X^2} - \frac{\partial V(X,T)}{\partial T} - V(X,T) = 0 \ . \tag{26}$$

Due to the linearity of the cable equation, each frequency of the input signal can be treated individually. It is then convenient to express the membrane potential in a complex form,

$$\mathbf{V} = \hat{\mathbf{V}}(x,\omega)e^{j\omega t} \ , \tag{27}$$

where $\hat{\mathbf{V}}$ is a complex number containing the amplitude and phase of the signal.

Within this framework the cable equation be simplified to

$$\frac{\mathrm{d}^2\hat{\mathbf{V}}}{\mathrm{d}X^2} - \mathbf{q}^2\hat{\mathbf{V}} = 0 \ , \tag{28}$$

where $\mathbf{q}^2 = 1 + j\omega\tau$, see [19] and [18].

The general solution to Eq. 28 can be expressed as

$$\hat{\mathbf{V}} = \mathbf{C}_1\cosh(\mathbf{q}L - \mathbf{q}X) + \mathbf{C}_2\sinh(\mathbf{q}L - \mathbf{q}X) \ . \tag{29}$$

A.1. **Sealed end boundary.** The part of the ball and stick neuron which is distally to the synaptic input is a stick where we apply the boundary condition $\hat{\mathbf{V}}_0$ at the synaptic site, and a sealed end boundary at the very distal tip. For simplicity we now use coordinates so that the synapse is placed in $X_d = 0$, hence the boundary condition become $\mathbf{V}(X_d = 0) = \hat{\mathbf{V}}_0$. We then define the distal stick to have length l_{d}, and the distal tip is positioned at $x = l_d$, in dimensionless length expressed $X_d = L_{\mathrm{d}}$. The boundary condition at the distal end corresponds to setting the axial current equal to zero in Eq. 23. From the boundary conditions the specific solution to the cable equation now becomes [19, 18],

$$\hat{\mathbf{V}}(X_d,\omega) = \frac{\hat{\mathbf{V}}_0\cosh(\mathbf{q}L_d - \mathbf{q}X_d)}{\cosh(\mathbf{q}L_d)} \ . \tag{30}$$

The current $\hat{\mathbf{I}}_{\mathrm{i}}(X_d,\omega)$ is then given by

$$\hat{\mathbf{I}}_{\mathrm{i}}(X_d,\omega) = \frac{\hat{\mathbf{V}}_0\mathbf{q}}{r_{\mathrm{i}}\lambda}\frac{\sinh(\mathbf{q}L_d - \mathbf{q}X_d)}{\cosh(\mathbf{q}L_d)} \ , \tag{31}$$

and the dendritic input admittance, $\mathbf{Y}_{\mathrm{in}}(\omega) = \hat{\mathbf{I}}_{\mathrm{i}}(X_d = 0, \omega)/\hat{\mathbf{V}}(X_d = 0, \omega) = -\hat{\mathbf{I}}_0/\hat{\mathbf{V}}_0$, is

$$\mathbf{Y}_{\mathrm{in}}(\omega) = \frac{\mathbf{q}}{r_{\mathrm{i}}\lambda} \tanh(\mathbf{q}L_d) \; . \tag{32}$$

Since $\lim\limits_{L\to\infty} \tanh(\mathbf{q}L) \to 1$, see Appendix C, the infinite stick admittance is expressed as $\mathbf{Y}_\infty(\omega) = \frac{\mathbf{q}}{r_{\mathrm{i}}\lambda}$ and the finite stick admittance can here be expressed $\mathbf{Y}_{\mathrm{in}}(\omega) = \mathbf{Y}_\infty(\omega)\tanh(\mathbf{q}L_d)$. From Eq. 25 the transfer function from an applied voltage $\hat{\mathbf{V}}_0$ in the dendritic end to a transmembrane current density expression can be expressed as [18]

$$\mathbf{H}(X_d, \omega) = \frac{\mathbf{q}^2}{r_{\mathrm{i}}\lambda^2} \frac{\cosh(\mathbf{q}L_d - \mathbf{q}X_d)}{\cosh(\mathbf{q}L_d)} \; , \tag{33}$$

with $\hat{\mathbf{i}}_{\mathrm{m}}(X_d, \omega) = \mathbf{H}(X_d, \omega)\hat{\mathbf{V}}_0$.

The complex dipole moment of the stick with a sealed end is given by the integral

$$\hat{\mathbf{p}}(\omega) = \int_0^l \hat{\mathbf{i}}_{\mathrm{m}}(x, \omega) x \; \mathrm{d}x = \frac{\hat{\mathbf{V}}_0}{r_{\mathrm{i}}}(1 - 1/\cosh(\mathbf{q}L_d)) \; . \tag{34}$$

A.2. **Lumped soma boundary.** Here we find the solution to a ball and stick neuron with a synaptic input at the *end* of the stick. Similarly to the distal stick we apply a boundary condition $\hat{\mathbf{V}}_0$ to the synaptic site and put this in $X_{\mathrm{p}} = 0$, so that $\mathbf{V}(X_{\mathrm{p}} = 0) = \hat{\mathbf{V}}_0$. The open end/lumped soma boundary condition means that the leak current out of the dendritic end is proportional to the leak admittance at the end (i.e., the soma admittance), see Fig. 2*A*. The stick is assumed to have length l_{p} and the soma site is at $X_{\mathrm{p}} = L_{\mathrm{p}}$. The voltage drop over the soma compartment is related to the somatic current through Ohm's law $\hat{\mathbf{I}}_{\mathrm{i}}(L_{\mathrm{p}}, \omega) = \hat{\mathbf{I}}_{\mathrm{s}} = \mathbf{Y}_{\mathrm{s}}\hat{\mathbf{V}}(L_{\mathrm{p}}, \omega) = \mathbf{Y}_{\mathrm{s}}\hat{\mathbf{V}}_{\mathrm{s}}$.

The boundary conditions then become

$$X_{\mathrm{p}} = 0 : \; \hat{\mathbf{V}}(0, \omega) = \hat{\mathbf{V}}_0 \; , \tag{35}$$

and, through Eq. 23,

$$X_{\mathrm{p}} = L_{\mathrm{p}} : \; \hat{\mathbf{I}}_{\mathrm{i}}(L_{\mathrm{p}}, \omega) = -\frac{1}{r_{\mathrm{i}}\lambda} \frac{\partial \hat{\mathbf{V}}(X_{\mathrm{p}}, \omega)}{\partial X_{\mathrm{p}}}\bigg|_{X_{\mathrm{p}} = L_{\mathrm{p}}} \; . \tag{36}$$

From Eq. 36 $\mathbf{C}_2$ is then found to be

$$\mathbf{C}_2 = \frac{\mathbf{Y}_{\mathrm{s}}\hat{\mathbf{V}}_{\mathrm{s}}\lambda r_{\mathrm{i}}}{\mathbf{q}} \; , \tag{37}$$

which, combined with Eq. 35, gives $\mathbf{C}_1$:

$$\mathbf{C}_1 = \frac{\hat{\mathbf{V}}_0}{\cosh(\mathbf{q}L_{\mathrm{p}})} - \frac{\mathbf{Y}_{\mathrm{s}}\hat{\mathbf{V}}_{\mathrm{s}}\lambda r_{\mathrm{i}}}{\mathbf{q}} \tanh(\mathbf{q}L_{\mathrm{p}}) \; . \tag{38}$$

Note that $r_{\mathrm{i}} = \frac{4R_{\mathrm{i}}}{\pi d^2}$ and $\lambda = \sqrt{\frac{dR_{\mathrm{m}}}{4R_{\mathrm{i}}}}$ gives $\mathbf{Y}_\infty(\omega) = \frac{\pi d^{3/2}\mathbf{q}}{2\sqrt{R_{\mathrm{m}}R_{\mathrm{i}}}} = \frac{\mathbf{q}}{\lambda r_{\mathrm{i}}}$. By substituting for $\mathbf{Y}_\infty$ as well as the constants $\mathbf{C}_1$ and $\mathbf{C}_2$, Eq. 29 gives

$$\hat{\mathbf{V}}_0/\hat{\mathbf{V}}_{\mathrm{s}} = \cosh(\mathbf{q}L_{\mathrm{p}})(1 + (\mathbf{Y}_{\mathrm{s}}/\mathbf{Y}_\infty)\tanh(\mathbf{q}L_{\mathrm{p}})) \; , \tag{39}$$

where we have also used $\hat{\mathbf{V}}_{\mathrm{s}} = \hat{\mathbf{V}}(L_{\mathrm{p}}, \omega)$.

By using Eq. 39 to substitute for $\hat{\mathbf{V}}_{\mathrm{s}}$ in the constants $\mathbf{C}_1$ and $\mathbf{C}_2$ we will after some algebraic manipulations arrive at the solution for the cable equation with the given boundary conditions,

$$\hat{\mathbf{V}}(X_{\mathrm{p}}, \omega) = \hat{\mathbf{V}}_0 \frac{\cosh(\mathbf{q}L_{\mathrm{p}} - \mathbf{q}X_{\mathrm{p}}) + (\hat{\mathbf{Y}}_{\mathrm{s}}/\hat{\mathbf{Y}}_\infty)\sinh(\mathbf{q}L_{\mathrm{p}} - \mathbf{q}X_{\mathrm{p}})}{\cosh(\mathbf{q}L_{\mathrm{p}}) + (\hat{\mathbf{Y}}_{\mathrm{s}}/\hat{\mathbf{Y}}_\infty)\sinh(\mathbf{q}L_{\mathrm{p}})} \; . \tag{40}$$

The axial current is through Eq. 23 given by,

$$\hat{\mathbf{I}}_{\mathrm{i}}(X_{\mathrm{p}},\omega) = \hat{\mathbf{V}}_0\mathbf{Y}_\infty \frac{\sinh(\mathbf{q}L_{\mathrm{p}} - \mathbf{q}X_{\mathrm{p}}) + (\mathbf{Y}_{\mathrm{s}}/\mathbf{Y}_\infty)\cosh(\mathbf{q}L_{\mathrm{p}} - \mathbf{q}X_{\mathrm{p}})}{\cosh(\mathbf{q}L_{\mathrm{p}}) + (\mathbf{Y}_{\mathrm{s}}/\mathbf{Y}_\infty)\sinh(\mathbf{q}L_{\mathrm{p}})} , \tag{41}$$

and the input admittance is through Ohm's law $\mathbf{Y}_{\mathrm{in}} = \hat{\mathbf{I}}_{\mathrm{i}}(0,\omega)/\hat{\mathbf{V}}_0$

$$\mathbf{Y}_{\mathrm{in}} = \mathbf{Y}_\infty \frac{\sinh(\mathbf{q}L_{\mathrm{p}}) + (\mathbf{Y}_{\mathrm{s}}/\mathbf{Y}_\infty)\cosh(\mathbf{q}L_{\mathrm{p}})}{\cosh(\mathbf{q}L_{\mathrm{p}}) + (\mathbf{Y}_{\mathrm{s}}/\mathbf{Y}_\infty)\sinh(\mathbf{q}L_{\mathrm{p}})} . \tag{42}$$

The axial current at $X_{\mathrm{p}} = L_{\mathrm{p}}$, i.e., the somatic transmembrane current, will then be

$$\hat{\mathbf{I}}_{\mathrm{s}} = \hat{\mathbf{I}}_{\mathrm{i}}(L_{\mathrm{p}},\omega) = \frac{\hat{\mathbf{V}}_0\mathbf{Y}_{\mathrm{s}}}{\cosh(\mathbf{q}L_{\mathrm{p}}) + (\mathbf{Y}_{\mathrm{s}}/\mathbf{Y}_\infty)\sinh(\mathbf{q}L_{\mathrm{p}})} , \tag{43}$$

and the axial current at $X_{\mathrm{p}} = 0$, i.e., the negative synaptic input current, $\hat{\mathbf{I}}_{\mathrm{i}}(0,\omega) = -\hat{\mathbf{I}}_0(\omega)$, will be

$$\hat{\mathbf{I}}_{\mathrm{i}}(0,\omega) = \hat{\mathbf{V}}_0\mathbf{Y}_\infty \frac{\sinh(\mathbf{q}L_{\mathrm{p}}) + (\mathbf{Y}_{\mathrm{s}}/\mathbf{Y}_\infty)\cosh(\mathbf{q}L_{\mathrm{p}})}{\cosh(\mathbf{q}L_{\mathrm{p}}) + (\mathbf{Y}_{\mathrm{s}}/\mathbf{Y}_\infty)\sinh(\mathbf{q}L_{\mathrm{p}})} . \tag{44}$$

The transfer function between the synaptic input current and the somatic membrane current will become,

$$\hat{\mathbf{I}}_{\mathrm{s}}(\omega) = -\frac{\mathbf{Y}_{\mathrm{s}}}{\mathbf{Y}_\infty} \frac{\hat{\mathbf{I}}_0(\omega)}{\sinh(\mathbf{q}L_{\mathrm{p}}) + (\mathbf{Y}_{\mathrm{s}}/\mathbf{Y}_\infty)\cosh(\mathbf{q}L_{\mathrm{p}})} , \tag{45}$$

and the transmembrane current density of the lumped soma neuron model is, through Eq. 25, found to be

$$\hat{\mathbf{i}}_{\mathrm{m}} = \frac{\mathbf{q}}{\lambda}\hat{\mathbf{V}}_0\mathbf{Y}_\infty \frac{\cosh(\mathbf{q}L_{\mathrm{p}} - \mathbf{q}X_{\mathrm{p}}) + (\mathbf{Y}_{\mathrm{s}}/\mathbf{Y}_\infty)\sinh(\mathbf{q}L_{\mathrm{p}} - \mathbf{q}X_{\mathrm{p}})}{\cosh(\mathbf{q}L_{\mathrm{p}}) + (\mathbf{Y}_{\mathrm{s}}/\mathbf{Y}_\infty)\sinh(\mathbf{q}L_{\mathrm{p}})} . \tag{46}$$

By an integration similar to Eq. 34 the dipole moment for the stick becomes

$$\hat{\mathbf{p}}_{\mathrm{stick}}(\omega) = \hat{\mathbf{V}}_0 \left[1/r_{\mathrm{i}} - \frac{l_{\mathrm{p}}\mathbf{Y}_{\mathrm{s}} + 1/r_{\mathrm{i}}}{\cosh(\mathbf{q}L_{\mathrm{p}}) + (\mathbf{Y}_{\mathrm{s}}/\mathbf{Y}_\infty)\sinh(\mathbf{q}L_{\mathrm{p}})} \right] . \tag{47}$$

The dipole moment due to the somatic return current is the product of the somatic current, Eq. 43, and the fixed synapse-soma dipole length, here assumed to equal the stick length l_{p},

$$\hat{\mathbf{p}}_{\mathrm{s}} = l_{\mathrm{p}}\hat{\mathbf{I}}_{\mathrm{s}} = \frac{l_{\mathrm{p}}\hat{\mathbf{V}}_0\mathbf{Y}_{\mathrm{s}}}{\cosh(\mathbf{q}L_{\mathrm{p}}) + (\mathbf{Y}_{\mathrm{s}}/\mathbf{Y}_\infty)\sinh(\mathbf{q}L_{\mathrm{p}})} . \tag{48}$$

The total dipole moment for a ball-and-stick neuron with synaptic input at the end of the stick is therefore

$$\hat{\mathbf{p}} = \hat{\mathbf{p}}_{\mathrm{s}} + \hat{\mathbf{p}}_{\mathrm{stick}} = \frac{\hat{\mathbf{V}}_0(-1/r_{\mathrm{i}})}{\cosh(\mathbf{q}L_{\mathrm{p}}) + (\mathbf{Y}_{\mathrm{s}}/\mathbf{Y}_\infty)\sinh(\mathbf{q}L_{\mathrm{p}})} + \frac{\hat{\mathbf{V}}_0}{r_{\mathrm{i}}} . \tag{49}$$

Expressed relative to the synaptic input current this becomes

$$\hat{\mathbf{p}} = -\frac{\hat{\mathbf{I}}_0}{\mathbf{Y}_\infty r_{\mathrm{i}}} \left[\frac{-(\mathbf{Y}_{\mathrm{s}}/\mathbf{Y}_\infty)^2\cosh(\mathbf{q}L_{\mathrm{p}}) + \cosh(\mathbf{q}L_{\mathrm{p}}) - 1}{(\mathbf{Y}_{\mathrm{s}}/\mathbf{Y}_\infty)\cosh(\mathbf{q}L_{\mathrm{p}}) + \sinh(\mathbf{q}L_{\mathrm{p}})} + \mathbf{Y}_{\mathrm{s}}/\mathbf{Y}_\infty \right] . \tag{50}$$

A.3. **Arbitrary input position.** Input at arbitrary position is achieved by superposition of the sealed end solution and the lumped soma solution, where the sealed end describes the dynamics in the stick distal to the synapse, and the lumped soma solution describes the solution proximal to the synapse. Note that we now use the same notation and coordinate system as in Fig. 2, i.e., $X_{\text{p}} = -X + L_{\text{p}}$ and $X_d = X - L_{\text{p}}$, and the sum of the stick lengths is $L = L_{\text{p}} + L_{\text{d}}$. The ball and stick dipole moment now becomes

$$\hat{\mathbf{p}}_{\text{general}} = -\frac{\hat{\mathbf{V}}_0}{r_{\text{i}}} \left[\frac{1}{\cosh(\mathbf{q}L - \mathbf{q}X)} + \frac{-1}{\cosh(\mathbf{q}X) + (\mathbf{Y}_{\text{s}}/\mathbf{Y}_\infty)\sinh(\mathbf{q}X)} \right] . \tag{51}$$

The total input admittance of the ball and stick neuron is given by the sum of the proximal admittance and the distal admittance

$$\mathbf{Y}_{\text{in}} = \mathbf{Y}_{\text{in,p}} + \mathbf{Y}_{\text{in,d}} = \mathbf{Y}_\infty \left[\frac{\sinh(\mathbf{q}L_{\text{p}}) + (\mathbf{Y}_{\text{s}}/\mathbf{Y}_\infty)\cosh(\mathbf{q}L_{\text{p}})}{\cosh(\mathbf{q}L_{\text{p}}) + (\mathbf{Y}_{\text{s}}/\mathbf{Y}_\infty)\sinh(\mathbf{q}L_{\text{p}})} + \tanh(\mathbf{q}L_{\text{d}}) \right] . \tag{52}$$

The synapse was put in $X_{\text{p}} = 0$ for the lumped soma solution and $X_{\text{d}} = 0$ for the distal stick solution. Substituting so that $L_{\text{p}} = X$, $L_{\text{d}} = L - X$ and $L = L_{\text{p}} + L_{\text{f}}$ gives

$$\mathbf{Y}_{\text{in}} = \mathbf{Y}_\infty \left[\frac{\sinh(\mathbf{q}X) + (\mathbf{Y}_{\text{s}}/\mathbf{Y}_\infty)\cosh(\mathbf{q}X)}{\cosh(\mathbf{q}X) + (\mathbf{Y}_{\text{s}}/\mathbf{Y}_\infty)\sinh(\mathbf{q}X)} + \tanh(\mathbf{q}(L - X)) \right] . \tag{53}$$

By substituting for $\hat{\mathbf{V}}_0$ in Eq. 51 and using the result in Eq. 53, the dipole moment becomes

$$\hat{\mathbf{p}}_{\text{general}} = -\frac{\hat{\mathbf{I}}_0}{\mathbf{Y}_\infty r_{\text{i}}} \frac{\cosh(\mathbf{q}L - \mathbf{q}X) + (\mathbf{Y}_{\text{s}}/\mathbf{Y}_\infty)\sinh(\mathbf{q}X) + \cosh(\mathbf{q}X)}{(\mathbf{Y}_{\text{s}}/\mathbf{Y}_\infty)\cosh(\mathbf{q}L) + \sinh(\mathbf{q}L)} . \tag{54}$$

Similarly, by substituting for $\hat{\mathbf{V}}_0$ in Eq. 43 and using the result in Eq. 53 the somatic current becomes

$$\begin{aligned} \hat{\mathbf{I}}_{\text{s}} &= \frac{1}{\mathbf{Y}_{\text{in}}} \frac{\hat{\mathbf{I}}_0 \mathbf{Y}_{\text{s}}}{\cosh(\mathbf{q}L_{\text{p}}) + (\mathbf{Y}_{\text{s}}/\mathbf{Y}_\infty)\sinh(\mathbf{q}L_{\text{p}})} \\ &= \frac{(\mathbf{Y}_{\text{s}}/\mathbf{Y}_\infty)\cosh(\mathbf{q}L - \mathbf{q}X)}{(\mathbf{Y}_{\text{s}}/\mathbf{Y}_\infty)\cosh(\mathbf{q}L) + \sinh(\mathbf{q}L)} \hat{\mathbf{I}}_0 . \end{aligned} \tag{55}$$

Appendix B. Ball and stick with uniform input

The PSD for the soma current, dipole moment and the soma potential is given by

$$PSD(\omega) = v(\omega) \left[\rho(1 - c(\omega)) \int_0^l |\mathbf{T}(x,\omega)|^2 \mathrm{d}x + \rho^2 c \left| \int_0^l \mathbf{T}(x,\omega) \mathrm{d}x \right|^2 \right] , \tag{56}$$

where $\mathbf{T}$ is a transfer function from an input current at an arbitrary position x to either soma current, dipole moment or soma potential. The transfer function for the soma current is, from Eq. 4, given by

$$\mathbf{T}_I = \frac{(\mathbf{Y}_{\text{s}}/\mathbf{Y}_\infty)\cosh(\mathbf{q}L - \mathbf{q}X)}{(\mathbf{Y}_{\text{s}}/\mathbf{Y}_\infty)\cosh(\mathbf{q}L) + \sinh(\mathbf{q}L)} , \tag{57}$$

and the transfer functions for the soma potential is simply $\mathbf{T}_V = \mathbf{T}_I/\mathbf{Y}_{\text{s}}$. The transfer function for the dipole moment is from Eq. 7

$$\mathbf{T}_p = -\frac{1}{\mathbf{Y}_\infty r_{\text{i}}} \frac{-\cosh(\mathbf{q}L - \mathbf{q}X) + (\mathbf{Y}_{\text{s}}/\mathbf{Y}_\infty)\sinh(\mathbf{q}X) + \cosh(\mathbf{q}X)}{(\mathbf{Y}_{\text{s}}/\mathbf{Y}_\infty)\cosh(\mathbf{q}L) + \sinh(\mathbf{q}L)} . \tag{58}$$

The PSDs of the soma current with *uncorrelated* white noise input only ($c = 0$) is denoted PSD_1 and is then given by $PSD_1 = A_1|\mathbf{q}||\mathrm{csch}(\mathbf{q}L)|^2 \int_0^l |\cosh(\mathbf{q}L - \mathbf{q}X)|^2 \mathrm{d}x/D_1 = A_1 N_1/D_1$, where A_1 is found in Table 1 and D_1 is defined in Eq. 20. Similarly, the soma current with *correlated* white noise input only ($c = 1$) is given by PSD_2, the dipole moment with *uncorrelated* white noise input only is given by PSD_3, the dipole moment with *correlated* white noise input only is given by PSD_4, the soma potential with *uncorrelated* white noise input only is given by PSD_5 and the soma potential with *correlated* white noise input only is given by PSD_6, all defined according to Eq. 11 as $PSD_n = A_n N_n / D_n$. The amplitudes A_n and denominators D_n are defined in Table 1 and by Eq. 20, respectively, and the expressions for the numerators N_n are then

$$N_n = \begin{cases} |\mathbf{q}||\mathrm{csch}(\mathbf{q}L)|^2 \int_0^l |\cosh(\mathbf{q}L - \mathbf{q}X)|^2 \mathrm{d}x, & \text{for } n = \{1,5\} \\ |\mathbf{q}\mathrm{csch}(\mathbf{q}L) \int_0^l \cosh(\mathbf{q}L - \mathbf{q}X)\mathrm{d}x|^2, & \text{for } n = \{2,6\} \\ (|\mathrm{csch}(\mathbf{q}L)|^2/|\mathbf{q}|) \int_0^l |\cosh(\mathbf{q}L - \mathbf{q}X) - \mathbf{q}B\sinh(\mathbf{q}X) - \cosh(\mathbf{q}X)|^2 \mathrm{d}x, & \text{for } n = 3 \\ |\mathrm{csch}(\mathbf{q}L) \int_0^l \cosh(\mathbf{q}L - \mathbf{q}X) - \mathbf{q}B\sinh(\mathbf{q}X) - \cosh(\mathbf{q}X)\mathrm{d}x|^2, & \text{for } n = 4 \ , \end{cases} \tag{59}$$

where $\mathrm{csch}(\mathbf{q}L) = 1/\sinh(\mathbf{q}L)$. To manipulate the expressions and solve the integrals in Eq. 59 we have used following algebraic relations

$$\cosh(\mathbf{q}L - \mathbf{q}X) = \cosh(\mathbf{q}L)\cosh(\mathbf{q}X) - \sinh(\mathbf{q}L)\sinh(\mathbf{q}X) \ , \tag{60}$$

$$|\cosh(\mathbf{q}X)|^2 = [\cosh(2\mathrm{Re}\{\mathbf{q}\}X) + \cos(2\mathrm{Im}\{\mathbf{q}\}X)]/2 \ , \tag{61}$$

$$|\sinh(\mathbf{q}X)|^2 = [\cosh(2\mathrm{Re}\{\mathbf{q}\}X) - \cos(2\mathrm{Im}\{\mathbf{q}\}X)]/2 \ , \tag{62}$$

$$\cosh(\mathbf{q}X)\sinh(\mathbf{q}^*X) = [\sinh(2\mathrm{Re}\{\mathbf{q}\}X) - j\sin(2\mathrm{Im}\{\mathbf{q}\}X)]/2 \ , \tag{63}$$

and the following integral solutions

$$\int_0^l \cosh(ax/\lambda)\mathrm{d}x = \lambda\sinh(al/\lambda)/a \ , \tag{64}$$

$$\int_0^l \sinh(ax/\lambda)\mathrm{d}x = \lambda[\cosh(al/\lambda) - 1]/a \ , \tag{65}$$

$$\int_0^l \cos(ax/\lambda)\mathrm{d}x = \lambda\sin(al/\lambda)/a \ , \tag{66}$$

$$\int_0^l \sin(ax/\lambda)\mathrm{d}x = \lambda[1 - \cos(al/\lambda)]/a \ , \tag{67}$$

where a is a constant. In addition, Mathematica [10] was used as a guide when computing the long algebraic expression N_3. The full solutions of N_n are given in Eq. 12.

Appendix C. Power-law approximations

From Eq. 14 the denominators, D_n, can be written

$$D_n = |\mathbf{q}|^{n-2}(|\mathbf{q}|^2\coth(\mathbf{q}L)\coth(\mathbf{q}^*L) + [\mathbf{q}^*\coth(\mathbf{q}^*L) + \mathbf{q}\coth(\mathbf{q}L)]/B + 1/B^2) \ . \tag{68}$$

To arrive at approximate power laws for the other terms of Eq. 68 the following relations were used:

$$\tanh(x+y) = \frac{\tanh x + \tanh y}{1 + \tanh x \tanh y} \ , \tag{69}$$

and

$$\tanh(jx) = j\tan x \ , \tag{70}$$

which gives

$$\coth(\mathbf{q}L) = \frac{1 + j\tanh(\mathrm{Re}\{\mathbf{q}\}L)\tan(\mathrm{Im}\{\mathbf{q}\}L)}{\tanh(\mathrm{Re}\{\mathbf{q}\}L) + j\tan(\mathrm{Im}\{\mathbf{q}\}L)} \ . \tag{71}$$

By using the identity

$$\frac{1 + \tanh(\mathrm{Re}\{\mathbf{q}\}L)^2\tan(\mathrm{Im}\{\mathbf{q}\}L)^2}{\tanh(\mathrm{Re}\{\mathbf{q}\}L)^2 + \tan(\mathrm{Im}\{\mathbf{q}\}L)^2} = \frac{2\cos(2\mathrm{Im}\{\mathbf{q}\}L)}{\cosh(2\mathrm{Re}\{\mathbf{q}\}L) - \cos(2\mathrm{Im}\{\mathbf{q}\}L)} + 1 \ , \tag{72}$$

it can be shown that

$$\begin{aligned} D_2 = &-[(B^2(\mathrm{Re}\{\mathbf{q}\}^2 + \mathrm{Im}\{\mathbf{q}\}^2) - 1)\cos(2\mathrm{Im}\{\mathbf{q}\}L) \\ &+ (B^2(\mathrm{Re}\{\mathbf{q}\}^2 + \mathrm{Im}\{\mathbf{q}\}^2) + 1)\cosh(2\mathrm{Re}\{\mathbf{q}\}L) \\ &+ 2\mathrm{Re}\{\mathbf{q}\}B\sinh(2\mathrm{Re}\{\mathbf{q}\}L) + 2\mathrm{Im}\{\mathbf{q}\}B\sin(2\mathrm{Im}\{\mathbf{q}\}L)] \\ &/[B^2(\cos(2\mathrm{Im}\{\mathbf{q}\}L) - \cosh(2\mathrm{Re}\{\mathbf{q}\}L))] \ . \end{aligned} \tag{73}$$

By multiplying both the numerator and denominator by $1/\cosh(2\mathrm{Re}\{\mathbf{q}\}L)$, the terms in Eq. 73 will either contain $\tanh(2\mathrm{Re}\{\mathbf{q}\}L)$ or $1/\cosh(2\mathrm{Re}\{\mathbf{q}\}L)$. By using the approximations $\lim_{x\to\infty} \tanh(x) \to 1$ and $\lim_{x\to\infty} 1/\cosh(x) \to 0$, Eq. 73 approximates to

$$D_2 \approx (\mathrm{Re}\{\mathbf{q}\}^2 + \mathrm{Im}\{\mathbf{q}\}^2) + 2\mathrm{Re}\{\mathbf{q}\}/B + 1/B^2 \ , \tag{74}$$

and in general

$$D_n \approx |\mathbf{q}|^{n-2}(\mathrm{Re}\{\mathbf{q}\}^2 + \mathrm{Im}\{\mathbf{q}\}^2) + 2\mathrm{Re}\{\mathbf{q}\}/B + 1/B^2 \ , \tag{75}$$

when $\mathrm{Re}\{\mathbf{q}\}L$ is large. By similar eliminations of the hyperbolic functions it can be shown that the numerators are approximated to

$$N_n = \begin{cases} 2^{3/2}|\mathbf{q}|\mathrm{Im}\{\mathbf{q}\}j/(\mathbf{q}^2 - (\mathbf{q}^*)^2), & \text{for } n = \{1,5\} \\ 1, & \text{for } n = \{2,4,6\} \\ (\mathrm{Re}\{\mathbf{q}\}^2 + \mathrm{Im}\{\mathbf{q}\}^2 + 2\mathrm{Re}\{\mathbf{q}\}/B + 2/B^2)/(\sqrt{2}\mathrm{Re}\{\mathbf{q}\}|\mathbf{q}|), & \text{for } n = 3, \end{cases} \tag{76}$$

The frequency dependence is given by the complex quantity $\mathbf{q}$, which can be written (see Appendix C in [18] for a derivation of this)

$$\mathbf{q} = \sqrt{1 + j\omega\tau} = (1+\omega^2\tau^2)^{1/4}[\sqrt{1 + 1/\sqrt{1+\omega^2\tau^2}}/\sqrt{2} + j\sqrt{1 - 1/\sqrt{1+\omega^2\tau^2}}/\sqrt{2}] \ , \tag{77}$$

and Eqs. 75 and 76 can be expanded asymptoticly for high frequencies by Taylor expansions of the square roots. The four first terms of the expansions are shown in Eq. 19 and 20.

References

[1] Bak, Tang, and Wiesenfeld. Self-organized criticality: An explanation of the 1/f noise. *Phys Rev Lett*, 59(4):381–384, Jul 1987.

[2] H. Berger. Über das elektrenkephalogramm des menschen. *European Archives of Psychiatry and Clinical Neuroscience*, 87:527–570, 1929.

[3] Sami El Boustani, Olivier Marre, Sébastien Béhuret, Pierre Baudot, Pierre Yger, Thierry Bal, Alain Destexhe, and Yves Frégnac. Network-state modulation of power-law frequency-scaling in visual cortical neurons. *PLoS Comput Biol*, 5(9):e1000519, Sep 2009.

[4] György Buzsáki. *Rythms of the brain.* Oxford University Press, 2006.

[5] Claude Bédard and Alain Destexhe. A modified cable formalism for modeling neuronal membranes at high frequencies. *Biophys J*, 94(4):1133–1143, Feb 2008.

[6] N. T. Carnevale and M. L. Hines. *The NEURON Book.* Cambridge University Press, 2006.

[7] Kamran Diba, Henry A Lester, and Christof Koch. Intrinsic noise in cultured hippocampal neurons: experiment and modeling. *J Neurosci*, 24(43):9723–9733, Oct 2004.

[8] Walter J Freeman, Mark D Holmes, Brian C Burke, and Sampsa Vanhatalo. Spatial spectra of scalp eeg and emg from awake humans. *Clin Neurophysiol*, 114(6):1053–1068, Jun 2003.

[9] Michael L Hines, Andrew P Davison, and Eilif Muller. Neuron and python. *Front Neuroinformatics*, 3:1, 2009.

[10] Wolfram Research Inc. Mathematica version 7.0. *Champaign, Illinois*, 2008.

[11] Gilad A Jacobson, Kamran Diba, Anat Yaron-Jakoubovitch, Yasmin Oz, Christof Koch, Idan Segev, and Yosef Yarom. Subthreshold voltage noise of rat neocortical pyramidal neurones. *J Physiol*, 564(Pt 1):145–160, Apr 2005.

[12] Christof Koch. *Biophysics of Computation, Information Processing in Single Neurons.* Oxford University Press, 1999.

[13] Henrik Lindén, Klas H Pettersen, and Gaute T Einevoll. Intrinsic dendritic filtering gives low-pass power spectra of local field potentials. *J Comput Neurosci*, May 2010.

[14] Z. F. Mainen and T. J. Sejnowski. Influence of dendritic structure on firing pattern in model neocortical neurons. *Nature*, 382(6589):363–366, Jul 1996.

[15] B. B. Mandelbrot. *The Fractal Geometry of Nature.* New York: W. H. Freeman and Co., 1977.

[16] Shingo Murakami and Yoshio Okada. Contributions of principal neocortical neurons to magnetoencephalography and electroencephalography signals. *J Physiol*, 575(Pt 3):925–936, Sep 2006.

[17] Paul L. Nunez and Ramesh Srinivasan. *Electric fields of the brain.* Oxford University Press, Inc., 2nd ed. edition, 2006.

[18] Klas H Pettersen and Gaute T Einevoll. Amplitude variability and extracellular low-pass filtering of neuronal spikes. *Biophys J*, 94(3):784–802, Feb 2008.

[19] Wilfrid Rall and Hagai Agmon-Snir. *In Methods in Neural Modeling: From Ions to Networks, second edition.* Christoph Koch and Idan Segev (editiors), MIT Press, 1998.

[20] Michael Rudolph, Joe Guillaume Pelletier, Denis Paré, and Alain Destexhe. Characterization of synaptic conductances and integrative properties during electrically induced eeg-activated states in neocortical neurons in vivo. *J Neurophysiol*, 94(4):2805–2821, Oct 2005.

[21] Anat Yaron-Jakoubovitch, Gilad A Jacobson, Christof Koch, Idan Segev, and Yosef Yarom. A paradoxical isopotentiality: a spatially uniform noise spectrum in neocortical pyramidal cells. *Front Cell Neurosci*, 2:3, 2008.

3.4 Paper IV

How local is the local field potential?

Henrik Lindén[1], Tom Tetzlaff[1], Tobias C. Potjans[2,3], Klas H. Pettersen[1],
Sonja Grün[4], Markus Diesmann[3,4], Gaute T. Einevoll[1]

[1] Dept. of Mathematical Sciences and Technology,
Norwegian University of Life Sciences,
Ås, Norway

[2] Institute of Neuroscience and Medicine,
Computational and Systems Neuroscience (INM-6),
Research Center Jülich,
Jülich, Germany

[3] Brain and Neural Systems Team,
RIKEN Computational Science Research Program,
Wako, Japan

[4] RIKEN Brain Science Institute
Wako, Japan

Abstract

The local field potential (LFP) reflects activity of many neurons in the vicinity of the recording electrode and is therefore useful for studying local network dynamics. Much of the nature of the LFP is however still unknown. There are, for instance, contradicting reports on how large the region generating the LFP signal is. Here, we use a modeling approach to investigate the size of the contributing region by simulating the LFP as a summed signal from a large number of neurons. We found that the size of the region contributing to the measured LFP depends on the neuron morphology, the synapse distribution and the correlation in synaptic activity. For uncorrelated activity, the LFP represents cells in a small region (within a radius of a few hundred micrometers). If the synaptic input between different cells is correlated, the size of the contributing region is determined by the spatial extent of the correlated activity.

Introduction

The local field potential (LFP) usually refers to the low-frequency part (<200-500 Hz) of an extracellular voltage signal recorded inside the brain and has been widely used to investigate cortical mechanisms involved in sensory processing (Henrie and Shapley, 2005; Belitski et al., 2008), motor planning (Scherberger et al., 2005; Roux et al., 2006), and higher cognitive processes including attention, memory and perception (Kreiman et al., 2006; Liu and Newsome, 2006; Pesaran et al., 2002; Womelsdorf et al., 2006). In combination with multi-unit activity (MUA), the high-frequency (>500 Hz) part of the extracellular voltage, it has been found useful for inferring properties of network dynamics (Denker et al., 2010; Kelly et al., 2010) and population-specific laminar activity (Einevoll et al., 2007). In addition, the LFP has been suggested as a candidate signal for steering motor prosthetic devices (Andersen et al., 2004; Mehring et al., 2003; Rickert et al., 2005) as it is relatively easy to record and more stable than single-unit activity.

Despite its wide use, there is still only limited knowledge about the relation between the LFP and the underlying neural activity. The LFP is believed to primarily reflect synaptic activity in a neural ensemble in the vicinity of the recording electrode (Mitzdorf, 1985) and to represent a weighted sum of all transmembrane currents following synaptic activation. The details of the extracelullar field from a single synapse depend on cell morphology as well as the relative spatial positions of the synapse and recording electrode (Lindén et al., 2010). The LFP most likely reflects the activity of several populations of different cell types, but due to their so-called "open-field" arrangement dendritic synapses on pyramidal cells have been hypothesized to be a major contributor to the LFP signal (Johnston and Wu, 1995; Mitzdorf, 1985). The interpretation of the LFP is further complicated by the fact that, in contrast to the MUA which represents the spiking output of a local population, the LFP represents the combined input to the population which might originate both from local recurrent connections as well as other more distant brain regions.

One key question for the interpretation of the LFP is how large the cortical region is that generates the LFP, or in other words, the spatial "reach" of LFP recordings. Several recent experimental studies have addressed this question (Kreiman et al., 2006; Liu and Newsome, 2006; Berens et al., 2008a; Katzner et al., 2009; Xing et al., 2009) but have presented different results ranging from a few hundred micrometers (Katzner et al., 2009; Xing et al., 2009) to several millimeters (Kreiman et al., 2006). One possible reason for this descrepancy is that the neuronal LFP generators may differ across species, resulting in different measures of the LFP reach. Moreover, in experimental setups it is difficult to precisely control the neural activity, and different stimulation paradigms may activate different patterns of activity in different neuronal populations. It has been suggested that the LFP is dominated by synchronous dendritic input on pyramidal cells (Mitzdorf, 1985), but it has until now been unclear how the amount and spatial extent of correlations in synaptic activity influences the reach of the LFP.

We were interested in the biophysical principles determining how large the region is that an LFP electrode can "see" and to what extent the size of this region is dependent on neural activity. We used a biophysical forward-modeling approach to address these questions (Holt and Koch, 1999; Pettersen et al., 2008; Lindén et al., 2010) and simulated the LFP signal from synaptically activated populations of morphologically reconstructed cortical cells. We determined the region generating the LFP by increasing the population radius until the LFP amplitude no longer increased and defined this radius as the reach of the LFP. We investigated how the LFP reach depends on cell morphology, depth position of the recording electrode, synaptic distribution and level of correlation in synaptic activity. We found that the LFP from particular cell types and synaptic distributions depends strongly on the level of correlation in the synaptic input, both in terms of LFP amplitude as well as the size of the generating population. Moreover, the LFP is limited only by the spatial scale of the correlated activity, suggesting that the LFP reach could in some situations be substantially larger than recent experimental studies have shown (Katzner et al., 2009; Xing et al., 2009). These findings were supported by analytical results using a simplified model of LFP generation.

Results

We investigate the "reach" of an extracellular electrode by studying the amplitude σ of the measured compound potential $\phi(t)$ generated by a neuron population surrounding the electrode (see Methods). As with increasing population size (radius) R more and more cells contribute to the compound signal $\phi(t)$, the amplitude $\sigma(R)$ generally increases with R. On the other hand, the potential $\phi_i(t)$ generated by a single cell i decreases with its distance r from the electrode. Intuitively, one might therefore expect that $\sigma(R)$ saturates if the population radius approaches a certain horizon. Neurons beyond this horizon would not be visible for the electrode. This intuition, however, can be misleading. A priori, it is not clear that such a 'horizon' exists[1]. In the following section, we will therefore consider a simplified model to demonstrate which general system properties determine the reach for a population signal and to illustrate under which conditions the reach is finite. In the remainder of the paper, we will numerically study the system properties determining the reach in more detail for the case of a population of cortical neurons with realistic morphologies.

Existence of a finite reach

The amplitude σ of the compound signal $\phi(t)$ generated by a population of senders (neurons) surrounding the receiver (electrode) is essentially controlled by 3 factors:

- the attenuation $f(r)$ of the single-source signal with increasing distance r (Fig. 1B),
- the increase in the number $N(r)$ of sources with increasing population radius r (Fig. 1C),
- the correlation c_ϕ between the signals generated by individual sources.

The distance dependent attenuation $f(r)$ of the extracellular potential generated by a neuron is determined by the shape of the underlying current-source density (Lindén et al., 2010). The potential generated by a pure dipole source, for example, decreases in amplitude as $1/r^2$ with distance r at a fixed angle to the center of the dipole (in the far-field limit, i.e. for $r \gg$

---

[1] We are not referring to the limit imposed by the finite size of the brain here.

dipole length; blue curve in Fig. 1B). A hypothetical point source, in contrast, would generate a potential amplitude which decays as $1/r$ (red curve in Fig. 1B). The decrease in amplitude is competing with the increase in the number of neurons with increasing population radius r.

In this article, we consider a population of neurons symmetrically distributed around the electrode in a 2D plane with a homogeneous (constant) density ρ. The number $N(r) = 2\pi r\rho$ of cells at distance r (circumference, Fig. 1C) grows linearly with the population radius. If the single-cell potentials are uncorrelated, the variance σ_r^2 of the compound signal generated by all cells positioned on a ring of radius r is proportional to $N(r)f(r)^2$. This number decreases with distance for both monopole ($N(r)f(r)^2 = 1/r$) and dipole sources ($N(r)f(r)^2 = 1/r^3$). Integrating over all rings up to a radius R leads to a function $\sigma^2(R)$ which saturates with increasing R for a population of dipoles (solid blue curve in Fig. 1D). For a population of monopoles, however, $\sigma^2(R)$ grows unbounded (solid red curve in Fig. 1D). If the single-cell potentials are correlated, the total variance for neurons on a ring of radius r is given by $\sigma_r^2 = [N(r)f(r)]^2$. In this case, both the monopole and the dipole population lead to diverging compound amplitudes $\sigma(R)$ (dashed curves in Fig. 1D).

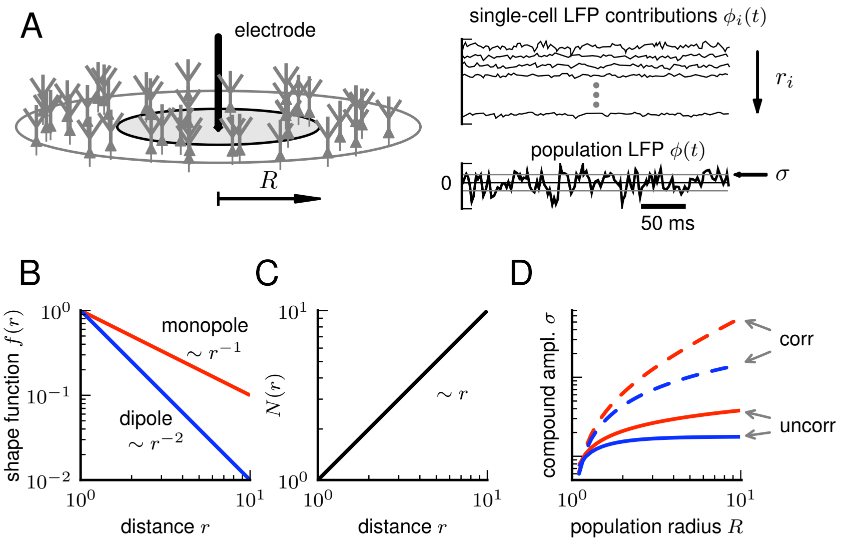

Figure 1. **The reach of LFP recordings** (**A**) Sketch of model setup. If cells are placed in a cylindrical volume V, how is the amplitude σ of the LFP signal expected to increase with the radius R of the cylinder? (**B**) Different neuronal current source density distributions give different distance dependence in the electric potential; monopoles (point sources) decrease as r^{-1} (red) whereas dipoles scale as r^{-2} (blue) as described by the shape function $f(r)$. (**C**) In a disk-like population the number of cells $N(r)$ at distance r increases approximately linearly with r. (**D**) Results from the simplified model; the amplitude σ of the compound LFP signal depends on the single-cell decay described by $f(r)$ and the level of correlation c_ϕ between single cell LFP contributions (c_ϕ=0 : solid lines, c_ϕ=1 : dashed lines).

In Methods, we derive a simplified model from biophysical principles to describe $\sigma(R)$ and its dependence on the shape of $f(r)$ and the correlation c_ϕ more rigorously. In this framework, the potential $\phi_i(t) = \xi_i(t)f(r_i)$ generated by a single neuron i factorises into a purely time-dependent part $\xi_i(t)$ reflecting the temporal structural of the total synaptic input and a purely distance dependent part, the shape function $f(\cdot)$, which is determined by the morphological and electrical properties of the neuron, its position and orientation with respect to the electrode tip and the distribution of synapses. The distance r_i denotes the radial distance of the cell soma from the electrode. Assuming a homogeneous population of neurons symmetrically surrounding the electrode tip, the variance $\sigma^2(R)$ of the compound

	$c_\phi = 0$	$c_\phi \neq 0$
$\gamma \leq 1$	diverging	diverging
$1 < \gamma \leq 2$	converging	diverging
$\gamma > 2$	converging	converging

Table 1. Convergence behaviour of the compound amplitude $\lim_{R\to\infty}\sigma(R)$ for a power-law shape function $f(r) \sim 1/r^\gamma$. Dependence on decay exponent γ and correlation c_ϕ.

signal $\phi(t) = \sum_{\{i|r_i \leq R\}} \phi_i(t)$ is found to be

$$\sigma^2(R) = (1 - c_\phi) g_0(R) + c_\phi g_1(R)\,. \tag{1}$$

Here, the two functions

$$g_0(R) := \int_0^R \mathrm{d}r\; N(r)\, f(r)^2 \quad \text{and} \quad g_1(R) := \left(\int_0^R \mathrm{d}r\; N(r)\, f(r) \right)^2 . \tag{2}$$

describe the competition between $f(r)$ and $N(r) = 2\pi r \rho$ for the uncorrelated and correlated case, respectively (see (18)). To illustrate that the convergence behaviour of $\sigma(R)$ is essentially determined by $f(r)$ and the correlation c_ϕ, we summarise the results for a power-law shape function $f(r) \sim 1/r^\gamma$ in Tab. 1 (see Methods, (21)). In the presence of correlations, $\sigma(R)$ approaches a finite value for increasing R only for decay exponents $\gamma > 2$.

Note that the contributions for uncorrelated and correlated input $g_0(R) \sim \rho$ and $g_1(R) \sim \rho^2$, respectively, are differently scaled by the neuron density ρ. For sufficiently high densities, the second term in (1) will dominate even for tiny correlations c_ϕ.

Distance dependence of single-cell contributions

To determine how the amplitude of a single cell LFP contribution varies with the cell's position within a population, we placed reconstructed morphologies of L3 pyramidal, L4 stellate and L5 pyramidal cells (Mainen and Sejnowski 1996) (Fig. 2A) at different radial distances r from a set of virtual recording electrodes (one in each cortical layer) and computed the mean LFP amplitude from 100 cells at each distance as the cells received synaptic input (see Methods). To resemble a scenario with a laminar cortical population all cells of a particular cell type were placed at the same cortical depth (according to cortical layer), but each cell was randomly rotated along its vertical axis. Synapses were randomly placed either homogeneously over the whole dendritic structure or only apically or basally (Fig. 2A). Each cell received 1000 stationary uncorrelated spike trains with an individual firing rate of 5 spikes/sec.

We found that for all combinations of cell type and recording position the amplitude of the LFP contribution from a cell placed sufficiently far away from the electrode decayed as $\sim 1/r^2$ with cell position r, with a less steep decay at the center of the population (Fig. 2B-D). The position where the transition to $1/r^2$-decay occured varied with recording position (Fig. 2D) as well as with the distribution of synapses over the dendrites (Fig. 2C). When we compared the three different cell types recorded in their respective cortical layer the differences were however rather small (Fig. 2B). The large variation with recording position for the L3 cell (Fig. 2D) can largely be attributed to the fact that cells at small radial distances, at the center of the population, are in fact relatively far from the electrode. As we will se next, this however has consequences for the size of the region of summation when recording the LFP from a laminar population above or below the active cortical layer.

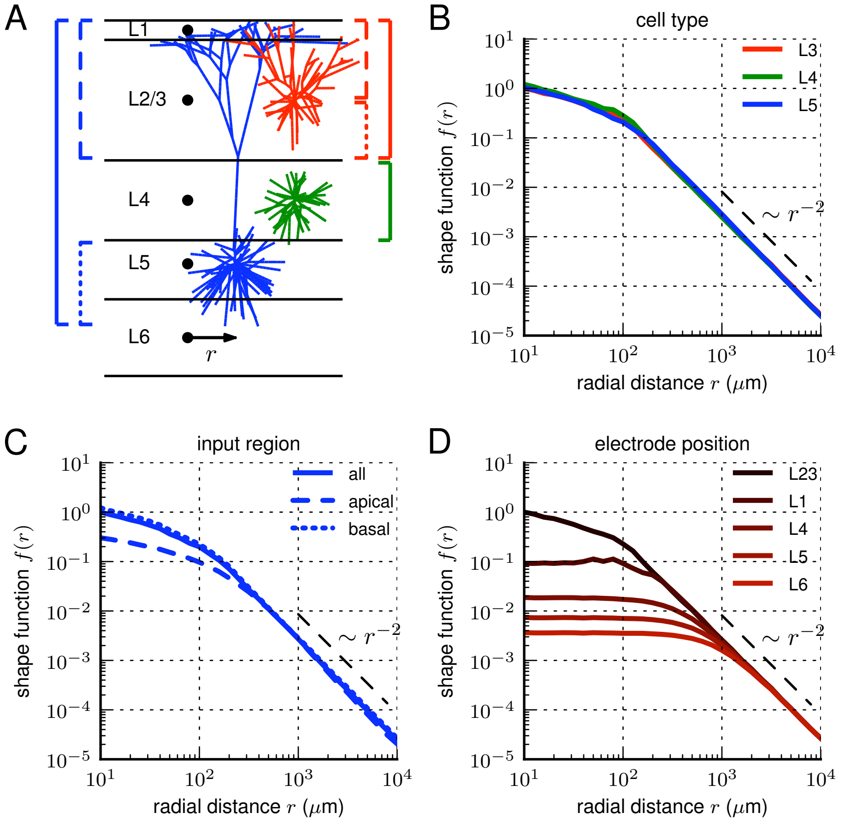

Figure 2. **Distance-dependence of amplitude of single cell LFP contributions**. (**A**) Reconstructed cell morphologies used in simulations: L3 pyramidal cell (red), L4 stellate cell (green) L5 pyramidal cell (blue) in relation to layer boundaries used for choosing electrode positions (black). Cells were placed at different radial positions r and the shape function $f(r)$ describing the amplitude of single cell LFP contributions was calculated for cells receiving either homogenous (solid), apical (dashed) or basal (dotted) synaptic input. (**B**) LFP amplitude for the three different cell types, recorded in the soma layer for each cell type. (**C**) LFP amplitude for L5 cell for different synapse distributions. (**D**) LFP amplitude at different recording depths for L3 cell with homogenous inputs. In B-D dashed lines indicate decay proportional to r^{-2}.

Dependence of LFP reach on cell morphology, synapse distribution and electrode depth

We next simulated laminar populations consisting of 10000 reconstructed cells placed in a cylindrical volume with a 1 mm radius (Fig. 1A) (see Methods). All cells in a population were positioned at the same cortical depth, with the depth position of the soma in the cortical layer corresponding to cell type (same as in Fig. 2, see Methods) but each cell was randomly rotated around its vertical axis. We first used uncorrelated spike trains as input and computed the amplitude σ of the LFP generated by cells positioned within a population radius R centered around a vertical recording electrode. Increasing the radius of the population quickly increased the LFP amplitude up to a constant value that did not change when the population radius was further increased. We defined the "reach" of the LFP as the population radius where the LFP amplitude had reached 95 % of the maximum value found for $R = R_{\text{max}}$ =1000 μm (Fig. 3A2). Plotting the reach as a function of depth position of the electrode revealed that the LFP reach was smallest in the soma layer of the corresponding population when synapses were homogeneously distributed over the dendrites, independent of cell type (Fig. 3C). For all three cell types 95% of the amplitude of the signal came from a region with a radius smaller than ∼200 μm when recording the population at the soma level. However, the soma layer

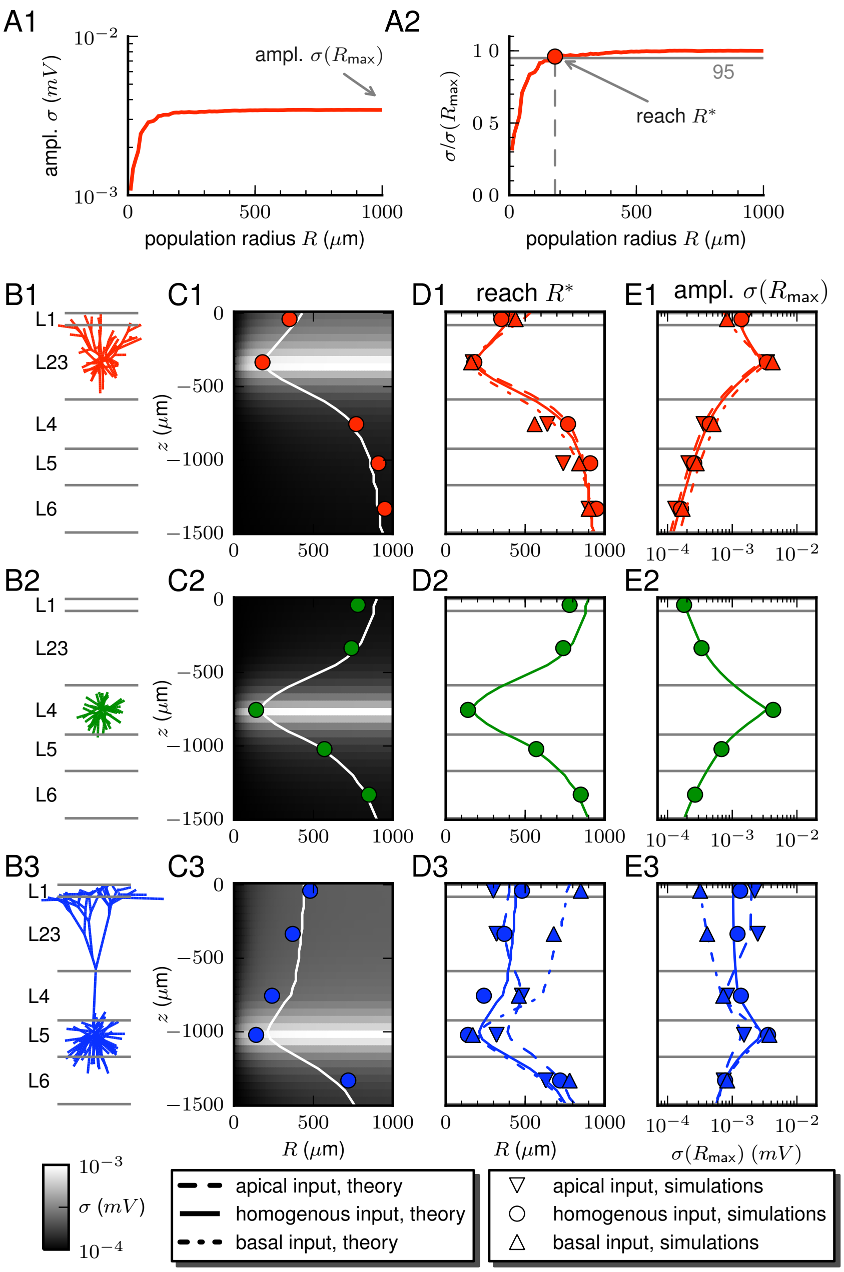

Figure 3. **Depth-dependence of the LFP reach for uncorrelated activity** (**A1**) LFP amplitude σ as a function of population radius R for a population of L3 cells receiving uncorrelated input. LFP was recorded at the soma level of L23. (**A2**) Normalized LFP amplitude for the same population as in (A1). LFP reach R^* was defined as the radius for which the LFP amplitude reaches 95% of the value for $R_{\max}$=1000 μm. (**B**) Cell morphologies and their vertical placement according to cortical layers. (**C**) LFP amplitude σ (gray scale: predictions from simplified model) and LFP reach (circles: simulations, white lines: simplified model) for uncorrelated homogenous synaptic input as a function of electrode depth z. (**D**) LFP reach R^* for different synaptic distributions. (**E**) LFP amplitude $\sigma(R_{\max})$ for different synaptic distributions. (symbols: simulation results, lines: simplified model)

was also the recording positions where the LFP amplitude was highest (Fig. 3E). When the synaptic activity was uncorrelated the LFP was thus rather local, both in terms of horizontal reach and amplitude in the vertical direction.

We next compared the numerical simulations with predictions of the simplified model; by using the detailed single-cell decay functions $f(r)$ obtained in previous section (Fig. 2) we numerically integrated the simplified model. The numerical population simulations and the simplified model with numerical estimates of single-cell decay gave very similar results. Changing the synaptic distributions to either only apical or basal dendrites gave a slightly different depth dependence for both the reach and amplitude of the LFP for the L5 population whereas the L3 population was largely unaffected (Fig. 3D-E).

Dependence on correlations in synaptic activity

How would these results change if the synaptic inputs to different cells in the population were correlated? We used the same simulation setup as in previous section with the difference that spike trains to different cells were drawn from the same pool of presynaptic spike trains (Fig. 4A). This induced a mean correlation c_ξ between the synaptic input currents to different cells due to common input. By varying the size of the pool of presynaptic spike trains n_{pool} we could vary the input correlations c_ξ (see Methods).

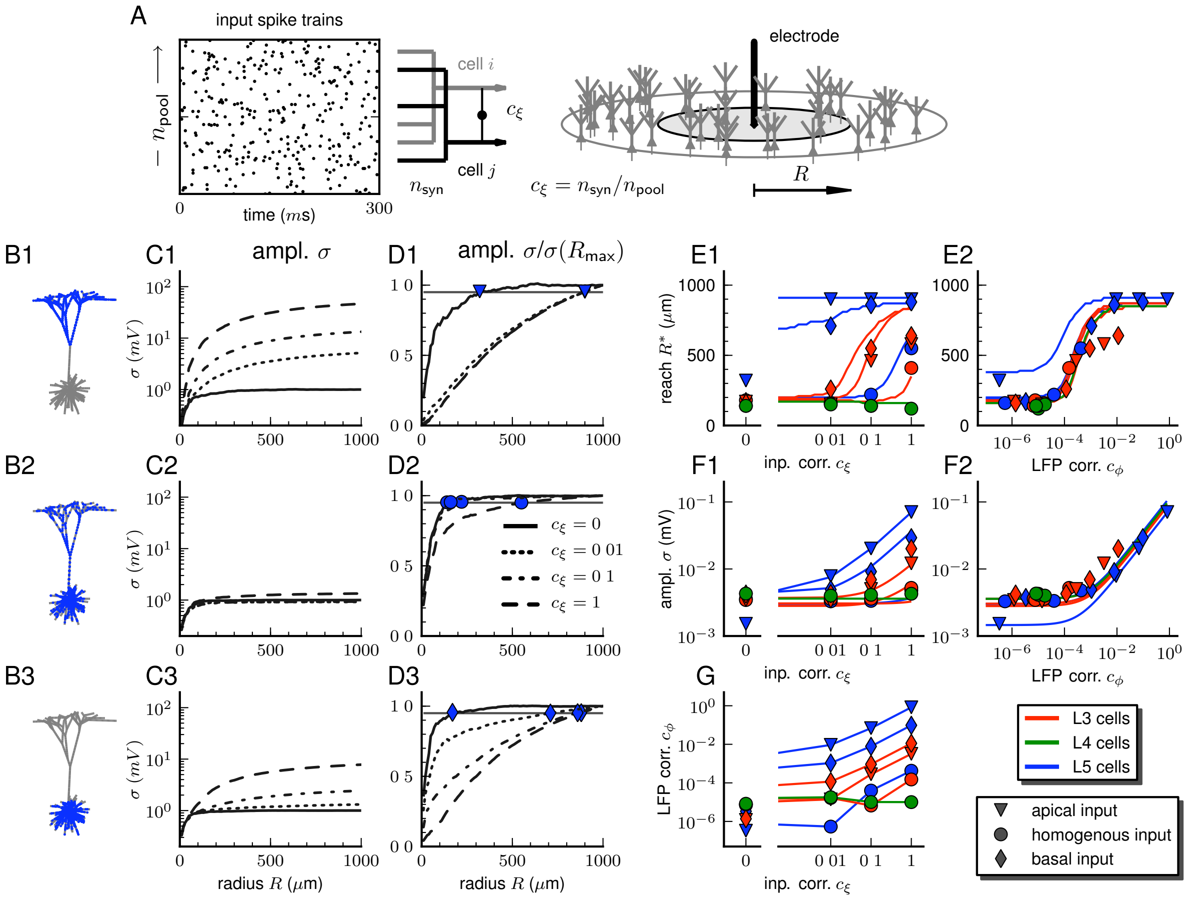

Figure 4. Reach of LFP depends on level of input correlations (**A**) Illustration of simulation setup. (**B-D**) LFP amplitude σ as a function of population radius R (C) and LFP reach R^* (D) for population of L5 pyramidal cells receiving synaptic input at apical dendrites (B1), homogenously distributed (B2) or at basal dendrites (B3) for LFP recorded at the soma level of the population. Reach R^* was defined as the radius R where the amplitude σ has reached 95% of the maximum value $\sigma(R_{\text{max}} = 1000\ \mu m)$. (**E-F**) LFP reach R^* and LFP amplitude $\sigma(R_{\text{max}} = 1000)\ \mu m)$ for different cell types and input scenarios, either as a function of input correlation c_ξ (E1,F1) or resulting mean pairwise correlation between single cell LFP contributions c_ϕ (E2,F2). (**G**) Relation between input correlation c_ξ and c_ϕ. In (E-G) lines represents results the from simplified model using numerically derived shape functions $f(r)$ and numerical values of correlation transfer (c_ξ to c_ϕ) and symbols represent simulation results.

As predicted by the simplified model, inducing correlations between single cell LFP contributions changed the total LFP amplitude in three respects: *1)* the LFP amplitude σ became higher (Fig. 4C,F1), *2)* the reach R^* of the LFP (as before defined as the population radius where the amplitude had reached 95% of the value for R=1000 μm) generally increased (Fig. 4D,E1), and *3)* the LFP amplitude σ no longer converged to a fixed constant value with increasing population radius. Performing population simulations for different cell types (L3 pyramid, L4 stellate and L5 pyramidal cells) and synaptic distributions (apical, homogeneous or basal) revealed that the extent to which correlations had an effect on the total LFP amplitude was highly dependent on cell type and spatial distribution of synapses on the dendritic structure. The effects were largest when the population consisted of L5 pyramidal cells whereas the LFP amplitude from L4 stellate cells was largely unaffected (Fig. 4E1,F1). However, it also depended on the distribution of synapses; there were pronounced effects for apical or basal input, but almost no effect for homogeneous synaptic distributions (Fig. 4E1,F1).

To explore these differences further we computed the mean pairwise correlation c_ϕ (see Methods, (26)) between single cell LFP contributions as a function of input correlation for the different cell types and input scenarios (Fig. 4G). This provided an explanation for why the effect of correlations was found to be so different for the different cell types and synaptic distributions; again the same trend was found: LFP contributions were more correlated for L5 pyramidal cells than the other cell types, and apical input gave higher correlations than basal or homogenous input. Thus, whether or not input correlations have an effect on the reach of LFP depends on how reliably the input correlations c_ξ are translated into correlations between LFP contributions c_ϕ. Again plotting the resulting LFP reach and amplitude, but now as function of the resulting LFP correlations, further emphasized this interpretation as all simulation results then falls on the same curve (Fig. 4E2,F2) demonstrating that the level of correlation between LFP contributions is the main determining factor for both the reach and amplitude of the LFP.

Spatial scale of correlations

Until now we have implicitly assumed that the synaptic input to different neurons are equally correlated througout the whole population, independent of the distance to the electrode. How would the results change if the level of correlation between LFP contributions were dependent on the radial distance to the electrode? We studied a simple case were LFP contributions were assumed to be homogeneously correlated only within a certain radius $R_c < R$ (Fig. 5A), outside this region the correlation was zero. We used the same simulation data as shown above but computed the LFP amplitude outside of the correlated region under the assumption of independence between LFP contributions (see Methods). Fig. 5B shows the LFP amplitude for a population of basally activated L5 pyramidal neurons for different values of R_c where input correlation $c+_\xi$ in the correlated region was set to 0.1. We found, for the chosen example values of R_c, that the LFP amplitude increased up to radius R_c and then quickly converged to a fixed value. This gave values of LFP reach (defined as before) slightly smaller than the values for R_c (Fig. 5C). Thus, neurons outside the region of correlated activity contribute only very little to the LFP amplitude, instead both the shape of LFP amplitude as a function of population radius and the reach of the LFP was largely determined by the spatial scale of the correlated activity. If other levels of input correlations were chosen, the LFP reach changed (Fig. 5D), due to the shape of the LFP amplitude as a function of population radius (compare Fig. 4D). Results also varied with synaptic distribution: as before the observed effects of correlations were large for apical and basal activation and almost negligible for homogeneous synaptic activation (Fig. 5E).

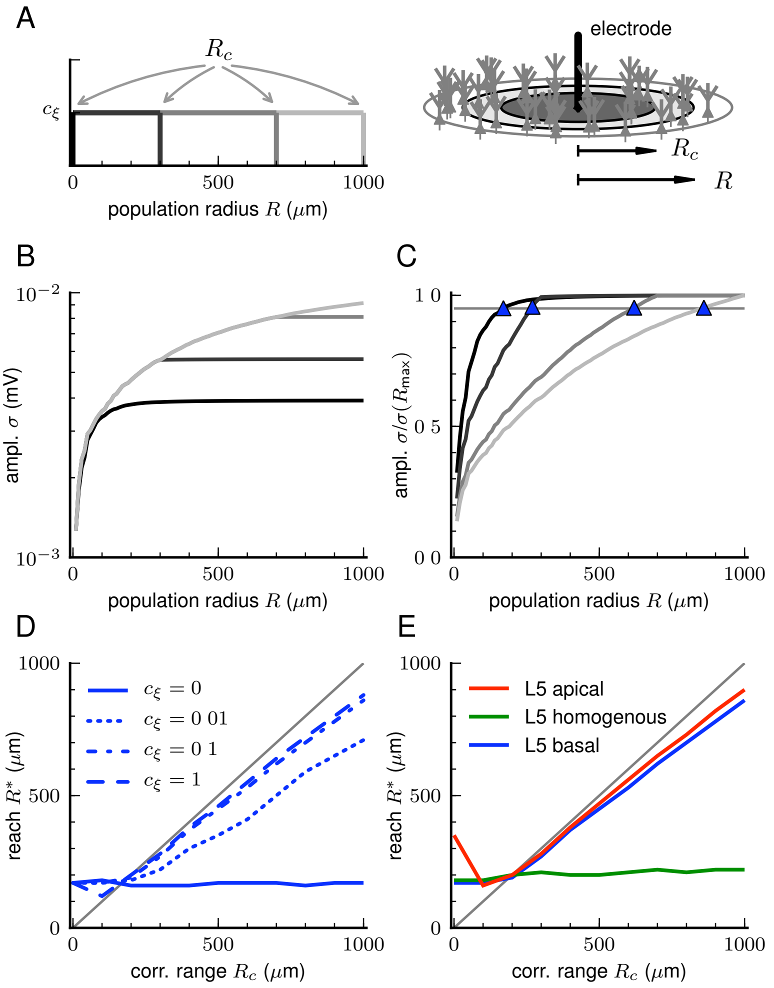

Figure 5. **Reach of LFP depends on spatial range of input correlations** (**A**) A situation was considered where the synaptic inputs to neurons within a radius R_c were uniformly correlated with correlation coefficients c_ξ and the inputs to neurons outside of this region were uncorrelated. (**B**) LFP amplitude σ for population of L5 cells with synapses distributed on basal dendrites for different values of R_c=[0,300,700,1000] μm (as indicated in A) while total population radius R was 1000 μm. Input correlation c_ξ was 0.1 (**C**) Same as in B but normalized to amplitude $\sigma(R_{\text{max}}$=1000 μm). Reach R^* was defined as the radius R where the amplitude σ had reached 95% of the maximum value $\sigma(R_{\text{max}}$=1000 μm) (blue triangles). (**D**) LFP reach for different values of c_ξ for population of L5 cells with basal activation. (**E**) LFP reach for different synaptic distributions when c_ξ=0.1 In (C-D) gray lines correspond to $R^* = R_c$.

Consistency with in vivo-like activity

Cortical populations *in vivo* receive a variety of inputs. These can be categorized as local inputs from the various cell types within the local cortical network and external long-range inputs from other cortical regions. The synaptic inputs to a single neuron are both excitatory and inhibitory, and may target different dendritic regions. Furthermore, spike trains from different neurons are potentially correlated, providing additional input correlation to that from shared input. We embedded the single-cell reconstructions in an *in vivo*-like environment to test if the range of input correlations c_ξ used so far were realistic, and if the results would pertain in situations where populations received a combination of excitatory, inhibitory and external (distant) inputs.

We developed a novel simulation framework to confirm that the obtained results generalize

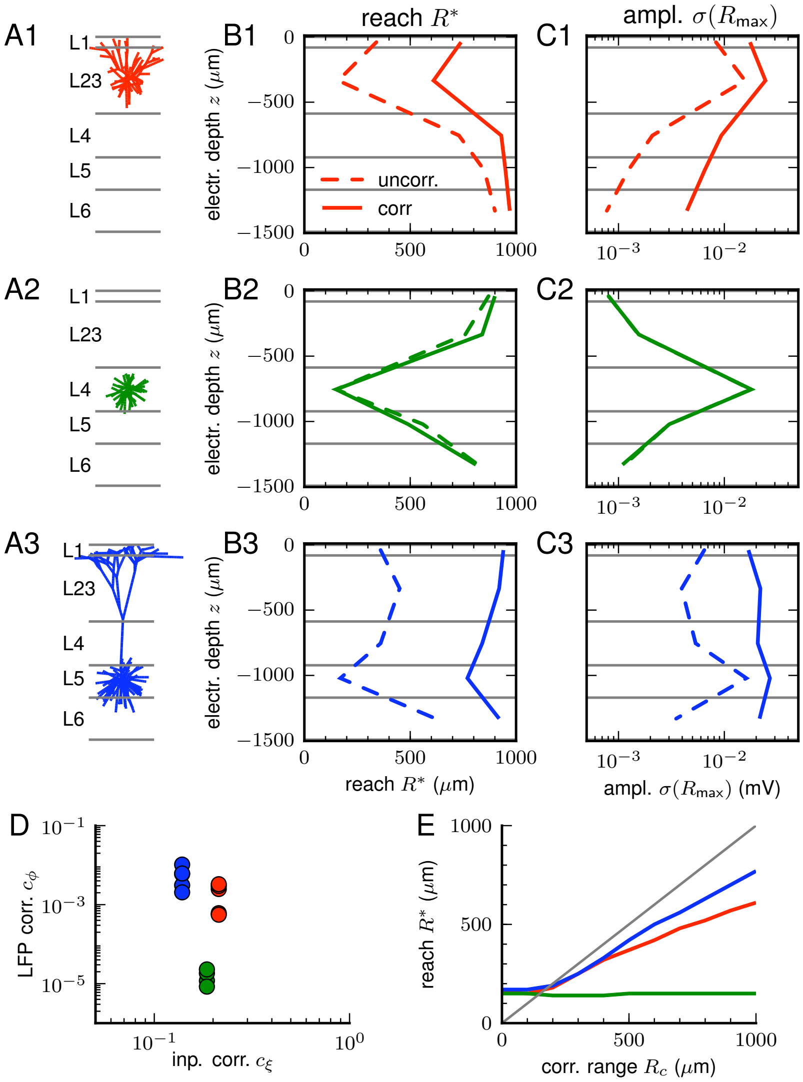

Figure 6. **Using spiking input from laminar network simulations** LFP from population simulations where input spike trains were generated by a laminar network of integrate-and-fire neurons. (**A**) Cell types of populations of L3 (A1), L4 (A2) and L5 (A3) cells. (**B**-**C**) Reach R^* and amplitude $\sigma(R_{\max}{=}1000\ \mu\text{m})$ of LFP as a function of electrode depth z for the three neuronal populations. Reach R^* was defined as the radius for which the LFP amplitude had reached 95% of the value of the amplitude $\sigma(R_{\max}{=}1000\ \mu\text{m})$. (**C**) LFP amplitude σ as function of population radius R at the soma level of each population. (**D**) Resulting correlation between single cell LFP contributions c_ϕ and input correlations c_ξ for the three different neuronal populations (indicated by colour). Different dots represent recording positions in the different cortical layers.

to a more realistic scenario: We simulated populations of reconstructed cells receiving spike trains generated by a laminar network of integrate-and-fire neurons representing a local cortical microcircuit (Potjans and Diesmann, 2008, 2010) (Fig. 6A). The network consisted of in total 80000 neurons divided into four layers, each with one excitatory and one inhibitory population. The number of neurons in each population was based on anatomical data from cat visual cortex. The size of the network was sufficiently large to incorporate the majority of local synapses. Most notably, the data based connectivity structure of the network (see Methods) resulted in cell-type specific firing rates consistent with *in vivo* data from rat cortex (e.g. de Kock and Sakmann (2009); Sakata and Harris (2009), equivalent activity data from cat cortex is to the best of our knowledge not available). In addition, we generated uncorrelated Poissonian spike trains representing background acitivity from distant cortical areas. The populations of reconstructed neurons received a selection of input spike trains from the laminar network and background activity based on the morphology and connectivity of each cell type. In this way, each cell in the population of reconstructed cells had on average the same number of incoming connections as a cell in the laminar network resulting in the same mean synaptic input (see Methods). Synapses were distributed differently onto the dendritic tree of the reconstructed cells depending on the origin of the presynaptic cell type (see Methods). This resulted in input correlations c_ξ and correlations between single cell LFP contributions c_ϕ, that were specific for each population.

This setup produced input correlations c_ξ between total input currents and LFP correlation c_ϕ comparable with previous simulations (compare Fig. 4G). We computed the LFP amplitude for three different populations consisting of L3, L4 or L5 cells (of the same types as before, Fig. 6B)) for different cortical depths. As seen also previously for the generic input scenarios and uncorrelated activity (Fig. 3), we found both the reach and amplitude to vary with cortical depth with a minimum reach R^*, but largest amplitude σ in the soma layer of each population. Further, we found that the level of input correlations provided by the stationary spiking activity of laminar network was sufficient to substantially increase both the reach and amplitude of the LFP for the L3 and L5 populations as compared to the situation where the LFP contributions from different cells would have been uncorrelated (Fig. 3C-D, dashed lines, by setting $R_c = 0$, see Methods (24)). The reach of the LFP from the L4 population was similar to the situation with uncorrelated synaptic input.

So far, we assumed that all cells throughout the whole population received the same input correlation. We next calculated the LFP reach assuming that only LFP contributions from cells within a radius of R_c were correlated and contributions from cells outside this region were uncorrelated (see Methods (24)). Also here we found that the LFP reach was largely determined by the spatial scale of correlated activity except for the L4 population for which the reach was largely unaffected by correlations (Fig. 6B2).

Discussion

We report results from a biophysically detailed model of LFP generation and provide a mathematical framework to interpret these results. We found that the size of the region that is generating the LFP is primarily determined by the spatial decay of single cell LFP contributions and by the amount and spatial extent of correlations in synaptic activity. While the spatial footprint of a single cell's LFP contribution is more or less fixed and independent of cell type, the reach of the population LFP is not fixed as it depends on whether LFP contributions from different cells add up constructively or cancel out. How well synaptic input correlations are translated into correlations between LFP contributions of different cells depends however on the morphology of the neurons in the population; asymmetric inputs onto L5 cells gave strongly correlated LFP contributions while the contributions from more symmetric L4 stellate cells were uncorrelated, independent of correlations in the synaptic input.

Our model suggests several possible explanations of the discrepancy between previously reported experimental results regarding the reach of the LFP (Berens et al., 2008a; Katzner et al., 2009; Kreiman et al., 2006; Liu and Newsome, 2006; Xing et al., 2009). First, these experimental studies were done using different stimulation paradigms that may induce very different patterns of neural activity. For instance, when using visual gratings Nauhaus et al. (2009) reported that high contrast stimuli results in more local activity than for low contrast stimuli. Our results indicate that the size of contributing region is highly dependent on the spatial scale of correlated synaptic activity. Therefore, if the synaptic activity patterns activated in the different stimulation paradigms have different spatial extent, our model reconciles these differing results.

Second, the above experimental studies were based on recordings in different species (cat, monkey) in different cortical areas (V1, MT, IT) where different neural populations may dominate the LFP signal. According to our model, that may also influence the LFP reach, as the cell type and synaptic distributions determines to which degree correlations in synaptic activity translates into correlations between LFP sources from different cells.

Third, depending on in which cortical layer the dominating neuronal populations are located, the LFP reach may differ for LFP recordings in different cortical layers. We found that the radius of the generating neuronal population is smallest the soma layer of the active cortical population. This is consistent with the findings by Xing et al. (2009) who found the spatial spread to be smallest in layer 4, if one assumes that this is were the visual input evokes the largest response.

When the electrode was placed below the generating population, as for recordings in L6 of an active L23 population, the reach was found to be substantially larger than for recordings in L23, but the amplitude was reduced. When the electrode was placed in a layer where a cell from a different layer has substantial dendritic processes (e.g. recordings in L23 of an active L5 population), the reach and the amplitude were comparable to the cortical layer of the active population. Therefore, we conclude that in an experimental setting, where the LFP consists of contributions from several populations, the recorded signal can be expected to be dominated by populations that have substantial dendritic processes in the recording layer. Future work is required to understand how the contributions from different cell types shape the laminar-specific LFP.

It has been established that tuning properties in the LFP in V1 is stronger at or above gamma frequencies (Liu and Newsome, 2006; Berens et al., 2008b) and as a possible explanation for this has been suggested that the contributing region to the LFP is larger for lower frequencies than for high frequencies due to capacative filtering in the extracellular medium (Bédard et al., 2004). This view is however problematic in light of a recent experimental study by Logothetis et al. (2007) who concluded that the extracellular medium has negligble capacative properties for biologically relevant frequencies. In the present study we modeled the extracellular medium as being purely resistive and did not perform any frequency-resolved analysis. It should be noted however that the mathematical framework presented here could alternatively be formulated for specific frequency components separately and thereby be extended to the case of a capacitive medium. Also in a purely resistive medium, there could be differences in the spatial footprint of different frequency components and in the coherence between LFP contributions in different frequency bands. In a recent study (Lindén et al., 2010) we found a substantial frequency filtering in the LFP due to dendritic filtering in the neuron. We found the frequency-dependence of the current dipole moment (Pettersen and Einevoll, 2008) to be a useful concept to qualitatively explain both this frequency filtering and spatial dependence of single cell LFP contributions. To understand how these frequency dependences influence the LFP reach of different frequency components is a topic that requires further investigation.

Simultaneously recorded LFP signals at different sites have been found to be highly correlated up to several millimeters apart with a spatial fall-off that depends on cortical state (Destexhe et al., 1999; Nauhaus et al., 2009). How should these correlations between LFP signals be interpreted? Does correlation betwen the recorded LFP signals imply an overlap in the LFP generating regions or does it reflect correlations in the neural activity at the recording sites? Even though we did not specifically model this scenario our results provides some hints towards an answer: we have shown that in the presence of correlations the LFP reach can be as large as the spatial scale of the correlated activity. Therefore, if two nearby LFP signals are correlated it is likely an indication that there is partial overlap between the regions generating the two signals. It should be added however that this depends on the cell type of the dominating neural populations; if the two signals stem mainly from symmetric cells, like the L4 stellate cells studied here, and the electrodes are placed more than a couple of hundreds of micrometers apart, the generating region of each signal is rather local but may be part of a larger region of correlated activity.

Methods

Simplified model

Single-source potential

Consider a population of N neurons $i = 1, \ldots, N$ within a cortical volume $\mathcal{V}$. Neuron i receives M_i inputs through its synapses $\{ij\}$ ($j = 1, \ldots, M_i$). A synaptic input current $\xi_{ij}(t)$ at synapse $\{ij\}$ causes a current-source density $\mathsf{csd}_{ij}(t, \vec{r})$ which, in turn, gives rise to an extracellular electrical potential $\phi_{ij}(t)$ measured by an electrode at position $\vec{r} = 0$. In a purely resistive medium with homogeneous conductivity κ, $\phi_{ij}(t)$ is –in the quasistatic approximation– given by (Nicholson and Freeman, 1975; Nunez, 2006)

$$\phi_{ij}(t) = (4\pi\kappa)^{-1} \iiint \mathrm{d}\vec{r}\, \frac{\mathsf{csd}_{ij}(t, \vec{r})}{|\vec{r}|}\,. \tag{3}$$

For linear synapses and dendrites, the time-dependence of $\mathsf{csd}_{ij}(t, \vec{r})$ can be described by a linear convolution[2]

$$\mathsf{csd}_{ij}(t, \vec{r}) = (\xi_{ij} * h_{ij}(\cdot, \vec{r}))(t) \tag{5}$$

between the synaptic input current $\xi_{ij}(t)$ and a current-source impulse response $h_{ij}(t, \vec{r})$ which is determined by the synapse position $\vec{r}_{ij}$ and the morphology and electrical properties of the postsynaptic cell i. In general, the Fourier transform $H_{ij}(\vec{r}, \omega) = \mathfrak{F}_t \left[h_{ij}(\vec{r}, t)\right](\omega)$ of the kernel $h_{ij}(\vec{r}, t)$ exhibits low-pass characteristics (Lindén et al., 2010). For the sake of simplicity, we will ignore its frequency dependence here and assume

$$h_{ij}(t, \vec{r}) = h_{ij}(\vec{r})\delta(t)\,. \tag{6}$$

The results obtained in this subsection can however easily be generalised to frequency-dependent filters $H_{ij}(\vec{r}, \omega)$ (not shown here). Under the assumption (6), the potential

$$\phi_{ij}(t) = f_{ij}\xi_{ij}(t) \tag{7}$$

decomposes into a time dependent part $\xi_{ij}(t)$ reflecting the temporal structure of the synaptic input and a time-independent shape factor

$$f_{ij} := (4\pi\kappa)^{-1} \iiint \mathrm{d}\vec{r}\, \frac{h_{ij}(\vec{r})}{|\vec{r}|} \tag{8}$$

describing the dependence of the potential on the position of synapse j, the morphological and electrical properties of neuron i, as well as its position and orientation with respect to the electrode tip.

Single-cell potential (mean-field model)

Due to the linearity of Maxwell's equations, the extracellular potential $\phi_i(t)$ generated by neuron i is the linear superposition

$$\phi_i(t) = \sum_{j=1}^{M_i} \phi_{ij}(t) = \sum_{j=1}^{M_i} \xi_{ij}(t) f_{ij} = M_i \mathsf{E}_j \left[\xi_{ij}(t) f_{ij}\right] \tag{9}$$

---

[2] The "$*$" operator denotes the convolution integral

$$(g * h)(t) := \int_{-\infty}^{t} \mathrm{d}s\; g(s)h(t-s)\,. \tag{4}$$

of the potentials $\phi_{ij}(t)$ caused by its inputs at the synapses $j = 1, \ldots, M_i$. The expectation operator $\mathsf{E}_j[\cdot]$ in (9) corresponds to the average across the ensemble of synapses. For a homogeneous synapse ensemble, i.e. if the synaptic inputs $\xi_{ij}(t)$ are independent of the shape factors f_{ij}, the expectation

$$\mathsf{E}_j[\xi_{ij}(t)f_{ij}] \approx \mathsf{E}_j[\xi_{ij}(t)]\,\mathsf{E}_j[f_{ij}] \tag{10}$$

factorises approximately and (9) can be written as

$$\phi_i(t) = \xi_i(t)f_i \tag{11}$$

(mean-field approximation). Here, $\xi_i(t) = M_i\mathsf{E}_j[\xi_{ij}(t)]$ denotes the total input to neuron i and $f_i = \mathsf{E}_j[f_{ij}]$ the ensemble-averaged shape factor.

For a heterogeneous ensemble of synapses, the above assumption (10) can, in general, not be justified. If, for example, different types of synapses (e.g. excitatory and inhibitory) systematically target different regions of the postsynaptic cell (e.g. distal or proximal dendrites), the synaptic input is not independent of the corresponding shape factor f_{ij}. In the present study, we investigate only homogeneous synapse ensembles (excitatory synapses with identical synaptic weights), such that (10) serves as a good approximation. For a more general description, one could split the sum in (9) into different contributions corresponding to different synapse types, and apply the mean-field approximation (10) to each of these contributions separately.

Distance dependence of the single-cell potential

The average shape factor f_i is determined by the morphology of the postsynaptic neuron i, the spatial distribution of the synapses across this neuron and the position and orientation of the cell relative to the electrode tip. For a homogeneous population of cells with identical morphologies and synapse distributions, f_i can be uniquely described by a function $f(\vec{r}_i)$ of the (soma) position $\vec{r}_i = (x_i, y_i, z_i)^\mathsf{T}$ of neuron i. In the present study, we investigate the extracellular potential generated by a population of cells homogeneously distributed around the electrode tip on a circular plane parallel to the cortex surface. As all cells have identical vertical positions $z = z_i$ $(\forall i)$, we consider only the horizontal distance $r_i = \sqrt{x_i^2 + y_i^2}$ of the soma of neuron i from the electrode at position $\vec{r} = 0$, i.e. $f_i = f(r_i)$. The dependence of f_i on the vertical position z of the cell is captured by the shape of $f(r_i)$.

Given the above assumptions, the single-cell potential reads

$$\phi_i(t) = \xi_i(t)f(r_i)\,. \tag{12}$$

In this framework, its time dependence is determined by the total synaptic input $\xi_i(t)$ alone. The shape function $f(r_i)$ describes the attenuation of the potential with increasing horizontal distance r_i between the cell body and the electrode tip. In the present study, $f(r_i)$ is obtained by single-cell simulations for different neuron morphologies (layer 2/3, 4, 5), input distributions (homogeneous, basal, apical) and electrode depths (vertical neuron positions).

Power of the compound potential

Let us now consider the compound signal, i.e. the sum

$$\phi(t) = \sum_{\{i|\vec{r}_i \in \mathcal{V}\}} \phi_i(t) = \sum_{\{i|\vec{r}_i \in \mathcal{V}\}} \xi_i(t)f(r_i) \tag{13}$$

of the potentials $\phi_i(t)$ generated by a population of neurons $\{i|\vec{r}_i \in \mathcal{V}\}$ within a certain volume $\mathcal{V}$. For simplicity, we assume homogeneity of the input statistics such that all input variances and correlations are identical:

$$\begin{aligned} \sigma_\xi^2 &:= \mathsf{E}_t\left[\xi_i(t)^2\right] \quad \forall i \quad \text{(input variance)} \\ c_\xi &:= \frac{\mathsf{E}_t\left[\xi_i(t)\xi_j(t)\right]}{\sigma_\xi^2} \quad \forall i \neq j \quad \text{(input correlation coefficient)}\,. \end{aligned} \tag{14}$$

Here, we assume–without loss of generality–that the synaptic inputs $\xi_i(t)$ have zero mean, $\mathsf{E}_t\left[\xi_i(t)\right] = 0$ ($\mathsf{E}_t\left[\cdot\right]$ denotes the time average). With the homogeneity assumption (14), the variance

$$\begin{aligned} \sigma^2 = \mathsf{E}_t\left[\phi(t)^2\right] &= \sum_{\{i|\vec{r}_i\in\mathcal{V}\}} \mathsf{E}_t\left[\phi_i(t)^2\right] + \sum_{\{i|\vec{r}_i\in\mathcal{V}\}}\ \sum_{\{j\neq i|\vec{r}_j\in\mathcal{V}\}} \mathsf{E}_t\left[\phi_i(t)\phi_j(t)\right] \\ &= \sum_{\{i|\vec{r}_i\in\mathcal{V}\}} \mathsf{E}_t\left[\xi_i(t)^2\right] f(r_i)^2 + \sum_{\{i|\vec{r}_i\in\mathcal{V}\}}\ \sum_{\{j\neq i|\vec{r}_j\in\mathcal{V}\}} \mathsf{E}_t\left[\xi_i(t)\xi_j(t)\right] f(r_i)f(r_j) \\ &= \sigma_\xi^2\left[\sum_{\{i|\vec{r}_i\in\mathcal{V}\}} f(r_i)^2 + c_\xi \sum_{\{i|\vec{r}_i\in\mathcal{V}\}}\ \sum_{\{j\neq i|\vec{r}_j\in\mathcal{V}\}} f(r_i)f(r_j)\right] \\ &= \sigma_\xi^2\left[(1-c_\xi)\sum_{\{i|\vec{r}_i\in\mathcal{V}\}} f(r_i)^2 + c_\xi\left(\sum_{\{i|\vec{r}_i\in\mathcal{V}\}} f(r_i)\right)^2\right] \\ &= \sigma_\xi^2\left[(1-c_\xi)g_0 + c_\xi g_1\right] \end{aligned} \tag{15}$$

of the compound potential $\phi(t)$ is a superposition of two terms $(1-c_\xi)g_0$ and $c_\xi g_1$ corresponding to uncorrelated ($c_\xi = 0$) and correlated input ($c_\xi = 1$), respectively. The two coefficients

$$g_0 := \sigma_\xi^2 \sum_{\{i|\vec{r}_i\in\mathcal{V}\}} f(r_i)^2 \quad \text{and} \quad g_1 := \sigma_\xi^2\left(\sum_{\{i|\vec{r}_i\in\mathcal{V}\}} f(r_i)\right)^2 \tag{16}$$

describe how these two contributions are weighted by the spatial distribution of neurons, their morphological and electrical properties and the distribution of synapses. For convenience, we will for the rest of this article assume that the input variance is $\sigma_\xi^2 = 1$. In the present study, we consider a population of neurons homogeneously distributed on a disc of radius R with the electrode in the center. For high cell densities ρ, the sums in (16) can be approximated by integrals [3]

$$g_0(R) := 2\pi\rho\int_0^R \mathrm{d}r\ r\, f(r)^2 \quad \text{and} \quad g_1(R) := 4\pi^2\rho^2\left(\int_0^R \mathrm{d}r\ r\, f(r)\right)^2\,. \tag{18}$$

The variance of the compound potential generated by neurons within a range R is thus given by

$$\sigma^2(R) = \sigma_\xi^2\left[(1-c_\xi)g_0(R) + c_\xi g_1(R)\right]\,. \tag{19}$$

---

[3]

$$\sum_{\{i|\vec{r}_i\in\mathcal{V}\}} \ldots = \sum_{\{i|r_i\leq R\}} \ldots \longrightarrow 2\pi\rho\int_0^R \mathrm{d}r\ r\ \ldots \tag{17}$$

Power-law shape function

The current source density of a neuron can, to first order, be approximated by a current dipole (Lindén et al., 2010). For large distances, this typically results in a shape function $f(r)$ decaying as $\sim 1/r^2$. In Results (Fig. 2), this is confirmed for neurons with realistic morphologies. Closer to the cell, the shape function typically becomes shallower. To illustrate how the shape of $f(r)$ determines the (existence of a) reach of a population signal, let us consider a power-law shape function

$$f(r) = \begin{cases} r^{-\gamma} & r \geq \epsilon \\ \epsilon^{-\gamma} = \text{const.} & r < \epsilon \end{cases} \tag{20}$$

with a decay exponent $\gamma \geq 0$ and a minimal distance ϵ. Introducing the minimal distance ϵ is necessary to avoid a singularity at $r = 0$. For convenience, all lengths (r, ϵ, R) are considered dimensionless here (i.e. measured in units of some length scale r_0). With (20), the functions $g_0(R)$ and $g_1(R)$ in (19) read

$$\begin{aligned} g_0(R) &= 2\pi\rho \left(\epsilon^{-\gamma+1} + \begin{cases} \ln\left(\frac{R}{\epsilon}\right) & \gamma = 1 \\ (\epsilon^{2-2\gamma} - R^{2-2\gamma})/(2\gamma-2) & \gamma \neq 1 \end{cases} \right) \\ g_1(R) &= 4\pi^2\rho^2 \left(\epsilon^{-2\gamma+1} + \begin{cases} \left[\ln\left(\frac{R}{\epsilon}\right)\right]^2 & \gamma = 2 \\ (\epsilon^{2-\gamma} - R^{2-\gamma})^2/(\gamma-2)^2 & \gamma \neq 2 \end{cases} \right) . \end{aligned} \tag{21}$$

Consider first the case $c_\xi = 0$ (uncorrelated input): If $\gamma > 1$, $g_0(R)$ converges with increasing population size R to a constant value. The variance $\sigma^2(R)$ of the compound signal saturates. For a population of current dipoles ($\gamma = 2$, in far-field approximation), the reach of the electrode can therefore be well defined. For $\gamma < 1$, however, $g_0(R)$ and, in turn, the compound variance $\sigma^2(R)$ diverge as R approaches infinity. In this case, a 'reach' doesn't exist. It is infinite. If the input is correlated ($c_\xi > 0$), the second term in (19) converges only for $\gamma > 2$. Here, even the potential of a population of dipoles diverges with increasing population size. Note that for large neuron densities ρ, the second term in (19) dominates even for small correlations c_ξ.

Comparison with simulation results

The simplified model presented here illustrates that the variance of the compound extracellular potential of a population of neurons depends essentially on the distance dependence $f(r)$ of the single-cell potentials and the statistics of the synaptic input given by σ_ξ^2 and c_ξ. For simplified cell morphologies (e.g. current dipoles), the shape function $f(r)$ can be calculated analytically. In the present study, however, we investigate the compound signal of a population of neurons with realistic morphologies. To compare the predictions of the simplified model with simulation results, we therefore extract the shape functions $f(r)$ for different morphologies, synapse distributions and electrode depths in single-neuron simulations (see Results, Fig. 2) and compute the corresponding functions $g_0(R)$ and $g_1(R)$ according to (18). For known input statistics σ_ξ and c_ξ, we can, by means of (19), predict the compound variance σ^2 for different population sizes R.

As a consequence of assumption (6), the synaptic input current $\xi_i(t)$ is proportional to the single-cell potential $\phi_i(t)$. The correlation coefficient c_ξ is therefore identical to the correlation $c_\phi = \mathsf{E}_t\left[\phi_i(t)\phi_j(t)\right] / \sqrt{\mathsf{E}_t\left[\phi_i^2(t)\right] \mathsf{E}_t\left[\phi_j^2(t)\right]}$ of the potentials $\phi_i(t)$. This would not hold if the filtering of the input currents by the synapses and dendrites was taken into account, i.e. if we dropped assumption (6) (see Tetzlaff et al., 2008). To compensate for the simplification

(6), we will therefore regard the 'input' $\xi_i(t)$ as the time-dependent part of the single-source potential $\phi_i(t)$ rather than as the total synaptic input current, and replace the correlation coefficient c_ξ in (19) by the correlation c_ϕ between single-cell potentials:

$$\sigma^2(R) = (1 - c_\phi)g_0(R) + c_\phi g_1(R)\,. \tag{22}$$

The transfer of correlations $c_\xi \rightarrow c_\phi$ from input currents to potentials is, in a realistic setting (i.e. for frequency dependent current-density filters $H_{ij}(\omega)$), non-trivial. A rigorous mathematical treatment of this is beyond the scope of this work. Instead, we investigate the current-potential correlation transfer for different neuron types and synapse distributions numerically (see Results, Fig. 4G).

Numerical simulations

Populations, geometrical arrangement

Multi-compartment neuron models with morphologies from digital cell reconstructions (see below) were randomly positioned in a cylindrical volume with radius 1000 μm. Each population consisted of 10000 cells with identical cell morphology but each cell was randomly rotated along the z-axis. The somata of all cells in a population were placed at the same cortical depth. This depth positioned was chosen as the midpoint of the corresponding cortical layer except the L5 cells which were shifted 25 μm upwards to assure that the apical dendrites reached into layer 1 (see Fig. 2). Layer boundaries were derived from (Stepanyants et al. (2008), A. Stepanyants, personal communication). We considered exclusively single populations. The same x- and y- coordinates were used for the three different populations to remove variability due to the exact cell positioning when comparing the populations of different cell types.

Neuron model

We used digital cell reconstructions of L3 pyramidal, L4 stellate and L5 pyramidal neurons (Mainen and Sejnowski, 1996) downloaded from ModelDB (*http://senselab.med.yale.edu/*) from which we removed axon compartments. Segmentation was done so that the length of each compartment was smaller than one tenth of the electrotonic length at 100 Hz resulting in 549 compartments for the L3 cell, 343 compartments for the L4 cell and 1072 compartments for the L5 cell. Passive parameters of the cell models were: specific membrane resistance R_m=30 kΩ cm^2, specific axial resistance R_a=150 Ω cm and specific membrane capacitance C_m=1.0 μF/cm^2. Simulations were performed with a time resolution of 0.0625 ms and resulting data was stored with a time resolution of 1.0 ms. Simulations were in all applications run for a time period of 1200 ms were the first 200 ms were removed before analysis to avoid any upstart effects in the simulations.

Synapse model

Synaptic input currents were modeled as α-currents where the injected current into each synapse followed

$$I(t) = I_0 \frac{t}{\tau} e^{1-(t-t_i)/\tau} \theta(t - t_i)$$

where θ is the Heaviside step function and t_i is the arrival time of presynaptic spike i. Synaptic time constant τ was set to 1 ms and current amplitude I_0 was set to +50 pA for excitatory synapses and -200 pA for inhibitory synapses to give the same ratio between the amplitude of excitatory and inhibitory input currents as in the laminar network simulation (see below). Since the neuron model is linear with respect to amplitude of current injection results would not change qualitatively with other values of I_0 (as long as the relative values for excitatory and inhibitory synapses is contant) except a rescaling of the resulting LFP amplitudes (see below). For results shown in Fig. 2-5 only excitatory synapses were used while both excitatory and inhibitory synapses were used when presynaptic spike trains were generated in laminar network simulations (Fig. 6) (see below).

Synapse placement

Distributions and number of synapses onto the dendrites of the neurons were different in simulations with uncorrelated input spike trains or spike trains using the common-input model (Fig. 2-5) as compared to if input spike trains were generated by the laminar network model (Fig. 6) (see below). Synapses were, depending on input model, randomly assigned to compartments within certain cortical depths where the probability for a synapses being placed on a specific compartment was proportional to the relative membrane area of that compartment compared to the total membrane area within allowed cortical depths. This resulted in homogeneous synapse densities with respect to membrane area of the dendrites. No synapses were placed on the soma.

Uncorrelated spike trains and common-input model: Each cell received a total of 1000 synapses that based on the input scenario were distributed onto the dendrites in the following cortical layers (see also Fig. 2A):

cell type	apical input region	homogeneous input region	basal input region
L3	upper half of L23	L1 and L23	lower half of L23
L4	-	L4	-
L5	L1 and L23	all layers	L5 and L6

Input from laminar network: In some simulations we generated the input spike trains by the laminar network model (see below) (Fig. 6). The inputs to each cell were placed specifically (in terms of cortical depth) for every presynaptic cell type. The number of inputs that every cell receives from the populations in the network model as well as from external sources was set to correspond to the mean number of incoming connections for a corresponding cell in the network simulation (Potjans and Diesmann, 2010). The distribution to the target layers corresponds to the modification of Peters' rule of Binzegger et al. (2004) (numerical values given in Izhikevich and Edelman (2008)).

L3 population: Each cell received in total 5048 excitatory and 1548 inhibitory synapses. For every presynaptic population, the synapses were assigned to dendritic compartments in the following cortical layers (regions):

	from **excitatory** population	from **inhibitory** population
presynaptic layer	**n**$_{syn}$ → **region**	**n**$_{syn}$ → **region**
L23	24 → L1	106 → L1
	2175 → L23	974 → L23
L4	980 → L23	468 → L23
L5	159 → L23	-
L6	110 → L23	-
external	1600 → 2xL1	-

where "2xL1" denotes the region from the cortical surface to twice the cortical depth of L1 which was chosen to avoid very high synapse densities in L1.

L4 population: Each cell received in total 4074 excitatory and 828 inhibitory synapses. For every presynaptic population, the synapses were assigned to dendritic compartments in the following cortical layers (regions):

presynaptic layer	from **excitatory** population **n**$_{syn}$ → **region**	from **inhibitory** population **n**$_{syn}$ → **region**
L23	159 → L4	34 → L4
L4	1116 → L4	794 → L4
L5	32 → L4	-
L6	667 → L4	-
external	2100 → L4	-

L5 population: Each cell received in total 6244 excitatory and 901 inhibitory synapses. For every presynaptic population, the synapses were assigned to dendritic compartments in the following cortical layers (regions):

presynaptic layer	from **excitatory** population **n**$_{syn}$ → **region**	from **inhibitory** population **n**$_{syn}$ → **region**
L23	221 → L1 539 → L23 18 → L4 1412 → L5 and L6	86 → L1 161 → L23 9 → L4 118 → L5 and L6
L4	5 → L1 248 → L23 238 → L4 645 → L5 and L6	- 4 → L23 26 → L4 1 → L5 and L6
L5	252 → L23 4 → L4 365 → L5 and L6	- - 496 → L5 and L6
L6	16 → L23 151 → L4 130 → L5 and L6	- - -
external	1354 → 2xL1 482 → L4 164 → L5 and L6	- - -

where "2xL1" denotes the region from the cortical surface to twice the cortical depth of L1 which was chosen to avoid very high synapse densities in L1.

Input models

Uncorrelated input

For the cases when cells received independent (uncorrelated) input, each synapse received a stationary Poissonian spike train with a rate of 5 spikes/sec. These were generated by first drawing the total number of spikes to each synapse from a Poissonian distribution and then distributing the spike times randomly (with uniform distribution) in the simulation time interval.

Common-input model

In simulations where cells received correlated input a pool of n_{pool} number of Poissonian spike trains with individual firing rates 5 spikes/sec was generated as above. Each cell received a random selection of n_{syn} spike trains from the pool of presynaptic spike trains which were distributed on to the dendrites (see above). This setup induced a correlation between the total synaptic input current to different cells with correlation coefficient $c_\xi = n_{\mathsf{syn}}/n_{\mathsf{pool}}$ due to common input. The input spike trains to each cell were drawn from the pool without resampling to make sure that each cell received uncorrelated input. This allowed for comparisons between uncorrelated and correlated input scenarios where the only difference was correlation between cells and not effects due to correlation in input to single cells.

Laminar network simulation

The spiking cortical network model consisted of one excitatory and one inhibitory population in layers 2/3, 4, 5 and 6. The populations consisted of current-based integrate-and-fire neurons with exponential synaptic currents and were randomly connected. The connection probabilities corresponded to a connectivity map that integrates a major part of the current knowledge on the cortical microcircuitry (Potjans and Diesmann, 2008, 2010); see below for more details). Every population received Poissonian background spike trains in addition to the specific sensory and attentional inputs. The firing rates of these inputs (Table 2) were based on layer-specific estimates of the number of long-range inputs (Potjans and Diesmann, 2010). Synaptic parameters were chosen such that the average shape (rise time and width) of an excitatory postsynaptic potential resembled the in vivo situation (Fetz et al., 1991). The synaptic weights and delays were drawn from a Gaussian distribution (prohibiting a change of sign of the synaptic weights and forcing delays to be positive and multiples of the simulation stepsize). The comprehensive model description according to Nordlie et al. (2009) is given in Table 1. The number of neurons, the connection probabilities and the Poissonian background firing rates as well as all neuronal and synaptic model parameters are given in Table 2.

The connectivity map of the layer-specific microcircuit was based on the integrated data set compiled by Potjans and Diesmann (2008, 2010). It is primarily based on the data derived from anatomical reconstructions by Binzegger et al. (2004) and the electrophysiological hit rate estimates from Thomson et al. (2002). Furthermore, it includes data from further electrophysiological studies (see references in Thomson and Lamy (2007)) as well as information from photostimulation studies (Dantzker and Callaway, 2000; Zarrinpar and Callaway, 2006) and electron microscopy (McGuire et al., 1984). The derivation of the integrated connectivity map takes into account specific differences of the underlying experimental procedures. The derived excitatory map is consistent with the recently published map by Lefort et al. (2009). The activity in the model, most notably with respect to the cell-type specific firing rates, is to a large extent consistent with experimentally observed *in vivo* activity (e.g. de Kock and Sakmann (2009),Sakata and Harris (2009)).

A: Model summary	
Populations	eight cortical populations
Topology	—
Connectivity	random connections
Neuron model	cortex: leaky integrate and fire, fixed voltage threshold, fixed absolute refractory period (voltage clamp)
Synapse model	exponential-shaped postsynaptic currents
Plasticity	—
Input	independent fixed-rate Poisson spike trains
Measurements	spike activity

B: Populations			
Type	**Elements**	**Number of populations**	**Population size**
Cortical network	iaf neurons	eight, two per layer	N (type-specific)

C: Connectivity	
Type	random connections with independently chosen pre- and postsynaptic neurons; see Table 2 for probabilities
Weights	fixed, drawn from Gaussian distribution
Delays	fixed, drawn from Gaussian distribution multiples of sim. stepsize

D: Neuron and synapse model	
Name	iaf neuron
Type	leaky integrate-and-fire, exponential-shaped synaptic current inputs
Subthreshold dynamics	$\frac{dV}{dt} = -\frac{V}{\tau_{\mathrm{m}}} + \frac{I(t)}{C_{\mathrm{m}}}$ if $(\mathrm{t} > \mathrm{t}^* + \tau_{\mathrm{ref}})$ $V(t) = V_{\mathrm{reset}}$ else $I_{\mathrm{syn}}(t) = w\, e^{-t/\tau_{\mathrm{syn}}}$
Spiking	If $V(t-) < \theta \wedge V(t+) \geq \theta$ 1. set $t^* = t$, 2. emit spike with time stamp t^*

E: Input		
Type	**Target**	**Description**
Background	iaf neurons	independent Poisson spikes (see Table 2)

F: Measurements
Spiking activity of all neurons in every population

Table 1: Model description of the laminar network simulation after Nordlie et al. (2009).

B+E: Populations and Inputs

Name	L2/3e	L2/3i	L4e	L4i	L5e	L5i	L6e	L6i
Population size N	20683	5834	21915	5479	4850	1065	14395	2948
External inputs k_{ext}	1600	1500	2100	1900	2000	1900	2900	2100
Background rate ν_{bg}	8 Hz							

C: Connectivity

Connectivity Map	L2/3e	L2/3i	L4e	L4i	L5e	L5i	L6e	L6i
L2/3e	0.101	0.169	0.044	0.082	0.032	0.0	0.008	0.0
L2/3i	0.135	0.137	0.032	0.052	0.075	0.0	0.004	0.0
L4e	0.007	0.006	0.050	0.135	0.007	0.0003	0.045	0.0
L4i	0.069	0.003	0.079	0.160	0.003	0.0	0.106	0.0
L5e	0.100	0.062	0.051	0.006	0.083	0.373	0.020	0.0
L5i	0.055	0.027	0.026	0.002	0.060	0.316	0.009	0.0
L6e	0.016	0.007	0.021	0.017	0.057	0.020	0.040	0.225
L6i	0.036	0.001	0.003	0.001	0.028	0.008	0.066	0.144

Name	**Value**	**Description**
$w \pm \delta w$	87.8 ± 8.8 pA	Excitatory synaptic strengths
g	-4	Relative inhibitory synaptic strength
$d \pm \delta d$	1.5 ± 0.75 ms	Synaptic transmission delays

D: Neuron Model

Name	**Value**	**Description**
τ_{m}	10 ms	Membrane time constant
τ_{ref}	2 ms	Absolut refractory period
τ_{syn}	0.5 ms	Postsynaptic current time constant
C_{m}	250 pA	Membrane capacity
V_{reset}	-65 mV	Reset potential
θ	-50 mV	Fixed firing threshold

Table 2: Parameter specification for the laminar network simulation. The categories refer to the model description in Table 1.

Calculation of LFP

We computed the LFP using the line-source method described by Holt and Koch (1999) (but see also (Holt, 1998) for method description). This involves summing over all transmembrane currents weighted with distance between the recording electrode and compartment of the multi-compartment neuron model. LFP for populations of neurons was computed by first calculating the contributions from single neurons separately and then summing over these contributions from alls cells within the population. Cells were assumed to be surrounded by a purely resistive infinite extracellular medium with conductivity set to 0.3 S/m. No filtering was applied to the resulting LFP signal.

Data analysis

LFP amplitude

The amplitude σ of the LFP signal from a population was computed through the variance over time in the 1000 ms simulation time interval:

$$\sigma^2(R) = \mathsf{E}_t\left[(\phi(t) - \mathsf{E}_t[\phi(t)])^2\right] \tag{23}$$

where $\mathsf{E}_t[\cdot]$ denotes time average and $\phi = \sum_{\{i|r_i<R\}} \phi_i$ is the sum of single cell LFP contributions ϕ_i within population radius R. In situations were LFP contributions were assumed to be correlated only within a region $R_c < R$ (Fig. 5, 6) the standard deviation σ was computed from

$$\sigma^2(R) = \mathsf{E}_t\left[(\phi_{R_c}(t) - \mathsf{E}_t[\phi_{R_c}(t)])^2\right] + \sum_{\{i|R_c<r_i<R\}} \mathsf{E}_t\left[(\phi_i(t) - \mathsf{E}_t[\phi_i(t)])^2\right] \tag{24}$$

where $\phi_{R_c} = \sum_{\{i|r_i<R_c\}} \phi_i$ is the summed LFP signal from cells within radius R_c.

LFP reach

The spatial reach of the LFP was defined as

$$R^* := \min(\{R|\sigma(R)/\sigma(R_{\mathsf{max}}) = 0.95\})\,. \tag{25}$$

Correlation coefficient

The mean correlation coefficent c between N signals x_i (being either total input currents ξ_i or LFP contributions ϕ_i) was computed by

$$c = \frac{\sigma^2_{\mathsf{norm}} - N}{N(N-1)} \tag{26}$$

where $\sigma^2_{\mathsf{norm}} = \mathsf{Var}\left[\sum_{i=1}^{N}\left(\frac{x_i(t)-\mathsf{E}_t[x_i(t)]}{\sigma[x_i(t)]}\right)\right]$, from the relation $\sigma^2 = N + cN(N-1)$ for a sum of N signals, each with zero mean and variance 1 (assured through the above normalization).

Software

Simulations of reconstructed cells were performed with NEURON (Carnevale and Hines, 2006)(*http://www.neuron.yale.edu*) using the supplied Python interface (Hines et al., 2009). The laminar network of integrate-and-fire neurons was simulated using NEST (Gewaltig and Diesmann, 2007) (*http://www.nest-initiative.org*). Data analysis and plotting was done in Python (*http://www.python.org*) using the IPython, Numpy, Scipy and Matplotlib packages.

Acknowledgements

This work was partially funded by the Research Council of Norway (eScience, NOTUR), EU Grant 15879 (FACETS), EU Grant 269921 (BrainScaleS), BMBF Grant 01GQ0420 to BCCN Freiburg, Next-Generation Supercomputer Project of MEXT, Japan, and the Helmholtz Alliance on Systems Biology.

Notation

Variable / Operator name	Description
$\mathrm{csd}_{ij}(t)$	current-source density generated by synapse j on postsynaptic neuron i
c_ξ	correlation coefficient of input-currents
c_ϕ	correlation coefficient of single-cell potentials
f_{ij}	shape factor of synapse $\{ij\}$
f_i	shape factor of neuron i (average over all synapses)
$\phi_{ij}(t)$	extracellular potential caused by synaptic input current at synapse $\{ij\}$
$\phi_i(t)$	extracellular potential generated by neuron i
$\phi(t)$	compound extracellular potential (generated by all neurons)
g_0	$= \sum_{\{i\vert\vec{r}_i\in\mathcal{V}\}} f(r_i)^2$, factor describing the contribution of uncorrelated input to the compound variance σ_ϕ^2
g_1	$= [\sum_{\{i\vert\vec{r}_i\in\mathcal{V}\}} f(r_i)]^2$, factor describing the contribution of correlated input to the compound variance σ_ϕ^2
$h_{ij}(t,\vec{r})$	impulse-response of current-source density for synapse $\{ij\}$
$H_{ij}(\omega,\vec{r})$	transfer function of current-source density for synapse $\{ij\}$
κ	conductivity of the extracellular medium
M_i	number of (incoming) synapses of neuron i (in-degree of neuron i)
N	number of neurons
ω	(angular) frequency
$\vec{r} = (x,y,z)^\mathsf{T}$	distance vector with horizontal components x, y and vertical component z
R	spatial extent of neuron population (disc radius)
ρ	neuron density
σ^2	variance of the compound potential (population signal)
σ_ξ^2	(total) input variance
t	time
$\mathcal{V}$	volume of described neuron population
$\xi_{ij}(t)$	synaptic input at synapse $\{ij\}$
$\xi_i(t)$	total synaptic input current of neuron i
$\mathfrak{F}_t\left[g(t)\right](\omega)$	Fourier transform of $g(t)$ with respect to t
$\mathsf{E}_i\left[q_i\right]$	expectation of q_i across ensemble $\{i\}$
$\mathsf{E}_t\left[\cdot\right]$	time average

References

Andersen, R. A., Musallam, S., and Pesaran, B. (2004). Selecting the signals for a brain-machine interface. *Curr Opin Neurobiol*, 14(6):720–6.

Bédard, C., Kröger, H., and Destexhe, A. (2004). Modeling extracellular field potentials and the frequency-filtering properties of extracellular space. *Biophysical Journal*, 86(3):1829–42.

Belitski, A., Gretton, A., Magri, C., Murayama, Y., Montemurro, M., Logothetis, N., and Panzeri, S. (2008). Low-frequency local field potentials and spikes in primary visual cortex convey independent visual information. *J Neurosci*, 28(22):5696.

Berens, P., Keliris, G. A., Ecker, A. S., Logothetis, N. K., and Tolias, A. S. (2008a). Comparing the feature selectivity of the gamma-band of the local field potential and the underlying spiking activity in primate visual cortex. *Frontiers in systems neuroscience*, 2:2.

Berens, P., Keliris, G. A., Ecker, A. S., Logothetis, N. K., and Tolias, A. S. (2008b). Feature selectivity of the gamma-band of the local field potential in primate primary visual cortex. *Frontiers in Neuroscience*.

Binzegger, T., Douglas, R., and Martin, K. (2004). A quantitative map of the circuit of cat primary visual cortex. *J Neurosci*, 24(39):8441.

Carnevale, N. T. and Hines, M. L. (2006). *The NEURON Book*. Cambridge University Press.

Dantzker, J. L. and Callaway, E. M. (2000). Laminar sources of synaptic input to cortical inhibitory interneurons and pyramidal neurons. *Nat Neurosci*, 3(7):701–7.

de Kock, C. P. J. and Sakmann, B. (2009). Spiking in primary somatosensory cortex during natural whisking in awake head-restrained rats is cell-type specific. *Proc Natl Acad Sci USA*, 106(38):16446–50.

Denker, M., Riehle, A., Diesmann, M., and Grün, S. (2010). Estimating the contribution of assembly activity to cortical dynamics from spike and population measures. *J Comput Neurosci*.

Destexhe, A., Contreras, D., and Steriade, M. (1999). Spatiotemporal analysis of local field potentials and unit discharges in cat cerebral cortex during natural wake and sleep states. *J Neurosci*, 19(11):4595–608.

Einevoll, G. T., Pettersen, K. H., Devor, A., Ulbert, I., Halgren, E., and Dale, A. M. (2007). Laminar population analysis: Estimating firing rates and evoked synaptic activity from multielectrode recordings in rat barrel cortex. *J Neurophysiol*, 97(3):2174–2190.

Fetz, E., Toyama, K., and Smith, W. (1991). Synaptic interactions between cortical neurons. In Peters, A., editor, *Cerebral Cortex*, volume 9, chapter 1, pages 1–47. Plenum Press, New York and London.

Gewaltig, M.-O. and Diesmann, M. (2007). Nest (neural simulation tool). *Scholarpedia*, 2(4):1430.

Henrie, J. A. and Shapley, R. (2005). Lfp power spectra in v1 cortex: the graded effect of stimulus contrast. *J Neurophysiol*, 94(1):479–90.

Hines, M. L., Davison, A. P., and Muller, E. (2009). Neuron and python. *Frontiers in neuroinformatics*, 3:1.

Holt, G. R. (1998). A critical reexamination of some assumptions and implications of cable theory in neurobiology. *PhD thesis, California Institute of Technology*, page 168.

Holt, G. R. and Koch, C. (1999). Electrical interactions via the extracellular potential near cell bodies. *J Comput Neurosci*, 6(2):169–84.

Izhikevich, E. M. and Edelman, G. M. (2008). Large-scale model of mammalian thalamocortical systems. *Proc Natl Acad Sci USA*, 105(9):3593–3598.

Johnston, D. and Wu, S. M.-S. (1995). *Foundations of cellular neurophysiology*. MIT Press.

Katzner, S., Nauhaus, I., Benucci, A., Bonin, V., Ringach, D., and Carandini, M. (2009). Local origin of field potentials in visual cortex. *Neuron*, 61(1):35–41.

Kelly, R. C., Smith, M. A., Kass, R. E., and Lee, T. S. (2010). Local field potentials indicate network state and account for neuronal response variability. *J Comput Neurosci*.

Kreiman, G., Hung, C. P., Kraskov, A., Quiroga, R. Q., Poggio, T., and DiCarlo, J. J. (2006). Object selectivity of local field potentials and spikes in the macaque inferior temporal cortex. *Neuron*, 49(3):433–45.

Lefort, S., Tomm, C., Sarria, J.-C. F., and Petersen, C. C. H. (2009). The excitatory neuronal network of the c2 barrel column in mouse primary somatosensory cortex. *Neuron*, 61(2):301–16.

Lindén, H., Pettersen, K. H., and Einevoll, G. T. (2010). Intrinsic dendritic filtering gives low-pass power spectra of local field potentials. *J Comput Neurosci*.

Liu, J. and Newsome, W. T. (2006). Local field potential in cortical area mt: stimulus tuning and behavioral correlations. *J Neurosci*, 26(30):7779–90.

Logothetis, N. K., Kayser, C., and Oeltermann, A. (2007). In vivo measurement of cortical impedance spectrum in monkeys: implications for signal propagation. *Neuron*, 55(5):809–23.

Mainen, Z. F. and Sejnowski, T. J. (1996). Influence of dendritic structure on firing pattern in model neocortical neurons. *Nature*, 382(6589):363–6.

McGuire, B. A., Hornung, J. P., Gilbert, C. D., and Wiesel, T. N. (1984). Patterns of synaptic input to layer 4 of cat striate cortex. *J Neurosci*, 4(12):3021–33.

Mehring, C., Rickert, J., Vaadia, E., de Oliveira, S. C., Aertsen, A., and Rotter, S. (2003). Inference of hand movements from local field potentials in monkey motor cortex. *Nat Neurosci*, 6(12):1253–4.

Mitzdorf, U. (1985). Current source-density method and application in cat cerebral cortex: investigation of evoked potentials and eeg phenomena. *Physiol Rev*, 65(1):37–100.

Nauhaus, I., Busse, L., Carandini, M., and Ringach, D. L. (2009). Stimulus contrast modulates functional connectivity in visual cortex. *Nat Neurosci*, 12(1):70–6.

Nicholson, C. and Freeman, J. A. (1975). Theory of current source-density analysis and determination of conductivity tensor for anuran cerebellum. *J Neurophysiol*, 38(2):356–68.

Nordlie, E., Gewaltig, M.-O., and Plesser, H. E. (2009). Towards reproducible descriptions of neuronal network models. *PLoS Comput Biol*, 5(8):e1000456.

Nunez, P. L. (2006). *Electric Fields of the Brain: The Neurophysics of EEG.* Oxford University Press.

Pesaran, B., Pezaris, J. S., Sahani, M., Mitra, P. P., and Andersen, R. A. (2002). Temporal structure in neuronal activity during working memory in macaque parietal cortex. *Nat Neurosci*, 5(8):805–11.

Pettersen, K. and Einevoll, G. (2008). Amplitude variability and extracellular low-pass filtering of neuronal spikes. *Biophysical Journal*, 94(3):784–802.

Pettersen, K. H., Hagen, E., and Einevoll, G. T. (2008). Estimation of population firing rates and current source densities from laminar electrode recordings. *J Comput Neurosci*, 24(3):291–313.

Potjans, T. C. and Diesmann, M. (2008). Consistency of *in vitro* and *in vivo* connectivity estimates: statistical assessment and application to cortical network modeling. In *Proceedings of the 38th annual meeting of the Society for Neuroscience, 16.1*.

Potjans, T. C. and Diesmann, M. (2010). The cell-type specific structure and activity of the local cortical network. submitted.

Rickert, J., de Oliveira, S. C., Vaadia, E., Aertsen, A., Rotter, S., and Mehring, C. (2005). Encoding of movement direction in different frequency ranges of motor cortical local field potentials. *J Neurosci*, 25(39):8815–24.

Roux, S., Mackay, W. A., and Riehle, A. (2006). The pre-movement component of motor cortical local field potentials reflects the level of expectancy. *Behav Brain Res*, 169(2):335–51.

Sakata, S. and Harris, K. D. (2009). Laminar structure of spontaneous and sensory-evoked population activity in auditory cortex. *Neuron*, 64(3):404–418.

Scherberger, H., Jarvis, M. R., and Andersen, R. A. (2005). Cortical local field potential encodes movement intentions in the posterior parietal cortex. *Neuron*, 46(2):347–54.

Stepanyants, A., Hirsch, J. A., Martinez, L. M., Kisvárday, Z. F., Ferecskó, A. S., and Chklovskii, D. B. (2008). Local potential connectivity in cat primary visual cortex. *Cereb Cortex*, 18(1):13–28.

Tetzlaff, T., Rotter, S., Stark, E., Abeles, M., Aertsen, A., and Diesmann, M. (2008). Dependence of neuronal correlations on filter characteristics and marginal spike train statistics. *Neural computation*, 20(9):2133–84.

Thomson, A. M. and Lamy, C. (2007). Functional maps of neocortical local circuitry. *Frontiers in Neuroscience*, 1(1):19–42.

Thomson, A. M., West, D. C., Wang, Y., and Bannister, A. P. (2002). Synaptic connections and small circuits involving excitatory and inhibitory neurons in layers 2-5 of adult rat and cat neocortex: triple intracellular recordings and biocytin labelling in vitro. *Cereb Cortex*, 12(9):936–53.

Womelsdorf, T., Fries, P., Mitra, P. P., and Desimone, R. (2006). Gamma-band synchronization in visual cortex predicts speed of change detection. *Nature*, 439(7077):733–6.

Xing, D., Yeh, C.-I., and Shapley, R. M. (2009). Spatial spread of the local field potential and its laminar variation in visual cortex. *J Neurosci*, 29(37):11540–9.

Zarrinpar, A. and Callaway, E. M. (2006). Local connections to specific types of layer 6 neurons in the rat visual cortex. *J Neurophysiol*, 95(3):1751–61.

3.5 Paper V

The local field potential reflects surplus spike synchrony

Michael Denker[1], Sébastien Roux[2], Henrik Lindén[3],
Markus Diesmann[1], Alexa Riehle[2], Sonja Grün[1,4]

[1] RIKEN Brain Science Institute,
Wako City, Japan

[2] Mediterranean Institute of Cognitive Neuroscience (INCM),
CNRS - University Aix-Marseille 2, Marseille, France

[3] Dept. of Mathematical Sciences and Technology,
Norwegian University of Life Sciences, Ås, Norway

[4] Bernstein Center for Computational Neuroscience,
Berlin, Germany

Abstract

The oscillatory nature of the cortical local field potential (LFP) is commonly interpreted as a reflection of synchronized network activity, but its relationship to observed transient coincident firing of neurons on the millisecond time-scale remains unclear. Here we present experimental evidence to reconcile the notions of synchrony at the level of neuronal spiking and at the mesoscopic scale. We demonstrate that only in time intervals of excess spike synchrony, coincident spikes are better entrained to the LFP than predicted by the locking of the individual spikes. This effect is enhanced in periods of large LFP amplitudes. A quantitative model explains the LFP dynamics by the orchestrated spiking activity in neuronal groups that contribute the observed surplus synchrony. From the correlation analysis, we infer that neurons participate in different constellations but contribute only a fraction of their spikes to temporally precise spike configurations, suggesting a dual coding scheme of rate and synchrony. This finding provides direct evidence for the hypothesized relation that precise spike synchrony constitutes a major temporally and spatially organized component of the LFP. Revealing that transient spike synchronization correlates not only with behavior, but with a mesoscopic brain signal corroborates its relevance in cortical processing.

Introduction

It is common belief that the local field potential (LFP), a population signal obtained from electrophysiological recordings of the brain, should reflect the synchronized spiking activity of neurons in the vicinity of the recording electrode. This assumption is rooted in the widely accepted biophysical explanation of the LFP as a spatially weighted average of the synaptic transmembrane currents (Mitzdorf, 1985; Viswanathan and Freeman, 2007). Indeed, the average postsynaptic effect in the LFP at a given recording site triggered on spikes initiated across a patch of cortex is predictive of the LFP (Nauhaus et al., 2009). In consequence, the oscillatory structure observed ubiquitously in the LFP is hypothesized to reflect predominantly oscillatory synchronized input (Logothetis and Wandell, 2004). Indeed, the LFP has been shown to correlate with membrane potential oscillations of nearby neurons (Poulet and Petersen, 2008) independent of the spiking activity (Okun et al., 2010). However, although the extension from membrane potential dynamics to coincident spiking activity is on everybody's mind, the hypothesis that synchronized action potentials are reflected in LFP oscillations has not been directly shown.

A large body of literature investigates the relationship of spikes and the LFP. To date, it has been established that neural spiking activity may become transiently coupled to the LFP in a rhythmic or non-oscillatory fashion (Eckhorn and Obermueller, 1993; Murthy and Fetz, 1996b). The degree of phase locking between neurons and the LFP depends in general on the strength of beta/gamma LFP oscillations (Denker et al., 2007), and both auto-correlations and cross-correlations between simultaneously recorded neurons tend to show an oscillatory structure during strong oscillatory episodes (Murthy and Fetz, 1996b). Such oscillatory periods are correlated with stimulus features (Engel et al., 1990) as well as top-down processes, such as attention (Fries et al., 2001), and are thus believed to be computationally informative (Fries et al., 2007). Indeed, firing rate profiles correlate with gamma band LFP power when the level of interneuronal rate correlation is high (Nir et al., 2007), and the power correlation between the spiking activity of different neuronal groups depends crucially on their phase relationship with the LFP (Womelsdorf, 2007). In addition, a number of studies indicate that across brain areas, inhibitory neurons play a crucial role in the generation of fast oscillations (Klausberger et al., 2003; Hasenstaub et al., 2005; Cardin, 2009). Excitatory-inhibitory loops (Berens et al., 2008) gate the temporal structure of activity projecting onto pyramidal cells (Buzsáki and Draguhn, 2004).

Despite the fact that oscillatory activity in the LFP is reflected on the level of membrane potentials and rate co-modulations, it remains unclear how the LFP oscillation is related to the precise synchronization of individual action potentials. Recent studies succeeded to directly relate synchronized slow subthreshold membrane potential oscillations to LFPs, but did not find such a relationship for synchronized action potentials of the same neurons (Poulet and Petersen, 2008). This discrepancy between subthreshold dynamics and spiking activity is in agreement with theoretical work linking subthreshold and suprathreshold dynamics (Tetzlaff et al., 2008). In consequence, the findings of Poulet and Petersen (2008) indicate that the occurrence of action potentials is governed by strong, precisely timed, and specific inputs to the cells suggesting these as independent activity riding on the co-modulating oscillations. Moreover, a recent study by Okun et al. (2010) questions the idea that network-wide population events dominate the LFP, suggesting that precise firing occurs in smaller groups of neurons, and therefore might only be subtly represented in the LFP.

One hypothesis that is compatible with such input characteristics states that specific common inputs force the precise synchronous discharge within a defined group of cells, termed the Hebbian cell assembly (Hebb, 1949). Early on, it has been conjectured that LFP oscillations may represent an alternative network-averaged signature of assembly activations (Donoghue et al., 1998; Singer, 1999) and enable the binding of features coded by different assemblies (Eckhorn et al., 1988). Indeed, distinct spike patterns across neurons and their phase relationship to LFP oscillations encode a substantial amount of surplus of information about the stimulus compared to information contained in the firing rate alone (Kayser et al., 2009). Nevertheless, the critical link between the dynamics of precise interneuronal spike correlations and the LFP on a trial-by-trial basis is missing. In particular in motor cortex, there is no intuitive correspondence between spatially extended (Fig. 1A; cf. also Rubino et al., 2006) LFP oscillations and spike synchronization in the absence of a network oscillation in the spiking activity (Fig. 1B-E; cf. also Nawrot et al., 2008).

On the spiking level, the hallmark signature of an activated assembly is the functionally

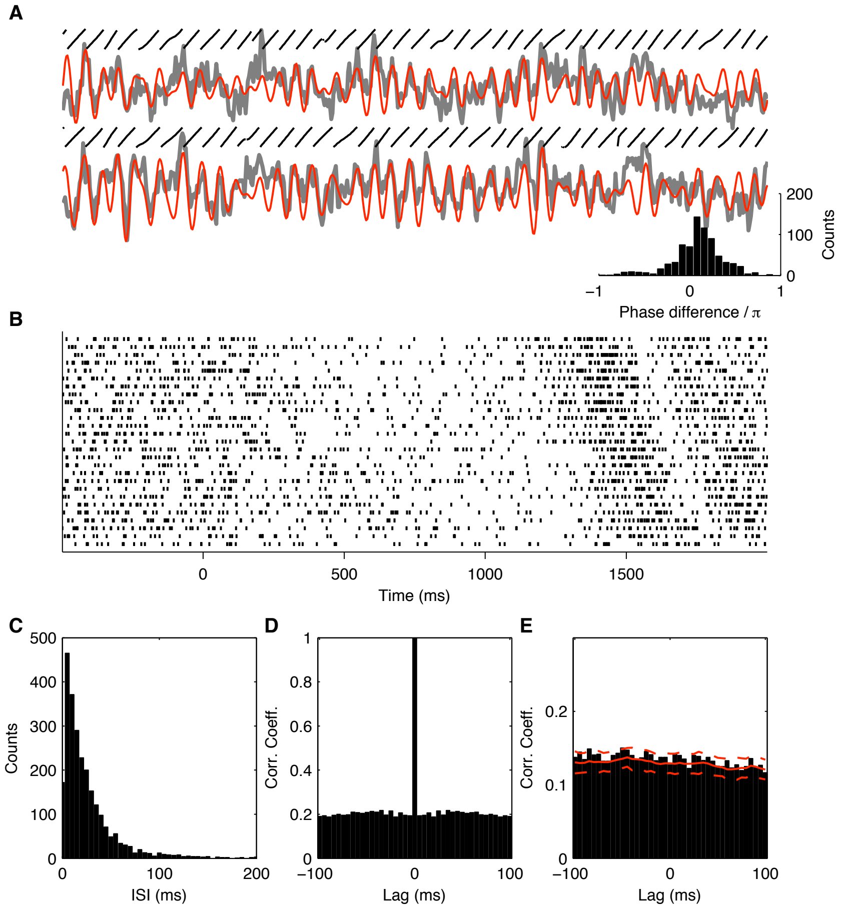

Figure 1: **Characteristics of LFP and spiking dynamics.** (A) Two single-trial LFPs recorded simultaneously (gray) at different electrodes (during long trials with movement to the right in the SELF task). Superimposed are the beta-filtered (10-22 Hz) signals (red) and their instantaneous oscillation phase (black lines). The histogram visualizes the phase differences between the two signals across all time bins. (B) Spike raster of one example neuron recorded in parallel to the LFP shown above. (C and D) Neither the trial-averaged inter-spike interval distribution (C) nor the normalized auto-correlograms (D) indicate an oscillatory nature of the neuron. (E) The cross-correlogram with a different neuron recorded in parallel (neuron 1 in supplemental Fig. S1) remains flat. Red lines indicate mean (solid) and 5% confidence intervals (dashed) of cross-correlograms obtained from surrogate spike trains where each spike was jittered uniformly in window of ±20 ms around its original position.

coordinated synchronous spiking with millisecond precision observed in parallel recordings of neuronal activity (Gerstein et al., 1989) that exceeds the expectation based on the neuronal firing rates (Aertsen et al., 1989). It is shown that not only LFP oscillations correlate with external stimuli (e.g., Montemurro et al., 2008), behavioral aspects (e.g., Scherberger et al., 2005), and internal processes (e.g., Murthy and Fetz, 1996a; Donoghue et al., 1998; Roux et al., 2006), but also precise spike synchrony is observed (Riehle et al., 1997; Vaadia et al., 1995) and modulated (Kilavik et al., 2009) in a functional context. For beta/gamma oscillations it remains an open question if LFPs reflect more than synchronization due to an underlying rate modulation, and if these oscillations may provide a framework for the occurrence of precisely coordinated spiking as predicted by an active assembly (Buzsáki, 2004; Jensen, 2006). Here, we uncover this missing link between observed spike synchrony and LFP oscillations by directly relating these observables.

Materials and Methods

Ethics Statement

Care and treatment of the animals during all stages of the experiments conformed to the European and French government regulations, according to the Weatherall report ('The use of non-human primates in research', December 2006).

Experimental design and electrophysiological recordings

All data were taken from recordings partially presented elsewhere (Roux et al., 2006; Kilavik et al., 2009). Two rhesus monkeys (monkey K and monkey O) were trained to perform arm movements from a center position to one of two possible peripheral targets left and right of the center in two different tasks involving an instructed delay. In the first, a choice reaction time task (chRT), both peripheral targets were presented simultaneously as a preparatory signal (PS), one in red and the other in green. The animal learned to attribute to each color one of two possible delay durations. If the (directionally non-informative) auditory response signal (RS) occurred after a short delay, the monkey had to select the red target, after a long delay the green one. Both the laterality of the colored targets and the presentation of the two durations were varied at random with equal probability. In contrast, in the second self-paced movement task (SELF), the presentation of only one peripheral target, either in red or green, either at the left or the right, required a self-initiated response after estimating one of the two delays as coded by PS. In both tasks (Roux et al., 2006), four different timing patterns were used to identify the short and long delay, respectively: (*i*) 500 ms and 1000 ms (monkey K); (*ii*) 500 ms and 1200 ms (monkey K); (*iii*) 600 ms and 1200 ms (monkey O); (*iv*) 1000 ms and 1400 ms (monkey O).

In this study we exclusively analyzed the delay activity, i.e. activity recorded during the preparatory period (PP) starting at PS and ending with either RS in the chRT task or the earliest allowed response time (AT) in the SELF task. Therefore, the trials were aligned to PS occurrence for the analysis. The neural activity related to movement execution, i.e. after RS or AT, respectively, is not analyzed. For both tasks, only correct trials were considered, in which the monkey responded within a time window (after the end of PP) of maximally 300 ms (monkey O) and 500 ms (monkey K) and in which movements were performed in the required movement direction.

In order to exclude effects due to pooling of neuronal activities of different behavioral contexts and different tasks, their activity was analyzed separately for the four possible behavioral conditions (combinations of short or long delay duration and left or right upcoming movement direction) and each experimental session. For the sake of simplicity, we refer in this manuscript to a recorded neuron by the combination of its identity and the behavioral context during which it was recorded. In this sense, data recorded from the same neuron may enter a population average up to eight times (maximum of four different conditions in two tasks).

Data acquisition and data analysis

LFPs and spikes were recorded simultaneously in primary motor cortex using a multielectrode device of 2-4 electrodes (MT-EPS, Alpha Omega). Spikes of single neurons were detected by an online sorting algorithm (MSD, Alpha Omega, Nazareth, Israel). The inter-electrode distance was on the order of 400 µm. LFPs were sampled at a resolution of 250-500 Hz and hardware filtered (band pass, 1-100 Hz). In total, we analyzed 53 recording sessions (monkey K: 25; O: 28), which yielded 143 single neurons or 570 combinations of neurons and behavioral conditions. On average 33±11 trials were recorded per experimental condition. In analyses that combine spikes and LFP, each neuron enters only once, and we never combined LFP and spikes that were recorded on the same electrode to exclude the possibility of spike artifacts in the signal. We confirmed that simultaneously recorded LFPs are highly synchronous in the frequency regimes of interest. Likewise, coincident activity between neurons was analyzed only from neurons recorded from different electrodes, totaling 123 analyzed pairs of neurons. All data analysis was performed using the Matlab software environment (The Mathworks Inc., Nattick MA).

Coincidence detection and Unitary Event Analysis

From simultaneously recorded spike data of individual sessions we extract all unique pair combinations of spike trains that are recorded from distinct electrodes. In a first step, we compute the number of coincident spike occurrences of the pairs of neurons in a time-dependent manner (compare supplemental Fig. S1). To allow coincidences with a temporal jitter up to a maximal coincidence width of b=3 ms, we apply the 'multiple-shift' approach (Grün et al., 1999; Grammont and Riehle, 2003). In this method exact coincidences (within the time resolution h=0.1 ms of the data) are detected for a range of shifts between -b to +b of the second spike train against the first (reference) spike train. To account for the non-stationarity of the neurons' firing rates, and to capture the dynamics of correlation, we perform the Unitary Event (UE) analysis in a sliding window fashion (Grün et al., 2002b). This is done by moving a window of fixed duration (here: T_w=100 ms) along the data to cover the duration of a trial, i.e. the duration of the PP. The length of the time window is chosen large enough to include at least one complete cycle of the beta oscillation. The window is advanced in steps corresponding to the time resolution h of the data. The first window position is centered at trial onset, and the last window at the end of the delay period.

Within each window position the total number of empirical coincidence counts n_{emp} is derived by summing the exact coincident spike events from each shift l and from all M trials j:

$$n_{\mathrm{emp}} = \sum_{j=1}^{M} \sum_{l=1}^{L} = n_{\mathrm{emp}}^{j,l}$$

with $L = 2(b/h) + 1$. To derive UEs this count is compared to the number of coincidences that would occur by chance given the firing rates of the neurons. This involves the following calculations. To account for non-stationary rates across trials (Grün et al., 2003), the relevant measures are obtained from the single trial and only subsequently summed across trials. Thus, within the analysis window the expected number of coincidences is calculated on the basis of the trial by trial firing probabilities $p_{i,j}$ which are estimated by the spike count $c_{i,j}$ of neuron i in trial j divided by the number of bins N within a window: $p_{i,j} = c_{i,j}/N$ with $N = T_w/h$. The joint probability for finding a coincidence by chance per trial is calculated by the product of the single neuron firing probabilities $p_{12,j} = p_{1,j}p_{2,j}$. The expected number of coincidences per trial j results from multiplying this probability with the number of bins N that are included in the analysis window and the number of shifts L: $n_{\mathrm{exp}}^{j} = NLp_{12,j}$. The total number of expected coincidences within the window is derived from the sum of the expected numbers per trial: $n_{\mathrm{exp}} = \sum_{j=1}^{M} n_{\mathrm{exp}}^{j}$.

Finally we compare the empirical n_{emp} to the expected number n_{exp} of coincidences to detect significant deviations. To this end, we calculate the joint-p-value jp, i.e. the probability of measuring the given number of empirical coincidences (or an even larger number) under the null-hypothesis of independent firing. The distribution under this null-hypothesis representing the probability to find a given number of coincidences is given analytically assuming Poisson processes (Grün et al., 1999). The latter assumption is shown to yield a conservative estimate for cortical spike trains considering their non-Poisson and non-renewal properties (Grün, 2009). Then the significance of n_{emp} yields (Grün et al., 2002a):

$$jp(n_{\mathrm{emp}}|n_{\mathrm{exp}}) = \sum \frac{n_{\mathrm{exp}}^{r}}{r!} e^{-n_{\mathrm{exp}}}$$

If its value is below an *a priori* threshold (here chosen as 5%) coincident firing is classified as significant and identified as Unitary Events. Spikes are labeled as UE if they are part of at least one sliding window identified to contain significant excess synchrony (for an illustrated summary of this analysis approach, see Maldonado et al., 2008). In addition, we require such time windows to exhibit a minimum firing rate of 5 Hz for each neuron. Spikes that are part of coincident events but not identified as UE with respect to any of the neurons recorded in parallel are labeled as chance coincidences (CC), all remaining spikes as isolated spikes (ISO).

Spectral analysis

Power spectra are used to assess the dominant frequencies in the LFP during the task. All power spectra are calculated using a Hamming window as taper. To illustrate the temporal modulation of power in different frequency bands, we use a time-resolved spectral analysis using 200 ms windows with a 50 ms overlap.

Spike-triggered averages

Spike-triggered averages (STAs) are computed by averaging LFP segments from time windows of 200 ms centered at each spike time. For the STA analysis, LFPs are filtered between 2-80 Hz to remove DC components. To compare STAs across recordings, in which electrode signals often differ in their absolute amplitude values, we z-transform each LFP before further analysis by subtracting its mean (calculated across trials) and dividing by its standard deviation. In order to quantify the magnitude (or size) of an STA, we calculate the total area the STA encloses with the time axis. Similar results to those presented here (not shown) are obtained using alternative measures of the STA magnitude, such as the area under its envelope, or the maximum of its absolute value. The magnitude of the STA is in general dependent on the number of trigger spikes. In order to compare STAs obtained from two sets of trigger spikes of different number of spikes n_1 and n_2 ($n_1 > n_2$) we construct 1000 STAs of set 1, each computed from n_2 randomly selected spikes. We define the STA of set 2 to be larger than that of set 1 if the magnitude of set 2 exceeds 50% of the re-computations of set 1, and significantly larger (at a level of 5%) if it exceeds 95% of the re-computations.

Peak-triggered spike histograms

We evaluate the population-averaged spiking discharge triggered on the peaks of the LFP oscillation (Destexhe et al., 1999). To this end we detect maxima of the LFP separated by a minimum time interval of 33 ms, which corresponds to a maximal oscillation frequency of 30 Hz. The spike histogram is calculated from data within a window of 200 ms around each peak, and averaged across all individual peaks in all neurons (see Eeckman and Freeman, 1990 for a different technique to relate spike times to EEG time course based on amplitude). Simultaneously, we also compute the peak-triggered LFP by averaging the z-transformed LFP aligned on its peaks.

Rate-amplitude correlation

To assess the degree of correlation between LFP oscillation strength and spike rates, we calculate the mean value of the rectified, z-transformed LFP along each trial with sliding windows of 200 ms length and 100 ms overlap. These values are then correlated with the rate profile of the neuron estimated as the spike count across trials in the same windows. Similar results as those shown here are obtained using alternative measures of LFP strength, including the mean value of the envelope of the beta-filtered signal (compare phase-locking analysis), or by using the total signal power in the beta range (10-22 Hz).

Phase analysis

After examination of the dominant beta frequencies on a session-by-session basis, LFPs of both monkeys are filtered with a zero-phase 10-22 Hz band pass filter (Butterworth, 8-pole). Short filter transients in the time domain allow for good estimates of the instantaneous LFP amplitude. In a subsequent step, we calculate the instantaneous phase of the LFP from the analytic signal $\xi(t) = x(t) + i\tilde{x}(t)$ obtained via the Hilbert transformation

$$\tilde{x}(t) = \frac{1}{\pi} P.V. \int \frac{x(t)}{t - \tau} \mathrm{d}\tau$$

of the original signal $x(t)$, where $P.V.$ denotes that the integral is to be taken as Cauchy principal value (Le Van Quyen et al., 2001). In this formalism, troughs of the LFP are identified by a phase of π. The calculation of the analytic signal can be applied to arbitrary signals, but its interpretation as instantaneous phase is difficult where either the signal amplitude becomes too small to discriminate the oscillation from background noise, or where the regular oscillation is disrupted (Boashash, 1992). To account for these effects, we discard phase values which violate the monotonicity of the phase time series or exhibit instantaneous phase jumps. To further corroborate our results, we exclude from our analysis those 10% of spikes per neuron that occur at the lowest LFP amplitudes.

We analyze the distributions of extracted phase values at the times of spike occurrences (Denker et al., 2007) using tools from circular statistics (Mardia and Jupp, 2000). The mean phase ϕ is obtained via the circular average

$$Re^{i\phi} = N^{-1} \sum e^{i\phi(t_i)}$$

where $\phi(t_i)$ indicates the phase of the field potential at time t_i of spike i. Furthermore, we utilize the transformation of the vector strength R to the circular standard deviation $\sigma = \sqrt{-2\log R}$ as a measure of the concentration of the phase distribution. For small values, σ relates to the standard deviation of a normal distribution, whereas for flat distributions it behaves as $\sigma \rightarrow \infty$. In all phase analysis, we discard neurons that fire in total (across trials) less than 25 spikes.

Additionally, we employ two measures to quantify whether spikes recorded from individual neurons show a significant phase preference to the LFP. For the first, we test against the null hypothesis that the phase sample is taken from the uniform circular distribution (Rayleigh test, cf. Mardia and Jupp, 2000), which is expected by assuming a regular (e.g., filtered) field potential and independent random spiking. However, spike trains that have a certain regular structure in time may display intrinsic locking to the LFP. To measure the degree of genuine locking that is not explained by the regularities of the two signals, we calculate as the second measure the degree of locking R in 1000 surrogates, each created by shuffling the inter-spike intervals of the spikes on a trial-by-trial basis (random placement of the first spike). This procedure preserves to first order the regularity manifested in the inter-spike interval distribution. A comparison with the measured value R yields the p-value for this surrogate test. Since the construction of such surrogates can only be performed on the complete spike train, this measure could not be sensibly applied to the subsets of spikes in our analysis (i.e., ISO, CC, UE, as well as Lo and Hi used in the amplitude analysis).

The phase distribution of spike coincidences may be trivially sharpened due to a preferred phase occurrence of individual spikes. To correct for this effect we calculated the expected phase distribution of coincident spikes (compare black curve in Figs. 5 and 6). To this end, we calculate the joint phase probability distribution of a neuron pair by the phase-by-phase multiplication of the occurrence probabilities of spikes at these phases. The predictor for the whole population is the average of the pair-wise phase distributions weighted by the relative number of coincidences between the two neurons.

In contrast to this predictor which considers the phase of spikes irrespective of the spike interval distribution, we also construct a predictor based on the reverse scenario. For each pair of simultaneously recorded neurons the inter-spike intervals of the spike trains of each neuron are shuffled on a trial-by-trial basis to create a set of 1000 surrogate pairs. For each surrogate, the variance σ is evaluated separately for the resulting sets of non-coincident and coincident spikes. Thus, we obtain for each neuron the variances σ of phase locking of coincident and non-coincident spikes for the original data and for the 1000 surrogates, allowing us to compare their distributions (Fig. 4).

Results

Synchrony based spike classification

We analyze spike data of 143 single units and simultaneously recorded LFP data from motor cortical areas in two monkeys during the instructed delay (preparatory period, PP) of two motor tasks (see Methods). Both spike synchrony (Kilavik et al., 2009) and LFP oscillations in the beta band (Murthy and Fetz, 1996a) have been shown to be behaviorally relevant to movement preparation. LFPs and spikes were recorded from different electrodes spaced at 400 μm (for a schematic illustration, see Fig. 2) to exclude trivial signal correlations induced by volume conductance effects (cf., e.g., Katzner et al., 2009). Using the Unitary Events analysis (Grün et al., 2002a,b), we identify transient periods where the spiking activity of simultaneously recorded sets of neurons shows a surplus of coincidence events compared to the number expected on the basis of the firing rates. During these periods we attribute the excess synchrony to the synchronous firing of both observed neurons as part of a network process that activates a specific subset of neurons: the assembly (Fig. 2 depicts the spikes of two different assemblies in green and blue). Based on this detection of precise spike synchrony (Grün et al., 1999) between all neuron pairs of a given neuron we classify the spikes recorded from each neuron (all spikes) exclusively into one of three sets: isolated spikes (ISO), chance coincidences (CC), and Unitary Events (UE). Spikes involved in pairwise coincidences (within 3 ms) are classified as CC if they occur during time periods where the observed coincidence rate is explained by the instantaneous trial-by-trial rates of the two involved neurons, and as UE if their number significantly exceeds the expectation (see Methods). In a given UE period a distinction between coincidences stemming from the activation of the assumed assembly and those due to chance is not possible. Therefore, a substantial fraction (see Discussion for an estimate) of coincidences in the UE group may be due to chance coincident spiking (e.g., the rightmost UE coincidence in Fig. 2). Spikes not classified as CC or UE with respect to any of the simultaneously recorded neurons (2-5) are classified as ISO. Consequently each spike is labeled according to the type of event it belongs to, and an individual spike train may contain spikes of different categories (compare gray, cyan, and red boxes in Fig. 2, respectively).

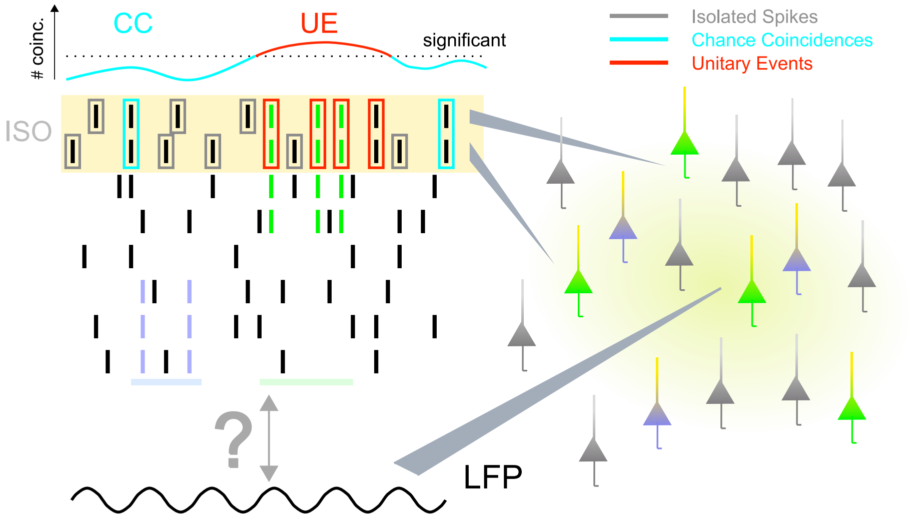

Figure 2: **Sketch of the analysis.** Spikes of two neurons (yellow background) and an LFP are recorded from electrodes separated by approximately 400 μm (right). Spikes are classified as isolated (ISO, gray), chance coincidence (CC, cyan), or Unitary Event (UE, red) depending on their precise synchronization with a spike of a second neuron recorded in parallel. In contrast to CCs, UEs identify coincidences in transient epochs where the high number of observed coincidences (top left) significantly exceeds the prediction based on the firing rates (in practice, coincidences are counted across trials, which is omitted here for illustrative purpose). In UE epochs, synchrony between both neurons in excess of the chance contribution is explained by their specific co-activation in a neuronal ensemble, termed assembly. Two assemblies are sketched in green and blue but the recorded neurons participate only in the green one. We investigate the relationship of the two types of observed spike synchrony (CC and UE) to the LFP population signal as a monitor of brain processing.

The magnitude of spike-triggered LFP averages increases with synchrony

As a first step, Fig. 3A compares the spike-triggered averages (STAs) of the LFP for the three sets, where each STA is pooled across all neuron-LFP pairs. We observe that the magnitude of the STAs of both chance coincidences (left, cyan) and Unitary Events (middle, red) significantly exceed that of the isolated spikes (gray). Moreover, the spike-triggered average of UE is larger than that of CC (right). The oscillatory structure of the STAs exhibits a strong beta frequency component, and the STAs are typically centered on the downward slope of the oscillation cycle. Non-averaged, single-neuron STAs also exhibit these differences, but to a lesser degree (see supplemental Fig. S2A for a typical example). The reason for this is two-fold: First, individual pairs have a substantially higher sampling variance, especially considering the typically low number of UE spikes. Second, STA shapes result from the combination of three effects: instantaneous LFP frequency, spike-LFP phase locking and oscillation amplitude. Nevertheless, the STA increase, in particular for UE spikes, is observed in a significant number of single neurons of both monkeys (Fig. 3B) and is consistently more pronounced for experiments where we were able to evaluate a larger number of partner neurons Np for potential coincidences (Fig. 3C), thus better separating the CC and UE groups.

Two mechanisms could underlie the differences in the STAs: changes in LFP amplitude or changes in the locking between LFP and spikes. However, the LFP amplitude does not co-vary with spike rate (Fig. 3D). Therefore increased amplitudes and the disproportionate increase of the chance coincidence count during periods of elevated rates is an improbable cause of the STA increase for CC. In addition, spike histograms triggered on the peaks of the LFP oscillations (supplemental Fig. S2B) reveal that spikes do not only tend to prefer the falling phase, but also avoid the rising phase of the LFP. This suggests that the three sets of spikes differ in the

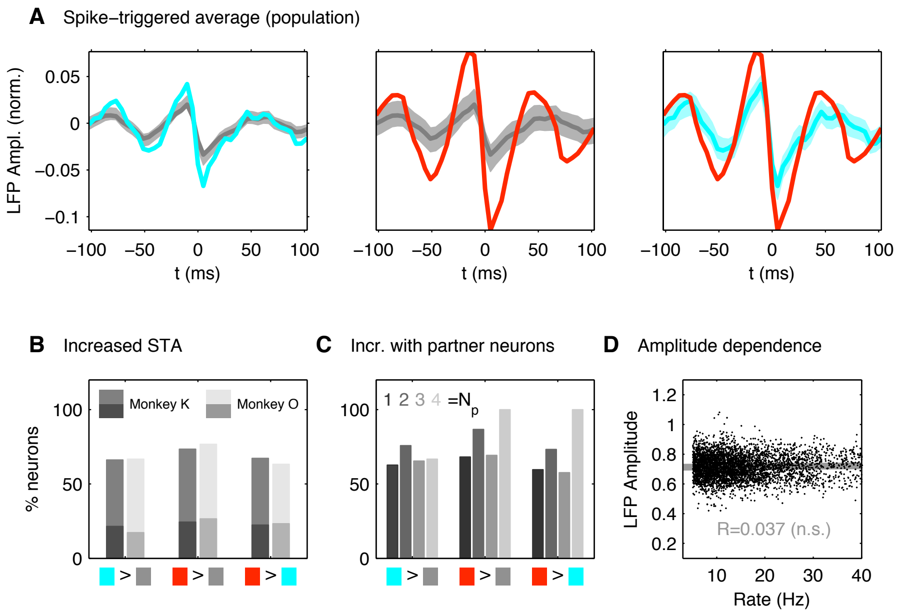

Figure 3: **The magnitude of the spike-triggered average (STA) depends on the occurrence of synchronized spiking activity.** (A) STA of the LFP averaged over all 123 neurons (n=297484 spikes total) for the three disjunct sets of spikes. The left panel compares STAs of ISO (dark gray curve, n=240455) to CC (cyan curve, n=44867). To account for the difference in variability due to sample sizes, the STA of ISO is repeatedly recomputed using only 44867 random trigger spikes. The light gray band encloses at each point in time 95% of all recomputed STAs. The middle and right panel compare STAs of UE (red curve, n=12162) to ISO and CC, respectively. (B) Relative number of neurons per animal (vertical) with the STA of one spike set exceeding (in area) the STA of the other set (horizontal, color codes). The STA of the first set qualifies as larger if it exceeds the other STA in 50% of 1000 recomputations (superimposed darker bars: 95%, i.e. α=5%). (C) The four bars distinguish STAs obtained for neurons with the same number Np of partner neurons used in coincidence detection. Same criteria (50%, both animals) as in B. (D) The correlation of LFP amplitude and spike rate is not significant (α=0.01, coefficient R).

degree of phase coupling to the LFP rather than in the accompanying amplitude of the LFP.

Increased spike synchrony improves spike-LFP phase coupling

Nevertheless, in order to clearly differentiate between these mechanisms, it is necessary to formally disentangle the dependence of spike timing on the amplitude of the LFP from its dependence on the phase. Fig. 4A explains the procedure (for details see Methods). For both monkeys we consistently observe a prominent beta oscillation (in both monkeys around 15 Hz) of the LFP during the preparatory period that stops with movement onset (Mvt). Therefore we focus on the beta frequency band and extract the instantaneous phase and amplitude (envelope) of the field potential for each spike time. Compared to the STA analysis, even individual neurons exhibit clear and specific differences between ISO, CC, and UE in both measures (Fig. 5, same example neuron as in Figs. 1 and 4). We are now prepared to study the two contributions in detail across the population.

Fig. 4B shows that across the population of neurons CC are systematically better locked (decreased circular standard deviation σ of the phase distribution) than ISO, and UE better than CC. As a suitable reference value to compare the fraction of locked neurons in the 3

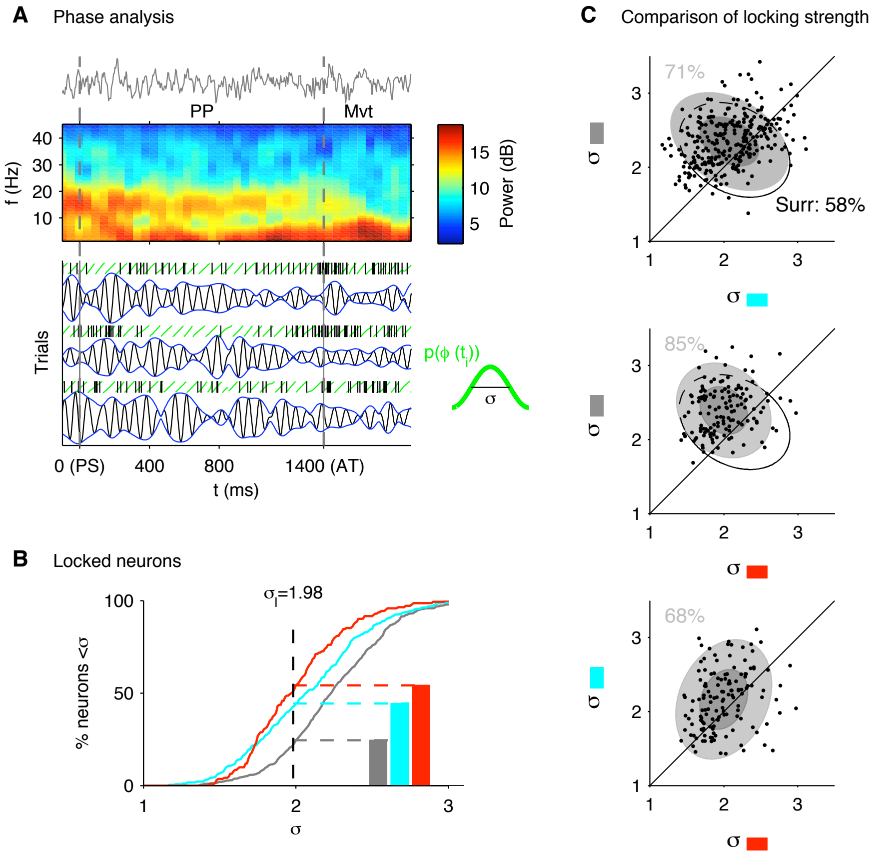

Figure 4: **LFP-spike phase coupling reveals locking increase for coincidences.** (A) Determination of phase and amplitude (example neuron). Top: single LFP trial; middle: trial-averaged power spectrogram. The beta activity during the preparatory period (PP, between PS and AT) disappears with movement (Mvt). Bottom: Phase (green) and amplitude (blue) of the beta-filtered LFP (upper trial shown in the top graph) extracted at the spike times (ticks). Resulting spike-triggered phase distributions (green) are characterized by their circular standard deviation σ. Same neuron as in Fig. 1. (B) Percentage of neurons in ISO (gray curve), CC (cyan), and UE (red) with a circular standard deviation of the phase distribution below σ (horizontal axis). For the average σ_l=1.97 of the set of significantly locked neurons (all spikes, α=0.05) the percentages are also shown as bars. (C) Comparisons of the circular standard deviations σ of the three sets in the individual neurons: ISO vs. CC (top, n=291), ISO vs. UE (middle, n=142), and CC vs. UE (bottom, n=136). Each dot represents one neuron in one experimental configuration. The percentages show the relative number of data points above the diagonal. The light (dark) gray ellipse covers 2 (1) standard deviations of the sample variance (outlined ellipse: surrogate data ISO vs. CC with shuffled ISIs).

sets we extracted the average locking strength σ_l=1.98 obtained for those neurons that are significantly locked if *all* spikes are considered (surrogate test). In the following we investigate how the systematic differences in locking strength between the three sets of spikes are affected by the intrinsic spike-LFP relationship of the neurons, i.e. if a neuron in general tends to lock well to the LFP or not. Differentiating groups of strongly (39%) and weakly (61%) locked neurons (i.e., significantly locked and unlocked neurons considering all their spikes) does not introduce a bias by affecting the percentage of neurons that exhibit CC and UE (supplemental Fig. S3A). Both groups exhibit the same general pattern of locking in the three groups (supplemental Fig. S3B) shown in Fig. 4B. As expected, the percentage of neurons better locked than σ_l in the ISO group differs considerably (53% vs. 6%, gray bars in supplemental Fig. S3B) between strongly and weakly locked neurons. However, this difference between strongly and weakly locked neurons is less pronounced for CCs (63% vs. 32%) and further decreases for UEs (65% vs. 46%). The conservation of the locking of UE spikes in strongly and weakly locked neurons compared to the declines for ISO and CC hints at different dynamical origins of the spikes in CC and UE.

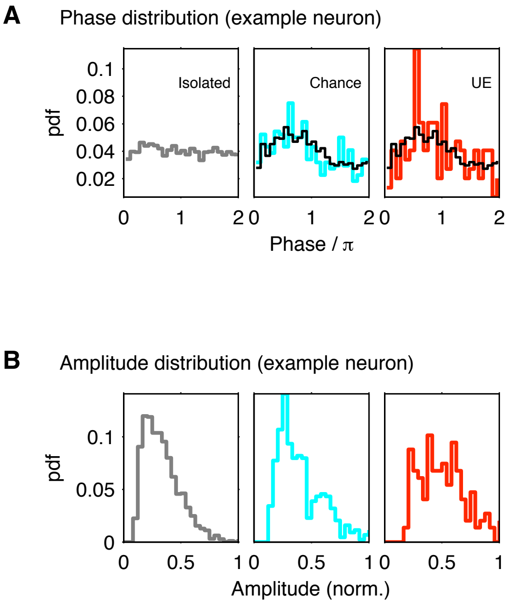

Figure 5: **Phase and amplitude distributions in a single neuron.** Same neuron as in Figs. 1 and 4. All distributions are normalized to unity area and are shown separately for ISO (left), CC (middle), and UE (right). (A) The modulation of the phase distribution increases from left to right. Phase π is the location of the trough of the LFP oscillation. The black curve in the middle and the right panel is the expected phase distribution of coincidences predicted from the phase distributions of the contributing neurons (see Methods). (B) Simultaneously to the increased locking, the amplitude distribution shifts to higher values.

Fig. 4C confirms that individual neurons are consistent with the findings for population ratios (Fig. 4B). The scatter plots of the circular standard deviation reveal that in 71% of the recorded neurons CC spikes are better locked than ISO spikes, and in 85% of the neurons UE spikes are better locked than ISO spikes. Finally, in 68% of all neurons UE spikes are better locked to the LFP than CC spikes. In contrast to the experimental data, only 58% of surrogate spike trains that retain the original inter-spike interval statistics show an increase in phase locking for coincident spikes (outlined ellipse).

Because of the consistency in the population, in the following we focus on the phase locking of strongly locked neurons. The rationale is to reduce the differences in locking between the three sets of spikes to obtain a conservative estimate of the locking (supplemental Fig. S3B). Comparable results are obtained for the complete set of recorded neurons. The phase distributions in the top panels of Fig. 6A show that locking of spikes to the LFP is strongest for Unitary Events, and weakest for isolated spikes.

The phase distribution exhibited already by isolated spikes modulates the spiking probability in time. Given the high level of synchrony between LFPs (Fig. 1A), one may therefore argue that the increased modulation of the phase distribution of CC trivially results from the individual phase locking distributions of the two neurons forming the coincidence (predictor assuming independence of neurons, see Methods). Interestingly, the phase distribution of CC is indeed largely in agreement with this predictor (black curve in Fig. 6A), while that of UE is not. Hence, despite the impossibility to remove the substantial fraction of chance coincidences from the UE group, the locking of UE cannot be explained on the basis of the intrinsic phase locking of the neurons forming the coincidences.

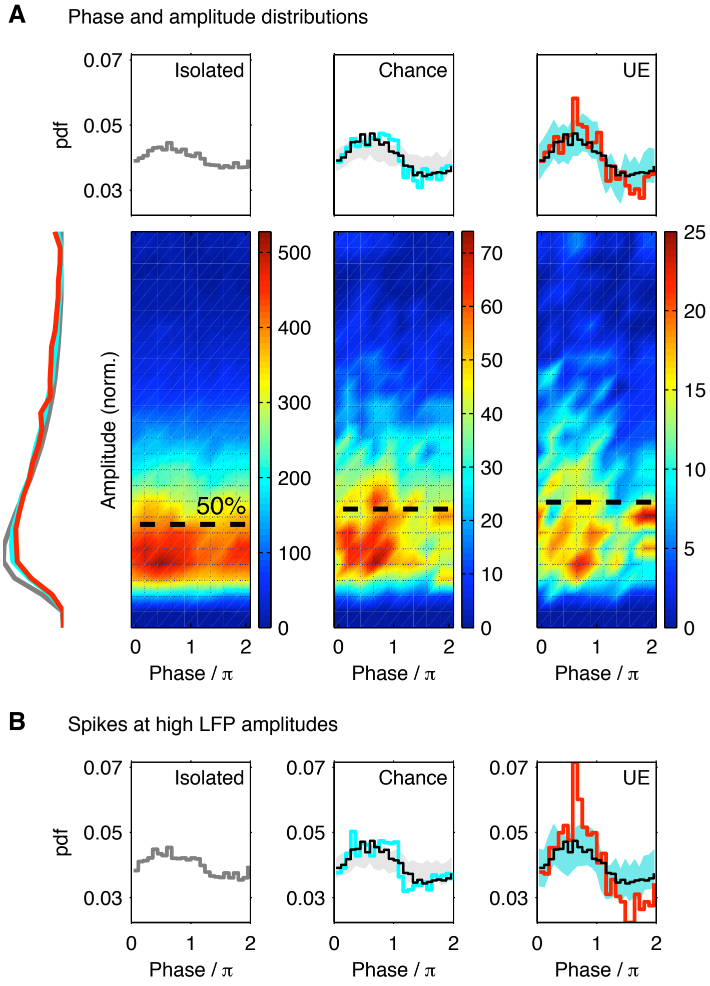

Figure 6: **Relation of spike synchrony to the interplay of phase and amplitude.** (A) Joint histograms of the phase and amplitude for ISO (left), CC (middle), and UE (right) pooled across the population (color bars indicate counts; phase π indicates LFP troughs). The top and left projections display the phase and amplitude distributions, respectively. The top middle and top right graph compare the phase distribution to the distribution shown in the graph to the left: The shaded areas enclose at each phase 95% of 1000 phase distributions randomly chosen from the set to the left with the same number of spikes as in the current set. Black curves are the predictions based on the phase distributions of the individual neurons. The histograms include the neurons that have a minimal spike count (total of 25 spikes and a mean rate of 5 Hz per trial) and for which the phase distribution of all spikes is significantly locked (α=0.05). (B) Phase distributions of the three sets, considering only 50% of spikes at the highest LFP amplitudes (above dashed black line in A).

Magnitude of global oscillations influences spike locking

Earlier studies (Murthy and Fetz, 1996b; Denker et al., 2007) demonstrate that spikes occurring during periods of high LFP amplitudes exhibit a stronger locking to the LFP. At a given time the amplitude of the LFP oscillation is defined by its envelope (blue curves in Fig. 4A). To examine the dependence of spike locking on the amplitude of the LFP (Denker et al., 2007), we form two exclusive sets of spikes, termed 'Hi' and 'Lo', based on whether a spike occurs at an amplitude above or below a certain value, respectively (Fig. 7A). We account for the session-by-session variability of the LFP amplitude by defining the threshold θ in terms of the fraction of spikes an individual neuron contributes to the Lo category (Fig. 7B).

For threshold ranges between 0.2 and 0.8 we observe that the percentage of significantly locked neurons (Rayleigh test, α=0.05) of the Hi set is only decaying slightly from 41% to 36% (Fig. 7C). This percentage is in the same range as the percentage of locked neurons considering all spikes (Fig. 4B). We emphasize that even for high thresholds, where only few spikes are included, the locking of neurons can be explained using Hi spikes only. In contrast, when considering spikes of the Lo set, the percentage of locked neurons starts at 9% and increases approximately linearly with θ at a much steeper slope, meaning that at increasingly higher amplitudes more and more spikes are included in the Lo set. This shows that locking of spikes to the local field potential is largely due to spikes that occur at high LFP amplitudes.

Combined effects of synchrony and LFP amplitude

Combination of the previous results raises the question of whether coincidences, and in particular Unitary Events, predominantly occur at high LFP amplitudes. Fig. 6A (density plots) shows the number of spikes as a function of both LFP phase and amplitude for each of the three sets ISO, CC, and UE. Here, CC and UE occur at similar amplitudes as ISO, even though the amplitude distributions (left) reveal a small shift towards high amplitudes for CC and UE. The phase distributions (top panels), however, clearly show a progressive increase in the degree of phase locking from ISO to CC to UE. Finally, observing that UEs exhibit similar amplitudes as CC, we can ask the reverse question of whether at high amplitudes ISO, CC and UE still exhibit the systematic increase in locking. Fig. 6B shows that for the 50% of the spikes occurring at the largest LFP amplitudes (above black dashed line in Fig. 6A) the effect of improved phase locking for the UE group is strongly amplified. In contrast, the ISO and CC phase distributions do not change. This finding reveals that those coincidences in UE periods that are responsible for the increased locking of UE are those that occur during strong LFP oscillations.

Discussion

In this report we explicitly reveal how the local field potential relates to precise excess spike synchrony in motor cortex. Spikes which are emitted at the same time as spikes of other neurons exhibit a better phase locking to the dominant beta-range LFP oscillation than those which occur in isolation. However, in time periods where the number of spike coincidences is at chance level, the quality of the locking is explained by a predictor assuming independence of the spikes constituting a coincidence. In contrast, the pronounced locking to the LFP in time periods with a significant excess of coincident spikes (Unitary Events) cannot be explained in this way. The probability of the occurrence of coincident spikes is only weakly coupled to changes in the magnitude of the LFP signal. Nonetheless, spikes that coincide with episodes of high LFP amplitudes are on average better locked to the LFP than those at low amplitudes. A separate analysis of these two factors, identified spike synchrony and LFP magnitude, demonstrates that both affect the strength of the spike-LFP coupling largely independent of each other. What conclusions about network dynamics and possible coding mechanisms do these results imply, in particular in the light of the distinctive role of Unitary Events?

Features of the LFP signal correlate with external stimuli (O'Leary and Hatsopoulos, 2006),

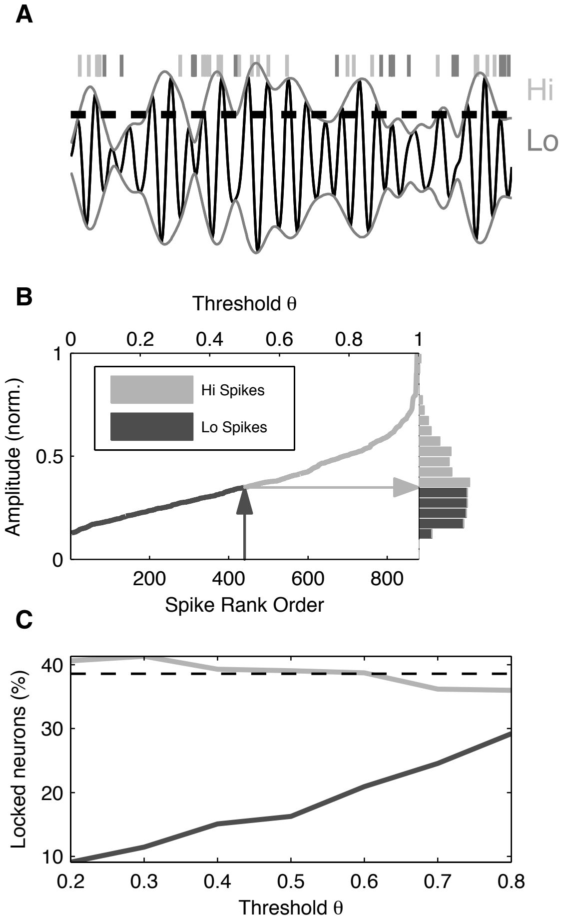

Figure 7: **Influence of oscillation magnitude on locking of spikes to LFP.** (A) Spikes in periods with an LFP magnitude (i.e. envelope of LFP, light gray curve) above a certain threshold (dashed line) are termed the 'Hi' set (light gray ticks) and the remainder the 'Lo' set (dark gray ticks). (B) Separation of spikes into Hi and Lo for the same example neuron as in Figs. 1, 4, and 5. Spikes are rank ordered according to LFP magnitude; the histogram on the right shows the distribution of the respective magnitudes. The threshold θ is defined as the relative number of spikes labeled as Lo. The dark gray arrow illustrates a threshold choice of θ=0.5, and corresponds to a data dependent relative amplitude (light gray arrow). Spikes at extremely low LFP amplitudes (lowest 10%) do not enter the analysis. (C) Percentage of neurons with significant (Rayleigh test, α=0.05) phase-locking of the Hi spikes (light gray curve) and of the Lo spikes (dark gray curve) as a function of magnitude threshold. Even for large θ (0.8) the set of Hi spikes shows significant locking in 36% of the neurons, although it consists of only few spikes. The dashed line shows as a reference the percentage (39%) of locked neurons computed if spikes are not separated into Hi and Lo (i.e. all spikes). Thus the locking of neurons is mainly explained by the locked Hi spikes, and their locking is approximately independent of θ.

behavioral aspects (Scherberger et al., 2005), internal processes (Murthy and Fetz, 1996a; Poulet and Petersen, 2008; Roux et al., 2006), and attentional modulation (Fries et al., 2001). In particular, several authors have elucidated the functional role of LFP oscillations in motor cortex in the beta and lower gamma range. These oscillations are only loosely correlated across trials, i.e. their phase is not time-locked to any external (e.g. stimulus) or internal (e.g. movement onset) event. Oscillatory beta range LFP activity in motor cortex is a unique feature of experimental protocols including a waiting period before movement execution and has been described in relation to attentional processes, movement preparation and motor maintenance

(Donoghue et al., 1998; O'Leary and Hatsopoulos, 2006; Murthy and Fetz, 1992, 1996a; Baker et al., 1997; Sanes and Donoghue, 1993). The oscillations terminate at movement onset and may well represent a top-down modulatory input from higher sensory areas (e.g., Lebedev and Wise, 2000). Furthermore, there is a large body of knowledge about delay-related spiking activity in motor cortical areas and its functional implication in sensorimotor integration and movement preparation (for a review, see Riehle, 2005). Finally, transient spike synchrony observed among individual neurons is remarkably well related to timing-related aspects of the behavioral task (Riehle et al., 1997; Kilavik et al., 2009) but does not depend on the mean firing rate of the participating neurons (Grammont and Riehle, 2003). However, only a few studies relate LFP oscillations to correlations of the spiking activity (Murthy and Fetz, 1996b; Nir et al., 2007). Reports in various brain areas demonstrate single neurons which selectively participate in oscillatory periods of the LFP by phase locking (Fries et al., 2001; Eckhorn and Obermueller, 1993; Baker et al., 1997; Destexhe et al., 1999), where occasionally the autocorrelations of the spike trains become oscillatory (Murthy and Fetz, 1996b; Lebedev and Wise, 2000). In conclusion, the apparent complexity of the simultaneous coding of neuronal activity for different aspects of motor cortical processing challenges the idea that LFP oscillations and the emergence of transient UEs are two reflections of only one single functional process performing the planning and preparation of movements.

We interpret the observed excess synchrony as a result of the specific activation of the observed neurons. An alternate hypothesis indicates that strong non-stationarities of the firing rates are the cause for false-positive detections of UE periods, which could explain the observed phase locking of UE if rates were co-modulated with the LFP oscillations cycles. To investigate this possibility, we reanalyzed the data by replacing the parametric distribution implementing the null hypothesis in the original UE analysis by a distribution derived by surrogates. The employed surrogate method (spike train dithering, see Grün, 2009) closely preserves the rate profiles and the inter-spike interval distributions, and leads to a conservative (Louis et al., 2010) classification of excess synchronous events. Despite the decreased sensitivity of the surrogate based method to detect excess synchrony, our analysis confirms the phase distributions for ISO, CC, and UE that are the essential finding of our study. Thus, they are not explained as a consequence of rate co-variations, but express excess synchrony as a reflection of coordinated network activity.

It is reasonable to assume that synchrony on a spike-by-spike level, and population oscillations expressed by the LFP both originate from network processes that involve the pulsed, synchronous co-activation of specific subsets of neurons. One may argue that in this case we should observe an even more distinct relationship between the two measures. However, our techniques to detect synchrony related to the activation of neuronal assemblies are limited. The Unitary Event analysis assesses indirectly which coincidences are more likely to originate from such activations based on the comparison of the time-resolved rate of observed and expected coincidences. Nevertheless, the set of UEs may be composed of coincidences resulting from assembly activation and a considerable fraction of chance coincidences (see estimate below). Therefore, although the difference in locking precision between significant (UE) and non-significant (CC) time segments seems small at first glance, in this light it is even more surprising that we are able to observe an enhanced phase locking for the UEs. The argument implies that the subset of coincidences caused by assembly activation has a tight locking to the LFP. This conclusion is supported by previous work demonstrating that coherent membrane potential oscillations do not generate synchronized output spikes, and that brief, simultaneous synaptic inputs to a cell are the likely drive for action potential generation (Poulet and Petersen, 2008).

Unitary Events prefer a particular phase of the LFP oscillation, a signal which is rather homogeneous across the motor cortex (Murthy and Fetz, 1996a; Rubino et al., 2006). This finding renders unlikely a model of processing where assemblies can be simultaneously active and still distinguished (multiplexed) by locking to different phases of the oscillatory cycle (e.g., Womelsdorf et al., 2007). Moreover, in such a model the waxing and waning of the LFP oscillation would likely show phase shifts as different assemblies become active. Our results insinuate that neurons participate in different assemblies at different times (see also Riehle et al., 1997), but predominantly at the same phase of the LFP (cf., Singer, 1999). We observe the phenomenon in 20-30% of the neurons in agreement with estimates from other studies (e.g., Murthy and Fetz, 1996b). However, even in this category of neurons we can attribute only a fraction of spikes to assembly activation. One hypothesis is that the motor cortex is involved in parallel coding schemes, where synchronous assembly activity can be dissociated from the rate-based continuous-time coding.

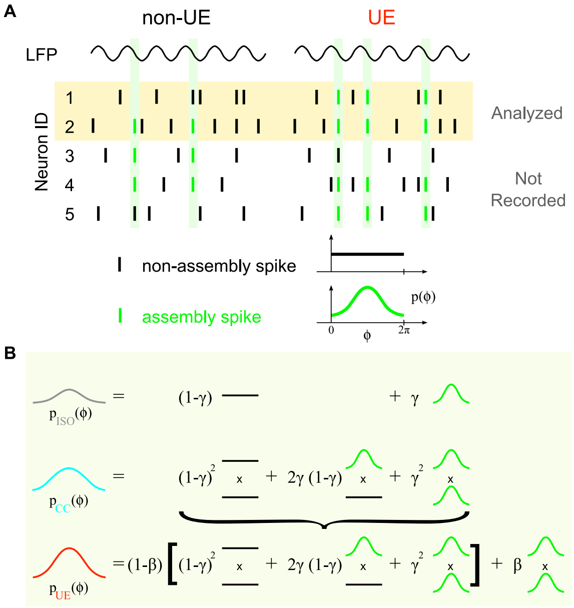

Figure 8: **A conceptual model relating increased LFP locking and assemblies.** (A) Sketch of the LFP (top) and the simultaneous spiking activity of five neurons (middle), of which only two are recorded (yellow background). Based on the latter, time periods where coincidences occur at chance level (non-UE, left) are distinguished from those with excess synchrony (UE, right). Each spike is either part of an assembly of co-active neurons (green) or not (black). In this simplified scenario, one assembly is active on the left, and a different one on the right; both observed neurons contribute to the latter. Only assembly spikes exhibit locking to the LFP, expressed by a non-uniform phase distribution $p(\varphi)$ (green). (B) Two ratios β and γ determine the composition of the phase distributions for ISO, CC, and UE (left) of assembly and non-assembly spikes. γ determines the overall probability that a spike is part of an assembly activation (top, ISO). $p_{CC}(\varphi)$ (middle) results from the combinatorics of two independent spike trains (ISO). $p_{UE}(\varphi)$ (bottom) differs from $p_{CC}(\varphi)$ by the relative excess β of assembly spikes in UE periods. A conservative (minimal) estimate of β, i.e., maximally locked $p_2\varphi$, is obtained by substituting $p_{UE}(\varphi)$ and $p_{CC}(\varphi)$ in the bottom equation by the experimental distributions. γ is determined from either of the top two equations by using $p(\varphi)$.

To better understand the implications for the organization of cortical processing we consider a conceptual model where spikes of a neuronal assembly are locked to the LFP (Fig. 8) based on (*i*) the assumption that UEs reflect assembly activity (Riehle et al., 1997) and (*ii*) our observation that UEs have the strongest locking to the LFP. A potential mechanism is that assembly spikes originate from synchronous synaptic input to local groups of neurons. The simplest explanation for the finding that ISO and CC also exhibit locking, albeit weaker than UE, is that the spikes of a neuron are composed of a mixture of non-assembly (unlocked) and assembly spikes (locked). The latter are not identified as UE due to the lack of corresponding partner neurons in the recording (Fig. 8A). Consequently, the phase histogram of the ISO spikes is a superposition of the histograms of non-assembly and assembly spikes, with a factor γ determining their ratio (Fig. 8B, top row). Chance coincidences are composed of spikes from independent sources (Fig. 8B, middle row) but the combinatorics of non-assembly and assembly spikes enhances the locking. Finally, periods identified as UE contain excess coincidences (Fig. 8B, bottom row) resulting from the activation of an assembly in which both neurons participate. Their relative contribution β leads to an enhanced locking of UE compared to CC. The structure of the model allows us to derive minimal estimates of the parameters γ and β from the experimental phase histograms. We find that outside of UE periods γ=13% of the spikes of a neuron participate in an assembly, and β=24% of the coincidences in UE periods result from the joint participation in an assembly. Even though this is clearly a highly simplified model, it provides a first quantitative bridge between functionally relevant spike synchrony (Riehle et al., 1997; Singer, 1999; Maldonado et al., 2008) and the LFP as a robust mesoscopic measure of brain activity (Mehring et al., 2003).

Our results show that neuronal mass signals like the LFP convey specific information about network processes. We directly demonstrate in the brain of a behaving animal that the LFP is related to excess spike synchronization. Nevertheless, there is a substantial fraction of spikes without an apparent relationship to the LFP. Thus the two measures are observables of the same neuronal network but do not necessarily carry the same information. Taken together, we interpret our results as evidence that LFP (beta) oscillations, especially at high amplitudes, are reflections of the activation of neuronal assemblies which propagate a synchronous volley through the network. Complementing recent advances in tackling the experimental (Euston et al., 2007; Fujisawa et al., 2008; Nicolelis et al., 1997) and theoretical (Brown et al., 2004; Grün, 2009) difficulties in finding signatures of coordinated activity in spike data alone, these findings indicate how the LFP may provide a valuable additional source of information to characterize the neuronal population dynamics. With massively parallel recordings becoming available we may be able to disambiguate the superposition of multiple neuronal assemblies. This gives us confidence that by improving our understanding of the various components of the LFP signal we will eventually be able to use the LFP as an antenna delivering news from several communicating network stations.

Funding

This work was supported by the Stifterverband für die Deutsche Wissenschaft; the Bundesministerium für Bildung und Forschung, Germany (BMBF, grant 01GQ0413 to BCCN Berlin); the Helmholtz Alliance on Systems Biology; the French National Research Agency (ANR-05-NEUR-045-01); the Deutscher Akademischer Austauschdienst (DAAD); The Research Council of Norway (eScience Programme) and the European Union (grant 15879, FACETS).

Acknowledgments

We thank Moshe Abeles, Walter Freeman, and George Gerstein for valuable comments on an earlier version of the manuscript.

References

Aertsen AM, Gerstein GL, Habib MK, Palm G. 1989. Dynamics of neuronal firing correlation: modulation of "effective connectivity". *J Neurophysiol.* 61: 900-917.

Baker SN, Olivier E, Lemon RN. 1997. Coherent oscillations in monkey motor cortex and hand muscle EMG show task-dependent modulation. *J Physiol.* 501: 225-241.

Berens P, Keliris GA, Ecker AS, Logothetis NK, Tolias AS. 2008. Feature selectivity of the gamma-band of the local field potential in primate primary visual cortex. *Front Neurosci.* 2: 199-207.

Boashash B. 1992. Estimating and interpreting the instantaneous frequency of a signal. I. Fundamentals. *Proc IEEE.* 80: 520-538.

Brown EN, Kass RE, Mitra PP. 2004. Multiple neural spike train data analysis: state-of-the-art and future challenges. *Nat Neurosci.* 7: 456-461.

Buzsáki G. 2004. Large-scale recording of neuronal ensembles. *Nat Neurosci.* 7: 446.

Buzsáki G, Draguhn, A. 2004. Neuronal oscillations in cortical networks. *Science.* 304: 1926-1929.

Cardin JA, Carlén M, Meletis K, Knoblich U, Zhang F, Deisseroth K, Tsai L-H, Moore CI. 2009. Driving fast-spiking cells induces gamma rhythm and controls sensory responses. *Nature.* 459: 663-667.

Denker M, Roux S, Timme M, Riehle A, Grün S. 2007. Phase synchronization between LFP and spiking activity in motor cortex during movement preparation. *Neurocomp.* 70: 2096-2101.

Destexhe A, Contreras D, Steriade M. 1999. Spatiotemporal analysis of local field potentials and unit discharges in cat cerebral cortex during natural wake and sleep phases. *J Neurosci.* 19: 4595-4608.

Donoghue JP, Sanes JN, Hatsopoulos NG, Gaál G. 1998. Neural discharge and local field potential oscillations in primate motor cortex during voluntary movements. *J Neurophysiol.* 79: 159-173.

Eckhorn R, Bauer R, Jordan W, Brosch M, Kruse W, Munk M, Reitboeck HJ. 1988. Coherent oscillations: a mechanism of feature linking in the visual cortex? Multiple electrode and correlation analyses in the cat. *Biol Cybern.* 60: 121-130.

Eckhorn R, Obermueller A. 1993. Single neurons are differently involved in stimulus-specific oscillations in cat visual cortex. *Exp Brain Res.* 95: 177-182.

Eeckman, FH, Freeman, WJ. 1990. Correlations between unit firing and EEG in the rat olfactory system. *Brain Res.* 528: 238-244.

Engel AK, König P, Gray CM, Singer W. 1990. Stimulus-Dependent Neuronal Oscillations in Cat Visual Cortex: Inter-Columnar Interaction as Determined by Cross-Correlation Analysis. *Eur J Neurosci.* 2: 588-606.

Euston DR, Tatsuno M, McNaughton BL. 2007. Fast-forward playback of recent memory sequences in prefrontal cortex during sleep. *Science.* 318: 1147-1150.

Friedrich RW, Habermann CJ, Laurent G. 2004. Multiplexing using synchrony in the zebrafish olfactory bulb. *Nat Neurosci.* 7: 862-871.

Fries P, Reynolds JH, Rorie AE, Desimone R. 2001. Modulation of oscillatory neuronal synchronization by selective visual attention. *Science.* 291: 1560-1563.

Fries P, Nikolić D, Singer W. 2007. The gamma cycle. *Trends Neurosci.* 30: 309-316.

Fujisawa S, Amarasingham A, Harrison MT, Buzsáki G. 2008. Behavior-dependent short-term assembly dynamics in the medial prefrontal cortex. *Nat Neurosci.* 11: 823-833.

Gerstein GL, Bedenbaugh P, Aertsen, MH. 1989. Neuronal assemblies. *IEEE Trans Biomed Eng.* 36: 4-14.

Grammont F, Riehle A. 2003. Spike synchronization and firing rate in a population of motor cortical neurons in relation to movement direction and reaction time. *Biol Cybern.* 88: 360-373.

Grün S. 2009. Data driven significance estimation of precise spike correlation. *J Neurophysiol.* 101: 1126-1140.

Grün S, Diesmann M, Aertsen A. 2002a. Unitary events in multiple single-neuron spiking activity: I. Detection and Significance. *Neural Comput.* 14: 43-80.

Grün S, Diesmann M, Aertsen A. 2002b. Unitary events in multiple single-neuron spiking activity: II. Nonstationary data. *Neural Comput.* 14: 81-119.

Grün S, Diesmann M, Grammont F, Riehle A, Aertsen A. 1999. Detecting unitary events without discretization of time. *J Neurosci Meth.* 94: 67-79.

Grün S, Riehle A, Diesmann M. 2003. Effect of cross-trial nonstationarity on joint-spike events. *Biol Cybern.* 88: 335-351.

Harris KD, Henze DA, Hirase H, Leinekugel X, Dragoi G, Czurkó A, Buzsáki G. 2002. Spike train dynamics predicts theta-related phase precession in hippocampal pyramidal cells. *Nature.* 417: 738-741.

Hasenstaub A, Shu Y, Haider B, Kraushaar U, Duque A, McCormick DA. 2005. Inhibitory postsynaptic potentials carry synchronized frequency information in active cortical networks. *Neuron.* 47: 423-435.

Hebb DO. 1949. *The Organization of Behavior: A Neuropsychological Theory*. New York (NY): Wiley.

Jensen O. 2006. Maintenance of multiple working memory items by temporal segmentation. *Neuroscience*. 139: 237.

Katzner S, Nauhaus I, Benucci A, Bonin V, Ringach DL, Carandini M. 2009. Local origin of field potentials in visual cortex. *Neuron*. 61: 35-41.

Kayser C, Montemurro MA, Logothetis NK, Panzeri S. 2009. Spike-phase coding boosts and stabilizes information carried by spatial and temporal spike patterns. *Neuron*. 61: 597-608.

Kilavik BE, Roux S, Ponce-Alvarez A, Confais J, Grün S, Riehle A. 2009. Long-term Modifications in Motor Cortical Dynamics induced by intensive practice. *J Neurosci.* 29: 12653-12663.

Klausberger T, Magill PJ, Márton LF, Roberts JDB, Cobden PM, Buzsáki G, Somogyi P. 2003. Brain-state- and cell-type-specific firing of hippocampal interneurons in vivo. *Nature.* 421: 844-848.

Lebedev MA, Wise SP. 2000. Oscillations in the premotor cortex: single-unit activity from awake, behaving monkeys. *Exp Brain Res.* 130: 195-215.

Le Van Quyen V, Foucher J, Lachaux J, Rodriguez E, Lutz A, Martinerie J, Varela FJ. 2001. Comparison of Hilbert transform and wavelet methods for the analysis of neuronal synchrony. *J Neurosci Meth.* 111: 83-98.

Logothetis NK, Wandell BA. 2004. Interpreting the BOLD signal. *Annu Rev Physiol.* 66: 735-769.

Louis S, Borgelt C, Grün S. 2010. Generation and selection of surrogate methods for correlation analysis. In: Grün S, Rotter S, editors. *Analysis of Parallel Spike Trains.* Springer, (in press).

Maldonado P, Babul C, Singer W, Rodriguez E, Berger D, Grün S. 2008. Synchronization of neuronal responses in primary visual cortex of monkeys viewing natural images. *J Neurophysiol.* 100: 1523-1532.

Mardia, KV, Jupp PE. 2000. *Directional Statistics*, Chichester: John Wiley & Sons Ltd.

Mehring C, Rickert J, Vaadia E, de Oliveira SC, Aertsen A, Rotter S. 2003. Inference of hand movements from local field potentials in monkey motor cortex. *Nat Neurosci.* 6: 1253-1254.

Mitzdorf U. 1985. Current source-density method and application in cat cerebral cortex: investigation of evoked potentials and EEG phenomena. *Physiol Rev.* 65: 37-100.

Murthy VN, Fetz EE. 1992. Coherent 25- to 35-Hz oscillations in the sensorimotor cortex of awake behaving monkeys. *Proc Natl Acad Sci. USA* 89: 5670-5674.

Murthy VN, Fetz EE. 1996a. Oscillatory activity in sensorimotor cortex of awake monkeys: synchronization of local field potentials and relation to behavior. *J Neurophysiol.* 76: 3949-3967.

Murthy VN, Fetz EE. 1996b. Synchronization of neurons during local field potential oscillations in sensorimotor cortex of awake monkeys. *J Neurophysiol.* 76: 3968-3982.

Nauhaus I, Busse L, Carandini M, Ringach DL. 2009. Stimulus contrast modulates functional connectivity in visual cortex. *Nat Neurosci.* 12: 70-76.

Nawrot MP, Boucsein C, Rodriguez-Molina V, Riehle A, Aertsen A, Grün S, Rotter S. 2008. Measurement of variability dynamics in cortical spike trains. *J Neurosci Meth.* 169: 374-390.

Nicolelis MA, Ghazanfar, AA, Faggin BM, Votaw S, Oliveira LM. 1997. Reconstructing the engram: simultaneous, multisite, many single neuron recordings. *Neuron.* 18: 529-537.

Nir Y, Fisch L, Mukamel R, Gelbard-Sagiv H, Arieli A, Fried I, Malach R. 2007. Coupling between neuronal firing rate, gamma LFP, and BOLD fMRI is related to interneuronal correlations. *Curr Biol.* 17: 1275-1285.

Okun M, Nain A, Lampl I. 2010. The subthreshold relation between cortical local field potential and neuronal firing unveiled by intracellular recordings in awake rats. *J Neurosci.* 20: 4440.

O'Leary JG, Hatsopoulos NG. 2006. Early visuomotor representations revealed from evoked local field potentials in motor and premotor cortical areas. *J Neurophysiol.* 96: 1492-1506.

Poulet JFA, Petersen CCH. 2008. Internal brain state regulates membrane potential synchrony in barrel cortex of behaving mice. *Nature.* 454: 881-885.

Riehle A. 2005. Preparation for action: one of the key functions of the motor cortex. In: Riehle A, Vaadia E , editors. *Motor cortex in voluntary movements: a distributed system for distributed functions.* Boca Raton, (FL): CRC-Press, pp. 213-240.

Riehle A, Grün S, Diesmann M, Aertsen A. 1997. Spike synchronization and rate modulation differentially involved in motor cortical function. *Science.* 278: 1950-1953.

Roux S, Mackay WA, Riehle A. 2006. The pre-movement component of motor cortical local field potentials reflects the level of expectancy. *Behav Brain Res.* 169: 335-351.

Rubino D, Robbins KA, Hatsopoulos NG. 2006. Propagating waves mediate information transfer in the motor cortex. *Nat Neurosci.* 9: 1549-1557.

Sanes JN, Donoghue JP. 1993. Oscillations in local field potentials of the primate motor cortex during voluntary movement. *Proc Natl Acad Sci. USA* 90: 4470-4474.

Scherberger H, Jarvis MR, Andersen RA. 2005. Cortical local field potential encodes movement intentions in the posterior parietal cortex. *Neuron.* 46: 347-354.

Singer W. 1999. Neuronal synchrony: a versatile code for the definition of relations? *Neuron.* 24: 49-65.

Tetzlaff T, Rotter S, Stark E, Abeles M, Aertsen A, Diesmann M. 2008. Dependence of neuronal correlations on filter characteristics and marginal spike train statistics. *Neural Comput.* 20: 2133-2184.

Vaadia E, Haalman I, Abeles M, Bergman H, Prut Y, Slovin H, Aertsen A. 1995. Dynamics of neuronal interaction in monkey cortex in relation to behavioral events. *Nature.* 373: 515-518.

Viswanathan A, Freeman RD. 2007. Neurometabolic coupling in cerebral cortex reflects synaptic more than spiking activity. *Nat Neurosci.* 10: 1308-1312.

Womelsdorf T, Schoffelen J, Oostenveld R, Singer W, Desimone R, Engel AK, Fries P. 2007. Modulation of neuronal interactions through neuronal synchronization. *Science.* 316: 1609-1612.

Supplementary Figures

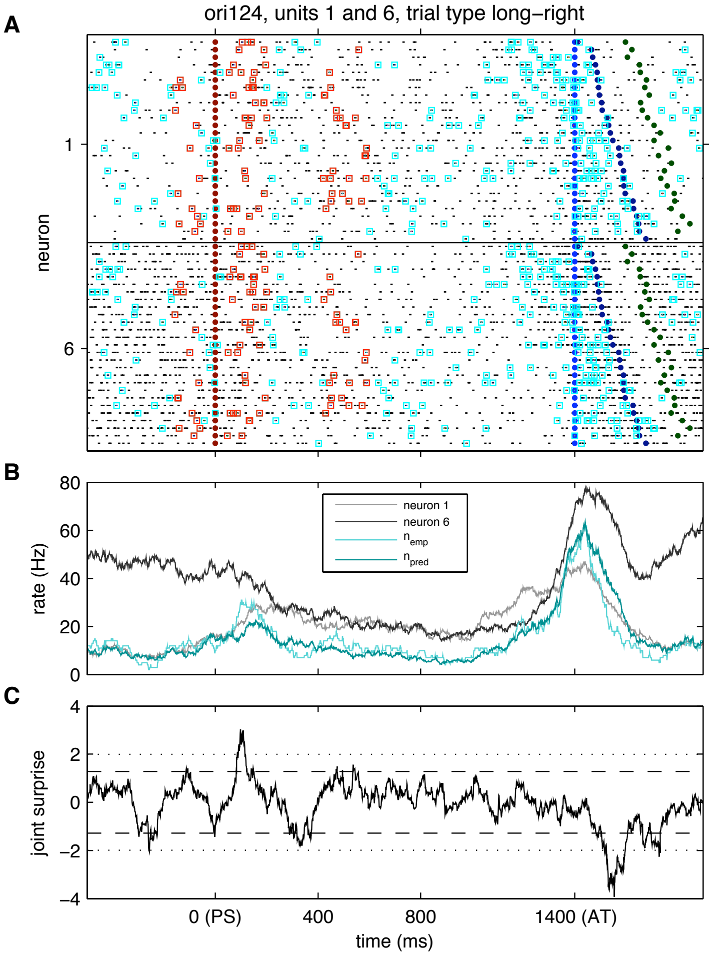

Figure 1: **Detection of Unitary Events.** (A) Spike rasters for the same neuron (neuron 6) shown in Figs. 1, 4, and 5 and one simultaneously recorded neuron (neuron 1). Each line in the rasters corresponds to one trial. Simultaneously recorded activities of the two neurons are shown on lines of the same height in the respective raster. Spikes are indicated by black dots, coincident spikes and Unitary Events are surrounded by a cyan or red square, respectively. Data shown are recorded during the self-paced task with long time delay (see Methods for experimental details). The corresponding behavioral events are marked in the rasters with differently colored filled circles: occurrence of the preparatory stimulus PS (dark red), allowed movement time AT (light blue), movement initiation (dark blue) and end of movement (dark green). (B) Firing and coincidence rates. The firing rates of the two neurons are shown in dark gray (neuron 6) and light gray (neuron 1), together with the rate of the empirical coincidences (light cyan) and the coincidence rate expected from the neurons' firing rates (dark cyan), calculated as the sum of the trial-by-trial rates. All rates are estimated in sliding windows of 100 ms width shifted by 0.1 ms. (C) Significance of empirical coincidences. The joint surprise (dark gray curve) results from the comparison of the empirical and the expected coincidence counts. Significant excess coincidences (i.e. UEs) are detected if the joint surprise is larger than the 5% level (dashed line). For comparison, the 1% level is also indicated (dotted line). UEs are found during a short period before PS occurrence, shortly after PS, and at 600 ms after PS. The latter is one of the short delay times that monkey was exposed to in parallel to the shown delay scheme. Note that although there is a considerable increase of coincident events in relation to the arm movement, they occur at chance level.

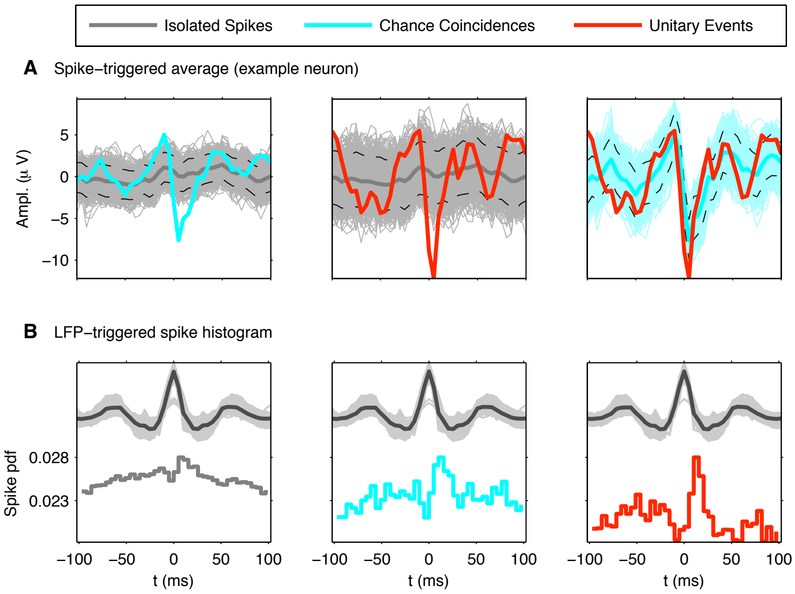

Figure 2: **Relationship of LFP and synchronized spiking behavior in a single neuron and LFP-triggered PSTHs of synchronized activity.** (A) STA of the LFP (filtered between 2-80 Hz to remove DC components) of one neuron (same neuron as in Figs. 1, 4, 5, and S1) for three disjunct sets of trigger spikes: not coincident with spikes from simultaneously recorded other neurons (isolated spikes, ISO, gray), involved in coincidences (within 3 ms) predicted by rate (chance coincidences, CC, cyan), and involved in significant coincidences (Unitary Events, UE, red). The left panel compares the STA of ISO (dark gray curve, n=4098) to the STA of CC (cyan curve, n=506). To account for the difference in variability due to sample sizes, the STA of ISO is recomputed using only 506 random trigger spikes. The light gray band results from the superposition of 1000 re-computations of which 95% are enclosed by the dashed curves at each point in time. Similarly, the middle and right panel compare the STA of UE (red curve, n=177) to the STA of ISO and CC, respectively. (B) Bottom: Population-averaged LFP-triggered histogram of ISO (left), CC (middle), and UE (right). The trigger times are the largest local maxima of the LFP that are separated by a minimum distance of 33 ms. The spikes of a neuron are triggered on exactly one LFP channel. Top: LFP averages for each neuron contributing to the histogram (light gray curves) based on the same trigger. The dark gray curve is the average of the single neuron LFP averages.

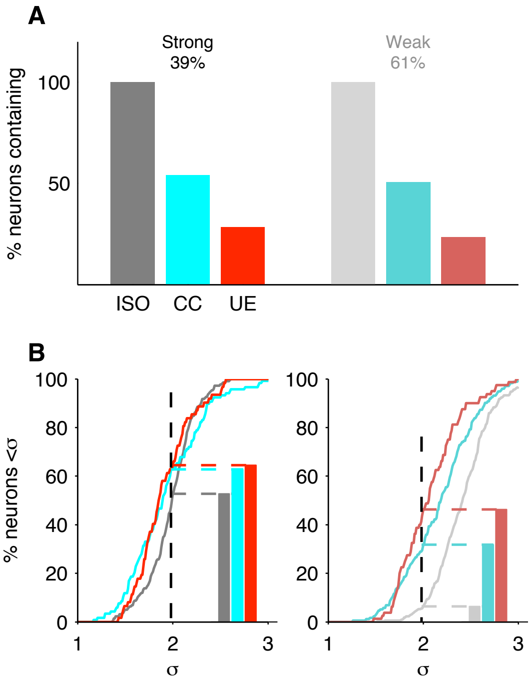

Figure 3: **The increased locking of UEs is independent of the overall degree of locking of the neuron.** (A) Fraction of neurons exhibiting (threshold of 25 spikes) ISO, CC and UE separately for the sets of strongly (left) locked and weakly (right) locked neurons (criterion: surrogate test (α=0.05) on original spike train containing all spikes). (B) Percentage of neurons with a locking stronger than σ_l in each of the two groups (strongly and weakly locked). For the selected value of σ_l=1.98 (average locking strength of strongly locked neurons) the percentages are shown as bars.